

Title	MOVPE growth and characterization of Al(Ga)N and InAlN/AlGaIn quantum wells for UV LED applications
Authors	Li, Haoning
Publication date	2015
Original Citation	Li, H. 2015. MOVPE growth and characterization of Al(Ga)N and InAlN/AlGaIn quantum wells for UV LED applications. PhD Thesis, University College Cork.
Type of publication	Doctoral thesis
Rights	© 2015, Haoning Li. - <a href="http://creativecommons.org/licenses/by-nc-nd/3.0/">http://creativecommons.org/licenses/by-nc-nd/3.0/</a>
Download date	2025-08-27 09:15:16
Item downloaded from	<a href="https://hdl.handle.net/10468/2283">https://hdl.handle.net/10468/2283</a>



**UCC**

Coláiste na hOllscoile Corcaigh, Éire  
University College Cork, Ireland

# **MOVPE Growth and Characterization of Al(Ga)N and InAlN/AlGaN Quantum Wells for UV LED Applications**

BY

**HAONING LI**

A THESIS SUBMITTED TO THE NATIONAL UNIVERSITY OF IRELAND, CORK  
FOR THE DEGREE OF  
**DOCTOR OF PHILOSOPHY**

**Tyndall National Institute, and School of Engineering,  
University College Cork,  
Ireland.**

**Research Supervisor: Prof. Peter Parbrook**

**Co-Supervisor: Brian Corbett**

**October 2015**



# Contents

---

<b>Declaration .....</b>	<b>I</b>
<b>Abstract .....</b>	<b>II</b>
<b>Publications and Presentations .....</b>	<b>IV</b>
<b>Acknowledgements .....</b>	<b>VI</b>
<b>Abbreviation .....</b>	<b>VIII</b>
<b>1. Introduction .....</b>	<b>1</b>
1.1 Motivation .....	1
1.2 Overview of this work .....	5
1.3 References .....	7
<b>2. Fundamentals of Group-III Nitrides .....</b>	<b>9</b>
2.1 Physical properties of group-III nitride materials .....	9
2.1.1 Structural properties .....	10
2.1.1.1 Chemical bonding .....	10
2.1.1.2 Crystal structure .....	11
2.1.2 Polarization of group-III nitrides .....	13
2.1.2.1 Spontaneous polarization .....	14
2.1.2.2 Piezoelectric polarization.....	15
2.2 Substrate materials .....	16
2.3 Crystal defects .....	19
2.3.1 Point defects (PDs) .....	20
2.3.2 Dislocations .....	22
2.3.2.1 Misfit dislocations (MDs) .....	23
2.3.2.2 Threading dislocations (TDs) .....	24
2.3.2.3 Dislocation reduction .....	25
2.3.3 Inversion domains (IDs).....	27
2.4 References .....	29

<b>3. The Principles of MOVPE and Experimental Techniques .....</b>	<b>35</b>
3.1 MOVPE reaction .....	35
3.2 MOVPE system.....	37
3.2.1 MO precursor and gas handling system .....	37
3.2.2 Reactor chamber .....	40
3.2.3 Exhaust scrubbing system .....	41
3.3 In-situ optical reflectivity monitor .....	42
3.4 Ex-situ Layer Characterization .....	46
3.4.1 Nomarski interference contrast microscopy .....	46
3.4.2 Atomic force microscopy (AFM).....	47
3.4.3 X-ray diffraction (XRD).....	50
3.4.3.1 Lattice parameter measurements, strain and alloy composition .....	51
3.4.3.2 Omega rocking curve .....	53
3.4.3.3 Reciprocal space map (RSM) .....	54
3.4.4 Photoluminescence (PL).....	55
3.4.5 Electrochemical Capacitance Voltage (ECV) .....	57
3.4.6 Hall Measurement (Hall).....	58
3.5 References .....	60
 <b>4. MOVPE Growth of AlN .....</b>	 <b>62</b>
4.1 Introduction .....	63
4.2 Chemical reaction mechanism of AlN .....	63
4.3 Direct growth process on sapphire .....	64
4.3.1 Experimental details .....	64
4.3.2 Results .....	65
4.3.3 Discussion and conclusion .....	68
4.4 Two-step growth of AlN .....	69
4.4.1 Series 2-I and 2-II: Impact of growth NL thickness and growth temperature .....	70
4.4.2 Series 2-III: HT-AlN surface morphology transition .....	73



4.4.3 Series 2-IV and 2-V: Impact of main AlN growth temperature and miscut angle of substrate .....	76
4.4.3.1 Experimental details .....	77
4.4.3.2 Results .....	79
4.4.3.3 Discussion and conclusion .....	82
4.5 Three-step growth of AlN .....	87
4.5.1 Series 3-I: HT-AlN interlayer thickness .....	88
4.5.2 Series 3-II: Impact of miscut angle .....	90
4.5.3 Series 3-III: Impact of AlN epilayer thickness .....	92
4.6 Conclusion .....	97
4.7 References .....	98
 <b>5. MOVPE Growth of Planar Undoped AlGa<sub>N</sub> on AlN Template .....</b>	<b>101</b>
5.1 Introduction .....	101
5.2 Experimental details .....	102
5.3 Results and discussion .....	104
5.3.1 Control of Al content in Al <sub>x</sub> Ga <sub>1-x</sub> N .....	104
5.3.2 Structural Properties .....	112
5.3.3 Control of the surface morphology .....	119
5.4 Summary .....	127
5.5 References .....	128
 <b>6. MOVPE Growth of Si-doped Al<sub>x</sub>Ga<sub>1-x</sub>N on AlN template .....</b>	<b>131</b>
6.1 Introduction .....	131
6.2 Experimental details .....	132
6.3 Results and discussion .....	134
6.3.1 Structural properties of n-type AlGa <sub>N</sub> epilayers .....	134
6.3.2 Morphological properties .....	140
6.3.3 Electrical properties of n-doped AlGa <sub>N</sub> epilayers .....	143
6.3.4 Optical properties of n-doped AlGa <sub>N</sub> epilayers .....	145
6.4 Conclusion.....	148

6.5 References .....	149
<b>7. InAlN/AlGaN structure .....</b>	<b>152</b>
7.1 Introduction .....	152
7.2 Growth of InAlN layers .....	153
7.2.1 Experimental details .....	153
7.2.2 Results and discussion .....	155
7.2.3 Conclusion .....	166
7.3 InAlN/AlGaN multiple quantum wells (MQWs) .....	169
7.3.1 Experimental details .....	169
7.3.2 Results and discussion .....	170
7.3.3 Conclusion .....	174
7.4 References .....	176
<b>8. Conclusion and Future Work .....</b>	<b>179</b>
8.1 Conclusion.....	179
8.2 Future work .....	181

## **Declaration**

I, 李皓宁, Haoning Li, certify that this Thesis is my own work and I have not obtained a degree in this University College Cork or elsewhere on the basis of this PhD Thesis.

---

李皓宁 Haoning Li

# Abstract

---

The study of III-nitride materials (InN, GaN and AlN) gained huge research momentum after breakthroughs in the production light emitting diodes (LEDs) and laser diodes (LDs) over the past two decades. Last year, the Nobel Prize in Physics was awarded jointly to Isamu Akasaki, Hiroshi Amano and Shuji Nakamura for inventing a new energy efficient and environmental friendly light source: blue light-emitting diode (LED) from III-nitride semiconductors in the early 1990s. Nowadays, III-nitride materials not only play an increasingly important role in the lighting technology, but also become prospective candidates in other areas, for example, the high frequency (RF) high electron mobility transistor (HEMT) and photovoltaics.

These devices require the growth of high quality III-nitride films, which can be prepared using metal organic vapour phase epitaxy (MOVPE). The main aim of my thesis is to study and develop the growth of III-nitride films, including AlN, u-AlGa<sub>N</sub>, Si-doped AlGa<sub>N</sub>, and InAlN, serving as sample wafers for fabrication of ultraviolet (UV) LEDs, in order to replace the conventional bulky, expensive and environmentally harmful mercury lamp as new UV light sources.

For application to UV LEDs, reducing the threading dislocation density (TDD) in AlN epilayers on sapphire substrates is a key parameter for achieving high-efficiency AlGa<sub>N</sub>-based UV emitters. In Chapter 4, after careful and systematic optimisation, a working set of conditions, the screw and edge type dislocation density in the AlN were reduced to around  $2.2 \times 10^8 \text{ cm}^{-2}$  and  $1.3 \times 10^9 \text{ cm}^{-2}$ , respectively, using an optimized three-step process, as estimated by TEM. An atomically smooth surface with an RMS roughness of around 0.3 nm achieved over  $5 \times 5 \text{ }\mu\text{m}^2$  AFM scale. Furthermore, the motion of the steps in a one dimension model has been proposed to describe surface morphology evolution, especially the step bunching feature found under non-optimal conditions.

In Chapter 5, control of alloy composition and the maintenance of compositional uniformity across a growing epilayer surface were demonstrated for the development of u-AlGa<sub>N</sub> epilayers. Optimized conditions (i.e. a high growth temperature of 1245 °C) produced uniform and smooth film with a low RMS roughness of around 2 nm achieved in  $20 \times 20 \text{ }\mu\text{m}^2$  AFM scan.

The dopant that is most commonly used to obtain n-type conductivity in  $\text{Al}_x\text{Ga}_{1-x}\text{N}$  is Si. However, the incorporation of Si has been found to increase the strain relaxation and promote unintentional incorporation of other impurities (O and C) during Si-doped AlGaN growth. In Chapter 6, reducing edge-type TDs is observed to be an effective approach to improve the electric and optical properties of Si-doped AlGaN epilayers. In addition, the maximum electron concentration of  $1.3 \times 10^{19} \text{ cm}^{-3}$  and  $6.4 \times 10^{18} \text{ cm}^{-3}$  were achieved in Si-doped  $\text{Al}_{0.48}\text{Ga}_{0.52}\text{N}$  and  $\text{Al}_{0.6}\text{Ga}_{0.4}\text{N}$  epilayers as measured using Hall effect.

Finally, in Chapter 7, studies on the growth of InAlN/AlGaN multiple quantum well (MQW) structures were performed, and exposing InAlN QW to a higher temperature during the ramp to the growth temperature of AlGaN barrier (around 1100 °C) will suffer a significant indium (In) desorption. To overcome this issue, quasi-two-temperature (Q2T) technique was applied to protect InAlN QW. After optimization, an intense UV emission from MQWs has been observed in the UV spectral range from 320 to 350 nm measured by room temperature photoluminescence.

# Publications and Presentations

---

The following is a list of publications and presentations during the course of the PhD project.

## Publications

- (1) **Haoning Li**, Thomas C. Sadler, and Peter J. Parbrook, “AlN heteroepitaxy on sapphire by metalorganic vapour phase epitaxy using low temperature nucleation layers,” *J. Cryst. Growth*, 312, 3536 (2010).
- (2) Gunnar Kusch, **Haoning Li**, Paul R. Edwards, Jochen Bruckbauer, Thomas C. Sadler, Peter J. Parbrook, and Robert W. Martin, “Influence of substrate miscut angle on surface morphology and luminescence properties of AlGaIn,” *Appl. Phys. Lett.*, 104, 092114 (2014).
- (3) Duc V. Dinh, **Haoning Li**, and Peter J. Parbrook, “Polar and semipolar (11-22) InAlN layers grown on AlN templates using MOVPE”, *Physica Status Solidi (b)*, 253, 99 (2016).
- (4) Michele Conroy, Vitaly Z. Zubialeovich, **Haoning Li**, Nikolay Petkov, Justion D. Holmes, and Peter J. Parbrook, “Epitaxial lateral overgrowth of AlN on selfassembled patterned nanorods”, *J. Mater. Chem. C*, 3, 431 (2015).
- (5) Michele Conroy, Vitaly Z. Zubialeovich, **Haoning Li**, Nikolay Petkov, Sally O. Donoghue, Justion D. Holmes, and Peter J. Parbrook, “Ultra-High Density Arrays of Defect Free AlN Nanorods: A ‘Space Filling’ Approach,” *ACS Nano*, (2015).
- (6) Matthew D. Smith, Thomas C. Sadler, **Haoning Li**, Vitaly Z. Zubialeovich, and Peter J. Parbrook, “The effect of a varied NH<sub>3</sub> flux on growth of AlN interlayers for InAlN/GaN heterostructures Structural and optical properties of Ga auto-incorporated InAlN epilayers,” *Applied Physics Letters*, 103, 081602 (2013).
- (7) Vitaly Z. Zubialeovich, Thomas C. Sadler, Duc V. Dinh, Shahab N. Alam, **Haoning Li**, Pietro Pampili, and Peter J. Parbrook, “Enhanced UV luminescence from InAlN quantum well structures using two temperature growth”, *Journal of Luminescence*, 155, 108 (2014).
- (8) M. D. Smith, E. Taylor, T. C. Sadler, V. Z. Zubialeovich, K. Lorenz, **H. N. Li**, J. O'Connell, E. Alves, J. D. Holmes, R. W. Martin and P. J. Parbrook, “Determination of Ga auto-incorporation in nominal InAlN epilayers grown by MOCVD,” *J. Mater. Chem. C*, 2, 5787 (2014).

- (9) E. Taylor, M. D. Smith, T. C. Sadler, K. Lorenz, **H. N. Li**, E. Alves, P. J. Parbrook, and R. W. Martin, Structural and optical properties of Ga auto-incorporated InAlN epilayers, *Journal of Crystal Growth*, 408, 97 (2014).
- (10) Vyacheslav Kachkanov, Igor Dolbnya, Kevin O'Donnell, Katharina Lorenz, Sergio Pereira, Ian Watson, Thomas Sadler, **Haoning Li**, Vitaly Zubialeovich and Peter Parbrook, “Characterization of III-nitride materials by synchrotron X-ray microdiffraction reciprocal space mapping,” *physica status solidi (c)*, 10, 481 (2013).

## **Presentations**

Oral contributions at the UK Nitride Consortium (Bath, UK, 2012, and Cardiff, UK, 2013), the 5th International Symposium on Growth of III-Nitrides (ISGN-5, Atlanta, Georgia, USA, 2014) and the 11th International Conference on Nitride Semiconductors (Beijing, China, 2015).

Poster contributions at the summer UK Nitride Consortium (Sheffield, UK, 2012) and the International Workshop on Nitride Semiconductors (Sapporo, Japan, 2012).

# Acknowledgements

---

Looking over the arduous and pleasurable journey past in the last five years for my Ph.D. study, I am very grateful to the great number of people who have offered their help to me, and to my family and girlfriend for being so supportive of me over these years.

My sincere thanks go to:

- My supervisor Prof. Peter Parbrook for giving me the opportunity to do Ph.D in Tyndall. He has been a truly great supervisor, continuously supportive and always providing invaluable advice, and while at the same time giving me freedom to explore my own ideas. Also I would like to show my highest respect to him for the intense discussions and corrections in my thesis.
- Mr. Brian Corbett for his gladly accepting to be my co-supervisor and support me all the time.
- Prof. Tao Wang and Dr. Alan Morrison for their kindly accepting to referee this work.
- Dr. Thomas Sadler for training me about the operation of MOVPE, XRD and AFM, introducing me the knowledge of III-nitride material, and for his valuable advices and discussions in my first trouble year.
- Dr. Vitaly Zubialeovich and Dr. Vanduc Dinh for further training and giving me the knowledge to characterize the samples, for their wonderful advices and discussions, and for kindly correcting and commenting my dissertation.
- Dr. Michele Conroy, Mr. Matthew Smith, Mr. Zhiheng Quan, Mr. Shahab Norouzian and Mr. Pietro Pampili for their useful advices and discussions, for their kind assistance to do TEM, Hall, PL, and many other measurements.
- Mr. Pleun Maaskant, Dr. Donagh O'Mahony, Dr. Mahbub Akhter and Mr. Silvino Presa for their fully support to any electrical measurements and wafer fabrication.
- Dr. Michael Schmidt for his worthy TEM measurements, and for his nice cooperation and discussions.
- Dr. Emanuele Pelucchi, Dr. Agnieszka Gocalinska, Dr. Kevin Thomas, Dr. Valeria Dimas, Dr. Marina Manganaro and Mr. Tung Chung for their generous helpfulness and valuable discussions.
- My all co-workers and collaborators for their support and sharing deep knowledge and experiences of semiconductors with me.



Last but not least, my deep gratitude goes to my father Jianhua Li and my mother Hui Liu, who supported me morally and financially through the years and whose love and help have never faltered, and the other members of my family for their affection and kind understanding.

.

# Abbreviations

---

## List of commonly used abbreviations

a, c	lattice vectors of wurtzite group III nitride alloys. $a = 1/3 [11 \bar{2}0]$ , $c = [0001]$ in figure captions or otherwise bold text these are given as a and c
AFM	Atomic force microscopy
b	Burger vector
BF	Bright field
DF	Dark field
$e_{ij}$	Piezoelectric tensor coefficients
$\epsilon_{xx}$	In-plane strain tensor
$\epsilon_{zz}$	Out-plane strain tensor
E	Young modulus
ECV	Electron capacitance voltage
ELOG	Epitaxial lateral overgrowth
FWHM	Full width at half maximum
LED	Light emitting diode
$\mu_e$	Electron mobility
MOVPE	Metal organic vapour phase epitaxy
NR	Nanorod
$n_s$	Sheet carrier density
$N_{\text{edge}}$	Dislocations with edge component
$N_{\text{screw}}$	Dislocations with screw component
$P_{\text{pz}}$	Piezoelectric polarization
$P_{\text{sp}}$	Spontaneous polarization
PD	Point defect
PL	Photoluminescence

RMS	Root Mean Square
R <sub>s</sub>	Sheet resistance
RSM	Reciprocal space map
SEM	Scanning electron microscopy
sccm	Standard cubic centimetres per minute
slm	Standard litres per minute
TDD	Threading dislocation density
TDPL	Temperature-dependent photoluminescence
TEM	Transmission electron microscopy
TMAI	Trimethylaluminium
TMIn	Trimethylindium
TMGa	Trimethylgallium
UV	Ultraviolet
V/III	Ratio of the NH <sub>3</sub> molar versus group-III molar flow
XRD	X-ray diffraction

# Introduction

---

## 1.1 Motivation

Since the invention of the incandescent bulb by Thomas Edison in 1879 (Figure 1.1), there has been a continuous motivation to come up with less expensive, more efficient and brighter lighting sources. According to International Energy Agency (IEA) estimates [1], about 19% of the global electricity consumption is currently used for lighting loads with a slightly smaller fraction used in the European Union (14%). Unfortunately, the conversion of electricity to light is very inefficient, for example, only 5% of the electricity supplied is converted into visible light by incandescent light bulbs and only 20% is converted to light by energy-saving compact fluorescent lamps [2]. Nowadays, our rapidly growing energy consumption demands that we should research into more efficient ways of producing light. This improving energy efficiency can both save our energy and reduce greenhouse gas (GHG) emissions.



Figure 1.1: Examples of candlelight, incandescent light bulb, compact fluorescent and solid-state light.

The solid-state light (SSL) namely light emitting diode (LED) based light sources have already shown its great potential as a source with very high electrical-to-optical (ETO) conversion [3]. Current SSL materials consist of three broad categories: (I) inorganic materials such as group-III nitrides [4, 5, 6], (II) hybrid organic-inorganic materials [7] and (III) organic material that are carbon-based compounds [8, 9, 10]. Among these SSL materials, group-III nitrides and their compounds are attractive semiconductor materials for optoelectronic device due to their excellent structural properties, high thermal and chemical stability [11, 12]. Our research project at the Tyndall National Institute for Nitride Material Group (NMG) is mainly focused on the growth of high quality III-nitride films serving as templates for ultraviolet (UV) LEDs by using metal organic vapour phase epitaxy (MOVPE) technology.

The “cooling rays” was firstly found by Johann Wilhelm Ritter’s unsuccessful research, which was largely inspired by the discovery of “heat rays” from William Herschel in 1800 [13]. This "chemical cooling rays" found by Ritter later became well known as UV radiation. To date, in the short wavelength regime, bright and efficient UV light sources are required for many applications in various fields as shown in Figure 1.2. Compared to conventional mercury (Hg) based UV lamps, UV LED is one of the most effective solutions due to their compact designs, environmental friendliness, low heat generation, low current consumption, long life time and high energy efficiency [14, 15].

The first 354 nm aluminium gallium nitride/gallium nitride (AlGa<sub>N</sub>/Ga<sub>N</sub>) quantum well (QW) UV LEDs on sapphire substrates were reported by J. Han et al. [16] in 1998. After that, Nishida and co-workers fabricated first high-power UV LEDs with 346 nm emission on SiC substrates in 1999 [17]. Since this time, AlGa<sub>N</sub> have attracted great interest in Group-III Nitride material to develop UV LEDs due to the direct bandgap ranging from ~3.42 eV for Ga<sub>N</sub> [18] to ~6.1 eV for AlN [19] corresponding to the wavelength range from 360 to 200 nm. To date, although the maximum reported external quantum efficiency (EQE) of blue indium gallium nitride (InGa<sub>N</sub>) LEDs surpasses 80% [20], published EQE values of the AlGa<sub>N</sub>-based UV LEDs with wavelength below 360 nm have not exceeded 15% [21, 22, 23]. Figure 1.3 shows published EQE values of the recent (2010-2015) progress in high-efficiency UV LEDs with wavelength below 360 nm developed by different companies and groups.

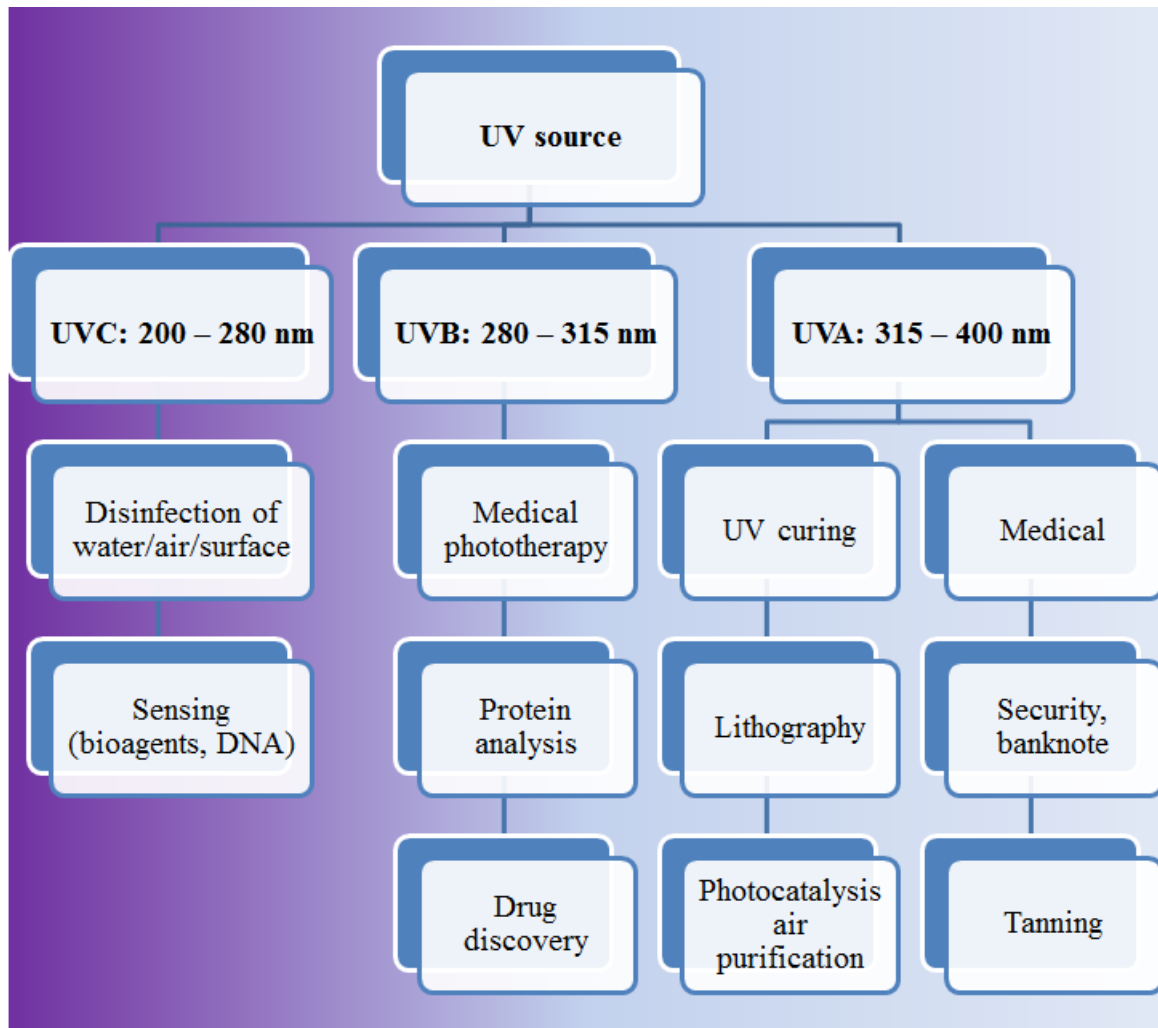


Figure 1.2: Applications of UV LEDs. The near ultraviolet spectrum (200 – 400 nm) can be subdivided into three regions of UVA (400 – 315 nm), UVB (315 – 280 nm) and UVC (280 – 200 nm) [13, 14].

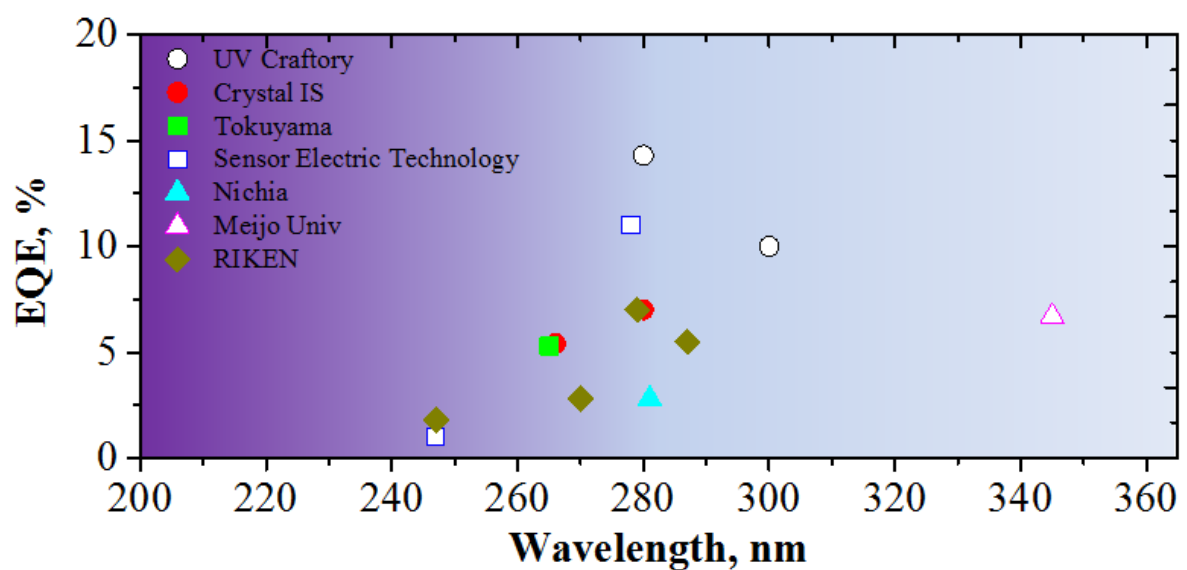


Figure 1.3: External quantum efficiency of UV-LEDs and DUV-LEDs [21, 22, 23].

In general, the limitation in the EQE of UV LEDs is attributed to three factors: (I) internal quantum efficiency (IQE), (II) carrier injection efficiency (CIE) and (III) light extraction efficiency (LEE). Among these, some possible causes for the origin of efficiency drop related to epitaxial growth are described as follows.

1) A decrease in IQE due to a high dislocation density in the active region.

Epitaxial AlGa<sub>x</sub>N layers are grown on AlN buffer layers over c-plane (0001) sapphire or Kyma<sup>®</sup> substrates (c-plane sapphire with a thin 50 nm AlN nucleation layer prepared commercially) in our research, because commercial AlN native substrates are too expensive (above \$2000 per inch). This hetero-epitaxial growth process generally results in epitaxial layers with high dislocation densities, which can act as non-radiative recombination centres leading to a poor radiative efficiency [24]. To improve crystal quality, we have found a simple method to reduce defect density for AlN templates, and an optimised approach to smooth AlGa<sub>x</sub>N buffer layers.

2) A decrease in the carrier localization effect due to a decrease of indium (In) composition in the active region [25, 26].

Al<sub>x</sub>Ga<sub>1-x</sub>N is the conventional III-nitride material for UV LEDs, which is more sensitive to defects than that of InGa<sub>x</sub>N due to its weaker localization effect [27, 28]. For InGa<sub>x</sub>N-based blue LEDs, when there is a relative high indium (In) composition, electrons and holes rapidly recombine before getting captured by a dislocation, but as the indium composition decreases, the charges interact more within dislocations. Therefore, we have proposed a method to promote In composition in the quantum well region, which is replaced from GaN or AlGa<sub>x</sub>N to InAlN.

3) A decrease in the CIE due to electron overflow into the p-type layers and/or insufficient holes supply into the active region [29, 30].

Currently, incorporation of a p-type electron blocking layer (EBL) [31, 32] is commonly known to be one of the most effective approaches to prevent the electron overflow due to the large potential barrier created by the EBL. However, it has been reported that the large polarization-field induced band bending and the valence band offset at the interfaces of p-GaN and EBL are considered to hinder the transport of holes into the MQWs region [33]. As a result, to reduce the polarization field in the EBL, such as graded EBL [34, 35, 36], InAlN

EBL [37], AlGaInN EBL [38], and AlGaIn/GaN superlattice EBL [39], to improve effectiveness of the EBL.

4) A decrease in the LEE due to UV absorption in the GaN buffer layer and p-type GaN contact layer.

UV with emission wavelength below around 360 nm is typically absorbed by the GaN buffer layer and p-type GaN contact layer. This effect can be weakened by growing AlGaIn directly over AlN templates.

## 1.2 Overview of this work

The scope of this thesis deals with study and development of the growth of III-nitride materials using MOVPE technology in order to investigate their applicability for near and middle UV LEDs with emission wavelength between 300 and 350 nm. Chapter 1 provides a motivation of this project and the outline of thesis.

An overview fundamental property of III-nitrides is described in Chapter 2. Choice of substrate materials is pointed out. The critical issue of structural and native defects are also summarized in this chapter.

Chapter 3 introduces the MOVPE growth technique and some of the characterization methods used in this work. These include in-situ and ex-situ characterization methods to characterize basic structural, electrical and optical properties.

Since the quality of the III-nitrides are crucial and can have a huge impact on device performance, we present our attempts to develop high quality AlN templates (buffer layers) for UV-LEDs in Chapter 4. Among several approaches, we try to grow AlN epilayers directly on c-plane sapphire substrates with a 3-step optimized method, which could realize AlN films with very smooth surfaces and low dislocation densities. Furthermore, a model based on surface diffusion and substrate miscut angle is proposed in order to describe the surface morphology evolution.

Chapter 5 describes the experimental results of  $\text{Al}_x\text{Ga}_{1-x}\text{N}$  growth on AlN templates. Special care is taken to determine the actual Al content by varying different growth conditions and AlN template types. In order to understand the strain relaxation mechanisms for  $\text{Al}_x\text{Ga}_{1-x}\text{N}$  epilayers, strain analysis based on X-ray diffraction (XRD), in-situ wafer curvature and transmission electron microscopy (TEM) were employed. Moreover, we have investigated



the surface inhomogeneity on a micro scale for different Al composition, and growth mode change through varying growth conditions.

Si-doped AlGa<sub>N</sub> for n-type conductivity is presented with the influence of the Si/III ratio on structural, electrical and optical properties in Chapter 6. In this part, we explain how Si/III ratio increases the tensile strain in epilayers associated with different templates. Electrical compensation arising from the unintentional incorporation of impurities has been also discussed.

In Chapter 7, In<sub>x</sub>Al<sub>1-x</sub>N thin films grown on Al<sub>x</sub>Ga<sub>1-x</sub>N buffer layers with different Al contents are studied with regard to the structural, morphological and optical properties. In addition, a new AlGa<sub>N</sub>/InAl<sub>N</sub> MQW structure with emission wavelength between 300 and 350 nm based on polar (c-plane) crystal orientation is described.

Finally, Chapter 8 offers a comprehensive summary of my work and an outlook for the future research in this field.

### 1.3 References:

- [1] A. D. Almeida, B. Santos, B. Paolo, and M. Quicheron, “Solid state lighting review – Potential and challenges in Europe,” *Renewable and Sustainable Energy Reviews*, vol. 34, pp. 30-48, 2014.
- [2] C. J. Humphreys, “Solid-State Lighting”, *MRS Bulletin.*, vol. 33, pp. 459-470, 2008.
- [3] I. L. Azevedo, M. G. Morgan, and F. Morgan, “The Transition to Solid-State Lighting,” *Proc. IEEE*, vol. 97, pp. 481-510, 2009.
- [4] N. Holonyak, Jr., and S. F. Bevacqua, *Appl. Phys. Lett.* 1, 82 (1962).
- [5] H. P. Maruska, *Mat. Res. Bull.* 7, 777 (1972).
- [6] G. P. Agrawal, *Semiconductor Lasers*. American Institute of Physics, Woodbury, New York. (1994).
- [7] V. M. Agranovich, D. M. Basko, G. C. La Rocca, and F. Bassani, *J. Phys.: Condens. Matter.* 10, 9369 (1998).
- [8] C. W. Tang, and S. A. VanSlyke, *Appl. Phys. Lett.* 51, 913 (1987).
- [9] J. H. Burroughes, D. D. C. Bradley, A. R. Brown, R. N. Marks, K. Mackay, R. H. Friend, P. L. Burns, and A. B. Holmes, *Nature.* 347, 539 (1990).
- [10] M. Halim, J. N. G. Pillow, D. W. Samuel, and P. L. Burn, *Adv. Mater.* 11, 371 (1999).
- [11] O. Ambacher, *J. Phys. D: Appl. Phys.* 31 2653 (1998).
- [12] J. W. Orton, and C. T. Foxon, *Rep. Prog. Phys.* 61, 1 (1998).
- [13] [https://en.wikipedia.org/wiki/Johann\\_Wilhelm\\_Ritter](https://en.wikipedia.org/wiki/Johann_Wilhelm_Ritter), (accessed 25 Aug 2015)
- [14] Yole development, *UV LED Technology and Application Trends*, 2013.
- [15] J. M. Phillips et al, “Basic research needs for solid-state lighting” 2006.
- [16] J. Han, M. H. Crawford, R. J. Shul, J. J. Figiel, M. Banas, L. Zhang, Y. K. Song, H. Zhou, and A. V. Nurmikko, *Appl. Phys. Lett.* 73, 1688 (1998).
- [17] T. Nishida, and N. Kobayashi, *Phys. Stat. Sol. (a)* 176, 45 (1999).
- [18] N. Nepal, J. Li, M. L. Nakarmi, J. Y. Lin, and H. X. Jiang, *Appl. Phys. Lett.* 87, 242104 (2005).
- [19] J. Li, K. B. Nam, M. L. Nakarmi, J. Y. Lin, H. X. Jiang, P. Carrier, and S. H. Wei, *Appl. Phys. Lett.* 83 (25), 5163 (2003).
- [20] Y. Narukawa, M. Ichikawa, D. Sanga, M. Sano, and T. Mukai, *J. Phys. D: Appl. Phys.* 43, 354002 (2010).
- [21] Y. Muramoto, M. Kimura, and S. Nouda, *Semicond. Sci. Technol.* 29, 084004 (2014).
- [22] H. Hirayama, N. Maeda, S. Fujikawa, S. Toyoda, and N. Kamata, *Jpn. J. Appl. Phys.* 53, 100209 (2014).

- [23] M. Shatalov, W. Sun, R. Jain, A. Lunev, X. Hu, A. Dobrinsky, Y. Bilenko, J. Yang, G. A. Garrett, L. E. Rodak, M. Wraback, M. Shur, and R. Gaska, *Semicond. Sci. Technol.* 29, 084007 (2014).
- [24] H. Amano, *Journal of Physics: Conference Series*. 326, 012002 (2011).
- [25] P. G. Eliseev, P. Perlin, J. Lee, and M. Osinski, *Appl. Phys. Lett.* 71, 569 (1997).
- [26] D. Watson-Parris, M. J. Godfrey, P. Dawson, R. A. Oliver, M. J. Galtrey, M. J. Kappers, and C. J. Humphreys, *Phys. Rev. B* 83, 115321 (2011).
- [27] S. F. Chichibu, A. Uedono, T. Onuma, B. A. Haskell, A. Chakraborty, T. Koyama, P. T. Fini, S. Keller, S. P. DenBaars, J. S. Speck, U. K. Mishra, S. Nakamura, S. Yamaguchi, S. Kamiyama, H. Amano, I. Akasaki, J. Han, and T. Sota, *Nat. Mater.* 5, 810 (2006).
- [28] R. A. Oliver, S. E. Bennett, T. Zhu, D. J. Beesley, M. J. Kappers, D. W. Saxey, A. Cerezo, and C. J. Humphreys, *J. Phys. D* 43, 354003 (2010).
- [29] M. H. Kim, M. F. Schubert, Q. Dai, J. K. Kim, E. F. Schubert, J. Piprek, and Y. Park, *Appl. Phys. Lett.* 91(18), 183507 (2007).
- [30] J. Piprek, *Phys. Stat. Sol. A* 207, 2217 (2010).
- [31] K. H. Kim, Z. Y. Fan, M. Khizar, M. L. Nakarmi, J. Y. Lin, and H. X. Jiang, *Appl. Phys. Lett.* 85, 4777 (2004).
- [32] C. S. Xia, Z. M. S. Li, W. Lu, Z. H. Zhang, Y. Sheng, W. D. Hu, and L. W. Cheng, *J. Appl. Phys.* 111(9), 094503 (2012).
- [33] J. Piprek, and Z. M. Simon Li, *Appl. Phys. Lett.* 102, 131103 (2013).
- [34] C. H. Wang, C. C. Ke, C. Y. Lee, S. P. Chang, W. T. Chang, J. C. Li, Z. Y. Li, H. C. Yang, H. C. Kuo, T. C. Lu, and S. C. Wang, *Appl. Phys. Lett.* 97, 261103 (2010).
- [35] Y. K. Kuo, J. Y. Chang, and M. C. Tsai, *Opt. Lett.* 35, 3285 (2010).
- [36] L. Zhang, X. C. Wei, N. X. Liu, H. X. Lu, J. P. Zeng, J. X. Wang, Y. P. Zeng, and J. M. Li, *Appl. Phys. Lett.* 98, 241111 (2011).
- [37] S. Choi, H. J. Kim, S. S. Kim, J. Liu, J. Kim, J. H. Ryou, R. D. Dupuis, A. M. Fischer, and F. A. Ponce, *Appl. Phys. Lett.* 96, 221105 (2010).
- [38] Y. K. Kuo, M. C. Tsai, and S. H. Yen, *Opt. Commun.* 282, 4252 (2009).
- [39] Y. Y. Zhang, and Y. A. Yin, *Appl. Phys. Lett.* 99, 221103 (2011).

# Fundamentals of Group-III Nitrides

The aims of this thesis are to investigate and develop AlN-based material on c-plane sapphire substrates. In this chapter, the fundamental properties of group-III nitride material will be described conceptually, e.g. crystal structure, chemical bonding, bandgap energy and polarization etc. Afterwards the structural and other properties of substrates which are commonly used for hetero- and homo-epitaxial will be summarized. Finally, the inherent defects of group-III nitride system and the evolution of structural defects during the growth are briefly introduced and discussed.

## 2.1 Physical properties of group-III nitride materials

Aluminum (Al), gallium (Ga) and indium (In) belonging to group-III combined with nitrogen (N) from group-V, form the III-V  $\text{Al}_x\text{Ga}_{1-y}\text{In}_{1-x-y}\text{N}$  compound semiconductor material system that includes AlN, GaN and InN,

and their ternary and quaternary alloys. This material system has a broad direct band-gap energy range, from ~0.7 eV for InN [1] to ~6.1 eV for AlN [2] at room temperature as shown roughly in Figure 2.1. This enables the nitride based emitters to cover the entire visible spectral range as well as the ultraviolet (UV) and infrared. As a result, group-III nitrides have become an important material to

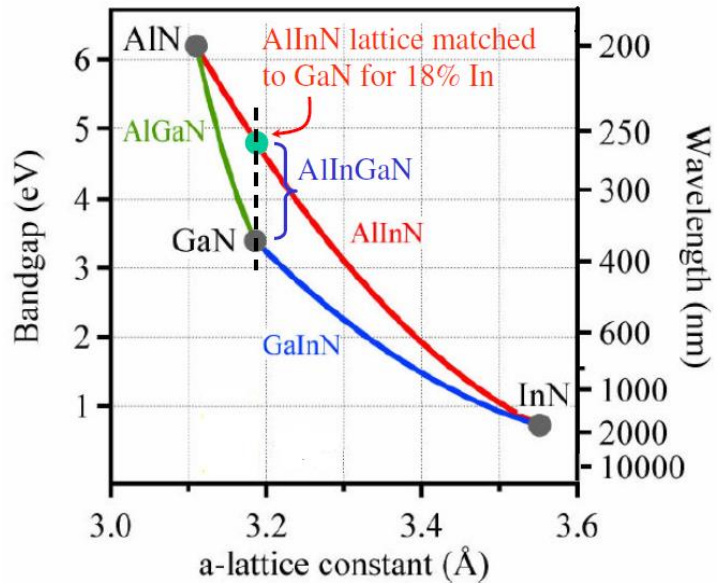


Figure 2.1: Band gap energy versus lattice constant for binary group-III nitride material system at room temperature [1, 2].

realize the high performance optical devices in the infrared to deep ultraviolet (DUV) regions, and also the high-power/high frequency electronic devices, which can be operated at high temperature and chemically harsh environments [3, 4, 5, 6, 7, 8].

## 2.1.1 Structural properties

### 2.1.1.1 Chemical bonding

Compared to other group III-V compound semiconductors e.g. GaAs and InP, the group-III nitrides have a group-III nitrogen covalent bond with stronger ionic component due to presence of nitrogen, which is the smallest and the most electronegative group-V element. Consequently, the electrons involved in such bonds are attracted by the stronger coulomb potential of the nitrogen atomic nucleus leading to the strong covalent bond between the metal and nitrogen. Additionally, the lattice parameters for the nitrides are significantly reduced due to the small covalent radius of N (0.7 Å, compared with 1.10 Å for P, 1.18 Å for As, 1.36 Å for Sb) [9, 10]. This induces high bond energies of group-III nitrides leading to high melting temperatures under very high N<sub>2</sub> pressures compared to group-III arsenides as shown in Figure 2.2 (a). The bond energy between group-III atoms and nitrogen atoms reveal large variations from the strongest bond energy of  $E_B$  (Al-N) = 2.88 eV to  $E_B$  (Ga-N) = 2.2 eV and  $E_B$  (In-N) = 1.93 eV of the nitrides AlN, GaN and InN, as shown in Figure 2.2 (b) [11]. In summary, these properties ensure the group-III nitrides are more chemically and thermodynamically stable and leads to their suitability for the device applications mentioned previously.

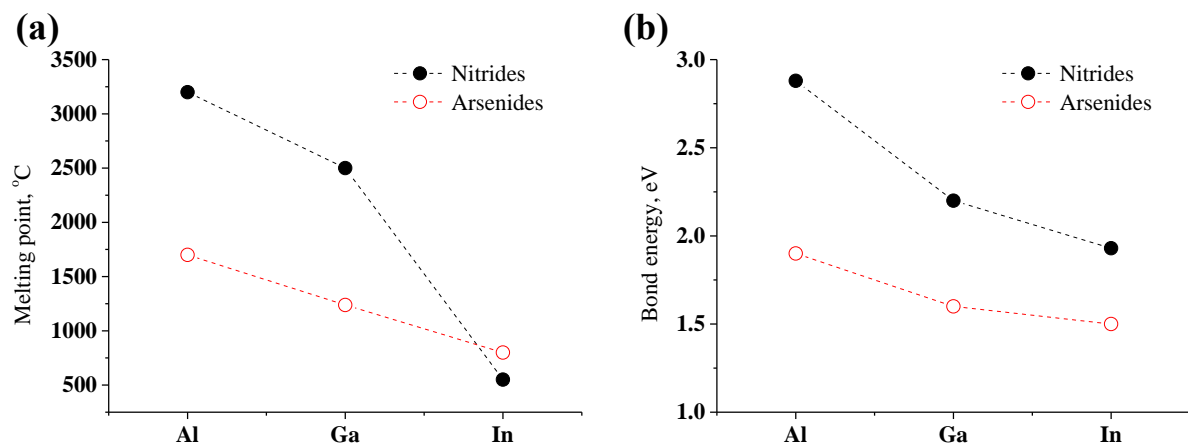


Figure 2.2: The melting points of group-III nitrides and arsenides (a) and binary bond energies for group-III nitrides and arsenides (b).

### 2.1.1.2 Crystal structure

The group-III nitrides can crystallize in rocksalt (RS), zincblende (ZB) and wurtzite (WZ). Among these structures, wurtzite structure is the preferred stable structure under normal conditions for InN, GaN and AlN. Therefore, only the wurtzite structure, which is a hexagonal structure, is presented and investigated in our research.

In the wurtzite structure, there are two interpenetrating hexagonal close-packed lattices, each lattice displaced from the other along the c-axis ideally by  $\frac{3}{8}$  of the cell height. The wurtzite unit cell and the lattice typical for AlN and GaN are shown in Figure 2.3. Along the c-axis group-III nitrides can crystallize in M-polar or N-polar orientation, where M corresponds to group-III metals (Ga, Al or In) and N to nitrogen atoms. The polarity of the crystal structure is determined by the atomic interface structure between group-III nitrides and substrates. If the bonds along the c-axis (single bonds) are from cation (Al) to anion (N) atoms, the polarity is said to be the Al-polar, and if from anion to cation atoms, it is N-polar. The growth polarity of III-nitrides is important because it indicates the direction of the polarization vector resulting from the spontaneous and strain-induced piezoelectric fields, discussed in the next section. Furthermore, surfaces of different polarity can have critical effects on crystal quality, surface morphology and physical characteristics such as Group-III metals and impurity incorporation rate [12, 13, 14].

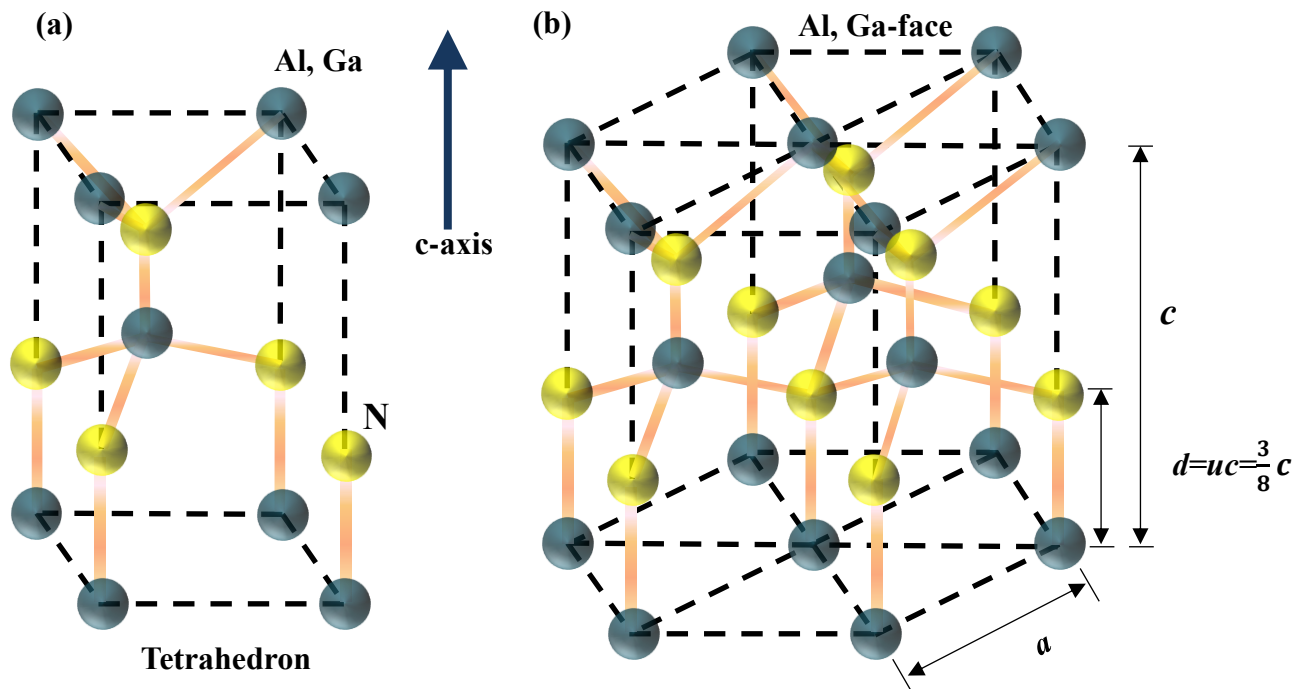
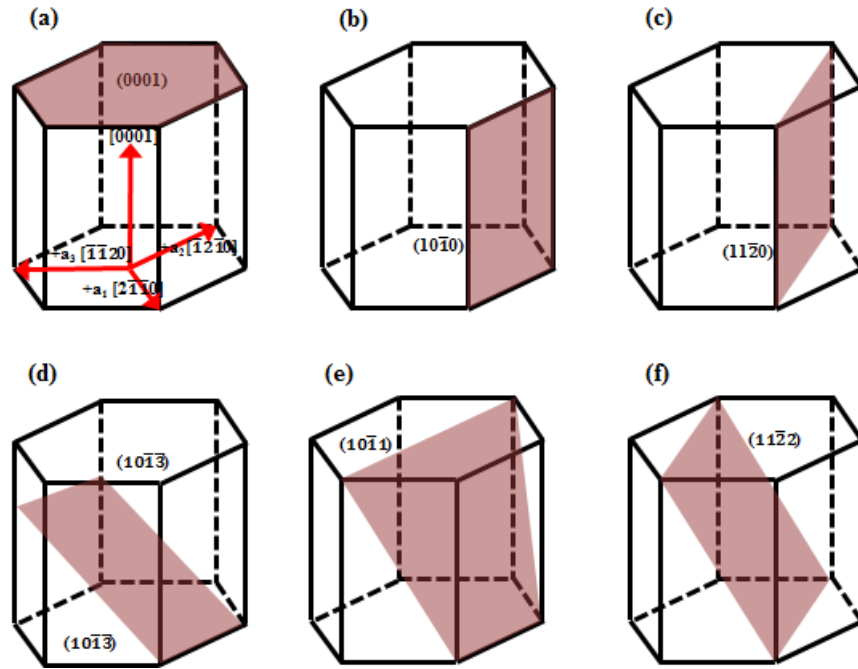


Figure 2.3: Unit cell of wurtzite structure of (Ga,Al)N (a) and wurtzite structure of (Ga,Al)N (b).

The wurtzite lattice is characterized by three parameters: the edge length of the basal hexagon ( $a$ ), the height of the hexagonal lattice cell ( $c$ ) and the cation-anion bond length ratio ( $u$ ) along the  $[0001]$  axis in units of  $c$  as shown graphically in Figure 2.3 (b). Each lattice displaces from the other along the  $c$ -axis ideally by  $3/8$  of the cell height,  $(3/8c)$ . Hence, in an ideal wurtzite crystal, the  $c/a$  ratio is 1.6330 and  $u(=a^2/c^2)$  is 0.375 [15]. Because of the different metal cations, the bond lengths and the resultant  $c/a$  ratio of AlN, GaN and InN are different. This fact is very important because the degree of non-ideality is a determining factor in the strength of polarization in the group-III nitrides.

As mentioned previously, most of the III-nitride research and applications development so far has been based on the growth along hexagonal wurtzite (0001)  $c$ -plane, which is also called the polar plane. In addition to polar  $c$ -plane, there are two alternative crystal planes: nonpolar and semipolar planes as shown in Figure 2.4. The nonpolar planes are perpendicular to the  $c$ -plane, which include the  $a$ -plane  $(11\bar{2}0)$  and the  $m$ -plane  $(1\bar{1}00)$  [see Figure 2.4 (b-c)]. A semipolar plane inclines to the  $c$ -plane between  $0 - 90^\circ$  such as  $(10\bar{1}\bar{3})$ ,  $(10\bar{1}1)$  and  $(11\bar{2}2)$  [see Figure 2.4 (d-f)].



**Figure 2.4: Different polar (a), non-polar (b-c) and semipolar (d-f) planes in the wurtzite crystal of group-III nitrides.**

In contrast to the polar structure, nonpolar and semipolar structures have two-fold surface symmetry instead of the six-fold surface symmetry of the  $c$ -plane, which strongly affect their properties such as morphological and structural properties [16]. Future challenges for the

growth of high quality nonpolar and semipolar films therefore include: improving surface roughness, understanding the origin of defects present in these films and the effect of growth conditions on them, controlling of the growth orientation and finding an effective method of defect reduction.

## 2.1.2 Polarization of group-III nitrides

The wurtzite structure of Group-III nitrides lacks centre of inversion symmetry grown along the [0001] direction. The absence of this inversion symmetry, besides the strong ionicity of the metal-nitrogen bond, potentially leads to an electrostatic field. This in turn leads to strong polarization fields pointing along [0001] or  $[000\bar{1}]$ , including the intrinsic spontaneous and strain-induced piezoelectric polarizations. In quantum wells the polarization charges can reduce the device efficiency due to the quantum confined stark effect (QCSE), and also cause other detrimental effects like wavelength-shifts and efficiency droop with increasing current densities [17]. The QCSE is caused by built-in electric field (band bending), so injected electrons shift to their lowest energy position on one side of the quantum well and holes find their lowest energy on the opposite side of the well. This spatial separation reduces the overlap of the electron and hole wavefunctions and decreases the recombination rate. Therefore, the QCSE can be weakened by optimising the quantum well (QW) width. The management of QW region and reduction of polarization field design in our InAlN/AlGaIn multiple quantum wells (MQWs) will be introduced in Chapter 7.

On the other hand, growing group-III nitrides on nonpolar and semipolar growth planes is widely studied. It exhibits no blue-shift in emission wavelength with increasing drive current, and the red-shift in emission wavelength with increasing well width is significantly smaller than for the c-plane equivalents, indicating the internal electric field is indeed smaller or eliminated on such planes [18, 19]. It also has been shown to have a significantly shorter radiative recombination time [20].

The group-III nitride materials have been grown epitaxially on the polar (0001) c-plane sapphire substrates in our experiment. In the absence of external fields, the total polarization  $P_{total}$  can be expressed in terms of two components spontaneous polarization ( $P_{sp}$ ) and piezoelectric polarization ( $P_{pe}$ ) [21],

$$\overrightarrow{P_{total}} = \overrightarrow{P_{sp}} + \overrightarrow{P_{pe}} \quad (2.1)$$



### 2.1.2.1 Spontaneous polarization

Spontaneous polarization constitutes nonzero dipole moments in the absence of external influence, i.e., strain and applied electric field. The direction of the spontaneous polarization is dependent on the polarity of the crystal. In the case of fully relaxed Group-III nitride material with a Al- or Ga-face layer, the spontaneous polarization field for GaN and AlN is negative pointing towards the  $[000\bar{1}]$  direction. In an N-polarity face, the net polarization would be in the opposite,  $[0001]$  direction parallel to the c-axis growth direction, as shown in Figure 2.5.

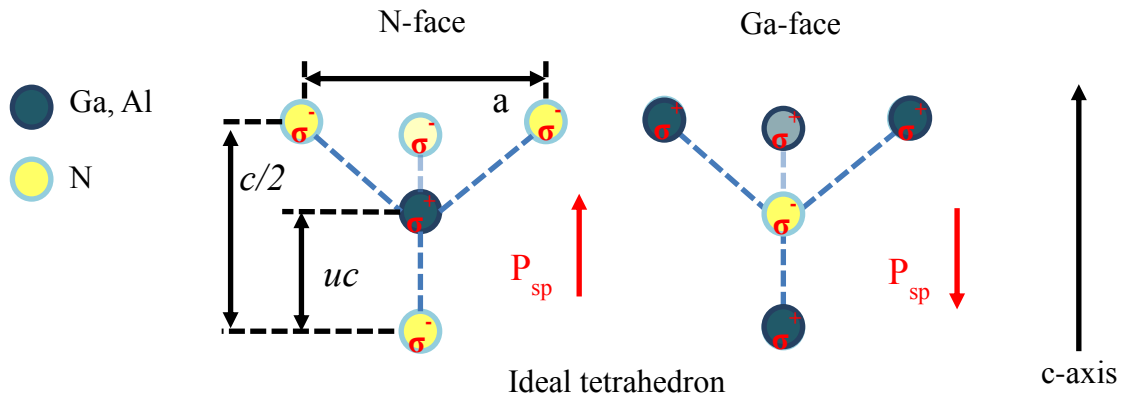


**Figure 2.5: Spontaneous polarization due to asymmetric second-nearest neighbour interaction, already in the case of an ideal tetrahedron, differences in electronegativity between cation and anion lead to spontaneous polarization [22, 23].**

Table 2.1 offers parameter sets for  $P_{sp}$  of the III-nitrides. For all III-nitrides, the effective  $P_{sp}$  is negative from GaN to InN to AlN. Zoroddu et al. [26] pointed out that the spontaneous polarization of relaxed alloys for a given composition depends linearly on the average  $u$  parameter, which indicates that spontaneous polarization differences between alloys of the same composition are mainly due to varying cation-anion bond length, whereas disorder has a negligible influence. However, because of the non-linear dependence of the lattice parameter on alloy composition under strained condition in practice, a non-linear behaviour of the spontaneous polarization versus alloy composition has to be expected and can be treated by using a bowing parameter for ternary and quaternary alloys [27].

Material (hexagonal)	GaN (C m <sup>-2</sup> )	AlN (C m <sup>-2</sup> )	InN (C m <sup>-2</sup> )	Ref
$P_{sp}$	-0.029	-0.081	-0.032	[24]
$P_{sp}$	-0.034	-0.09	-0.042	[25]

Table 2.1: Parameter sets for  $P_{sp}$  of binary III-nitrides [24, 25].

### 2.1.2.2 Piezoelectric polarization

The piezoelectric effect can be induced by two components, both of which lead to lattice distortion in an epitaxial layer. One is due to lattice mismatch (misfit) strain while the other is due to thermal strain from the thermal expansion coefficient difference between the substrate and the epitaxial layers. The magnitude and direction of this piezoelectric component depends on the stress in the crystal. The piezoelectric polarization vector is given by [28]

$$\overrightarrow{P_{pe}} = \vec{e} \vec{\epsilon} \quad (2.2)$$

Where  $\vec{e}$  and  $\vec{\epsilon}$  are the piezoelectric and the stress tensors. In wurtzite nitrides, the preferred growth direction is the polar [0001] or [000 $\bar{1}$ ] axis, so that in-plane mismatch automatically generates piezoelectric effects along the growth c-direction. The  $\overrightarrow{P_{pe}}$  is calculated using the piezoelectric tensor ( $e_{ij}$ ) of hexagonal P6<sub>3</sub>mc symmetry by [29]

$$\begin{bmatrix} P_x \\ P_y \\ P_z \end{bmatrix} = \begin{bmatrix} 0 & 0 & 0 & 0 & e_{15} & 0 \\ 0 & 0 & 0 & e_{24} & 0 & 0 \\ e_{31} & e_{31} & e_{33} & 0 & 0 & 0 \end{bmatrix} \begin{bmatrix} \epsilon_{xx} \\ \epsilon_{yy} \\ \epsilon_{zz} \\ \epsilon_{yz} \\ \epsilon_{xz} \\ \epsilon_{xy} \end{bmatrix} \quad (2.3)$$

Note that  $e_{24}=e_{15}$  for hexagonal symmetry that reduces to [29]

$$\begin{bmatrix} P_x \\ P_y \\ P_z \end{bmatrix} = \begin{bmatrix} e_{15}\epsilon_{xz} \\ (e_{24} = e_{15})\epsilon_{yz} \\ e_{31}(\epsilon_{xx} + \epsilon_{yy}) + e_{33}\epsilon_{zz} \end{bmatrix} \quad (2.4)$$

It is clear from Equation 2.4 that the  $\overrightarrow{P_{pe}}$  along the [0001] c-direction,

$$P_{pe} = e_{31}(\epsilon_{xx} + \epsilon_{yy}) + e_{33} \epsilon_{zz} \quad (2.5)$$

If only a isotropic biaxial strain is present, the in-plane strain  $\epsilon_{\parallel}$  is equal to  $\epsilon_{xx}$  and  $\epsilon_{yy}$  expressed by

$$\varepsilon_{\parallel} = \varepsilon_{xx} = \varepsilon_{yy} = \frac{a-a_0}{a_0} \quad (2.6)$$

Where  $a$  and  $a_0$  represent the in-plane lattice parameters for the strained and relaxed epitaxial layer respectively. The expression of the out-of-plane strain is

$$\varepsilon_{\perp} = \varepsilon_{zz} = \frac{c-c_0}{c_0} \quad (2.7)$$

Similarly,  $c$  and  $c_0$  represent the strained and relaxed the out-of-plane lattice parameters. In hexagonal symmetry, strain in the out-of-plane direction can be expressed in terms of the in-plane strain through the use of Poisson's ratio ( $\nu$ ), which is expressed in terms of elastic coefficients  $C_{ij}$  as [30, 31]

$$\varepsilon_{\perp} = -2 \frac{C_{13}}{C_{33}} \varepsilon_{\parallel} = -2 \frac{\nu}{1-\nu} \varepsilon_{\parallel} \quad (2.8)$$

$$\frac{c-c_0}{c_0} = -2 \frac{C_{13}}{C_{33}} \left( \frac{a-a_0}{a_0} \right) = -2 \frac{\nu}{1-\nu} \left( \frac{a-a_0}{a_0} \right) \quad (2.9)$$

Where  $C_{13}$  and  $C_{33}$  are elastic constants. Hence, for an isotropic biaxially strained layer the effective piezoelectric polarization is given by

$$\overrightarrow{P_{pe}} = \left( e_{31} - e_{33} \frac{C_{13}}{C_{33}} \right) \frac{c-c_0}{c_0} \quad (2.10)$$

Elastic and piezoelectric constants are summarized in Table 2.2. Figure 2.6 shows a schematic representation of compressive and tensile strain states of a crystal lattice where  $a_{relaxed}$  ( $a_r$ ) and  $c_{relaxed}$  ( $c_r$ ) are lattice parameters of the fully relaxed layer, and  $a_s$  and  $c_s$  are lattice parameters of a strained layer. The biaxial strain in the layer is due to the existence of a strong correlation between the  $c/a$  and the cell internal parameter  $u$  so that when  $c/a$  decreases (tensile strain), the  $u$  parameter increases in a manner to keep the four tetrahedral distances (bond distances) nearly constant through a distortion of tetrahedral angles (bond angles).

Material (hexagonal)	$C_{11}$ (GPa)	$C_{13}$ (GPa)	$e_{31}$ (Cm <sup>-2</sup> )	$e_{33}$ (Cm <sup>-2</sup> )
InN	190	121	-0.57	0.97
GaN	390	106	-0.49	0.73
AlN	345	120	-0.60	1.46

**Table 2.2: The elastic constants of group-III nitride materials [30,32].**

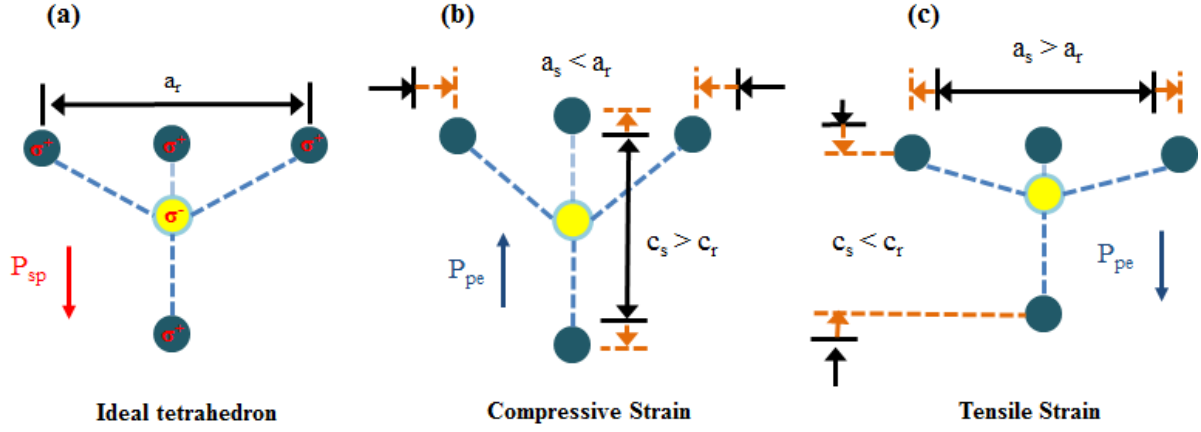


Figure 2.6: Ideal tetrahedron without  $P_{pe}$  and strain [biaxially compressive (b) and tensile (c)] leads to piezoelectricity.

## 2.2 Substrate materials

Group-III nitride materials have been grown heteroepitaxially on a number of foreign substrates. In theory, the best substrate for Group-III nitride material epitaxial growth would be selected from the same material as the epitaxial material itself. For example most commercial semiconductor devices are based on their native substrates, such as Si devices on single-crystal Si substrates, GaAs based devices on GaAs substrates, and other As- and P-based compound semiconductors. GaN single crystal substrates with low defect density have been used for fabrication of homoepitaxial high efficiency LEDs and high-voltage HFETs in practice [33, 34]. AlN single crystalline substrates can be grown by physical vapour transport (PVT), the oxygen contamination can be difficult to control during growth [35]. Recently, a promising method to preparing bulk AlN crystals is to grown by hydride vapour phase epitaxy (HVPE) AlN on a PVT-AlN substrate base which can lead to material of the quality, summarized in Table 2.3 [36, 37]. However, these III-nitride native substrates are still an expensive option and most devices are still prepared heteroepitaxially.

Table 2.4 is a compilation of the lattice parameters and thermal characteristics of a number of substrates that have been used for group-III nitride materials growth. For selection of substrate for nitride epitaxy, it should ideally have similar properties to the film to be grown over it. One significant parameter of the substrate is the degree of mismatch between substrate and epitaxial film which can determine the number of defects present in the device. These defects are believed to act as non-radiative recombination centres and limit the device performance [38, 39]. Such defects however can be reduced by appropriate “growth

engineering” to cause a significant fraction to annihilate. Meanwhile, the lateral thermal expansion coefficient is also important which ideally should be matched with the film to be grown to avoid problems during the temperature changes in the growth process, especially on cooling down, because extra strain and stress may be introduced resulting in elastic or plastic deformation, for example film cracking. The crystal orientation of the substrate is also important. It determines the growth plane, the crystal structure or orientation of the film. A mis-orientation (miscut) in the crystal orientation of the substrate can significantly modify the growth process, as discussed in later chapters.

	<b>HVPE</b>	<b>PVT</b>
<b>Diameter</b>	2 inch	2 inch
<b>Threading Dislocation Density (TDD)</b>	$> 10^7 \text{ cm}^{-2}$ (on SiC or Sapphire) $\sim 10^4 \text{ cm}^{-2}$ (on PVT-AlN)	$< 10^4 \text{ cm}^{-2}$
<b>Growth Rate</b>	$\sim 25 \text{ }\mu\text{m/h}$	$> 100 \text{ }\mu\text{m/h}$
<b>Growth Temperature</b>	1450 °C	2000-2300 °C
<b>Optical Transparency</b>	$\sim 200 \text{ nm}$	$\sim 290 \text{ nm}$ (due to high impurity concentrations of C, O and Al vacancy)

**Table 2.3: The comparison of bulk AlN substrate by HVPE and PVT [37].**

C-plane sapphire substrates are used in our heteroepitaxial growth due to their low cost, the availability of two inch diameter crystals, its stability at high temperature and transparency to UV light. However, the limitation of sapphire is its dielectric characteristics, in particular its electrical insulating nature. The electric contacts as a result should be mounted on the front side of a device. In this case the working area of the device is reduced, and the device engineering and fabrication procedure is made more complicated. Sapphire has other disadvantages including its poor thermal conductivity. One technique that has been used to overcome these challenges is to use laser lift-off (LLO) to remove the sapphire potentially allowing a back contact device with lower series resistance due to its vertical current transport [40, 41, 42].

Material	Lattice parameter (Å)	Thermal expansion coefficient ( $10^{-6}/K$ )	Thermal conductivity ( $W m^{-1} K^{-1}$ )	Resistivity ( $\Omega cm$ )	Melting point ( $^{\circ}C$ )	Price 2 inch wafer (\$)
AlN (hexagonal)	a=3.112 c=4.982	$a_{th,a}=4.2$ $a_{th,c}=5.3$	200-320	$\geq 10^{12}$	2400 @30bar	~ 4450 to 5250 (1 inch)
GaN (hexagonal)	a=3.189 c=5.185	$a_{th,a}=5.59$ $a_{th,c}=3.17$	130-230	$\geq 10^9$	>1700 @2kbar	>1000
Al <sub>2</sub> O <sub>3</sub> (Sapphire)	a=4.763 c=13.003	$a_{th,a}=7.5$ $a_{th,c}=8.57$	30-50	$\geq 10^{11}$	2030	~10-20
6H-SiC (hexagonal)	a=3.0817 c=15.1123	$a_{th,a}=4.2$ $a_{th,c}=4.68$	490	$\geq 10^{11}$	~2700 sublimes	>500
Si (cubic)	a=5.4301	$a_{th,a}=3.59$	150	$\leq 5 \times 10^4$	1415	5

**Table 2.4: Basic properties of substrate and group-III nitride materials [43, 44]**

## 2.3 Crystal defects

Material quality has always been a critical issue for the technological development of semiconductors. The performance of semiconductor devices is always limited by the impact of defects on band structure, carrier mobility, optical properties and the incorporation of impurities. It is particularly acute in III-nitride material due to the general lack of availability of native substrates in the commercial sense. As a result, AlN epitaxial layers have been mainly grown on foreign substrates such as sapphire, SiC and Si. To improve the quality of epilayers, much attention has been devoted to the understanding of point defects and extend defects. The formation of such defects during growth can be classified by their dimensionality as shown Table 2.5 [45, 46]. In this work, we particularly concerned with 0, 1 and 3 dimensional defects such as point defects (PDs), threading dislocations (TDs) and

inversion domains (IDs) which can disturb the crystal structure. These defects will be introduced in the following sections.

	Defect	Definition
<b>Zero dimension</b> (Point defect)	Vacancy	An empty atomic site
	Interstice	An atom occupies somewhere except an atomic site
	Antisite	An ordered alloy or compound when atoms of different type exchange position
	Substitution	Some “foreign” species on an atomic site, for example donor and acceptor
<b>One dimension</b> (Line defect)	Dislocations	Edge: a portion of an extra plane of atoms
		Screw: helical atomic displacement around a line and extending through the crystal
<b>Two dimension</b> (Planar defect)	Grain boundaries	Dislocations pile up
	Stacking faults	Dislocations border a two dimensional defect
	Inversion domain boundary	Adjacent domains with opposite polarity
<b>Three dimension</b> (Volume defect)	Inversion domain	Adjacent domains with opposite polarity in three dimensional volume
	Voids	The absence of a number of atoms to form internal surfaces
	Cracks	Broken bonds at the surface due to tensile stress in-plane during the epitaxial growth
	Nanopipes	Tunnel-like defects which are aligned along the growth direction of the crystal and penetrate the film

**Table 2.5: General classification of defects in dimension.**

### 2.3.1 Point defects (PDs)

A point defect disturbs the wurtzite crystal structure at an isolated site, which is classified by intrinsic and extrinsic defects. They can affect the electrical and optical properties of the host material [47, 48, 49, 50, 51]. Therefore, the control of point defects (i.e., donors and acceptors) either in the form of impurities or intrinsic defects is the key to the fabrication of useful devices in group-III nitrides.

In general, there are three types of intrinsic point defects: vacancy, interstice and antisite. Figures 2.7 displays AlN incorporating the (a) vacancies [aluminium vacancy ( $V_{Al}$ ) and nitrogen vacancy ( $V_N$ )] and (b) antisites [N site there is an Al atom ( $N_{Al}$ ) and Al site there is

an N atom], respectively. However, these intrinsic point defects are unlikely to form spontaneously during undoped GaN and AlN growth due to very high defect formation energies [49, 52]. Their formation energies are dependent on Fermi-level and/or extreme growth environment (N-rich or group-III metal rich condition). For example, the  $V_{Ga}$  has relatively low formation energy in n-type GaN when the Fermi level is close to the conduction band [49]. In the case of AlN growth, the typical experimental growth conditions are expected to fall nearer the Al-rich extreme and the  $V_N$  is favourable compared to the  $V_{Al}$  [53]. Therefore, control of Fermi level at the surface becomes a potential solution to change point defect incorporation during growth, which has been demonstrated in Mg-doped GaN and Si-doped  $Al_{0.65}Ga_{0.35}N$  by NCSU group [54, 55].

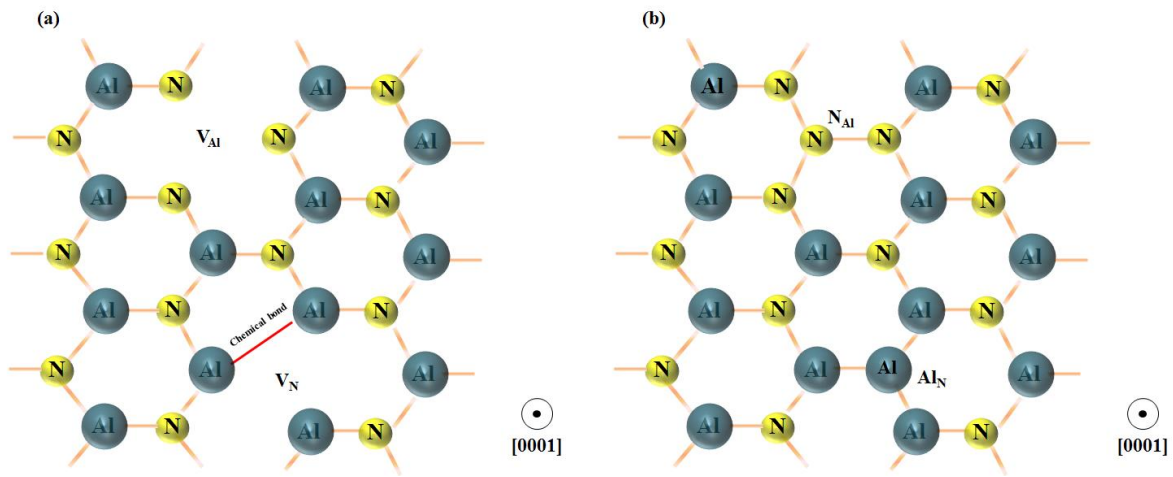


**Figure 2.7:** (a) vacancies ( $V_{Ga}$  and  $V_N$ ) and (b) antisites ( $N_{Al}$  and  $Al_N$ ) in AlN, inserted with growth direction [0001].

The extrinsic point defects are foreign atoms, which are called impurities if they are not intentionally added to the material, and are called dopants (i.e., donors and acceptors) if they are intentionally added to the material. These foreign atoms may occupy atomic sites, in which case they are called substitutions.

The shallow residual oxygen (O), silicon (Si) and carbon (C) impurities were observed as unintentionally incorporated impurities during GaN and AlN growth [49, 7]. O or Si substituted into a N site ( $O_N$  or  $Si_N$ ) act as a shallow donor and may lead to the n-type conductivity for undoped GaN [56]. In contrast to GaN, unintentionally doped  $Al_xGa_{1-x}N$  is normally resistive or insulating at high Al contents [57]. The different behaviour compared to GaN was attributed to the O donor that is believed to become a deep donor at Al contents above  $x > 0.3$  [58, 59] or by the much lower formation energy for cation vacancy related complexes ( $V_{III}$ -complexes) that act as deep acceptors and may therefore be abundant in



unintentionally  $\text{Al}_x\text{Ga}_{1-x}\text{N}$  and lead to compensation of free carriers [60]. In the case of c-plane bulk AlN growth, Collazo et al. identified that absorption in the deep UV at 4.7 eV ( $\sim 265$  nm) is due to the incorporation of substitutional C acting as deep acceptors on the nitrogen site ( $\text{C}_\text{N}$ ) by combining experiment with hybrid-exchange density functional theory (DFT) calculations [61, 62].

On the other hand, dopants are usually intentionally added to III-nitride materials to control the (n- or p-) type and concentration of charge carriers. For example, Figure 2.8 shows (a) magnesium (Mg) act as an acceptor and (b) silicon (Si) act as a donor in GaN, respectively. The more details of Si-doped  $\text{Al}_x\text{Ga}_{1-x}\text{N}$  doping experiments will be described in Chapter 5.

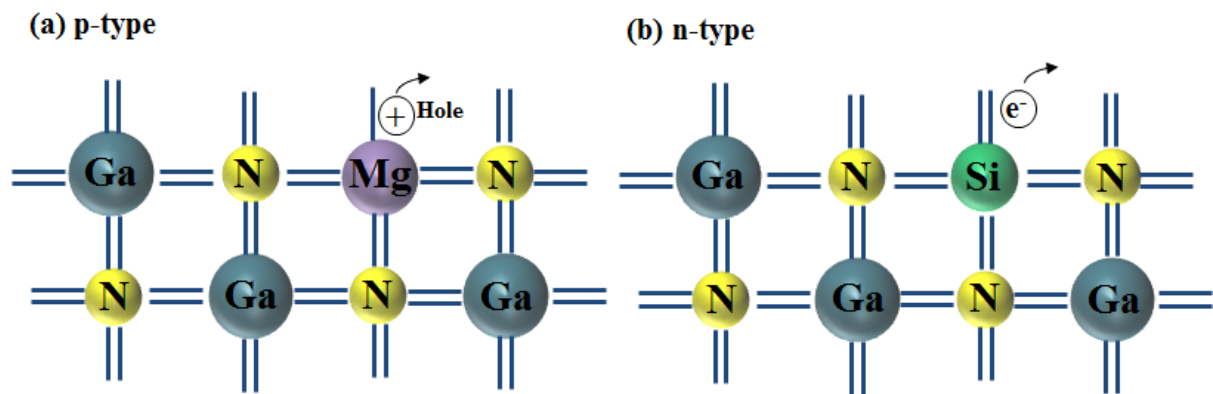


**Figure 2.8** (a) bonding around a Mg acceptor, showing a hole (+), and (b) bonding around a Si donor, showing an electron (–) in GaN, respectively.

The details of impurity transitions in III-nitrides can be characterized by deep UV photoluminescence (PL) spectroscopy and cathodoluminescence (CL) microscopy measurements [49, 50, 51]. The impurity concentrations can be measured by secondary ion mass spectrometry (SIMS) in detectable level.

### 2.3.2 Dislocations

For Group-III nitride materials heteroepitaxial layers, dislocations are line defects which can be divided into two groups: misfit dislocations (MDs) and threading dislocations (TDs). The character of dislocation is completely determined by two quantities: an oriented line direction  $\mathbf{l}$  and a Burgers vectors  $\mathbf{b}$ , which is a mathematical vector that represents the magnitude and direction of the distortion in a dislocation in a crystal lattice. Furthermore, dislocations either end at a crystal surface or form a complete loop.

### 2.3.2.1 Misfit dislocations (MDs)

Misfit dislocations are generated due to a different lattice parameter and a different thermal expansion coefficient on heteroepitaxy, which lie in the heteroepitaxial interface. In homoepitaxial growth, epilayer will grow on the native (lattice-matched) “template” under fully relaxed state. However, epilayer grown on the lattice-mismatched “template” will be under either compressive or tensile strain depending on the in-plane lattice parameter of the underlying material as compared to the in-plane lattice parameter of epilayer material being deposited as shown in Figure 2.9 (a) and (d). If the fully relaxed in-plane lattice parameter of growing epilayer is larger, then it will be under compressive strain [Figure 2.9 (b)]. In the case of tensile strain, the fully relaxed in-plane lattice parameter of the epilayer would be smaller. Alternatively, cracks can form in the epilayer in order to release the tensile stress. [Figure 2.9 (e)].

Below the critical thickness  $h_c$ , the film can be grown pseudomorphically ( $a_{sub}=a_{epi}$ ). As further growing, the strain energy will be higher with increasing layer thickness. Once the thickness is greater than  $h_c$ , it becomes energetically favourable for some form of relaxation to occur. This minimisation of the system energy can occur for example by forming dangling bonds and creating defects or rows of defects known as misfit dislocations as shown in Figure 2.9 (c) and (f) [63]. Several theoretical models for calculating the critical thickness in isotropic materials have been published over the years, but these were typically developed to examine cubic material, such as SiGe/Si and InGaAs/GaAs [63, 64, 65]. For GaN-based semiconductors, various theories have been used to try to explain experimentally obtained values of  $h_c$  in the  $In_xGa_{1-x}N/GaN$  system. However, these tend to provide a wide range of critical thickness predictions [66, 67, 68]. A few experimental techniques exist to determine the critical thickness: (I) transmission electron microscopy (TEM) can directly observe the misfit dislocations in the interface [66, 69, 70, 71], (II) photoluminescence microscopy (PLM) can also observe dislocations in the interface [43], and (III) x-ray diffraction (XRD) provides accurate data for determining the in-plane (perpendicular to the growth direction) lattice constants by analysing the peaks of x-ray rocking curves. After the critical thickness is reached, relaxation of the film can occur and the separation of the peaks corresponding to the two layers and the substrate can be observed to change. [67, 69, 72, 73]. In general, misfit dislocations are efficient in relieving strain. However, such dislocations are usually terminated by threading dislocations [74].

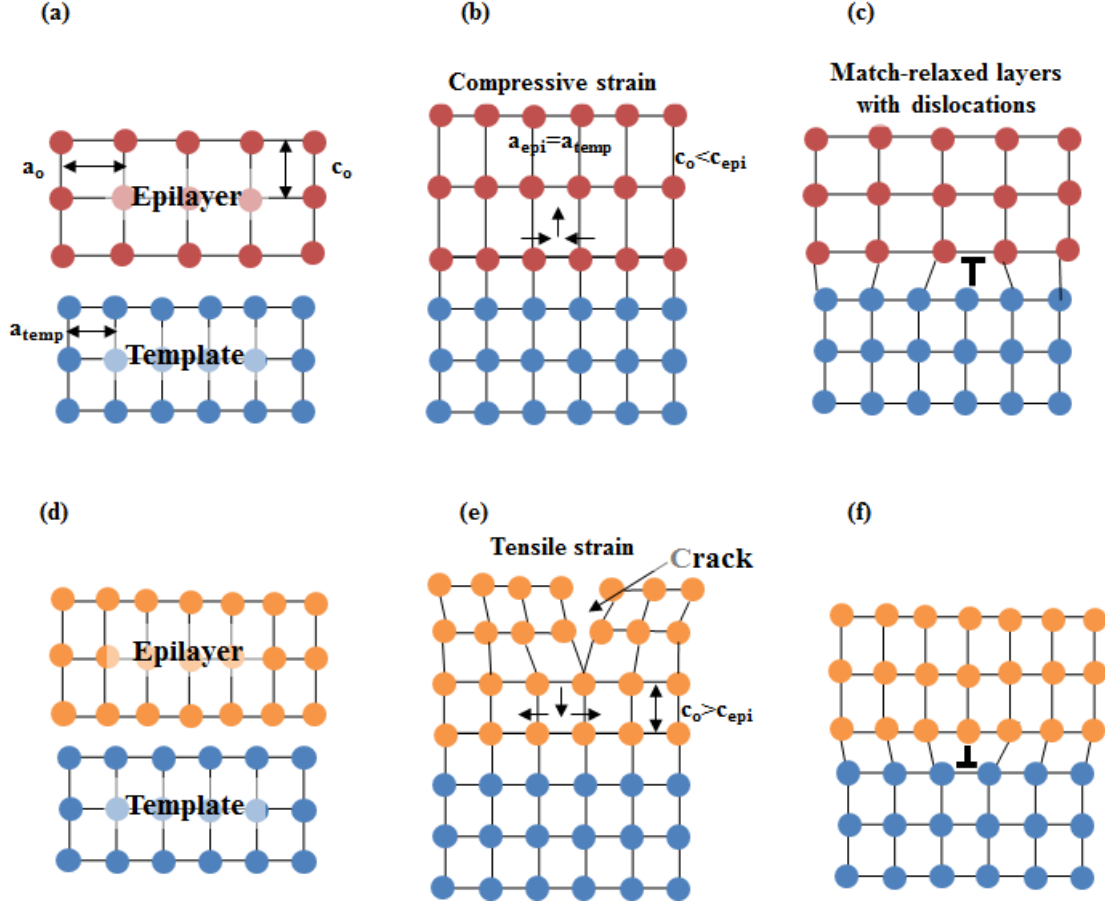
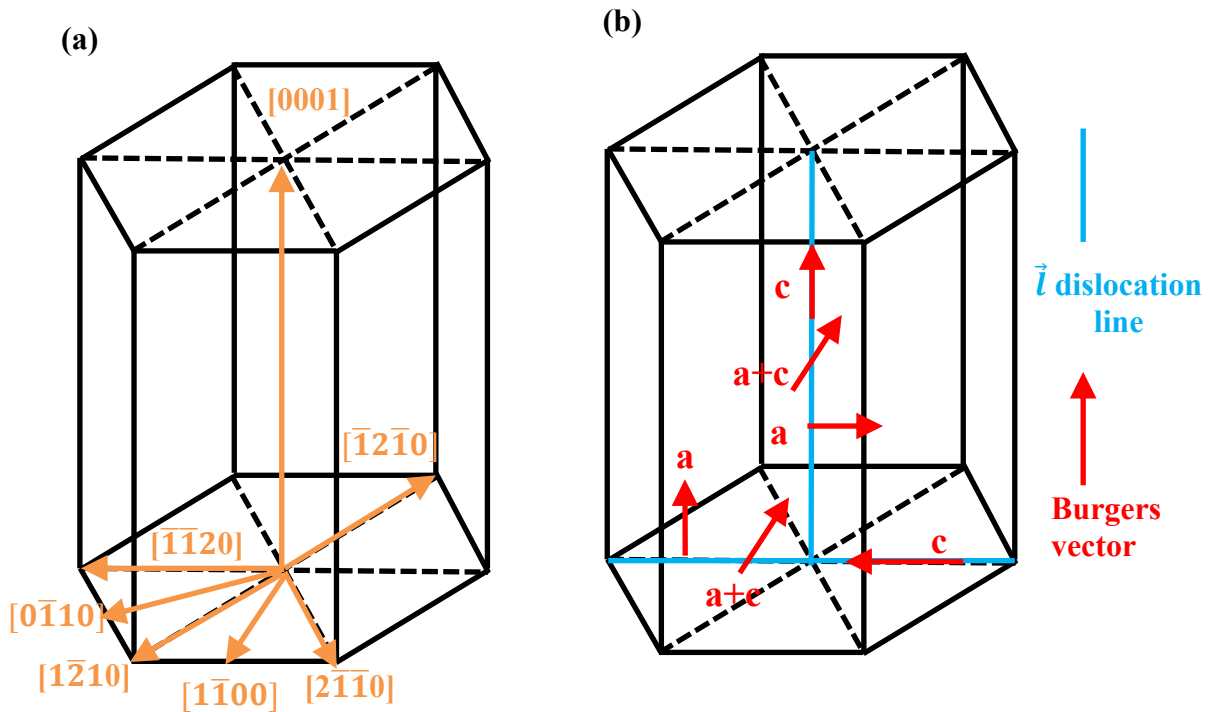


Figure 2.9: Schematic of epitaxy and relaxation epilayers on templates. (a) a epilayer is grown on a template of smaller lattice parameter [ $a_{temp} < a_0$ ]. (b) pseudomorphic grown layer with compressive strain [ $a_{temp} = a_{epi} < a_0$ ]. (c) The compression in the epilayer with misfit dislocations. (d) a epilayer is grown on a template of larger lattice parameter [ $a_{temp} > a_0$ ]. (e) The tension in the epilayer is relaxed by cracking. (f) The tension in the epilayer is relaxed with misfit dislocations.

### 2.3.3.2 Threading dislocations (TDs)

Threading dislocations are those that upwards through layer reaching the final surface. They are most typically generated at a highly mismatch interface, such as that between a substrate and heteroepitaxial layer. Based on the relation of line direction  $\mathbf{l}$  and Burgers vector  $\mathbf{b}$ , there are three main types of threading dislocation in the group-III nitride system: edge (a-type), screw (c-type), and mixed (a+c type) type dislocations corresponding to Burger's vector  $\mathbf{b} = 1/3\langle 11\bar{2}0 \rangle$ ,  $\langle 0001 \rangle$ , and  $1/3\langle 11\bar{2}3 \rangle$ , respectively [75]. The schematic Burger vectors of these dislocations are illustrated in Figure 2.10. In an edge dislocation, the Burgers vector is perpendicular to the dislocation line. Screw dislocations result when planes are displaced relative to each other through shear. In this case, the Burgers vector is parallel to the dislocation line [76]. A mixed type dislocation is a part of screw and a part of edge, and has displacement component along the dislocation and in the plane perpendicular to  $\mathbf{l}$ .

The density of TDs can be measured directly by TEM. Additionally, defect selective etching can be combined with atomic force microscopy (AFM), where the number of etched pits displayed on the AFM scanned image is used to disclose the etch pit density (EPD) [50]. Some solutions have been used to carry out the defect selective etching or so called orthodox etching, such as molten salts (KOH+NaOH), hot acids ( $H_2SO_4$ ,  $H_3PO_4$ ), and vapour phase HCl [50,77]. However, these processes are destructive. Several non-destructive methods have been developed to estimate the dislocation density. These include XRD rocking curve analysis, which is widely applied technology to evaluate the crystalline perfection of epitaxial layers, and cathodoluminescence (CL) which examine the threading dislocation density by a non-radiative process showing dark spots on CL.



**Figure 2.10:** (a) schematic showing the hexagonal unit cell with direction indices and (b) the three types of dislocation observed in c-plane (0001) and a-plane ( $11\bar{2}0$ ) group-III nitride system, Burger vectors for the screw ( $c$ ), edge ( $a$ ) and mixed ( $a+c$ ).

### 2.3.2.3 Dislocation reduction

In order to develop more effective methods to reduce the threading dislocation densities (TDDs) in heteroepitaxial films, it is important to understand the characteristic of dislocation movement during growth. Generally, there are two types of dislocation movement. Glide (slip) or conservative motion [Figure 2.11(a)], in which the dislocation moves in the plane which contains both its dislocation line and the Burger vector. The second process is climb

or non-conservative motion [Figure 2.11(b)] in which the dislocation moves out of the glide plane and normal to the Burgers vector [78]. However, previous studies have pointed out that the favourable slip systems in the wurtzite structure would be  $1/3\langle 11\bar{2}0 \rangle(0001)$ ,  $1/3\langle 11\bar{2}\bar{3} \rangle\{11\bar{2}\bar{2}\}$ , and possibly  $1/3\langle 11\bar{2}\bar{0} \rangle\{10\bar{1}0\}$ , which are unlikely to be activated since most threading dislocations in c-plane GaN and AlN are oriented along the  $[0001]$  direction [79,80,81]. The Cambridge group has shown evidence for dislocation climb in GaN and AlN films grown on c-sapphire, because the absence of suitable slip systems, and in-plane shear stresses imply that glide is unlikely to occur, while point defect concentrations at growth temperatures appear to be at equilibrium [82, 83]. Therefore, dislocations move primarily by vacancy-assisted climb, which appears to be driven by the high in-plane biaxial stresses present during growth. On the other hand, annealing GaN and AlN films promotes dislocation climb and thus potentially reduces both dislocation densities and in-plane stresses at high temperature.

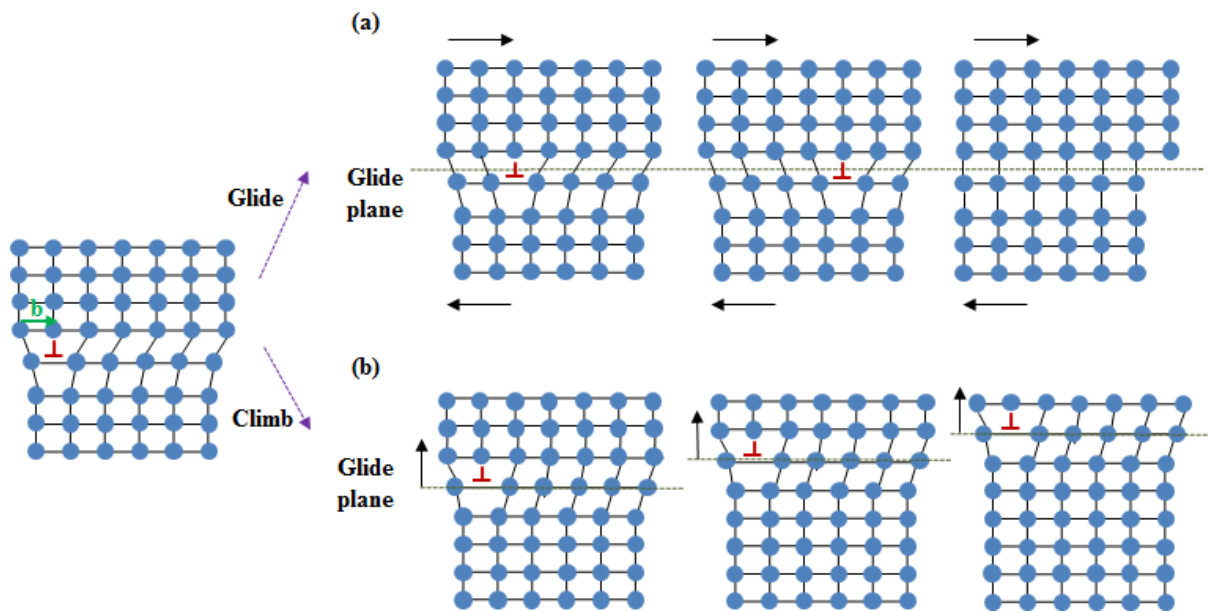


**Figure 2.11: Movement of an edge dislocation with the Burgers vector  $\mathbf{b}$ . The dislocation line is perpendicular to the diagram plane. (a) Dislocation glide: A dislocation moves to the right and eventually vanishes at the crystal surface. The arrows indicated the applied shear stress and the dashed line marks the glide plane. (b) Dislocation climb: the vacancy in the lattice diffuses to the dislocation, producing a climb of the dislocation [84].**

It was observed that the number of dislocations decreases with increasing layer thickness due to dislocation interaction [85, 86, 87, 88]. This means that parallel dislocations can interact, when the distance between them is within the range of a few tens of nanometers (e.g. high density of dislocations). Dislocation line directions should be inclined, promoting interaction between different types of dislocations.

Another dislocation reduction mechanism is dislocation bending. The bending of TDs behaviour has been observed in epitaxial lateral overgrowth (ELOG) and nanorods (NRs) at the sidewalls or voids [89, 90, 91, 92]. In the vicinity of such a facet the dislocation can minimize its energy when the dislocation line can bend from the original threading c-direction towards the normal of the side facet by the bending angle. Therefore, it can reduce the TD density resulting in dislocation-free regions in the upper part of the film.

### **2.3.3 Inversion domains (IDs)**

The Wurtzite Group-III nitride crystal structure lack a centre of symmetry, therefore an epilayer grown on c-plane sapphire can have two different polarities, named as [0001] for group-III or  $[000\bar{1}]$  for nitrogen (N). Group-III nitride epilayers grown along the [0001] direction have alternating layers of group-III atom(s) and N atom(s) that are connected with each other either by the three bonds between these atoms (inclined toward the growth direction) or by the single bond parallel to the growth direction. A single bond is always easier to break than the three bonds, therefore the atom on the surface from which a single dangling bond points upward (along growth direction) determines the growth polarity [93]. The polarity of group-III nitrides is particular important for the development of III-nitrides application, which can strongly affect the surface structure and chemistry of materials [94, 95].

An IDs is defined as a region of group-III nitrides with the opposite polarity to the primary matrix as schematically depicted in Figure 2.9, where one section is group-III polarity and other section is N polarity. The boundaries between them are called inversion domain boundaries (IDBs). Such IDs have been observed in III-nitride epitaxial materials due to issue at the substrate-epilayer interface leading to localised areas of group-III and N polarity material forming with vertical or inclined IDBs and with diameters ranging from few to tens of nanometers have been observed [96, 97, 98, 99, 100]. Such issue can lead to rough surfaces due to the difference of growth rates of these two faces [98].

Simple methods to recognize the presence of IDs include using KOH based etching due to different etching rate in N- and group-III polar materials and scanning electron microscopy (SEM) [101,102,103]. The nature of the defects can be determined using transmission electron microscopy (TEM) and convergent beam electron diffraction (CBED) modelling to interpret the images [93].

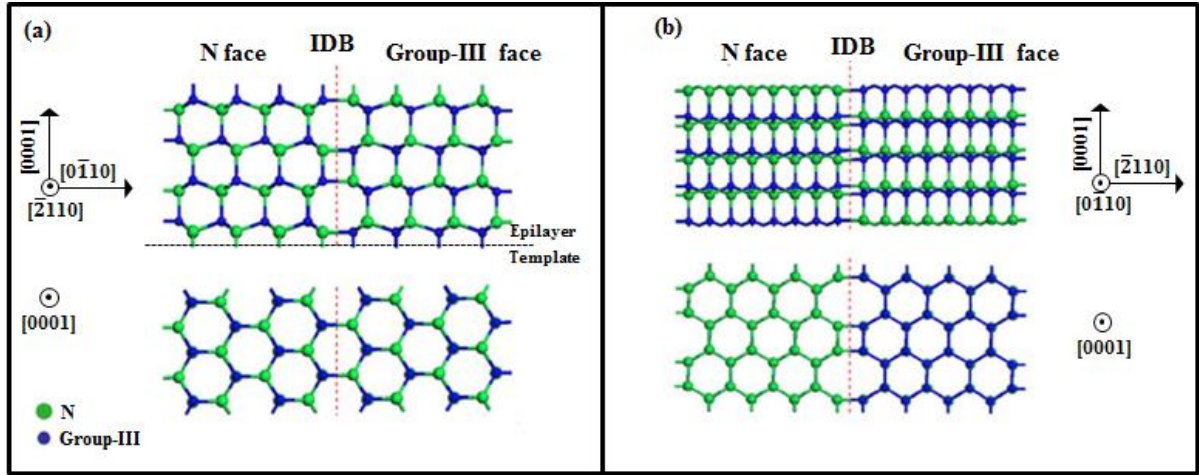


**Figure 2.12:** Schematic of two theoretical group-III nitrides IDB models. (a) Cross-sectional view top in the  $[2110]$  projection and its corresponding top-down view (bottom), where the IDB is on the  $(0110)$  plane. (b) Cross-sectional view (top) in the  $[0110]$  projection and its corresponding top-down view (bottom), where the IDB is on the  $(2110)$  plane (reorganize image [104]).

## 2.4 References:

- [1] K. O'Donnell, I. Fernandez-Torrente, P. Edwards, and R. Martin, *J. Crystal Growth* 269, 100 (2004).
- [2] J. Li, K. B. Nam, M. L. Nakarmi, J. Y. Lin, H. X. Jiang, P. Carrier, and S. H. Wei, *Appl. Phys. Lett.* 83 (25), 5163 (2003).
- [3] M. Kneissl, T. Kolbe, C. Chua, V. Kueller, N. Lobo, J. Stellmach, A. Knauer, H. Rodriguez, S. Einfeldt, Z. Yang, N. M. Johnson, and M. Weyers, *Semicond. Sci. Technol.* 26, 014036 (2011).
- [4] H. Hirayama, N. Noguchi, S. Fujikawa, J. Norimatsu, N. Kamata, T. Takano, and K. Tsubaki, *Proc. SPIE* 7216, 721621 (2009).
- [5] H. Yoshida, Y. Yamashita, M. Kuwabara, and H. Kan, *Appl. Phys. Lett.* 93, 241106 (2008).
- [6] Q. Wang, Y. P. Gong, J. F. Zhang, J. Bai, F. Ranalli, and T. Wang, *Appl. Phys. Lett.* 95, 161904 (2009).
- [7] D. S. Lee, X. Gao, S. Guo, D. Kopp, P. Fay, and T. Palacios, *IEEE Electron Device Lett.* 32, 1525 (2011).
- [8] V. Kumar, W. Lu, R. Schwindt, A. Kuliev, G. Simin, J. Yang, M. Asif Khan, and I. Adesida, *IEEE Electron Device Lett.* 23, 455 (2002).
- [9] B. Baranov, L. Däweritz, V. R. Gutan, G. Jungk, H. Neumann and H. Raidt, *Phys. Status Solidi A: Appl. Res.* 49, 629 (1978).
- [10] C. H. Park, and D. J. Chadi, *Phys. Rev. B.* 55, 12995 (1997).
- [11] S. Keller, and S. P. DenBaars, *J. Crystal Growth.* 248, 479 (2003).
- [12] M. Sumiya, and S. Fuke, *MRS Internet J. Nitride Semicond. Res.* 9, 1 (2004).
- [13] S. F. Li, S. Fuendling, X. Wang, S. Merzsch, M. A. M. Al-Suleiman, J. D. Wei, H. H. Wehmann, A. Waag, W. Bergbauer, and M. Strassburg, *Cryst. Growth Des.* 11, 1573 (2011).
- [14] D. Zhuang and J. H. Edgar, *Mater. Sci. Eng., R.* 48, 1 (2005).
- [15] M. A. Moram, and M. E. Vickers, *Rep. Prog. Phys.* 72, 036502 (2009).
- [16] Duc V. Dinh, "MOVPE growth of InN and InGaN with different surface orientations", PhD dissertation, Institute of Solid State Physics, Technische Universität Berlin, 2012.
- [17] J. Cho, E. F. Schubert, and J. K. Kim, *Laser Photonics Rev.* 7, 408 (2013).
- [18] M. D. Craven, P. Waltereit, J. S. Speck, and S. P. DenBaars, *Appl. Phys. Lett.* 84, 496 (2003).
- [19] B. Gil, P. Bigenwald, and O. Briot, *phys. stat. sol. (RRL)*, 1, 268 (2007).
- [20] M. Funato, and Y. Kawakami, *J. Appl. Phys.* 103, 093501 (2008).



- [21] O. Ambacher, J. Smart, J. R. Shealy, N. G. Weimann, K. Chu, M. Murphy, W. J. Schaff, and L. F. Eastman, *J. Appl. Phys.* 85, 3222 (1999).
- [22] F. Bernardini, V. Fiorentini, and D. Vanderbilt, *Phys. Rev. B.* 56, 10024 (1997).
- [23] O. Ambacher, J. Majewski, C. Miskys, A. Link, M. Hermann, M. Eickhoff, M. Stutzmann, F. Bernardini, V. Fiorentini, and V. Tilak, *J. Phys.: Condens. Matter* 14, 3399 (2002).
- [24] F. Bernardini, V. Fiorentini and D. Vanderbilt, *Phys. Rev. B* 56, R10024 (1997).
- [25] I. Vurgaftman, and J. Meyer, *J. Appl. Phys.* 94, 3675 (2003).
- [26] A. Zoroddu, F. Bernardini, P. Ruggerone, and V. Fiorentini, *Phys. Rev. B.* 64, 45208 (2001).
- [27] O. Ambacher, J. Majewski, C. Miskys, A. Link, M. Hermann, M. Eickhoff, M. Stutzmann, F. Bernardini, V. Fiorentini, V. Tilak, B. Schaff, and L.F. Eastman, *J. Phys. Condens. Matter* 14, 3399 (2002).
- [28] V. Fiorentini, F. Bernardini, F. D. Sala, A. D. Carlo, and P. Lugli, *Phys. Rev. B* 60, 8849 (1999).
- [29] D. L. Rode, *Phys. Rev. B* 2, 4036 (1970).
- [30] A. F. Wright, *J. Appl. Phys.* 82, 2833 (1997).
- [31] G. D. O’Clock Jr and M. T. Duffy, *Appl. Phys. Lett.* 23, 55 (1973).
- [32] F. Bernardini, V. Fiorentini, and D. Vanderbilt, *Phys. Rev. B* 56 R10 024 (1997).
- [33] K. Motoki, T. Okahisa, S. Nakahata, N. Matsumoto, H. Kimura, H. Kasai, K. Takemoto, K. Uematsu, M. Ueno, Y. Kumagai, A. Koukitu, and H. Seki, *J. Cryst. Growth* 237, 912 (2002).
- [34] P. Kruszewski, P. Prystawko, I. Kasalynas, A. Nowakowska-Siwinska, M. Krysko, J. Plesiewicz, J. Smalc-Koziorowska, R. Dwilinski, M. Zajac, R. Kucharski, and M. Leszczynski, *Semicond. Sci. Technol.* 29, 075004 (2014).
- [35] R. Dalmau, S. Craft, B. Moody, R. Schlessner, S. Mita, J. Xie, R. Collazo, A. Rice, J. Tweedie, and Z. Sitar, “Challenges in AlN crystal growth and prospects of the AlN-based technology,” in CS MANTECH Conference Digests Paper (2011).
- [36] P. Lu, R. Collazo, R.F. Dalmau, G. Durkaya, N. Dietz, B. Raghoechamachar, M. Dudley, and Z. Sitar, *J. Crystal Growth* 312, 58 (2009).
- [37] Y. Kumagai, Y. Kubota, T. Nagashima, T. Kinoshita, R. Dalmau, R. Schlessner, B. Moody, J. Xie, H. Murakami, A. Koukitu, and Z. Sitar, *Appl. Phys. Express* 5, 055504 (2012).
- [38] A. Hangleiter, F. Hitzel, C. Netzel, D. Fuhrmann, U. Rossow, G. Ade, and P. Hinze, *Phys. Rev. Lett.* 95, 127402 (2005).
- [39] J. Abella, and T.D. Moustakas, *Appl. Phys. Lett.* 92, 091901 (2008).

- [40] M. K. Kelly, R. P. Vaudo, V. M. Phanse, L. Gorgens, O. Ambacher, and M. Stutzmann, *Jpn. J. Appl. Phys.* 38, L217 (1999).
- [41] W. S. Wong, T. Sands, N. W. Cheung, M. Kneissl, D. P. Bour, P. Mei, L. T. Romano, and N. M. Johnson, *Appl. Phys. Lett.* 77, 2822 (2000).
- [42] T. Ueda, M. Ishida, and M. Yuri, *Jpn. J. Appl. Phys.* 50, 041001 (2011).
- [43] M. Levinshtein, S. Rumyantsev, and M. Shur, “Properties of Advanced Semiconductor Materials: GaN, AlN, InN, BN, SiC, SiGe”, Wiley (2001).
- [44] M. Bass, C. DeCusatis, J. Enoch, V. Lakshminarayanan, G. Li, C. MacDonald, V. Mahajan, and E. Van Stryland, “Handbook of Optics, Third Edition Volume IV: Optical Properties of Materials, Nonlinear Optics, Quantum Optics, Handbook of Optics”, (McGraw-hill Education (2009).
- [45] B. V. Spitsyn, G. Popovici, and M. A. Prelas, 2nd Int. Conf. On the Applications of Diamond Films and Related Materials, edited by Yoshikawa, M., MY, Tokyo. (1993).
- [46] F. K. Yam, L. L. Low, S. A. Oh, and Z. Hassan, “Optoelectronics - Materials and Techniques, Chapter 4 Gallium Nitride: An Overview of Structural Defect”, InTech, pp. 101 (2011).
- [47] S. J. Pearton, J. C. Zolper, R. J. Shul, and F. Ren, *J. Appl. Phys.* 86, 1 (1999).
- [48] A. Hierro, M. Hansen, L. Zhao, J.S. Speck, U.K. Mishra, S.P. DenBaars, and S.A. Ringe, *Phys. Stat. Sol. (b)* 228 937 (2001).
- [49] M. A. Reshchikov, and H. Morkoc, *J. Appl. Phys.* 97, 061301 (2005).
- [50] N. Nepal, M. L. Nakarmi, J. Y. Lin, and H. X. Jiang, *Appl. Phys. Lett.* 89, 092107 (2006).
- [51] B. Bastek, F. Bertram, J. Christen, T. Hempel, A. Dadgar, and A. Krost, *Appl. Phys. Lett.* 95, 032106 (2009).
- [52] E. de Almeida, F. de Brito Mota, C. M. C. de Castilho, A. Kakanakova-Georgieva, and G. Gueorguiev, *Eur. Phys. J. B.* 85, 48 (2012).
- [53] B. E. Gaddy, Z. Bryan, I. Bryan, R. Kirste, J. Xie, R. Dalmau, B. Moody, Y. Kumagai, T. Nagashima, Y. Kubota, T. Kinoshita, A. Koukitu, Z. Sitar, R. Collazo, and D. L. Irving, *Appl. Phys. Lett.* 103, 161901 (2013).
- [54] Z. Bryan, M. Hoffmann, J. Tweedie, R. Kirste, G. Callsen, I. Bryan, A. Rice, M. Bobea, S. Mita, J. Xie, Z. Sitar, and R. Collazo, *Journal of Electronic Materials* 42 (5), 815 (2012).
- [55] Z. Bryan, I. Bryan, B. E. Gaddy, P. Reddy, L. Hussey, M. Bobea, W. Guo, M. Hoffmann, R. Kirste, J. Tweedie, M. Gerhold, D. L. Irving, Z. Sitar, and R. Collazo, *Appl. Phys. Lett.* 105, 222101 (2014).
- [56] T. Zhu, and R. A. Olive, *Phys. Chem. Chem. Phys.* 14, 9558 (2012).

- [57] R. Zeisel, M. W. Bayerl, S. T. B. Goennenwein, R. Dimitrov, O. Ambacher, M. S. Brandt, and M. Stutzmann, *Phys. Rev. B.* 61, R16283 (2000).
- [58] C. Wetzel, T. Suski, J. W. Ager III, E. R. Weber, and E. E. Haller, *Phys. Rev. Lett.* 78, 3923 (1997).
- [59] M. D. McCluskey, N. M. Johnson, C. G. Van de Walle, D. P. Bour, and M. Kneissl. *Phys. Rev. Lett.* 80, 4008 (1998).
- [60] L. Silvestri, K. Dunn, S. Praver, and F. Ladouceur, *EPL*. 98, 36003 (2012)
- [61] R. Collazo, J. Xie, B. E. Gaddy, Z. Bryan, R. Kirste, M. Hoffmann, R. Dalmau, B. Moody, Y. Kumagai, T. Nagashima, Y. Kubota, T. Kinoshita, A. Koukitu, D. L. Irving, and Z. Sitar, *Appl. Phys. Lett.* 100, 191914 (2012).
- [62] B. E. Gaddy, Z. Bryan, I. Bryan, J. Xie, R. Dalmau, B. Moody, Y. Kumagai, T. Nagashima, Y. Kubota, T. Kinoshita, A. Koukitu, R. Kirste, Z. Sitar, R. Collazo, and D. L. Irving, *Appl. Phys. Lett.* 104, 202106 (2014).
- [63] J. W. Matthews, and A. E. Blakeslee, *J. Crystal Growth.* 27, 118 (1974).
- [64] A. Fischer, H. Kuhne, and H. Richter, *Phys. Rev. Lett.* 73, 2712 (1994).
- [65] R. People, and J. C. Bean, *Appl. Phys. Lett.* 47, 322 (1985).
- [66] S. Srinivasan, L. Geng, R. Liu, F.A. Ponce, Y. Narukawa, and S. Tanaka, *Appl. Phys. Lett.* 83, 5187 (2003).
- [67] S. E. Park, O. Byungsung, and C. R. Lee, *J. Crystal Growth.* 249, 455 (2003).
- [68] W. Lu, D. B. Li, C. R. Li, and Z. Zhang, *J. Appl. Phys.* 96, 5267 (2004).
- [69] J. C. Bean, L. C. Feldman, A. T. Fiory, S. Nakahara, and I. K. Robinson, *J. Vac. Sci. Technol. A*, 2, 436 (1984).
- [70] D. Holec, P. M. F. J. Costa, M. J. Kappers, and C. J. Humphreys, *J. Crystal Growth.* 303, 314 (2007).
- [71] C. A. Parker, J. C. Roberts, S. M. Bedair, M. J. Reed, S. X. Liu, and N.A. El-Masry, *Appl. Phys. Lett.* 75, 2776 (1999).
- [72] P. L. Gourley, I. J. Fritz, and L. R. Dawson, *Appl. Phys. Lett.* 52, 377 (1988).
- [73] P. J. Orders and B. F. Usher, *Appl. Phys. Lett.* 50, 980 (1987).
- [74] Th. Kehagias, Ph. Komninou, G. Nouet, P. Ruterana, and Th. Karakostas, *Phys. Rev. B.* 64, 195329 (2001).
- [75] G. P. Dimitrakopoulos, Ph. Komninou, Th. Karakostas, and R. C. Pond, Topological analysis of defects in nitride semiconductors, in: P. Ruterana, M. Albrecht, J. Neugebauer (Eds.), *Nitride Semiconductors: Handbook on Materials and Devices*, Wiley-VCH Verlag GmbH & Co. KGaA, Weinheim, 321-377, (2003).

- [76] S. K. Mathis, A. E. Romanov, L. F. Chen, G. E. Beltz, W. Pompe, and J. S. Speck, *J. Crystal Growth*. 231, 371 (2001).
- [77] J. L. Weyher, *Superlattices Microstruct.* 40, 279 (2006).
- [78] D. Hull, and D. J. Bacon, *Introduction to Dislocations*, Elsevier Ltd., 5th Ed (2011).
- [79] S. Srinivasan, L. Geng, R. Liu, F.A. Ponce, Y. Narukawa, and S. Tanaka, *Appl. Phys. Lett.* 83, 5187 (2003).
- [80] V. Audurier, J. L. Demenet, and J. Rabier, *Philos. Mag.* A77, 843 (1998).
- [81] B. Jahnen, M. Albrecht, W. Dorsch, S. Christiansen, H. P. Strunk, D. Hanser, and R.F. Davis, *MRS Internet J. Nitride Semicond. Res.* 3, 39 (1998).
- [82] M. A. Moram, T. C. Sadler, M. Häberlen, M. J. Kappers, and C. J. Humphreys, *Appl. Phys. Lett.* 97, 261907 (2010).
- [83] W. Y. Fu, M. J. Kappers, Y. Zhang, C. J. Humphreys, and M. A. Moram, *Appl. Phys. Express.* 4, 065503 (2011).
- [84] A. H. Cottrell, *Theory of Crystal Dislocations*, Gordon and Breach, New York, 1964.
- [85] J. Jasinski, *Phys. Stat. Sol.* 2, 994 (2005).
- [86] M. Albrecht, I. P. Nikitina, A. E. Nikolaev, Yu.V. Melnik, V. A. Dmitriev, and H. P. Strunk, *Phys. Stat. Sol.* 176, 453 (1999).
- [87] S. K. Mathis, A. E. Romanov, L. F. Chena, G. E. Beltz, W. Pompe, and J. S. Specka, *Phys. Stat. Sol. (a)* 179, 125 (2000).
- [88] J. Jasinski, and Z. Liliental-Weber, *J. Electron. Mater.* 31, 429 (2002).
- [89] P. Gibart, *Rep. Prog. Phys.* 67, 667 (2004).
- [90] R. A. Oliver, S. E. Bennett, J. Sumner, M. J. Kappers, and C. J. Humphreys, *J. Phys.: Conf. Ser.* 209, 012049 (2010).
- [91] A Urban, J. Malindretos, J-H Klein-Wiele, P Simon, and A Rizzi, *New J. Phys.* 15 053045 (2013).
- [92] M. Conroy, V. Z. Zubialevich, H. Li, N. Petkov, J. D. Holmes, and P. J. Parbrook, *J. Mater. Chem. C*, 3, 431 (2014).
- [93] Z. Liliental-Weber, *Jpn. J. Appl. Phys.* 53, 100205 (2014).
- [94] J. Jasinski, Z. Liliental-Weber, Q. S. Paduano, and D. W. Weyburne, *Appl. Phys. Lett.* 83, 2811 (2003).
- [95] L. T. Romano, and T. H. Myers, *Appl. Phys. Lett.* 71, 3486 (1997).
- [96] J. Jasinski, Z. Liliental-Weber, Q.S. Paduano, and D.W. Weburne, *Appl. Phys. Lett.* 83, 2811 (2003).

- [97] Y. Wu, A. Hanlon, J.F. Kaeding, R. Sharma, P.T. Fini, S. Nakamura, and S. Speck, Appl. Phys. Lett. 84, 912 (2004).
- [98] Q. S. Paduano, D. W. Weyburne, J. Jasinski, and Z. Liliental-Webe, J. Crystal Growth. 261, 259 (2004).
- [99] L. Hussey, R. M. White, R. Kirste, S. Mita, I. Bryan, W. Guo, K. Osterman, B. Haidet, Z. Bryan, M. Bobea, R. Collazo, and Z. Sitar, Appl. Phys. Lett. 104, 032104 (2014).
- [100] H. D. Li, T. Wang, N. Jiang, Y. H. Liu, J. Bai, and S. Sakai, J. Cryst. Growth. 247, 28 (2003).
- [101] D. Zhuang, and J. H. Edgar, Mater. Sci. Eng. R, 48, 1 (2005).
- [102] O. Ledyev, M. Pandikunta, and S. Nikishin, Jpn. J. Appl. Phys. 53, 050306 (2014)
- [103] M. D. Brubaker, I. Levin, A.V. Davydov, D. M. Rourke, N. A. Sanford, V. M. Bright, and K. A. Bertness, J. Appl. Phys. 110 053506 (2011).
- [104] F. Liu, R. Collazo, S. Mita, Z. Sitar, G. Duscher, and S. J. Pennycook, Appl. Phys. Lett. 91, 203115 (2007).

# The Principles of MOVPE and Experimental Techniques

---

An Aixtron Close Coupled Showerhead (CCS) 3×2 Flip-Top (FT) metal-organic vapour phase epitaxy (MOVPE) reactor equipped with an in-situ optical reflectivity monitor (ORS/LayTec) was used to grow the group-III nitride materials reported here. Ex-situ characterisation techniques with the capabilities of extracting structural, compositional, electrical and optical properties from the samples at appropriate scale ranges are extremely important to understand the material growth. The film crystallinity is mainly analysed x-ray diffraction (XRD). The surface morphologies are investigated by Nomarski microscopy and atomic force microscopy (AFM). Photoluminescence (PL) is used to characterize the optical properties. For electric properties, electrochemical capacitance voltage (ECV) and Hall measurements (Hall) are used to determine the doping type, doping concentration and carrier mobility of n- or p-type samples. In this chapter, the basic principles of MOVPE will be briefly described. Furthermore, the principles of all characterization methods applied in this work are summarized.

## 3.1 MOVPE reaction

MOVPE is a type of chemical vapour deposition which has been applied both to academic research and to an impressive array of commercial devices including light emitting diodes, lasers, transistors, photodetectors and solar cells. It is based on the chemical vapour transport of the precursors and subsequent reactions of metal-organic precursors [organic radical (R) + group-III metal (M), e.g. tri-methyl Ga, In, Al, etc.] and hydrides [hydrogen compound of group-V (EH), e.g. NH<sub>3</sub>, etc.] on a heated substrate producing single or polycrystalline thin films which finally establishes the equilibrium of the system. A general reaction to grow group-III nitride material can be simply written as follows,



MOVPE requires carrier gas ( $H_2$  or  $N_2$ ) to transport precursor molecules from bubblers to undergo decomposition reactions at the heated zone of the susceptor. Resulting species diffuse from a boundary layer to the surface and absorb on the surface. They will diffuse along the surface before the final incorporation (absorption) reactions at favoured energy sites such as edges, kinks and steps on the surface and the resulting product will be incorporated by forming a new bond to grow the film. Also, the species can desorb from the surface or react with other surface species. Gaseous by-products desorb from the surface and diffuse in the carrier gas away from the deposition zone towards the reactor exhaust. The steps of the MOVPE growth process are shown in Figure 3.1. The major variables in MOVPE are the ratio of group-V and group-III flows, the magnitude of those flows, total flow rates, the growth temperature, the reactor pressure and the type of carrier gas which all together determine the deposition rate and the properties of the epitaxial film. Doping of  $Al_{1-x}Ga_xN$  is achieved using silicon for n-type and magnesium for p-type, which are supplied using disilane ( $Si_2H_6$ ) and bis-cyclopentadienyl magnesium ( $Cp_2Mg$ ), respectively.

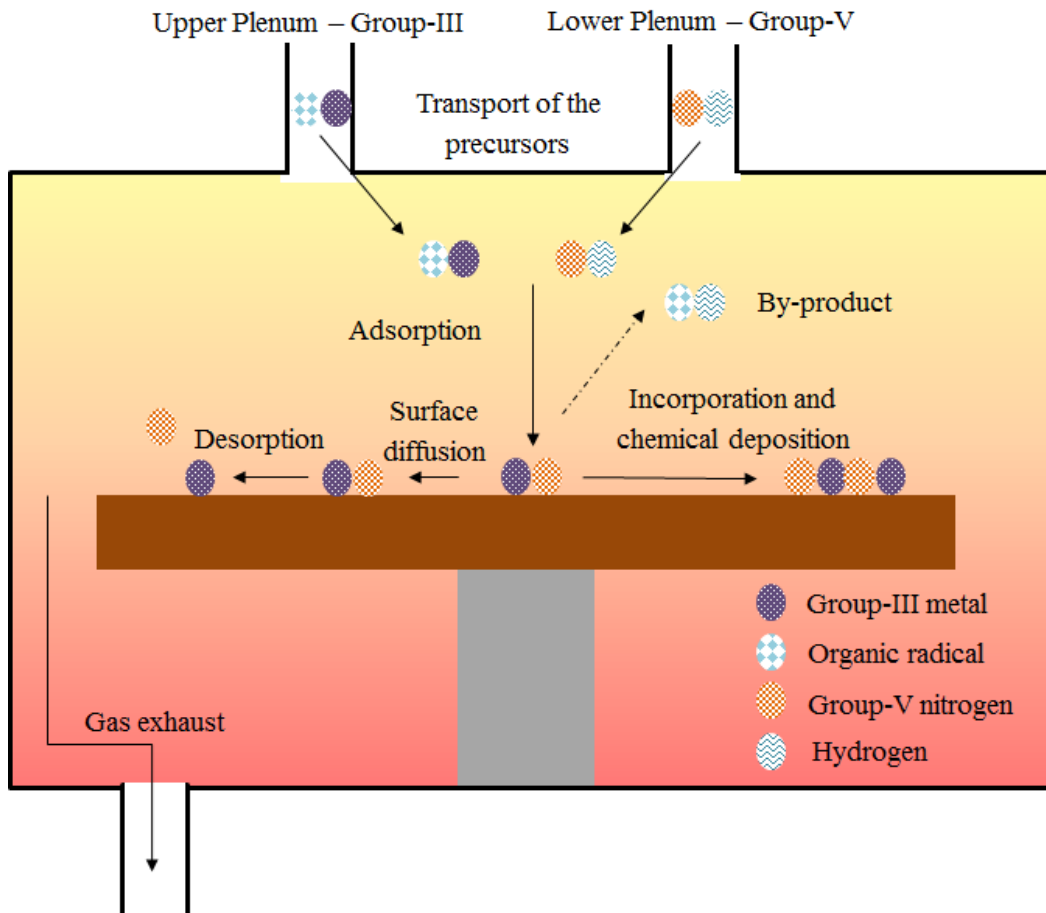


Figure 3.1: Schematic of chemical vapour deposition reaction steps.

### 3.2 MOVPE system

An MOVPE system consists of three main parts: (1) metal-organic (MO) precursor and gas handling system, (2) reactor chamber and (3) exhaust scrubbing system. Figure 3.2 is a basic diagram of an MOVPE system.

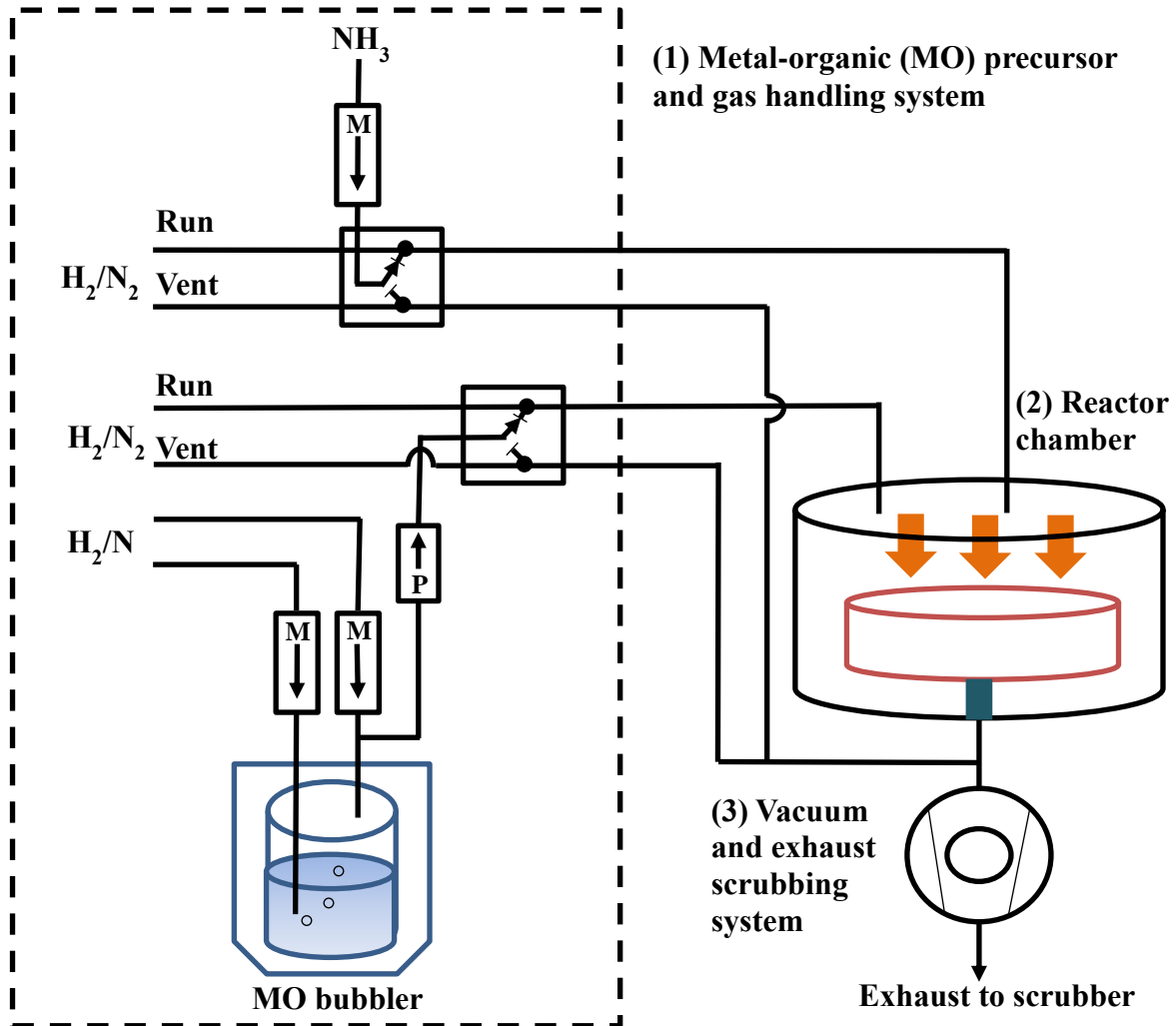


Figure 3.2: schematic of MOVPE system with three major parts.

#### 3.2.1 MO precursor and gas handling system

The MO precursor and gas handling system controls the supply of precursors to the reactor chamber. For the growth of group-III nitride material, the MO precursors include trimethyl-gallium (TMGa), trimethyl-aluminium (TMAI) and trimethyl-indium (TMIn) as group-III sources and ammonia ( $\text{NH}_3$ ) as the nitrogen source. Furthermore disilane ( $\text{Si}_2\text{H}_6$ ) gas diluted in helium (He) is used as a Si doping source and biscyclopentadienyl-magnesium ( $\text{Cp}_2\text{Mg}$ ) is frequently used as the Mg doping source. However, unpredictable Mg concentration profiles



may greatly vary after the reactor has been perturbed or even from run to run, which is associated with the Mg memory effect [1, 2].

MO precursors are supplied in stainless steel containers called bubblers in which material is picked up by an injection gas. The bubblers are maintained in thermostatically controlled baths at a constant temperature ideally between the precursor's melting and boiling points. This can exactly control the vapour pressure of the MO precursors. For example 0 °C for TMGa and 20 °C for TMAI. The schematic of typical TMGa and TMAI bubblers are shown in Figure 3.3. On the other hand, TMIn bubbler design uses a solid indium precursor with a porous structure to increase the surface area and increase the sublimation rate. An Epison controller is used to monitor the concentration of TMIn in nitrogen, as shown in the Figure 3.4. This device allows the measurement of the composition of a gas at constant temperature by measuring the speed of sound ( $V=d/\Delta T$ ) through it, done by passing a sound wave through using ultrasonic transceiver.

The mass flow controller (MFCs) and pressure controllers (PCs) are located in the gas mixing cabinet and control the accurate flow rate of MO precursors into reactor chamber. The vapour partial pressure of MO precursor depends on bubbler temperature and the relation can be expressed by the Antoine equation [3]:

$$P_{MO} = 10^{(a-\frac{b}{T})} \times \frac{1013.25}{760} \text{ mbar} \quad (3.2)$$

Where a and b are vapour pressure constants depending on the MO precursor, T is the bubbler temperature. Table 3.1 gives the values of parameters a and b for common MO precursors and the bath temperature used in these studies.

The molar flow rate of MO precursors flow into the reactor chamber controlled by the MFCs given in unit of standard cubic centimetre per minute (sccm) is regulated by the molar fraction of MO vapour resulting from changing the MO vapour partial pressure. With raising bubbler temperature, the MO vapour pressure increases according to equation (3.2). The molar flow rate of metal-organic precursors through MFCs can be expressed as ideal gas mixtures law,

$$F_{M,MO} = \left( \frac{F_{V,injection\ gas}}{22.4 \times 10^3 \text{ cm}^3} \right) \times \frac{P_{M,MO}}{P_{total}} \quad (3.3)$$

Where  $F_{M, MO}$  is the molar flow rate (mol/min) of the MO precursor,  $F_{V, injection\ gas}$  is the volume flow rate of the injection gas (in sccm),  $P_{M,MO}$  and  $P_{total}$  are the vapour partial pressure of the MO precursor and the total pressure of the gas mixture (in mbar).

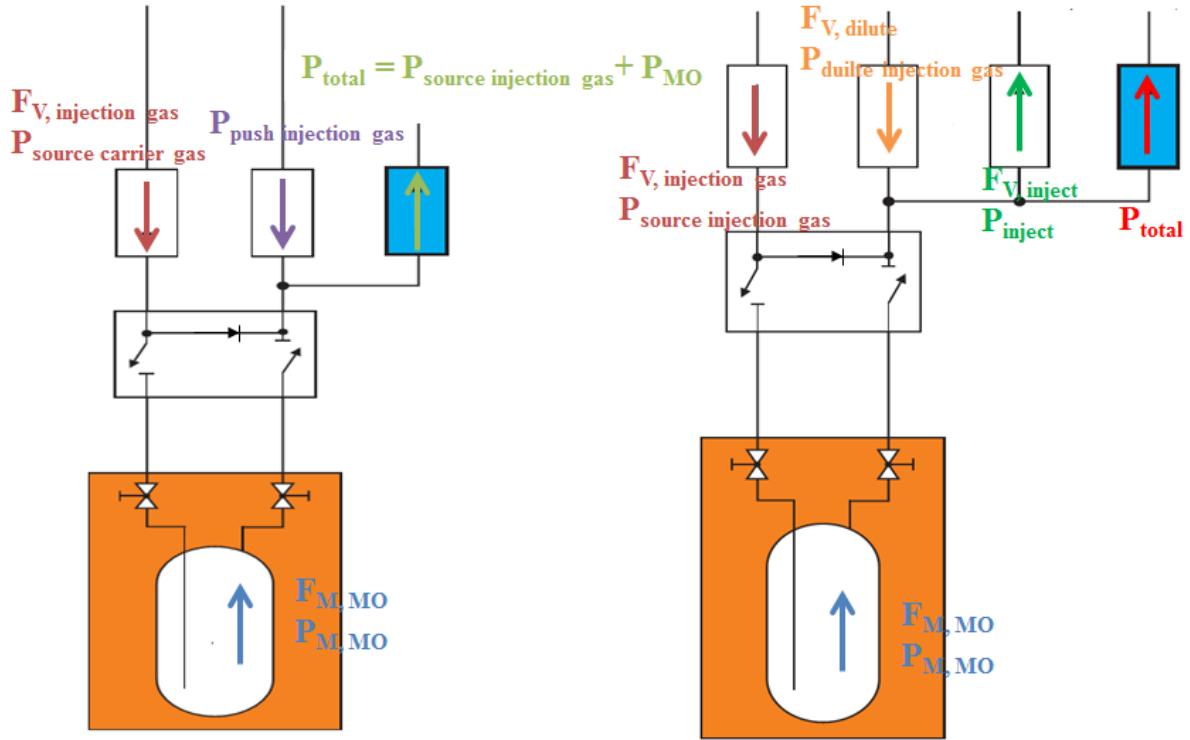


Figure 3.3: The schematic of Standard MO source (left) and Double Dilute MO source (right).

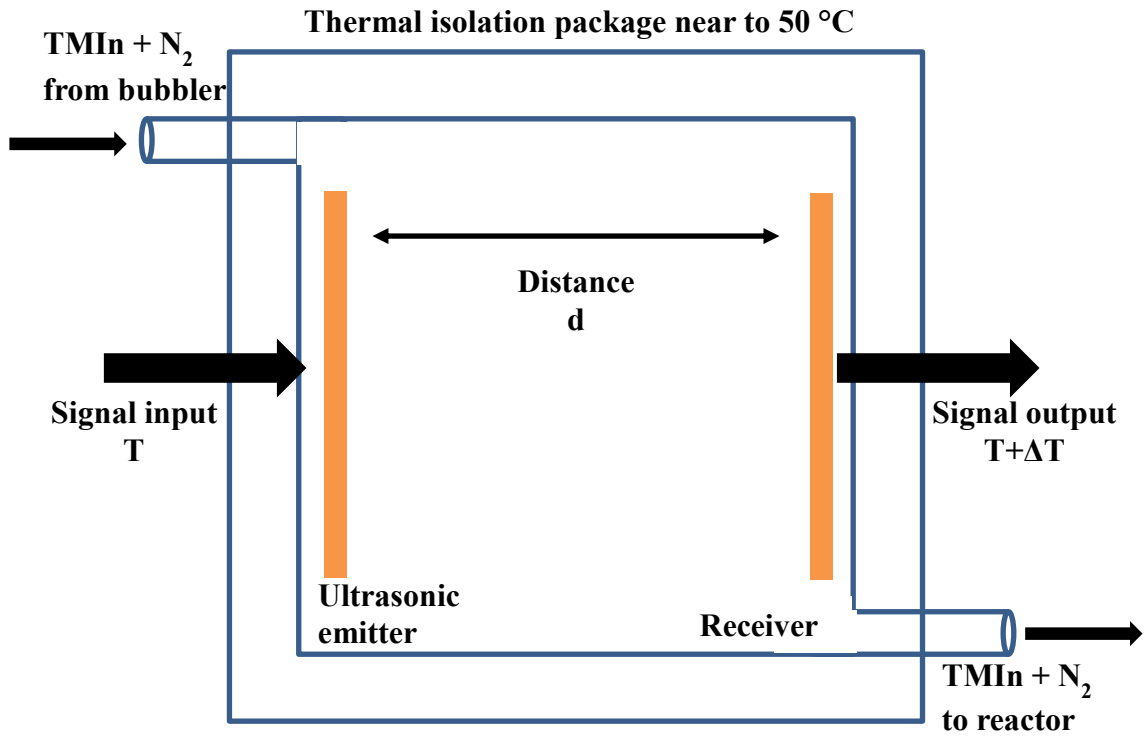


Figure 3.4: A schematic of the operating principles of an EPISON gas flow controller [4].

At the end, the injection and carrier gas can be switched between nitrogen (N<sub>2</sub>) and hydrogen (H<sub>2</sub>) depending on the process requirement. In order to prevent pre-reactions occurring,

group-III and group-V precursors are transported separately to the reactor chamber (Run MO and Run Hydride lines) where a heated substrate is placed to form a layer from the precursors. For each run line, there is also a corresponding vent line which leads the process gas bypassing the reactor into the vacuum system. As a result the flows are pressure-wise control in order to avoid pressure compensation reactions during the switching operation between run and vent lines.

	Formula	a	b (K)	Melting Temperature (°C)	Bubbler temperature (°C)	Vapour partial pressure (mbar)
TMGa	(CH <sub>3</sub> ) <sub>3</sub> Ga	8.07	1703	-15.8	0	89.4
TMAI	(CH <sub>3</sub> ) <sub>3</sub> Al	8.22	2134	15.4	20	11.5
TMIn	(CH <sub>3</sub> ) <sub>3</sub> In	10.52	3104	88	25	3.4
Cp <sub>2</sub> Mg	(C <sub>2</sub> H <sub>5</sub> ) <sub>2</sub> Mg	4198	25.14	176	20	0.028

**Table 3.1: Physical properties of common MO precursors for MOVPE [5, 6]**

### 3.2.2 Reactor chamber

The reactor chamber is a container made of stainless steel and quartz, which includes showerhead, susceptor, heater and chamber exhaust. A schematic of reactor chamber is shown in Figure 3.4 (a). This showerhead reactor takes advantage of the vertical geometry where MO precursors and NH<sub>3</sub> are separately fed into the reactor to prevent pre-reaction, see Figure 3.4 (b).

In the reactor chamber, wafers are placed onto a wafer carrier, called the susceptor. The wafers are held very close to the showerhead where its spacing is normally set to 11 mm. The susceptor is generally a graphite disk with an approximately 100 µm SiC coating. It is located on top of the susceptor support, which rotates in a clockwise direction to ensure homogeneous temperature and enhance the layer homogeneity during the growth. NH<sub>3</sub> would attack and react with the inner graphite during high temperature and hence result carbon

impurity pollution [ $C+NH_3 \rightarrow HCN+H_2$  ( $>1000\text{ }^\circ\text{C}$ )] [7]. Thus, the SiC coating plays an important role for protection against corrosion and oxidation.

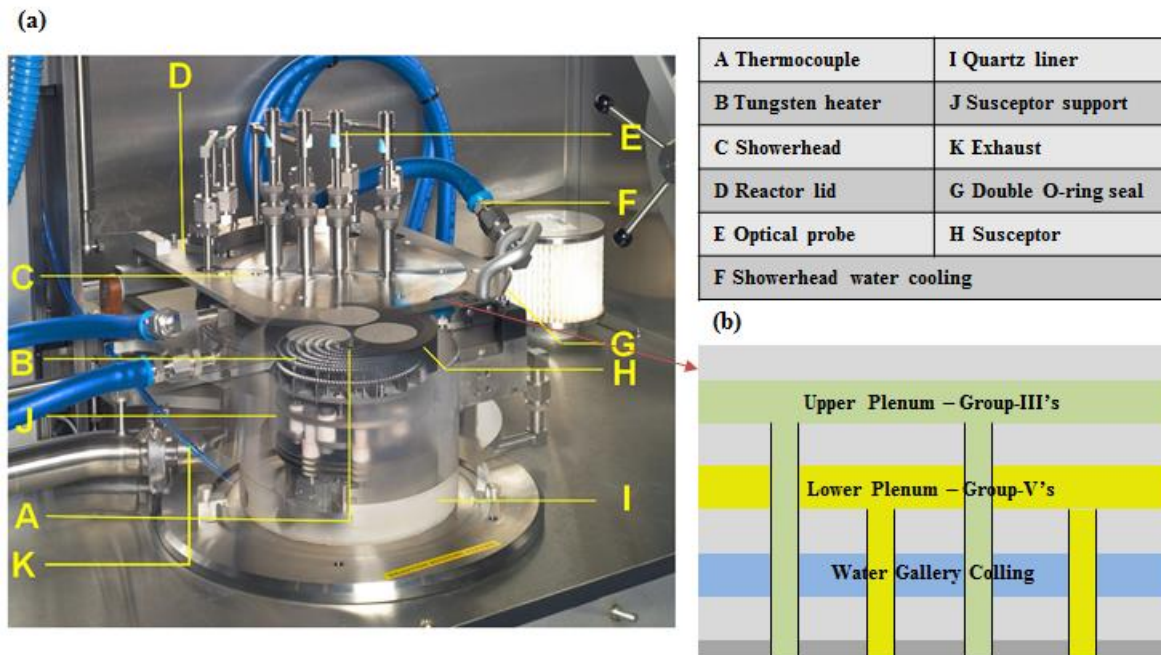


**Figure 3.4:** (a) Schematic diagram of AIXTRON CCS 3x2FT system and (b) cross section of showerhead (Courtesy of AIXTRON Ltd.). [8]

The system temperature is directly controlled by a three-zone heater, consisting of three independently powered sets of coils to obtain uniform temperature, made of tungsten rhenium (example shown in Figure 3.5). The reactor is cooled by a water recirculating system.

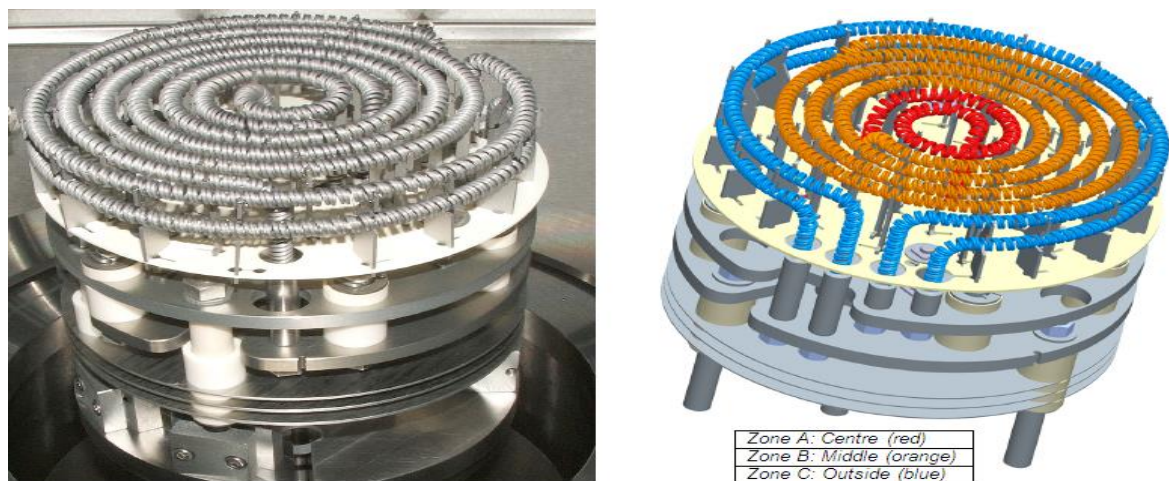


**Figure 3.5:** The image of tungsten heater (left) and the three parts designation of the heater coils (right) (Courtesy of AIXTRON Ltd.). [8]

### 3.2.3 Exhaust scrubbing system

The exhaust scrubbing system of an MOVPE system has two important functions: (1) maintaining a steady state pressure condition in the reactor chamber during process and (2) removal of unused precursors and by-products of the reaction from the chamber.

Typical growth pressure for nitride-based devices is range from 50 to 500 mbar due to material properties and the limitations of the reactor. For sub-atmospheric pressure growth, vacuum pump and pressure controllers are required to control the growth pressure during process. The reactor system is equipped with an exhaust filtration system which can protect the vacuum pump from large particles. Gases exhausted from the growth chamber or vent line flow through the replaceable filter and the vacuum pump into a scrubber system for effluent treatment.

### 3.3 In-situ optical reflectivity monitor

An Optical Reference Systems (ORS) (used for samples NT0001 to NT0247) / LayTec (measured samples starting from NT0248) optical instrument has been used for in-situ monitoring the epitaxial growth during the MOVPE process. The system is designed to measure the reflectance and temperature during the thin film deposition process.

The ORS EpiEYE<sup>®</sup> is a triple wavelength laser reflectometer (operating at 405nm, 635nm and 950nm) and emissivity corrected pyrometer (operating at the same wavelength as the infra-red reflectometer). LayTec EpiCurve<sup>®</sup> TT system combines measurements of temperature (pyrometry wavelength and bandwidth 950±1 nm), reflectance at three wavelengths (LED reflectometer operating at 405±5 nm, 633±1 nm and 950±1 nm) and wafer curvature measurements with a double beam laser (light source for curvature measurements compact two 656 nm semiconductor lasers) in one tool.

For optically smooth films growing at a constant rate and exhibiting minimal absorption, it is well known that thin-film interference (also can be described by Fabry–Perot interference) causes periodic variations in the intensity of reflected light. The relation between the growth rate ( $G$ ), film refractive index ( $n$ ), period of reflectance oscillations ( $P$ ), and monitoring wavelength ( $\lambda_m$ ) [9],

$$G = \frac{\lambda_m}{2nP} \quad (3.4)$$

The thickness of the layer ( $d$ ) which is grown during one oscillation (from peak to peak or from trough to trough) of the reflectometer curve can be approximately calculated using the following equation.

$$d = \frac{\lambda_m}{2n} \quad (3.5)$$

The refractive index of III-nitrides shows a dependence on temperature, which is known as thermo-optic effect [10]. These indices can be estimated by Laytec software according to the growth temperature and detection wavelength used to examine the growing layer. Hence, the in-situ reflectometer can provide information on any change of growth environment (temperature, pressure, fluxes rate) that affects either growth rate (change of oscillation rate) and/or surface roughness (change of oscillation amplitude) with time.

It is worth noting that the detectable wavelength of light or laser should be longer than absorption wavelength of the epitaxial layers. For example, the GaN layers are observed to absorb light at 405 nm causing oscillations to disappear. Since the growth temperature for the GaN is above 1000 °C, the bandgap of GaN shrinks below 2.8 eV according to the Varshni equation [11, 12],

$$E_g(T) = E_g(0) - \frac{\alpha T^2}{\beta + T} \quad (3.6)$$

where  $E_g(0)$  is the bandgap at 0 K,  $\alpha$  is the  $T \rightarrow \infty$  limiting value of the bandgap shrinkage coefficient  $dE_g(T)/dT$  and  $\beta$  is a material specific parameter. Typical values of Varshni coefficients can be found in Reference [11]. Meanwhile, the light intensity as a function of depth ( $x$ ) into the epitaxial layer can be described as

$$I(x) = I_0 e^{-\alpha x} \quad (3.7)$$

where  $I_0$  is the incident intensity and  $\alpha$  is the absorption coefficient. Typically, the majority of light is absorbed as the thickness of GaN above 100 nm, if the photon energy exceeds the material's bandgap.

Figure 3.6 shows the ORS in-situ reflectance curves obtained from two different AlN growth runs. The oscillations of the AlN-1 have almost equal amplitude and the curve is horizontally aligned. It is an indication of the growing epilayer surface remaining optically flat. The AlN-2 has an overall downward slope and the amplitude of the oscillations is also decreasing,

which is called damping. This is an indication of increasing roughness of the grown epilayer surface.

The comparison of reflectance measurement between ORS and LayTec is shown in Figure 3.7. A strong damping behaviour was invariably observed in LayTec LED-based reflection measurement at 405 nm during AlN growth, because the broad spectral halfwidth ( $\Delta\lambda$ ) of the violet LED leaded to constructive interference for different parts of spectrum occur at different thicknesses. However, the damping behaviour was not observed in ORS laser-based system due to small  $\Delta\lambda$ . On the other hand, AFM images indicated that the root-mean square roughness (RMS) of AlN was only around 0.4 nm which was consistent with Laytec red reflectivity (635 nm) and ORS both reflectivities. Furthermore, high noise reflectance signal was found when used ORS due to laser stability issue.

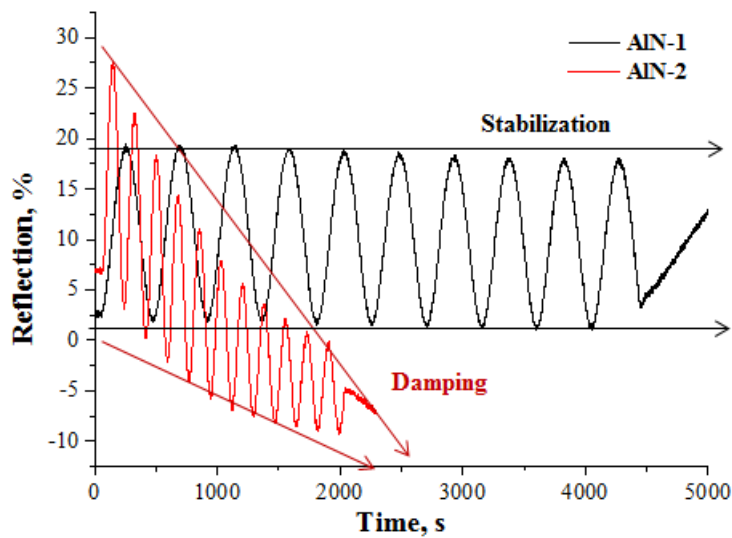


**Figure 3.6:** ORS in-situ reflectance curves obtained from two different AlN growth runs by 405 nm laser signal.

Wafer curvature measurements monitor the distance between two laser spots of reflected laser beams, which can be converted to a curvature value by this expression [13],

$$K = \frac{1}{R} \approx \frac{d_0 - d}{2d_0 \cdot L} \quad (3.8)$$

where  $d_0$  is the initial distance between the two incident laser spots [see Figure 3.8 (a)],  $d$  is the distance between the two laser spots of the reflected laser beams, and  $L$  is the optical path length of the laser beam. The relationship between the curvature radius and the bow can be converted with the formula,

$$b = R \cdot (1 - \cos \frac{r}{R}) \quad (3.9)$$

Where  $K$  is the curvature value ( $\text{m}^{-1}$ ),  $R$  is the curvature radius (m),  $r$  is wafer radius and  $b$  is the bow. During the growth process curvature may be changed due to vertical temperature gradient, lattice mismatch and thermal stress (thermal expansion different). The definitions of curvature are shown in Figure 3.8. In situ wafer bow trace data were collected using the LayTec Epicurve<sup>®</sup>TT system. More curvature studies of group-III nitride materials during growth will be shown and discussed in following chapters.

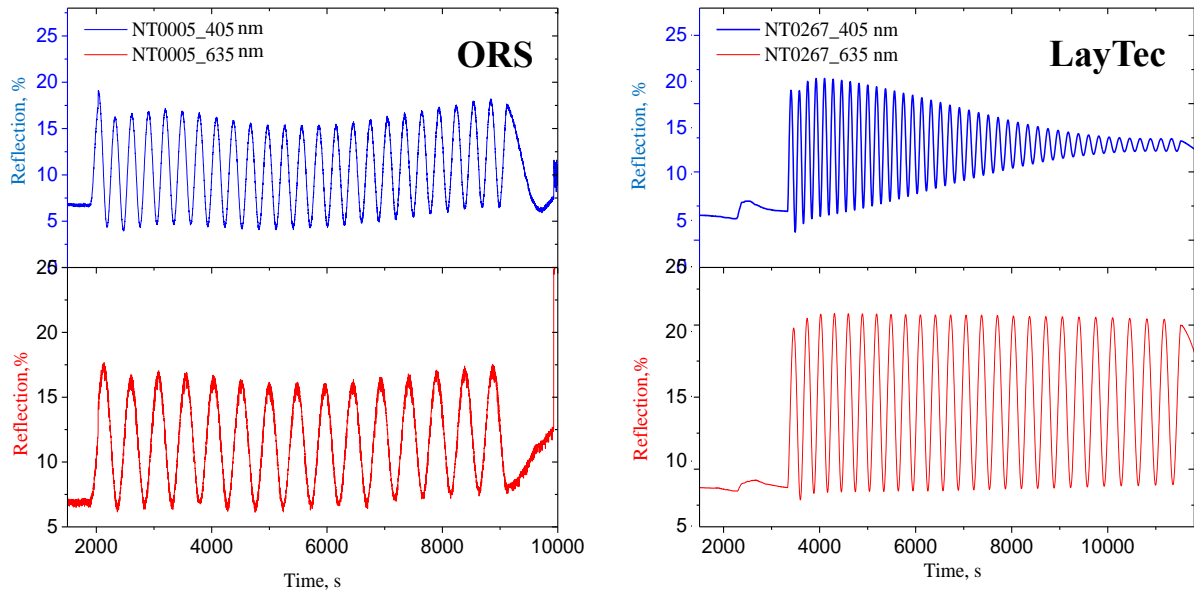


**Figure 3.7: The comparison of reflectance measurement between ORS and LayTec obtained from two different AlN growth runs by 405 and 635 nm laser (left, ORS) or LED (right, LayTec) signals.**



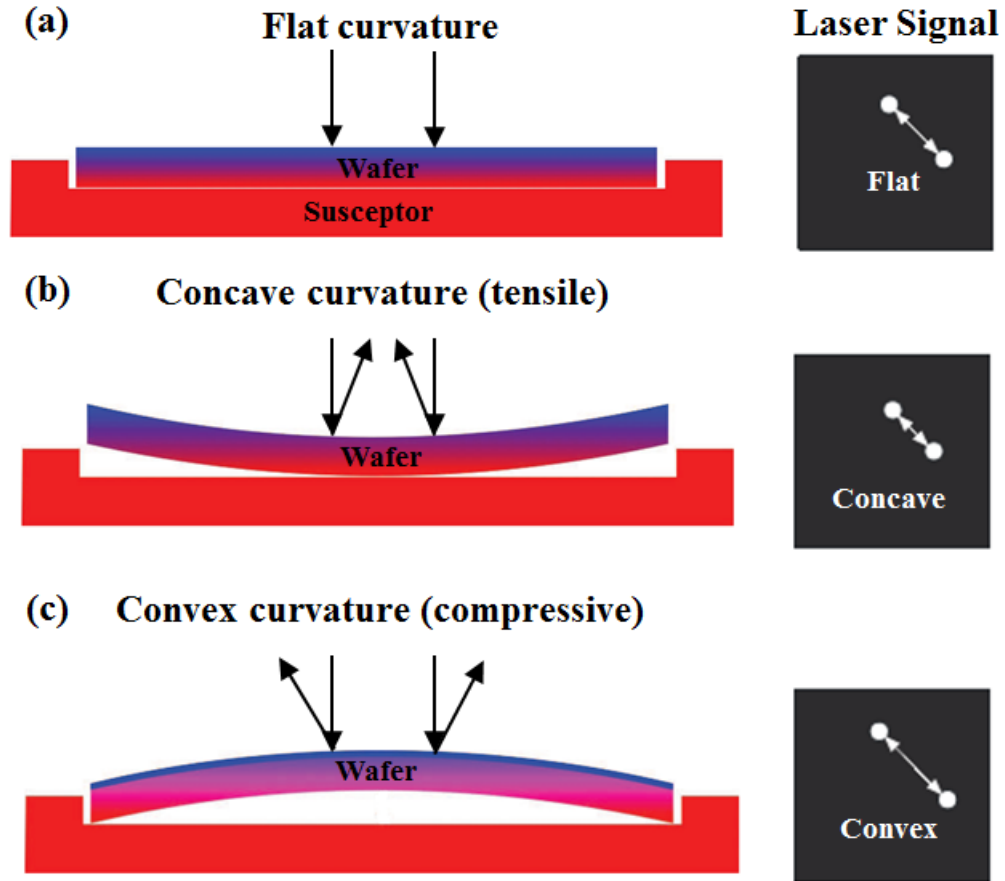


Figure 3.8: Wafer curvature definitions: (a) Flat, (b) Concave and (c) Convex.

### 3.4 Ex-situ Layer Characterization

In order to improve growth process, ex-situ characterization techniques are employed in addition to in-situ characterization. Characterization techniques used in this thesis will be presented in detail in the following section.

#### 3.4.1 Nomarski interference contrast microscopy

Nomarski interference contrast (NIC) microscopy is widely applied in evaluation of semiconductor layers and devices, it also known as differential interference contrast (DIC) microscopy or a polarization interference contrast microscopy. After growth, the micro scale surface morphology of the nitride materials can be directly inspected with using Olympus BX51M Microscope, as well as for locating defects using suitable chemical etching.

The Figure 3.9 shows a schematic of Olympus microscope. The light source is split into two parallel beams when it passes through a Wollaston prism. If two beams have the same path length then they will be in-phase and there will be no contrast. However, if there is an optical

path difference, here caused by a local difference in the samples surface height then there will be a phase difference between the beams and this will be revealed as contrast by the system. Pits, defects and cracks will stand out clearly in this interference contrast. The optical microscope resolution ( $d$ ) is given by Abbe's law in the formula [14]

$$d = \frac{0.612\lambda}{n\sin\theta} = \frac{0.612\lambda}{NA} \quad (3.10)$$

Where  $\lambda$  is the wavelength used to illuminate an object,  $n$  is a refraction index of the medium through which  $\lambda$  travels, and  $\theta$  is an aperture angle. The maximum resolution that can be achieved using blue-green light ( $\lambda$  is approximately 550 nm) incorporated into the Nomarski optical microscope used in this thesis is approximately 370 nm ( $NA=0.9$ ).

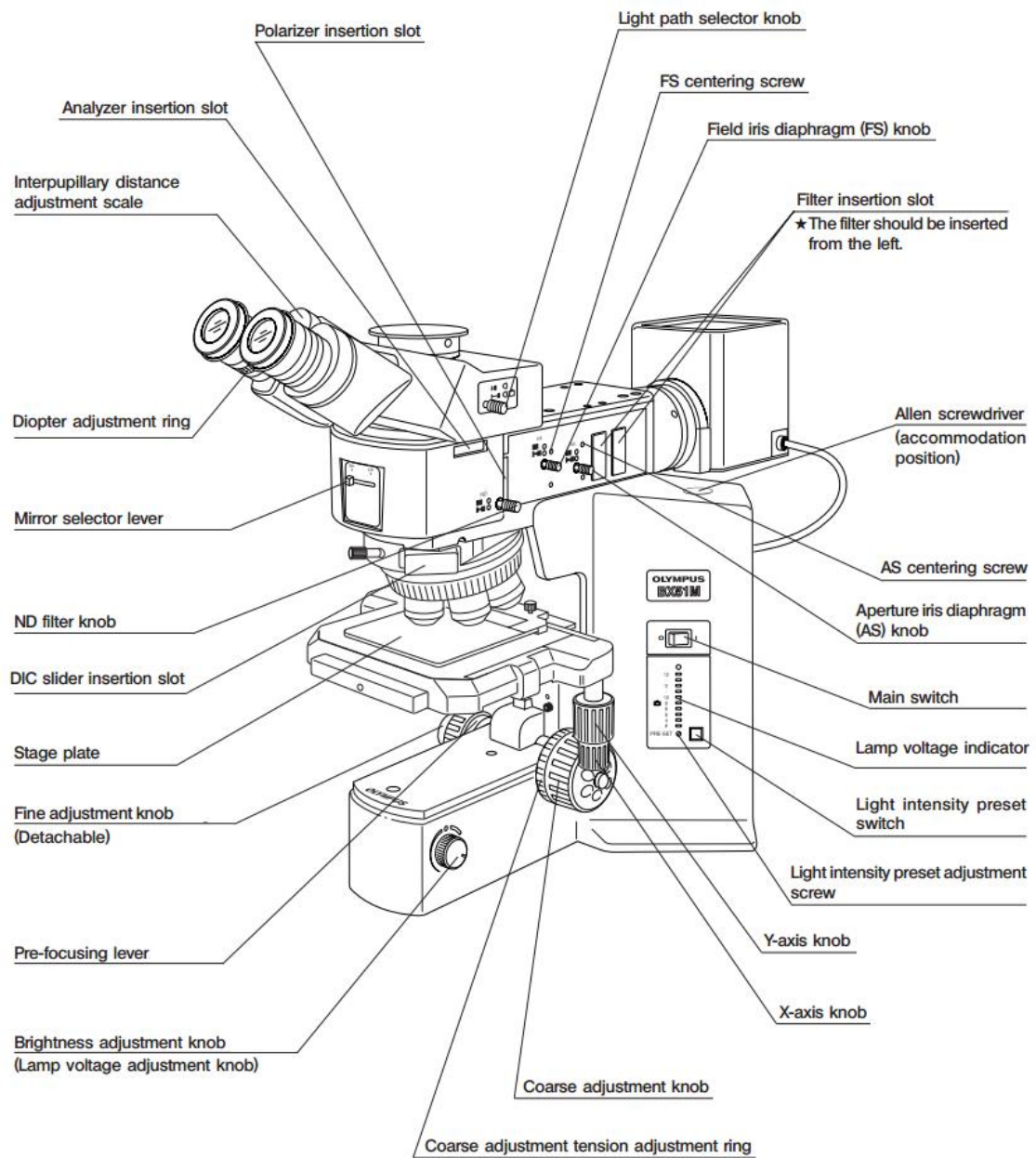
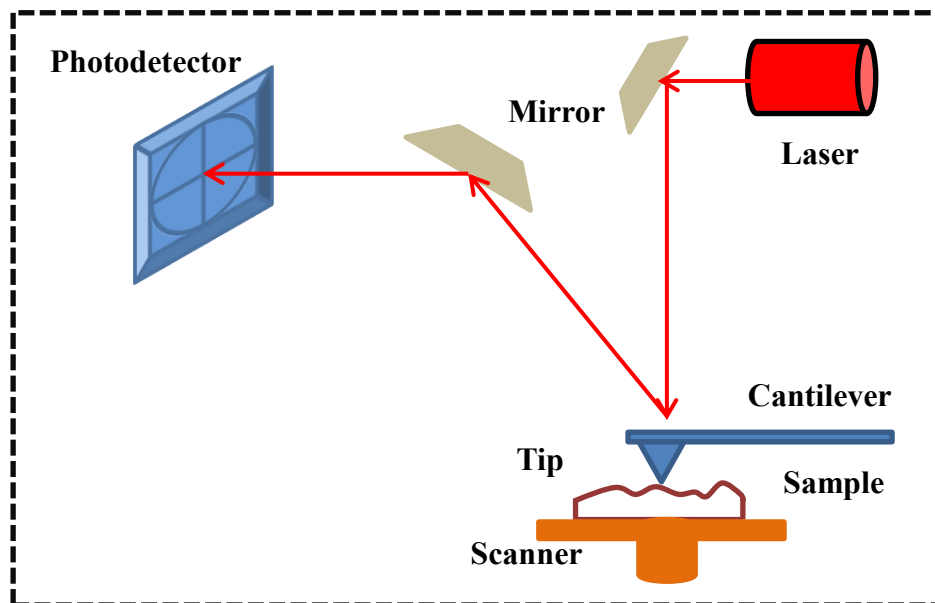


Figure 3.9: Schematic of Olympus BX51M Microscope [15].

### 3.4.2 Atomic force microscopy (AFM)

Atomic force microscopy (AFM) can be used to measure and create images of surface morphology with a three-dimensional picture. A surface image is produced when the microscopic tip contacts over the surface of the sample and interaction between the tip and the sample lead to a deflection of the cantilever due to Hooke's law. The deflection is monitored by using a laser beam reflected off the back of the cantilever into sensitive photodetector. A schematic of AFM is shown in Figure 3.10.



**Figure 3.10:** The basic operating principle of AFM. The sample is scanned with a sharp tip, which is on a cantilever. The deflection of the cantilever is measured with a laser beam.

In general, three scanning modes are available depending on the physical contact between the tip and the sample surface: contact mode, tapping mode (intermittent contact mode) and non-contact mode. The contact mode is the most common method which known as repulsive mode due to the associated force between the tip and the sample. An AFM tip gradually approaches the sample surface until the atoms are in contact. The cantilever will bend to keep the tip away from the surface due to repulsive Van der Waals forces between the tip and the atoms. However, the disadvantages of the contact mode are probable surface damage and lateral force due to the changes in friction and slope.

In our study, the surface morphologies of samples are investigated using tapping mode which consists of oscillating the cantilever near its resonance frequency. The resonance frequency changes when tip is brought closer to the sample surface due to change of effective spring constant of the cantilever is changed. It is described by the formula [16]

$$\omega = \omega_0 \sqrt{1 - \frac{1}{\kappa} \frac{dF}{dz}} \quad (3.11)$$

Where  $dF/dz$  is the force gradient, this allows the local electrostatic forces to be monitored by (for a constant cantilever drive frequency) observing changes in either the amplitude or phase of the cantilever vibration. These vertical tip movements are recorded to produce a AFM map of surface topography. Better resolution can be achieved by optimising the amplitude setpoint.

Surface features can be observed by AFM which may include surface roughness, growth mode changes and threading dislocation density. By counting the number of growth step termination defects at the surface, the mixed type and pure screw type dislocation density could be estimated [17]. However, the series of artifacts can affect the quality of images which include the tip, the scanner, vibrations, the feedback circuit and image-processing software. For example, the image resolution can be worse if the tip becomes blunt or acquires dust during scanning. Avoiding this tip artifact is achieved by changing the tip.

AFM was performed on a Veeco Multimode Scanning Probe Microscope (SPM). A better laser signal is achieved by optimising the photodiode and laser adjustment knobs before scanning, which are shown in Figure 3.11. Meanwhile, a slow scan rate and low amplitude set-point (distance between the tip and surface) are recommend to minimise tip damage and obtain good feedback.

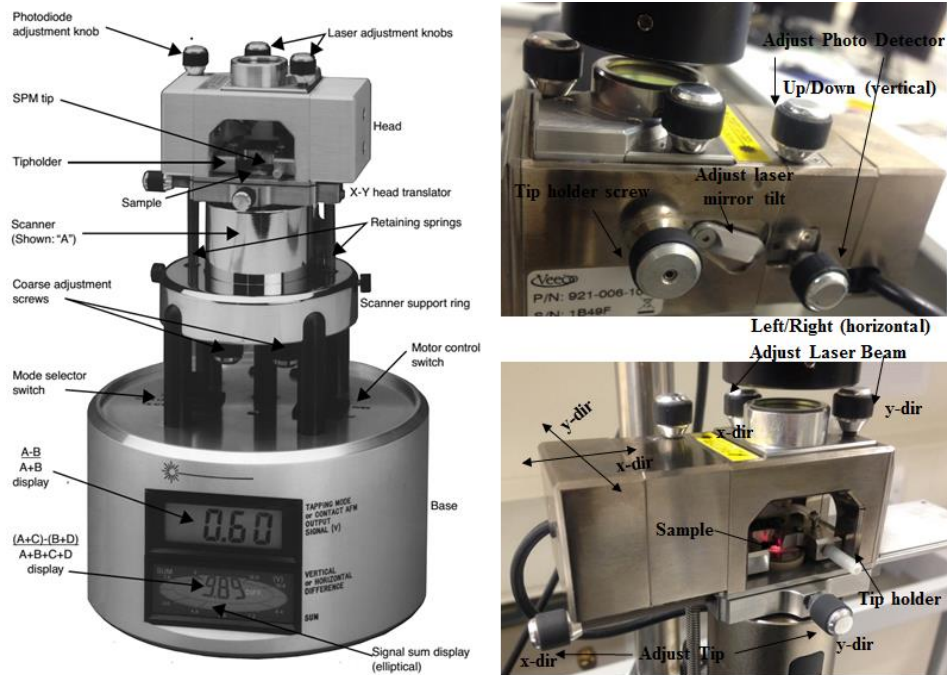


**Figure 3.11: Veeco MultiMode SPM and Scanner head (front and back views) [18].**

### 3.4.3 X-ray diffraction (XRD)

All XRD measurements were performed in the PANalytical X'Pert x-ray diffractometer using Cu  $K\alpha_1$  radiation of wavelength = 1.54056 Å. A typical simple diffractometer consists of a source of x-ray radiation, an incident beam hybrid monochromator (a hybrid 2-bounce asymmetric Ge (220) monochromator) to offset the x-ray beam (filter out extraneous wavelengths), slits to adjust the shape of the beam, an automatic beam attenuator (can be utilized to extend the dynamic range of the system and protect the detector, a sample stage with magnetic sample holder (high accurate goniometer for find adjustment of the sample position and orientation), analyser (3-bounce symmetric analyser crystal) to accept an angular range of about 0.003° and a detector to collect diffracted x-rays. It is shown in the following Figure 3.12.

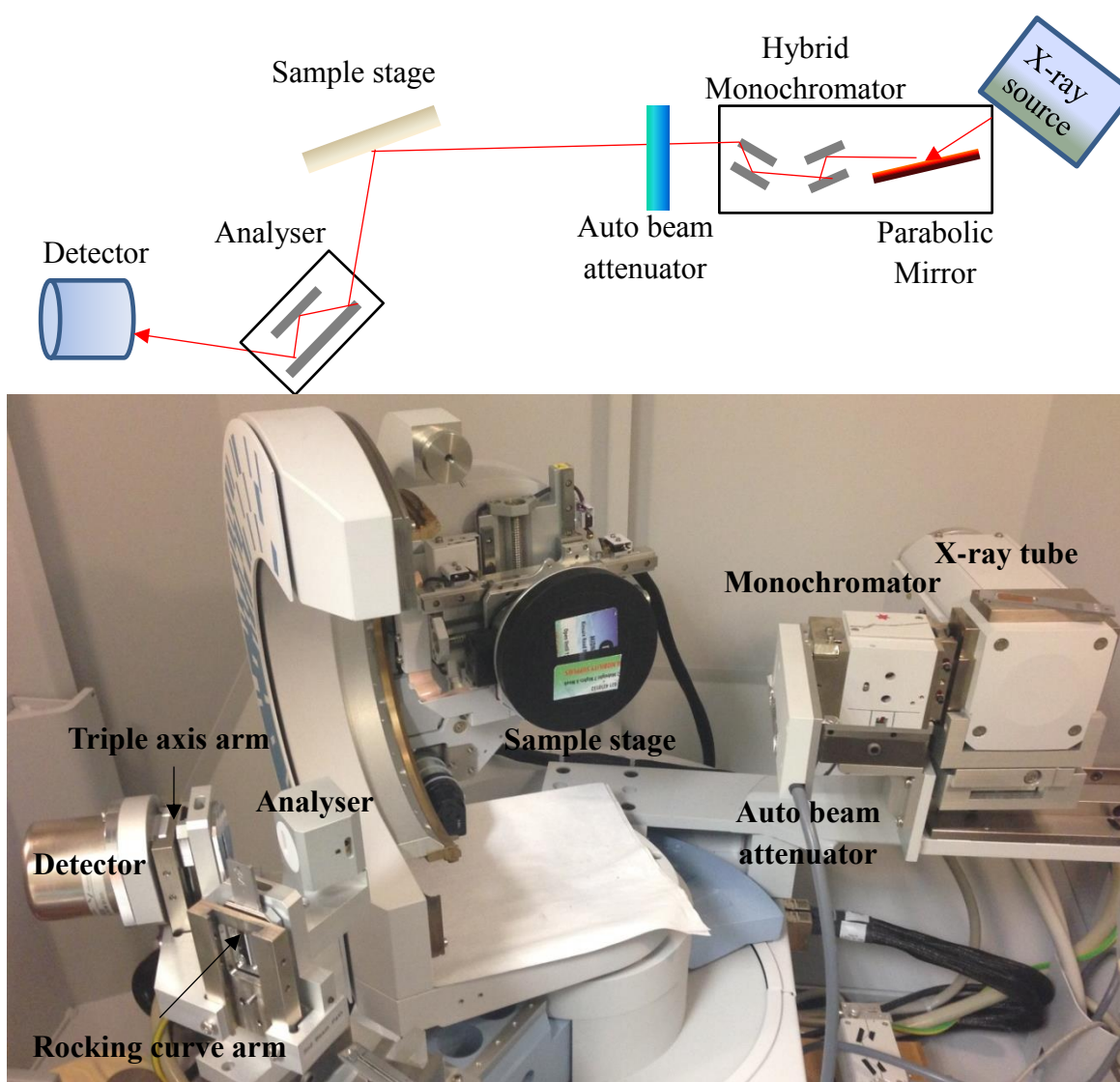


Figure 3.12: Illustration and photograph of a typical experimental arrangement showing, from right to left, X-ray tube, mirror, hybrid monochromator, sample, analyser and detector.



From the diffraction patterns of the reflected x-ray beam after interacting with a crystalline sample, information on lattice parameter, composition, uniformity of epitaxial layers, layer thickness, strain state, relaxation state and the crystal quality according to their crystal orientations can be obtained. In principle, the diffraction of x-rays is described by the Bragg law,

$$n\lambda = 2d_{hkl}\sin\theta_B \quad (3.12)$$

Where  $n$  is an integer,  $\lambda$  is the x-ray wavelength,  $d_{hkl}$  is the distance between each hkl plane in the atomic lattice and  $2\theta_B$  is the angle between the incident x-ray and the diffracted x-ray or the detector.

### 3.4.3.1 Lattice parameter measurements, strain and alloy composition

The method studied herein utilized relative measurements to determine the lattice parameters on the c-plane of group-III nitride crystals. These measurements not only provide information of lattice parameters  $a$  (in-plane) and  $c$  (out-of-plane), but also strain and alloy composition of the epilayers.

The incident beam angle ( $\omega$ ) is equal to half detected beam angle ( $\theta$ ) which is known as symmetric scan. Usually, multiple symmetric reflections (0002, 0004 and/or 0006) are measured (giving  $d_{0002}$ ,  $d_{0004}$  and/or  $d_{0006}$ ) in order to confirm the accuracy of lattice parameter. By the measured  $2\theta$  position with  $\omega$ - $2\theta$  scans in the triple-axis configuration, spacing  $d$  and  $c$  lattice parameter are obtained by,

$$d_{0002} = \frac{c_{0002}}{2} \cdot \frac{and}{or} d_{0004} = \frac{c_{0004}}{4} \quad (3.13)$$

Using  $d_{0002}$  and  $d_{0004}$  find average  $c$  lattice parameter. Then one or two asymmetric reflections ( $10\bar{1}5$ ,  $20\bar{2}4$  and/or  $20\bar{2}5$ ) are measured to determine a lattice parameter. The asymmetric scans also named as offset scan in which  $\omega$  is not equal to  $\theta$ . ( $\omega$ - $\theta$ ) is called the offset. With the measured  $2\theta$  position from reciprocal space maps (RSM), spacing  $d$  and a lattice parameter finally obtained by,

$$d_{105} = \frac{1}{\sqrt{\frac{4}{3}\left(\frac{1^2+1^2+5^2}{a^2}\right)+\frac{1^2}{c^2}}} \text{ and/or } d_{204} = \frac{1}{\sqrt{\frac{4}{3}\left(\frac{2^2+2^2+4^2}{a^2}\right)+\frac{2^2}{c^2}}} \quad (3.14)$$

The determination of the alloy composition is based on a unique relationship between the lattice parameter and the composition. If epilayer is assumed to be fully relaxed grown on

substrate, Vegard's law is usually applied. Strain-free  $\text{Al}_x\text{Ga}_{1-x}\text{N}$  layers should be depend linearly on the composition,

$$c_{\text{AlGaN}} = c_{\text{GaN}}(1 - x) + c_{\text{AlN}}x \quad (3.15)$$

$$a_{\text{AlGaN}} = a_{\text{GaN}}(1 - x) + a_{\text{AlN}}x \quad (3.16)$$

However, biaxial strain is generally assumed for the group-III nitride materials [19], which cause a distortion of the hexagonal unit cell and a change of the  $c/a$  ratio, illustrated in Figure 3.13. For a simple biaxial strain in a hexagonal system the out-of-plane strain  $\varepsilon_{zz}$  is related to the in-plane strain  $\varepsilon_{xx}$  by the distortion factor  $D$  [20, 21],

$$\varepsilon_{zz} = -D\varepsilon_{xx} = -\frac{2\nu}{1-\nu}\varepsilon_{xx} = -\frac{2C_{13}}{C_{33}} \quad (3.17)$$

Where  $\nu$  is the Poisson ratio and  $C_{13}$  and  $C_{33}$  are the components of the elastic stiffness tensor. Substituting for strain,

$$\frac{c-c_0}{c_0} = -\frac{2\nu}{1-\nu} \frac{a-a_0}{a_0} \quad (3.18)$$

Where  $a$  and  $c$  are the measured lattice parameters and determined through previous average calculation,  $a_0$  and  $c_0$  are the relaxed lattice parameters, respectively. For Poisson's ratio as a first-order approximation, a linear relationship is applied,

$$\nu_{\text{AlGaN}} = \nu_{\text{GaN}}(1 - x) + \nu_{\text{AlN}}x \quad (3.19)$$

The reference lattice parameters and Poisson ratio for group-III nitride materials used in this study are summarized in table 3.2. Equations (3.17) and (3.18) are combined and the solution is usually obtained iteratively. The alloy composition can be obtained by solving cubic equation of one unknown,

$$Ax^3 + Bx^2 + Cx + D = 0 \quad (3.20)$$

Where  $A$ ,  $B$ ,  $C$  and  $D$  are the constant coefficients. Once composition is known, relaxed lattice parameter values can be found from Vegard's rule. Relaxation is then determined according to the following expression,

$$R(\%) = \frac{a-a_s}{a_0-a_s} \times 100 \quad (3.21)$$

Where  $a$  is the measured lattice parameter,  $a_s$  is the substrate or template lattice parameter, and  $a_0$  is the fully relaxed lattice parameter.

	Lattice parameter (Å)	Poisson ratio
InN	a=3.540	0.272
	c=5.705	
GaN	a=3.189	0.183
	c=5.185	
AlN	a=3.111	0.203
	c=4.981	

Table 3.2: Summary of lattice parameters and Poisson ratio for group-III nitride materials [19, 22, 23, 24].

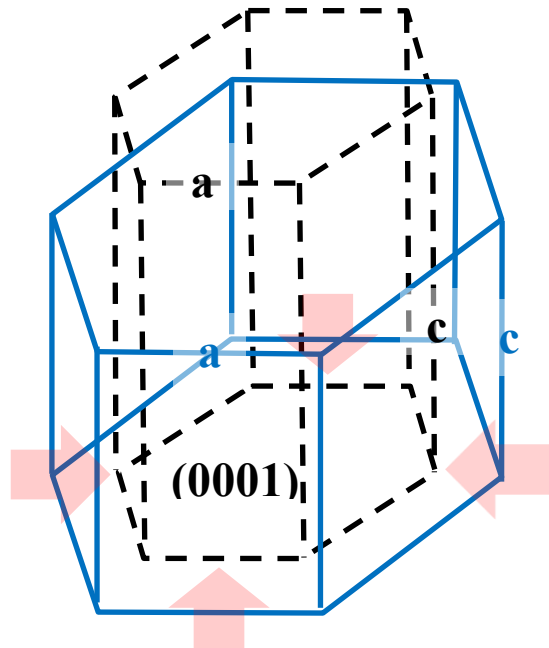


Figure 3.13: Hexagonal unit cell under biaxial compressive strain.

### 3.4.3.2 Omega rocking curve

The crystal quality of group-III nitride materials can be characterized by the line width of XRD rocking curve measurements ( $\omega$  scans), for example as the full width at half maximum (FWHM). The type of dislocation information can be extracted from symmetric or asymmetric rocking curves using open detector (without analyser), whereby the detector remains stationary at  $2\theta$  and the sample is rotated about the  $\omega$  axis.

There are major two parts which govern the crystal quality of the epilayer structure: (i) tilt,  $\omega$  scans of (0001) planes are used to measure the lattice tilt from mixed or screw dislocations and (ii) twist is caused by edge and mixed dislocations and is usually measured with  $\omega$ -scans



of off-axis reflections [25, 26]. Screw and edge TD densities can be estimated using several well-known empirical formulas from Kurtz et al. [27], Dunn and Koch [28] and Kaganer et al [29]. However, XRD rocking curve measurements is broadened not only by angular rotation at dislocations, but also lattice strain at dislocations, limited correlation lengths and strong bow of the samples [23, 30]. To distinguish between the different contributions to the broadening, a reduced beam size is required with point focus or divergence slit. Unfortunately, extremely low detected intensity is observed in point focus setup for our facility. In general, omega rocking curve measurement can qualitatively state that the smaller the FWHM value, the smaller is the number of structural disturbances in the material measured.

### 3.4.3.3 Reciprocal space map (RSM)

Symmetric (0004) and asymmetric ( $10\bar{1}5$ ) reciprocal space map (RSM) measurements were performed to study the structural properties of epilayers such as strain relaxation, group-III alloy composition and structural quality in grown samples of mismatched materials. A 2-axis RSM is obtained by measuring a series of  $\omega/2\theta$  scans each for a sequence of  $\omega$  offset values. The shape and positions of reciprocal lattice spots, a colour bitmap, or the intensity contour plots are also able to reveal more information. The horizontal and vertical positions of the reciprocal lattice spots have been found to yield information about the in-plane (a) and out-of-plane (c) lattice parameters, respectively. The narrow width of the lattice spot of the layer vertically aligned with that of the substrate indicates a high quality epitaxial layer. On the other hand, for the broader and wider lattice spot means to a structurally less uniform layer or low quality with high misorientations. The vertical elongation and interference fringes are due to the small finite layer thickness of superlattice or quantum well structures.

The  $\text{Al}_x\text{Ga}_{1-x}\text{N}$  of the RSM of ( $10\bar{1}5$ ) asymmetric reflection measured by asymmetrical XRD is shown in Figure 3.14 with diffraction space units. This measurement was performed to investigate the strain state, variation of composition, lattice parameters and mismatch of  $\text{Al}_x\text{Ga}_{1-x}\text{N}$  layers grown on AlN buffer layers. The diffraction space coordinates ( $Q_x$ ,  $Q_z$ ) are expressed with reference to the angular position as follows [31]:

$$Q_x = \frac{1}{2}(\cos\omega - \cos(2\theta - \omega)) \quad (3.22)$$

$$Q_z = \frac{1}{2}(\sin\omega + \sin(2\theta - \omega)) \quad (3.23)$$

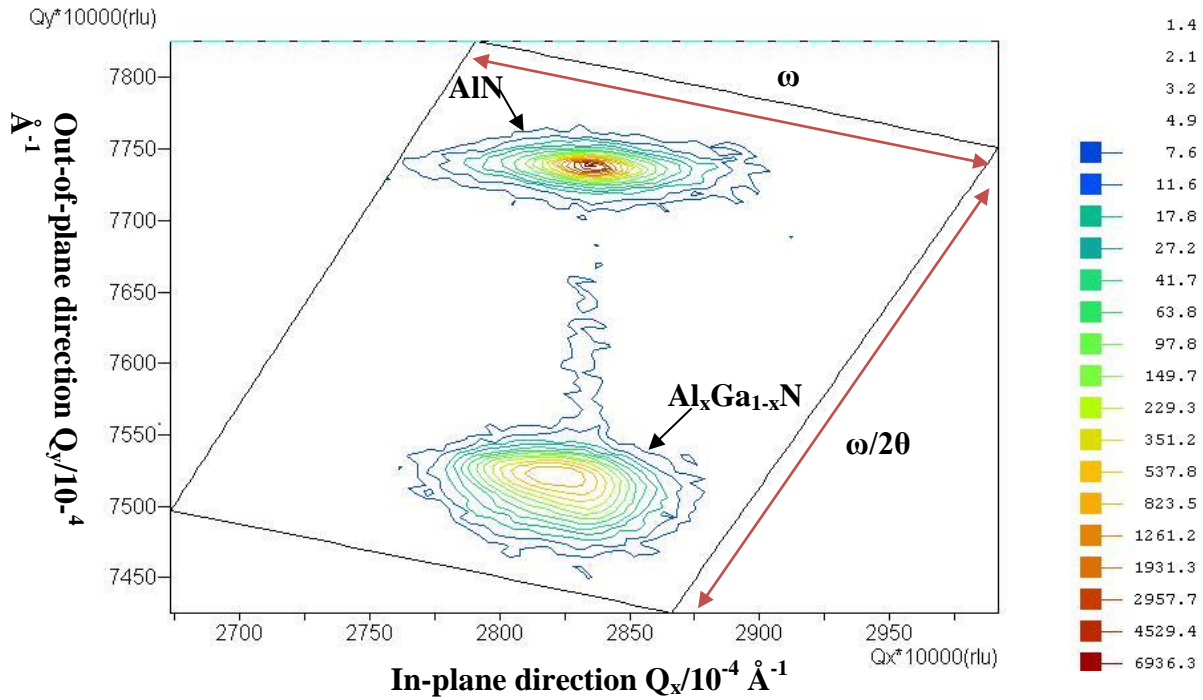


**Figure 3.14:**  $\omega/2\theta$  versus  $\omega$  map presented in  $10\bar{1}5$  reciprocal space units against intensity, which is determined the lattice parameters and strain state. The respective peaks originate from the AlN and AlGa<sub>x</sub>N.

### 3.4.4 Photoluminescence (PL)

Photoluminescence (PL) spectroscopy is a non-destructive tool for investigating both intrinsic and impurity related electronic transitions of semiconductor materials. The PL spectrum is obtained by recording the emission as a function of wavelength. The sample is excited using a laser or other source that has a photon energy above the sample bandgap. Thus electron-hole pairs are generated since electrons are excited from valence band (VB) and leaving holes behind. At the bottom of the conduction band (CB), electrons can recombine via two main recombination processes, each emitting energy by photon and/or phonons.

The quantity or intensity of the emitted light from epilayer is related to the relative contribution of the radiative process. Radiative recombination which includes band to band recombination, free exciton emission and emission related to dopants. On the other hand, non-radiative recombination has Auger recombination, surface recombination and recombination at defects, as illustrated in Figure 3.15.

Group-III nitride materials may emit below band edge energy light due to optical transition between shallow-level or deep-level defects in the crystal structure. The photoluminescence energy associated with these levels can be used to identify specific defects, and the amount of

photoluminescence can be used to crudely estimate their density. The native defect luminescence most often observed appear at about 2.2 eV and 2.9 eV in undoped GaN, referred to as the yellow luminescence and blue emission, respectively [32]. More information concerning the defect luminescence measurements of AlGaN will be discussed in Chapter 5.

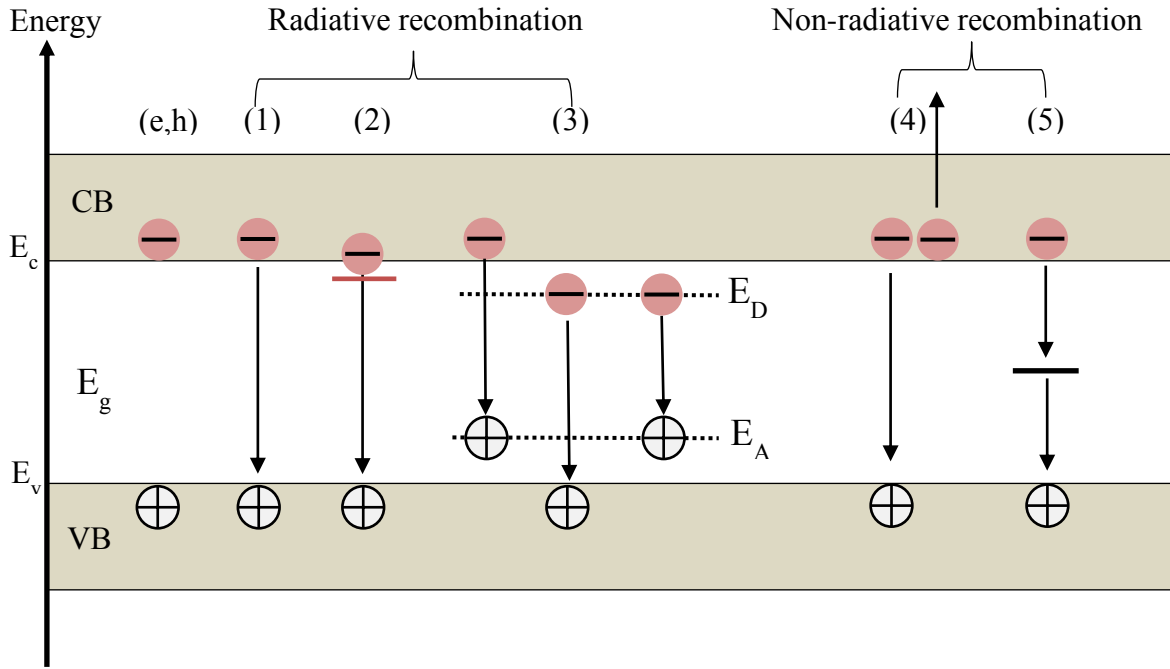


**Figure 3.15: Typical group-III nitride materials recombination processes. (e, h) stand for free electrons and holes respectively. The following recombination are considered: (1) band to band emission, (2) free exciton, (3) dopants related emissions, (4) Auger recombination and (5) defect level transition.**

In this work, the second harmonic (244 nm, 50 mW) of a CW Ar-ion laser is used for excitation of photoluminescence in the studied samples. In the optical setup this light is first focused onto a sample surface, then photoluminescence from the sample is collected by a pair of lenses on imaging spectrometer entrance slits and then recorded by a charge coupled device (CCD) camera. A closed-cycle helium cryostat is used to control temperature in the range from 10 to 450 K thus allowing temperature dependent PL measurements.

Photoluminescence excitation spectroscopy (PLE) is also applied to investigate absorption processes in luminescence. The detection wavelength is fixed and the excitation wavelength is scanned. It allows the absorption spectrum to be measured because the signal strength is simply proportional to the carrier density, and in turn is determined by absorption coefficient [33].

### 3.4.5 Electrochemical capacitance voltage (ECV)

The common doping profile measurement methods include spreading resistance profiling (SRP), secondary ion mass spectroscopy (SIMS) and electrochemical capacitance voltage (ECV). These techniques are compared in Table 3.3. In contrast with other techniques, the ECV method provides only the electrically active dopants and has a depth resolution in the sub-nm range, which also has easy sample preparation. The ECV wafer profiler CVP21 from WEP was employed in all experiments.

Application requirement	SRP	SIMS	ECV
The concentration of electrically activated dopants	O	×	O
Doping type (n or p type)	×	×	O
Depth resolution in the 1nm range possible	×	O	O

Table 3.3: The comparison of SRP, SIMS and ECV.

In a CV measurement, a semiconductor is placed in contact with a metal, the diffusion of surface conduction carriers into the metal leads to depletion of carriers at the semiconductor interface. This type of interface is known as a Schottky barrier [34]. In ECV, an electrolyte is chosen which can replace the metal to form a Schottky barrier, wetting an area of 1 mm<sup>2</sup> delimited by a sealing ring. In reverse bias condition, this interface acts as a Schottky-like contact and with common CV technique the concentration of (ionized and neutral) donors and acceptors can be evaluated in n-type and p-type material, respectively. In forward bias (for p-type layers) or by illuminating the interface with UV light (for n-type layers), the semiconductor is etched [35]. The standard equation used to determine the carrier concentration for the Schottky diode is based on equation [34],

$$N = \frac{-2}{q\epsilon_R\epsilon_0 A^2 \frac{d(\frac{1}{C^2})}{dV}} \quad (3.24)$$

Where N is the carrier concentration, C is the capacitance, A is the etch area (sealing ring area of the equipment), V is the external voltage applied to the depletion zone, q is the electron charge,  $\epsilon_R$  is the semiconductor dielectric constant and  $\epsilon_0$  is vacuum permittivity ( $8.85 \times 10^{-12}$  C/V). The size of the etch area (A) should be determined as accurately as possible, which is the main source of errors. By measuring the geometry of the etch area after the ECV measurement it can be found that the contact area differs from the sealing ring area [36]. A

nonuniform etching of GaN (or InGaN) surface has been observed [37]. Hence, two-stage modification of technique is more preferable [38].

During ECV measurement, the etch process is not a “real chemical etching”. It is a cyclic oxide thickening and oxide removal process under strict control of pH. KOH is only used to set the pH to 12, so KOH is 0.01 mol and not 1 mol due to inhibition of the oxide creation.

In ECV measurement, if there is no or very low etch current, then typically either concentration too low (=high resistivity) or the concentration is very high ( $> 5 \times 10^{18} \text{ cm}^{-3}$ ). In this case the depletion width is too thin to get reasonable UV light absorption within depletion zone. Only the light absorbed within the intrinsic field of depletion zone will lead to holes and electrons which are separated, holes being driven to the surface by the intrinsic field of the depletion zone. In the case of n-type AlGaN measurement, etch current is always low due to wider bandgap, and thus smaller light absorption, and also due to usually worse material quality and thus more recombination centres killing holes, thus killing the etch current.

### 3.4.6 Hall measurement

Hall measurement is a quick and simple analysis tool for determining electrical properties of semiconductors such as resistivity ( $\rho$ ), sheet resistance ( $R_s$ ), the carrier concentration ( $N$ ) and the mobility of charge carriers ( $\mu$ ) at 300 K and 77 K (using liquid  $N_2$ ). The Hall effect is caused by the deflection of moving charged particles (i.e. electrons) by a magnetic field ( $B$ ) perpendicular to the current ( $I$ ), the principle is demonstrated schematically in Figure 3.16. With the use of a magnetic field (0.32 T for experiment in our lab) perpendicular to the current flow, the electrons accumulate on one side of the sample resulting in an electric field which compensates the Lorentz force. By measuring the voltage associated with this the carrier concentration can be obtained. For a bar shaped sample with the thickness  $d$  the carrier concentration is given by the following expression,

$$N = -\frac{I_x B_z}{q d V_H} \quad (3.25)$$

Where  $q$  is the electronic charge,  $d$  is thickness of sample and  $V_H$  is the measured Hall voltage. The sign of the charge carriers can be found from the sign of the Hall voltage. Therefore, it can be used to determine doping type of sample.

The equation for sample resistivity can be written in terms of the mobility of the carriers as,

$$\rho = \frac{1}{q(n\mu_n + p\mu_p)} \quad (3.26)$$

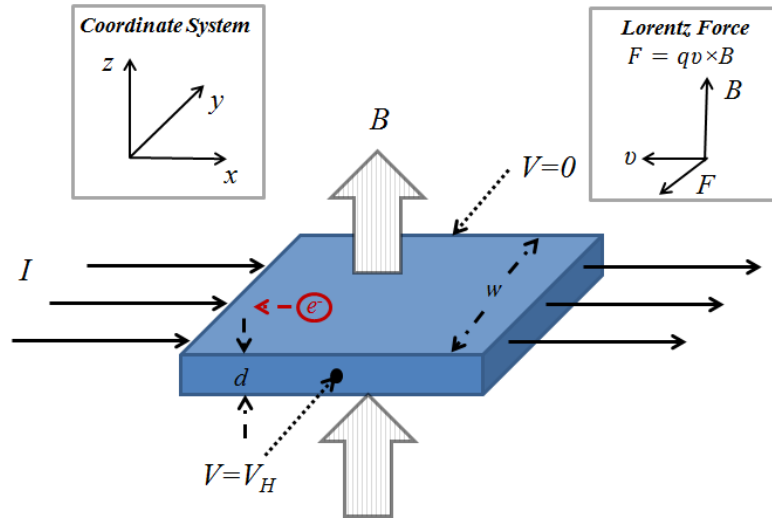


Figure 3.16: Schematics of the Hall measurement.

Where  $\mu_n$ ,  $\mu_p$  are the electron and hole mobility, respectively. For example, if sample is n-type,  $n\mu_n$  should be much higher than  $p\mu_p$ . The Hall mobility can be obtained, when additionally sheet resistance  $R$  of the sample is measured. Then it is given by

$$\rho = \frac{1}{qN\mu_n} \Rightarrow R_s = \frac{1}{qdN\mu_n} \Rightarrow \mu_n = \frac{1}{qdNR_s} \quad (3.27)$$

With this method the mobility and carrier concentration of square shaped samples can be determined as long as there are no cracks and non-conducting islands.

The wafer is diced into  $6 \times 6$  or  $8 \times 8$  mm<sup>2</sup> square size by diamond scribe. It is mounted on the printed circuit board (PCB) and connected by four wire bonds with indium (In) balls, as shown in Figure 3.17. The four contacts should be sufficiently small and close to the edge as possible. The In balls were annealed at 400 °C for 3-4 minutes in order to achieve ohmic contacts. The success with ohmic contacts to p-type GaN and AlGaN are much more limited than n-type material due to large acceptor ionization energies and large work function. To date, the best contact metallization for p-type GaN is based on gold (Au), platinum (Pt), nickel (Ni) and/or palladium (Pd) [39, 40, 41], which can be deposited using metal evaporation in the clean room. Ohmic contact quality must be checked in the current-voltage (I-V) measurement for sample uniformity. A linear I-V curve indicates good ohmic contacts. Meanwhile, a good set of results should be repeatable at different currents.



Figure 3.17: Schematics of PCB sample holder.

### 3.5 References:

- [1] S. R. Jeon, Z. Ren, G. Cui, J. Su, M. Gherasimova, J. Han, H. K. Cho, and L. Zhou, Appl. Phys. Lett. 86, 082107 (2005).
- [2] Y. Ohba, and A. Hatano, J. Cryst. Growth. 145, 214 (1994).
- [3] C. Antoine, Compt. rend.107, 681 (1888).
- [4] T. Webb, Epison III Manual, Thomas Swan Scientific Equipment LTD (1999).
- [5] P. D. Dapkus, Annu. Rev. Mater. Sci. 12,243 (1982).
- [6] M. J. Ludowise, J. Appl. Phys. 58, R31 (1985).
- [7] K. L. Choy, Progress in Materials Science 48, 57 (2003).
- [8] Aixtron 3×2 FT MOVPE system manual, rev 1.6 (2009).
- [9] W. G. Breiland, and K. P. Killeen, J. Appl. Phys. 78, 6726 (1995).
- [10] N. Watanabe, T. Kimoto, and J. Suda J. Appl. Phys. 104, 106101 (2008).
- [11] Y. P. Varshni, Physica. 34, 149 (1967).
- [12] K. B. Nam, J. Li, J. Y. Lin, and H. X. Jiang, Appl. Phys. Lett. 85, 3489 (2004).
- [13] EpiCurve® TT for AIXTRON CloseCoupleShowerhead® MOCVD systems manual book, p 5-7.
- [14] R. E. Lee, Prentice Hall, Englewood Cliffs, New Jersey (1993).
- [15] Instructions BX51M system metallurgical microscope (<http://tfnl.khu.ac.kr/download/op.pdf>) (accessed 14 Nov 2014).
- [16] R. A. Oliver, Rep. Prog. Phys. 71, 076501 (2008).
- [17] S. E. Bennett, D. Holec, M. J. Kappers, C. J. Humphreys, and R. A. Oliver, Rev. Sci. Instrum. 81, 063701 (2010).
- [18] Digital Instruments Multimode AFM Handbook.
- [19] M. A. Moram, and M. E. Vickers, Rep. Prog. Phys. 72, 036502 (2009).
- [20] N. Herres, L. Kirste, H. Obloh, K. Kohler, J. Wagner, and P. Koidl, Mater. Sci. Eng. B91, 425 (2002).
- [21] M. Schuster, P. O. Gervais, B. Jobst, W. Hosler, R. Averbeck, H. Riechert, A. Iberl, and R. Stommer, J. Phys. D:Appl. Phys. 32 A56 (1999).
- [22] K. Wang, and R. R. Reeber, Appl. Phys. Lett. 79, 1602 (2001).
- [23] M. A Moram, Z. H Barber, and C.J Humphreys, J. Appl. Phys. 102, 023505 (2007).
- [24] A. F. Wright, J. Appl. Phys. 82, 2833 (1997).

- [25] H. Heinke, V. Kirchner, S. Einfeldt, and D. Hommel, *Phys. Status. Solidi. A* 176, 391 (1999).
- [26] V. Srikant, J. S. Speck, and D. R. Clarke, *J. Appl. Phys.* 82 4286 (1997).
- [27] R. Chierchia, T. Böttcher, H. Heinke, S. Einfeldt, S. Figge, and D. Hommel, *J. Appl. Phys.* 93, 8918 (2003).
- [28] C. G. Dunn, and E. F. Koch, *Acta. Metall.* 5, 548 (1957).
- [29] V. M. Kaganer, O. Brandt, A. Trampert, and K. H. Ploog, *Phys. Rev. B* 72, 045423 (2005).
- [30] M. A. Moram, M. E. Vickers, M. J. Kappers, and C. J. Humphreys, *J. Appl. Phys.* 103, 093528 (2008).
- [31] P. Kidd, *XRD of Gallium Nitride and Related Compounds: Strain, Composition and Layer Thickness* (Panalytical, Almelo, 2009).
- [32] M. A. Reshchikov, and H. Morkoc, *J. Appl. Phys.* 97, 061301 (2005).
- [33] M. Fox, *Optical Properties of Solids* (Oxford University Press, Oxford, 2002).
- [34] S. Sze, and K. Kwok, *Physics of Semiconductor Devices*. Wiley - VCH, 2007.
- [35] P. Blood, *Semicond. Sci. Technol.* 1, 7 (1986).
- [36] R. Bock, P. P. Altermatt, and J. Schmidt, presented at *Proceedings of the 23rd EU PVSEC*, Valencia, Spain, 2008.
- [37] V. Zubkov, O. Kucherova, D. Frolov, and A. Zubkova, *Phys. Status. Solidi. C* 10, 342 (2013).
- [38] T. Wolff, M. Rapp, and T. Rotter, *Phys. Status. Solidi. A* 201, 2067 (2004).
- [39] A. G. Baca, F. Ren, J. C. Zolper, R. D. Briggs, and S. J. Pearton, *Thin Solid Films*, 599, 308 (1997).
- [40] J. K. Ho, C. S. Jong, C. C. Chiu, C. N. Huang, K. K. Shih, L. C. Chen, F. R. Chen, and J. J. Kai, *J. Appl. Phys.* 86, 4491 (1999).
- [41] Y. L. Li, E. F. Schubert, J. W. Graff, A. Osinsky, and W. F. Schaff, *Appl. Phys. Lett.* 76, 2728 (2000).



# MOVPE growth of AlN

---

## 4.1 Introduction

Aluminium nitride (AlN) is an important wide band-gap semiconductor material that has attracted much interest for its use in electronic and optoelectronic devices. At present, the lifetime and performance of most nitride devices is limited by the relatively poor quality of heteroepitaxial material grown on lattice mismatched substrates such as sapphire, SiC and Si [1, 2, 3]. Although significant growth progress has been achieved in high quality bulk AlN single crystal by some companies such as HexaTech Inc, CrystAl-N GmbH and Nitride Crystals Inc, these commercial native substrates are very expensive (above €2,000 per inch) comparing with foreign substrates. Therefore, AlN epilayers grown on (0001) c-plane sapphire substrates were primary choice in our experiments to form a high quality template for device overgrowth.

The MOVPE growth of AlN is a challenge. The major problems arise predominantly from the higher Al-N bond strength of 2.88 eV than Ga-N bond strength of 2.2 eV [4]. As a consequence, pre-reactions increase, and the adsorbed Al atoms possess a low surface mobility due to high incorporation energies (surface energy quantifies the disruption of intermolecular bonds that occur when a surface is created) [5]. Therefore, the crystalline quality and surface morphology of AlN can be improved by reduction of the carrier gas flow rate at relatively low V/III ratios, high growth temperature, and by total reactor pressure decrease due to enhancement of surface migration of Al atoms and suppression of strong parasitic reactions in the gas phase [5, 6, 7, 8].

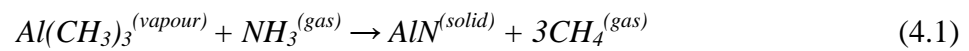
Several MOVPE growth methods have been proposed in the literature in order to reduce dislocation density for AlN grown on c-plane sapphire substrate: for example, high temperature (HT) growth AlN [8,9,10,11], epitaxial lateral overgrown AlN [12], patterned sapphire prior to AlN growth [13], use of alternating V/III ratio [14, 15] and use of AlN

interlayers grown at low temperature [15]. In the following sections, the direct, two-step and three-step growth processes will be presented.

In this chapter, the AlN epilayers were grown by the MOVPE technique in Aixtron CCS 3×2 FT reactor. The influence of independent growth parameters such as pre-treatment, V/III ratio, growth temperature, epilayer thickness and substrate miscut angle on the initial and/or subsequent layers of AlN was investigated. Finally, an optimum growth condition is empirically determined. The surface features and structural properties were evaluated using Nomarski microscopy, spectroscopic in-situ reflectometer, atomic force microscopy (AFM), X-ray diffraction (XRD) and transmission electron microscopy (TEM).

## 4.2 Chemical reaction mechanism of AlN

Hydrogen/Nitrogen (H<sub>2</sub>/N<sub>2</sub>) carrier gas delivers the trimethylaluminium (TMAI) precursor into the reactor chamber (the selection of carrier gas depends on growth process requirement) and react with NH<sub>3</sub> that is introduced in other separate line. This reaction can be simply expressed as,



However, chemistry of epitaxial growth of AlN is very complex and involves a number of gas phase and surface reactions as shown in Figure 4.1 [16, 17]. Parasitic reactions between TMAI and NH<sub>3</sub> can create (TMAI:NH<sub>3</sub>) adduct, which is difficult to avoid since the adduct (and its by-products) forms already at room temperature [5]. These parasitic reactions can influence the growth rate and the mole fraction of Al in AlGaN growth due to them being more severe for AlN growth than for GaN growth. The adduct decomposition can form (Al(CH<sub>3</sub>)<sub>2</sub>:NH<sub>2</sub>)<sub>n</sub> compounds. Monomers (n=1) and dimers (n=2) are expected to contribute to the growth while the higher order oligomers (n>2) have a low vapour pressure and therefore have sufficient energy to lose methyl groups to form AlN particles in the gas phase at high growth temperatures [5]. To prevent the gas phase reactions, AlN is typically grown at low reactor pressure (between 40 and 100 mbar), e.g. to obtain a high velocity of the carrier gases and therefore only a short residence time in the gas phase, and also to enhance the mobility of adatoms on the surface [5, 16]. The equilibrium of the initial (CH<sub>3</sub>)<sub>3</sub>Al:NH<sub>3</sub> adduct formation reaction can shift and stabilize TMAI at low V/III ratios and thus avoid severe losses by parasitic reactions [18]. Finally, the showerhead gap is also a critical parameter to minimize the parasitic reactions. For example, reducing showerhead gap results



simultaneous start (no pre-flow:  $\text{NH}_3$  and TMAI introduced simultaneously) for the initiation of AlN growth, and pre-flow of TMAI or  $\text{NH}_3$  prior introducing the other precursor.

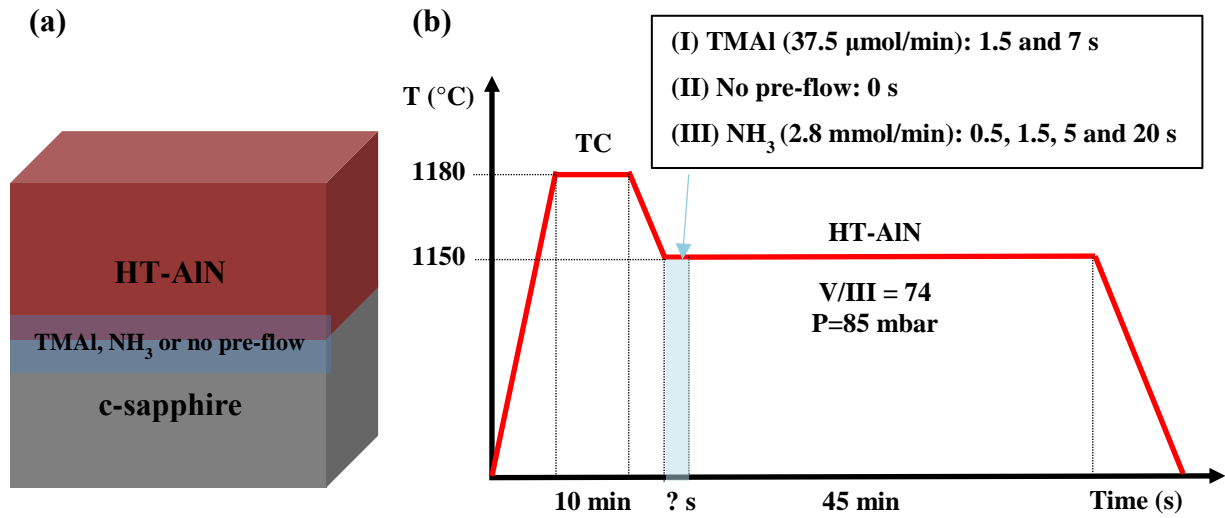


Figure 4.2: (a) Schematic of the structure and (b) growth sequence for an AlN epilayer with different pre-treatment.

### 4.3.2 Results

The photographs of AlN epilayers grown on sapphire wafers are shown in Figure 4.3. For a simultaneous start a faint rough area in the centre of the wafer was observed (not visible in the image). This rough area became larger and more visible by increasing the  $\text{NH}_3$  pre-treatment time. Conversely applying a TMAI pre-treatment lead to its suppression. It was found that rough areas were easily scratched by tweezer whilst the smooth areas robust to such treatment.

For the sample NT0044 (5 seconds  $\text{NH}_3$  pre-flow), two distinctive features can be seen from AFM images taken in smooth and rough area, shown in Figure 4.4. The surface micro-morphology of the sample with the smooth area [Figure 4.4(a)] is relatively flat but with step bunching features (RMS roughness is around 2.5 nm average estimated from multiple  $10 \times 10 \mu\text{m}^2$  AFM images). Pyramidal surface features are observed in the rough area, which have much higher RMS roughness of above 19 nm. This entirely different morphology of the sample might be due to incomplete coverage of N-polar AlN on sapphire surface: when exposing sapphire to  $\text{NH}_3$ , the very first oxygen layers are substituted by nitrogen. The underlying Al atoms experience these nitrogen atoms and N-polarity is established [25]. However, the surface roughness is high due to non-uniform of N-polar material on sapphire

surface even after 1 hour of nitridation [26]. Therefore, inversion domains (IDs) are dominant in the layers (mixed polarity).

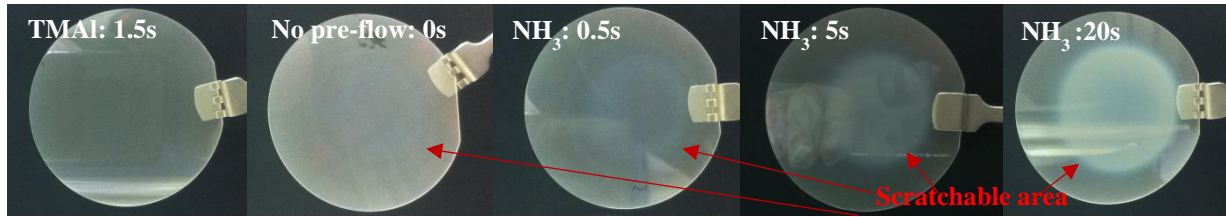


**Figure 4.3: photographs of AlN epilayers on c-plane sapphire with different pre-treatment.**

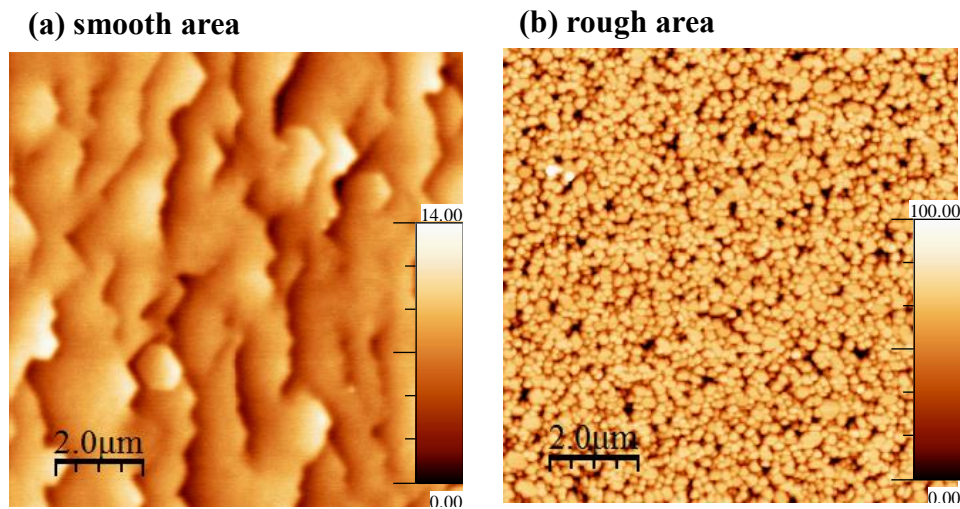


**Figure 4.4:  $10 \times 10 \mu\text{m}^2$  AFM scans of  $1 \mu\text{m}$  thick AlN buffer layers taken from rough (a) and smooth (b) area, respectively. The unit of Z scale bars are nanometer.**

Figure 4.5 shows in-situ reflectance curves measured at the wafer centre during the AlN growth runs under different pre-treatments. The first observation is that the growth rates of all the HT-AlN layer are similar around  $0.37 \text{ nm/s}$  ( $1.33 \mu\text{m/min}$ ). Second, the average reflectance value only stays nearly constant for a sample grown with a TMAI pre-treatment substrate. The decreasing average reflectance indicates roughening grown on the intentional nitrided ( $\text{NH}_3$  pre-flow) surface and for the no pre-flow sample. The result is in good agreement with the previous microscopy images (Figure 4.3).

XRD is sensitive to tilt and twist in the whole sample and can thus be used as an indirect measure of total TD densities [27]. Figure 4.6 shows the FWHM values from symmetric (0002) and asymmetric ( $10\bar{1}1$ ) peaks measured by XRD rocking curves as a function of pre-treatment time. The tendency in the (0002) reflections is that the FWHM reduces with decreasing the TMAI pre-flow time. The FWHM of the (0002) reflections improve from 970 to 239 arcsec. In contrast, the trend from the ( $10\bar{1}1$ )  $\omega$ -FWHMs suggests a minimum number

of threading dislocations (TDs) with an edge component when the 7s of TMAI pre-treatment is employed, the longest pre-treatment time used in this study.

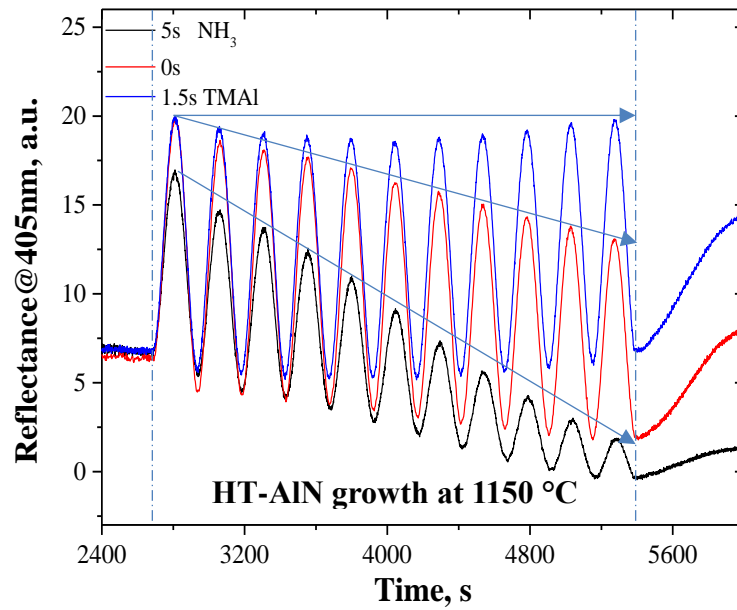


Figure 4.5: Reflectance measured in-situ (at a wavelength of 405 nm). The strong damping upon nitridation (dashed line) indicates surface roughening. Extended alumination results in a change in reflectivity before NL growth.

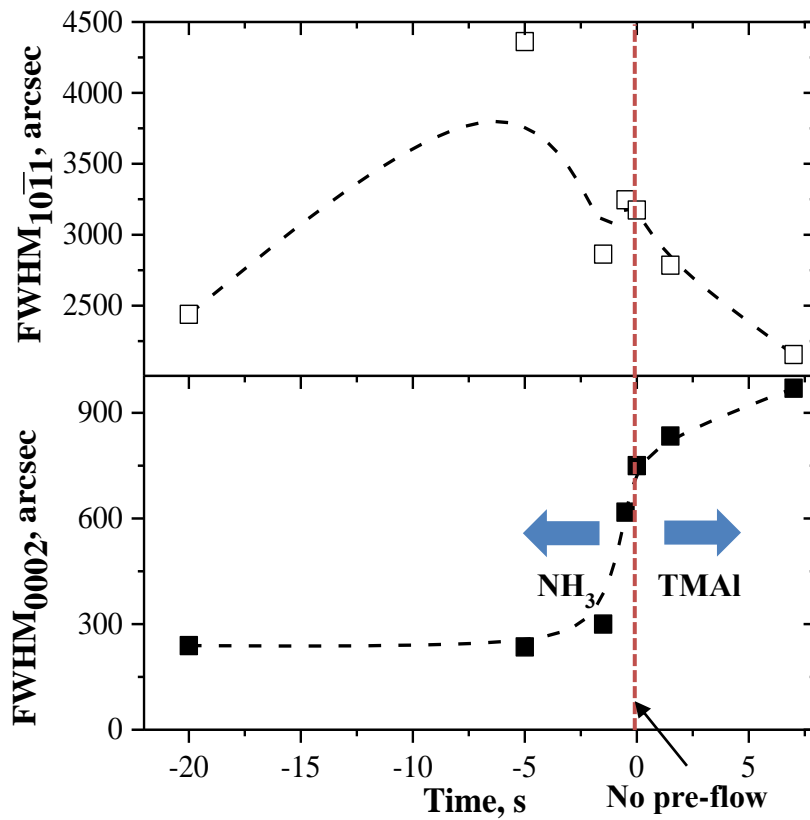


Figure 4.6: FWHM values of (0002) and (10 $\bar{1}1$ ) XRD rocking curves as a function of TMAI (positive) and NH<sub>3</sub> (negative) pre-treatment time.

### 4.3.3 Discussion and conclusion

The results here differ significantly from that reported by the University of Sheffield [24], in our experiments, a TMAI pre-treatment was required to prevent rough N-polar AlN growth occurring. It is clear from this that AlN recipes can be particularly difficult to transfer between reactors, even those from the same design family. The effect we attribute to the difference of the initial chemical condition of the reactors, whereby small changes in the reactor design can have significant effects on growth leading to different material quality. Further evident of this sensitivity is given by the fact that we have observed changes in quality depending on the history of growths undertaken immediately before growing an AlN on sapphire substrate.

This study suggests that the polarity of AlN epilayers depends on the surface state of the sapphire substrate directly before growth. The consequence of the preparation conditions with respect to the polarity control are summarized in Figure 4.7. N-polar AlN regions were always found by growing directly on “nitride” sapphire, while Al-polar AlN was obtained, if the TMAI pre-flow of the sapphire substrate was long enough.

Experiments long bake time carried out and was generally found to make the roughening problem more severe for an equivalent pre-treatment directly before growth. This indicates that residual N coating compounds from previous growths may desorb from the reactor showerhead and/or J-liner walls and give an effective nitridation of the sapphire prior to growth.

For AlN growth a smooth Al-polar surface is critical to act as a template for subsequent device overgrowth. Hence a TMAI pre-treatment step is generally applied to obtain this.

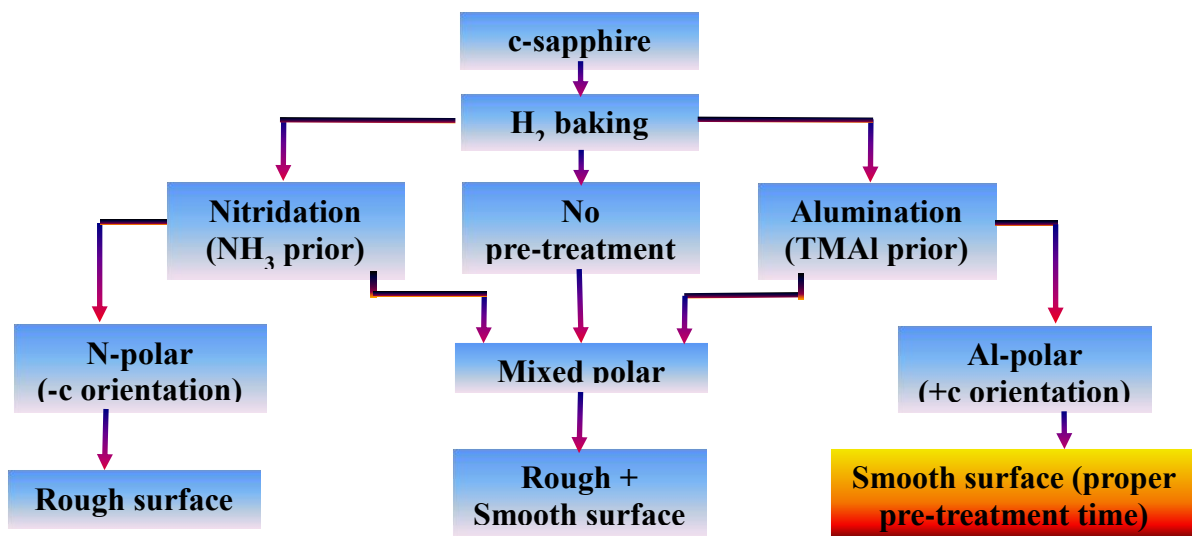


Figure 4.7: Schematic diagram of the AlN polarity control scheme.

## 4.4 Two-step growth of AlN

A number of approaches have been used to obtain low dislocation density in AlN. One route to improve AlN epilayer quality is using a thin low temperature nucleation layer in a two-step process, partly inspired by the early work of Amano et al. [28]. They reported the first successful growth of high quality GaN layers using a two-step growth process in 1986, where a low temperature AlN layer was used as a base for the GaN. This process established basis for the standard methods for the epitaxial growth of group-III nitride materials by MOVPE [29,30].

To overcome the problem of a large lattice mismatch and a large thermal expansion coefficient between wurtzite group-III nitride materials and sapphire substrates, a low temperature (LT) (below 1000 °C) AlN layer was employed as an initial growth step before the deposition of the main layer. The LT-AlN acts as a nucleation layer (NL) and polarity control layer (PCL) between the sapphire and the subsequent epilayers. It is noteworthy to mention here that the surface of the LT-AlN needs a proper pre-treatment step using TMAI (covered by a thin molten layer of Al) to avoid a mixed polar form at the initial stage. After that the main HT-AlN layer was deposited as shown in Figure 4.8 (a).

In this section, a clear impact on the structural and surface quality of AlN layers were observed in five series: (2-I) variation of LT-AlN thickness, (2-II) variation of LT-AlN growth temperature, (2-III) variation of HT-AlN thickness, (2-IV) variation of HT-AlN growth temperature and (2-V) variation of miscut angle of c-plane sapphire. During optimization of each part, the growth conditions of the other parts were kept constant.

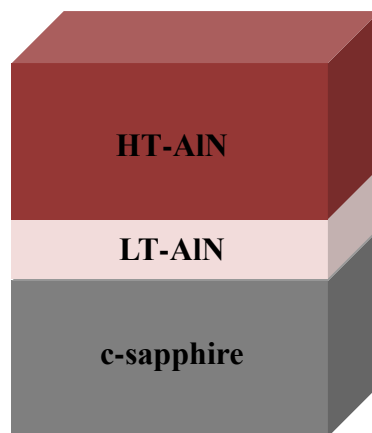


**Figure 4.8:** Schematic structures of the AlN epilayers grown on sapphire using two-step recipe.



#### 4.4.1 Series 2-I and 2-II: Impact of growth NL thickness and growth temperature

For these first studies, we used c-plane sapphire substrates with a miscut angle of  $0.36^{\circ} \pm 0.04^{\circ}$  towards m-plane. The average sapphire thickness is  $435 \pm 5 \mu\text{m}$ . In the beginning, samples were thermally cleaned in  $\text{H}_2$  ambient at  $1180^{\circ}\text{C}$  for 10 minutes, and then went to LT-AlN growth condition. TMAI was initially supplied for 40s at a flux of  $5 \mu\text{mol/min}$  in order to ensure full coverage of Al-polar material. It was confirmed that ID features were eliminated after a sufficient TMAI pre-treatment. During the optimization of the LT-AlN, the growth conditions of the subsequently deposited AlN epilayers were kept constant as given in Table 4.1.

Growth Parameters	LT-AlN	Main AlN layer
Growth ( $^{\circ}\text{C}$ )	(2-II) 600-1000	1250
Growth Pressure (mbar)	100	100
V/III Ratio	1000	100
TMAI ( $\mu\text{mol/min}$ )	5	20
$\text{NH}_3$ ( $\mu\text{mol/min}$ )	5000	2000
Growth Thickness (nm)	(2-I) 0 to 45	1000
Total Flow (sccm)	8000	8000

**Table 4.1: Growth conditions of subsequently deposited AlN epilayer on LT-AlN and range of growth parameters for LT-AlN optimization.**

In series 2-I, the thickness of LT-AlN was varied and optimised. It should not be very thick otherwise not only the LT-AlN but also the successive layer may become polycrystalline. The layer thickness is dependent not only the growth duration but also other growth parameters like the growth temperature, pressure and precursor flow rate. The growth temperature was fixed at  $600^{\circ}\text{C}$  for the LT-AlN, the V/III ratio at 1000 and the pressure at 100 mbar. The LT-AlN growth rate was taken as approximately  $0.074 \text{ nm/s}$  ( $0.266 \mu\text{m/h}$ ), based on the thickness of a 45 nm layer and assuming that the growth rate did not change with thickness. After that a  $1 \mu\text{m}$  thick HT-AlN layer was deposited at  $1250^{\circ}\text{C}$  with a V/III ratio of 100. Figure 4.9 (a) exhibits the effect of the NL thickness on the FWHM of (0002) and  $(10\bar{1}1)$   $\omega$ -scans. The minimum FWHM of (0002) was 450 arcsec, achieved at a low thickness. The surface

morphology of the AlN epilayers is shown in the Figure 4.9 (b). All samples have similar surface feature. The surface is formed from large steps, typically around 6 nm high and 1  $\mu\text{m}$  wide, but atomically smooth between the steps. Close examination of step termination sites shows a staircase of single and double atomic steps, showing that large steps are formed by atomic steps bunching together, perhaps initially pinned by surface pits. The measured room-mean-square (RMS) surface roughness is  $2.1 \pm 0.2$  nm, from four  $10 \times 10$   $\mu\text{m}^2$  scans.

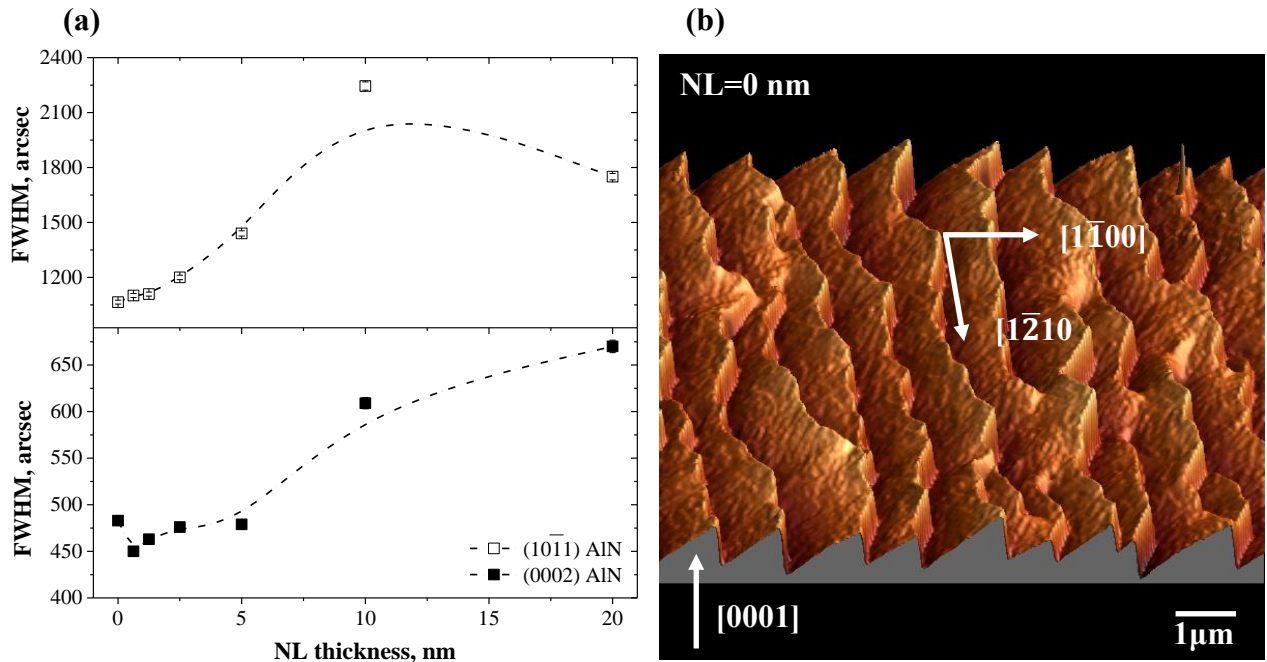


**Figure 4.9:** (a) Series 2-I: the impact of different LT-AlN thickness on the FWHM values of  $\sim 1 \mu\text{m}$  AlN epilayer measured by XRD  $\omega$ -scans using (0002) (closed squares) and (10 $\bar{1}1$ ) (open circles) reflections, which are associated with screw and mixed type dislocations and to edge and mixed type dislocations, respectively. Error bars represent instrument limitations and the unit of Z scale bars are nanometer. The insets show  $10 \times 10$   $\mu\text{m}^2$  AFM 3D view scan for selected LT-AlN thickness [0 nm (b)] indicating the step bunched surface feature.

The growth temperature of the LT-AlN is also an important parameter since the decomposition of the precursors, homogeneous and heterogeneous gas phase reactions and the mobility of the precursor species on the substrate are all strongly temperature dependent phenomena. In order to investigate the influence of the growth temperature, LT-AlN as deposited at four temperatures between 600  $^{\circ}\text{C}$  and 1000  $^{\circ}\text{C}$  in series 2-II. A thickness of 0.75 nm was chosen based on the FWHM values from series 2-I. During the optimisation of the LT-AlN growth, the growth conditions of the subsequently deposited  $1 \mu\text{m}$  thick HT-AlN layers were kept constant.

The FWHM values showed a minimum of 400 and 940 arcsec for (0002) and (10 $\bar{1}1$ ) at the growth temperature of 800  $^{\circ}\text{C}$  in Figure 4.10 (a). Figure 4.10 (b) shows the short-wavelength

(405nm) ORS in-situ monitoring curves vs. time sequence of samples NT0073 ( $T_{\text{LT-AIN}}=800\text{ }^{\circ}\text{C}$ ) and NT0072 ( $T_{\text{LT-AIN}}=1000\text{ }^{\circ}\text{C}$ ), used to observe the evolution of AlN growth. For sample NT0073, the reflectance intensity of the 405 nm in-situ monitoring curve first decreased and then became stronger until it reached a steady state. This indicated that the growth mode of underwent a transition from 3D island growth to quasi-two-dimensional (2D) layer-by-layer growth. For sample NT0072, the reflectance intensity increased to a steady state quickly, indicating that 2D growth dominated the whole HT-AlN growth process. However, surface morphologies still show clear step bunching feature in both samples [Figure 4.10 (c) and (d)], while incomplete coalescence co-existence with some hillock surface features was achieved in sample NT0073.

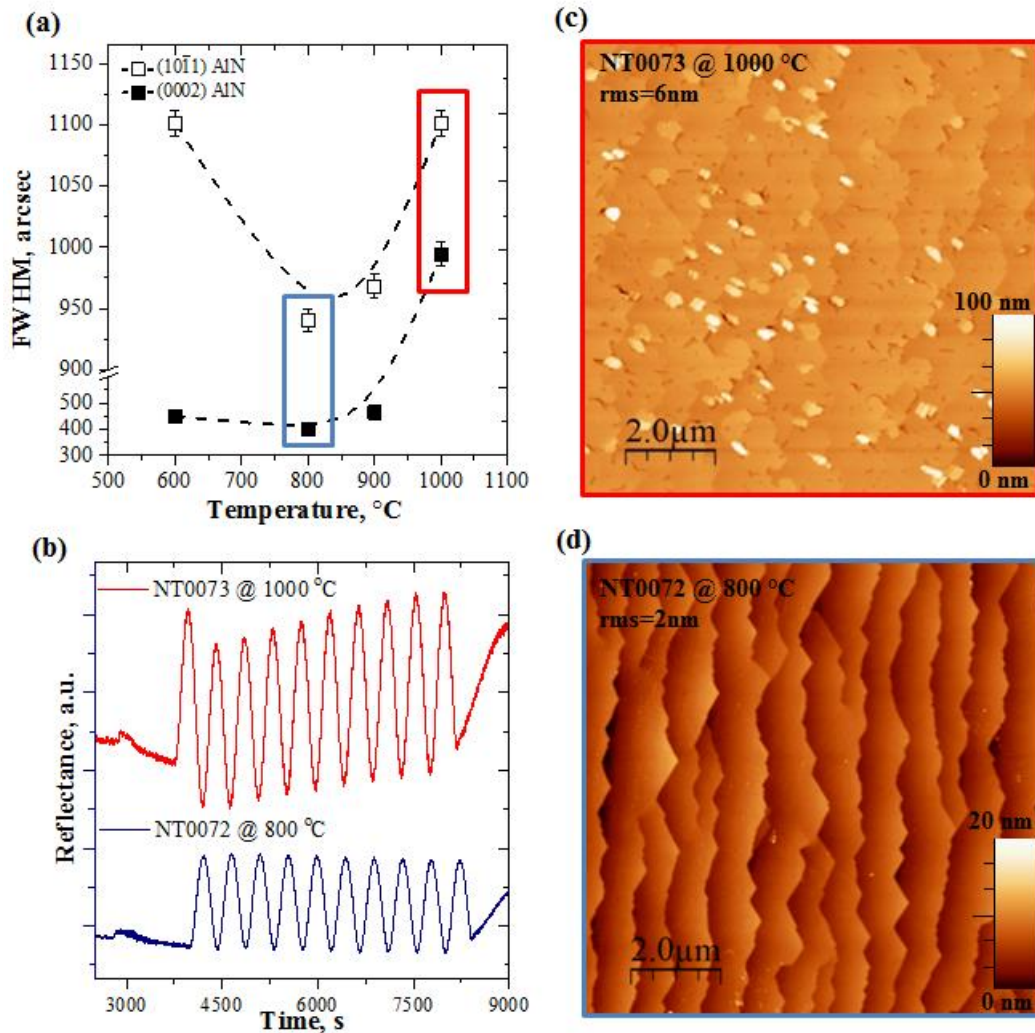


**Figure 4.4:** (a) XRD  $\omega$ -scan FWHM of the (0002) and (10 $\bar{1}$ 1) reflections dependence of the NL growth temperature. (b) The 405 nm wavelength in situ monitoring curve vs. time sequence. The insets show  $10 \times 10\text{ }\mu\text{m}^2$  AFM scans for selected NL growth temperature [1000 °C (c) and 800 °C (d)].

#### 4.4.2 Series 2-III: HT-AlN surface morphology transition

In series 2-III, HT-AlN was deposited in different thickness to find the thickness at which the surface steps start to bunch together. The expected defect density reduction with increasing epilayer thickness is verified by FWHM values of XRD  $\omega$ -scans in Figure 4.11 (a). The 405 nm wavelength reflectance curve reached a steady state quickly shown in Figure 4.11 (b), which indicated that 2D layer-by-layer growth is dominant at HT-AlN.

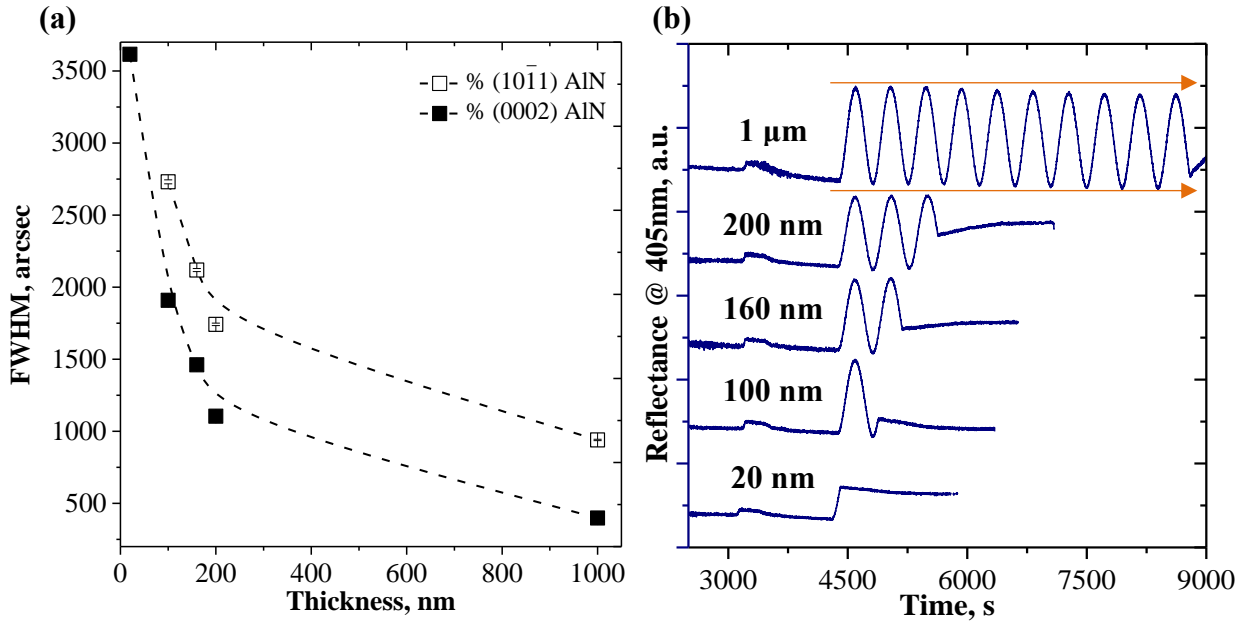


**Figure 4.11:** (a) The impact of different HL thickness ranging from 20 nm to 1  $\mu\text{m}$  on the symmetric (0002) and skew-symmetric (10-11) FWHM (not included FWHM of (10-11) for 20 nm, because epilayer is thin and large defect density), and (b) ORS In-situ 405nm laser signals recorded for two-step process from 20 nm to 1  $\mu\text{m}$  thick.

AFM measurements were used to study the AlN surface morphology during the different growth stages. Figure 4.12 (a) displays the AlN morphology just after the initial nucleation with thickness of 20 nm. Figure 4.12 (b) shows a 100 nm thick AlN layer. There are remaining openings/pits due to the incomplete island coalescence. Further increasing the AlN thickness promoted coalescence. Macro steps (step height  $\sim 1$  nm) were observed for the 160 nm thick in Figure 4.12 (c). The pits and defects reduced significantly as thickness increases. As demonstrated in Figure 4.12 (d), the sample surface shows clear step bunching features at a thickness of 200 nm. In this stage, bunched steps formed ridges that were running essentially parallel to each other, which resemble the ultimate surface morphology of Figure 4.12 (e). It should be pointed out that the continuous step bunching ridges are aligned along the sapphire substrate miscut. AFM image reveals vicinal surfaces inclined at an angle ( $\theta$ ) of  $0.42 \pm 0.04^\circ$ , which is close to the sapphire miscut angle. An average step height ( $h$ ) of  $6.0 \pm 0.5$



nm and step width (w) of  $0.9 \pm 0.05 \mu\text{m}$  were observed by cross-sectional height profile Figure 4.12 (f). Finally, the RMS surface roughness, estimated from multiple offset-flattened  $10 \times 10 \mu\text{m}^2$  AFM images is 2 nm.

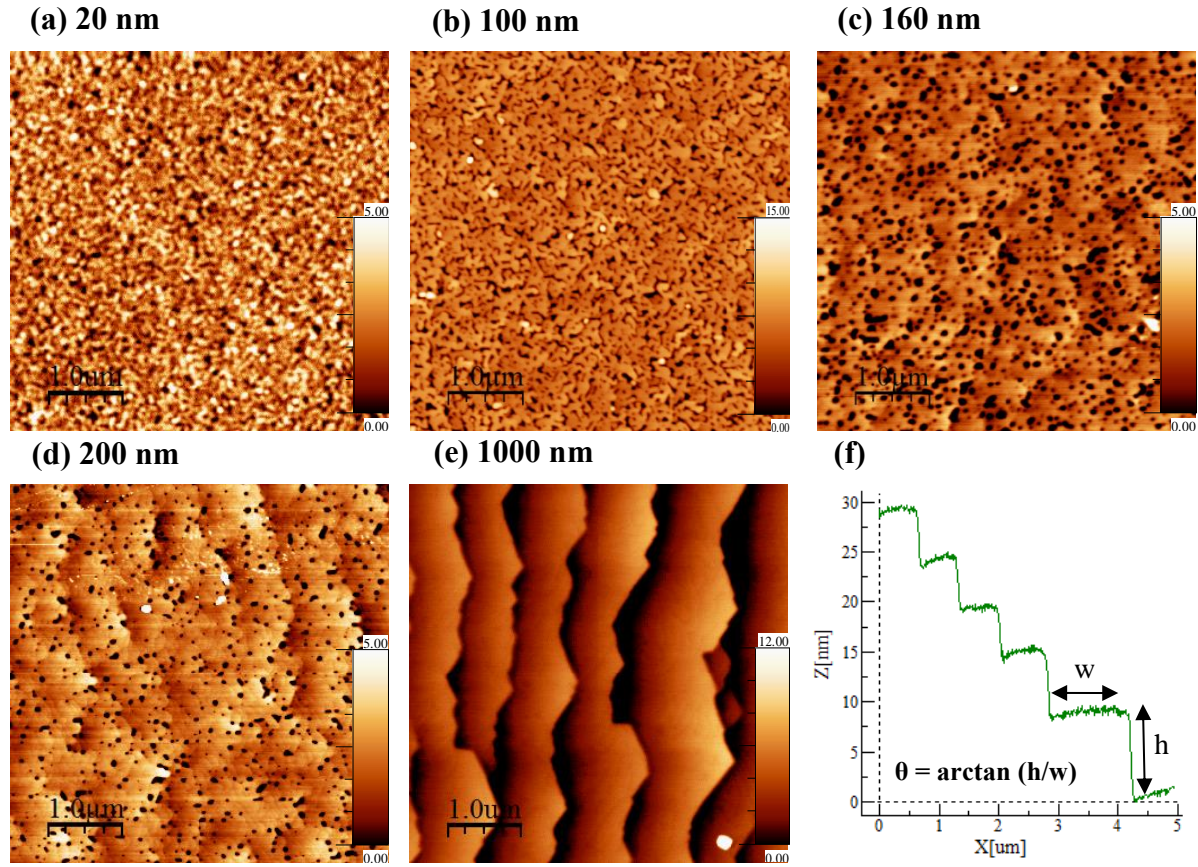


**Figure 4.12:** (a-e)  $5 \times 5 \mu\text{m}^2$  AFM scans of AlN grown on sapphire grown showing the evolution of HT-AlN epilayer in 20 nm, 100 nm, 160 nm, 200 nm and 1 μm thick, and (f) cross-sectional height profile of 1 μm thick AlN epilayer using line flattened with a local plane fit by WSxM software. The calculation of the misorientation  $\theta$  is illustrated. The unit of Z scale bars are nanometer.

Figure 4.13 indicates the variation in surface roughness as the film coalesced and the step bunching growth mode took over. Initially, the RMS surface roughness was low, because of the small islands formed on the surface [Figure 4.13 (a)]. As the small islands coalesce to become larger [Figure 4.13 (b)], the surface roughness increases. From 100 to 160 nm, the effect of the lateral growth increases and the surface roughness drops significantly. However at the same time, the first evidence of the step bunching growth mode begins to appear resulting in the increased surface roughness at 200 nm. A histogram of scan line RMS roughness from a 1 μm thick HT-AlN revealed steps height distribution [Figure 4.13 (c)]. The presence of step bunching feature in the 1 μm thick AlN indicates that it is difficult to

recover a flat surface under HT growth. To understand and explain the feature morphology, substrate and growth conditions (growth temperature and V/III ratio) should be considered.

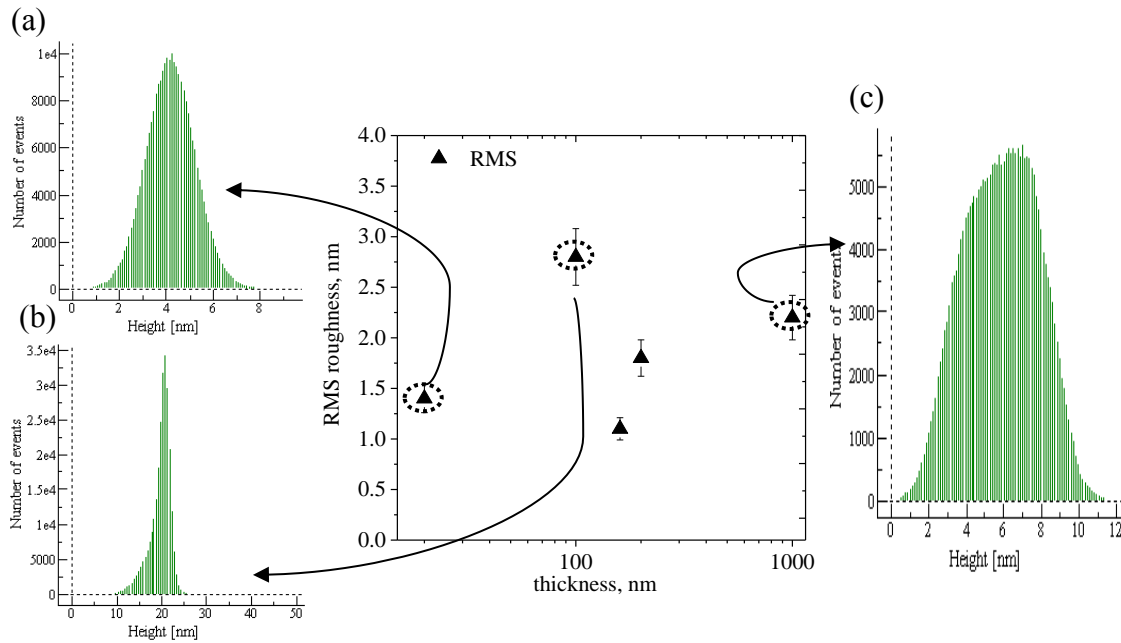


**Figure 4.13: Variation in the RMS surface roughness with the layer thickness. Insets show the surface height histograms for samples (a) 20 nm, (b) 100 nm and (c) 1  $\mu$ m.**

When a miscut substrate is used for growth, steps are usually formed due to the vicinal effect. A uniform vicinal surface has been reported to be vulnerable to two main types of instability: step meandering and step bunching. For most III-V materials, the step bunching tends to be more frequently observed. This behaviour can be explained by the difference in molecular dissociation from above and below step edges [31].

Kasu and Kobayashi (KK) [32] explained the step bunching in terms of the surface diffusion and 2D nucleus formation. In the crystal growth theory, there is a direct correspondence between growth parameters (growth temperature, flow rate, V/III ratio and reactor pressure) and surface diffusion. Generally, if the mean surface diffusion length of Al atoms is greater than or equal to the half step terrace width, the atoms only tend to incorporate into the steps and kink sites that locate at the two side of one terrace, keeping the stable step morphology, namely, step flow growth mode. However, if the diffusion length is much longer than the step terrace width, the atoms can migrate over these steps and diffuse to the neighbouring upper and lower terraces, providing a possibility for the formation of macro steps and even bunched steps, we call this a step bunching growth mode. The more details will be discussed in the following section.

### 4.4.3 Series 2-IV and 2-V: Impact of main AlN growth temperature and miscut angle of substrate

Step bunching features were observed in previous growth runs, might cause by a diffusion length greater than the terrace width of the substrate. Therefore, the step bunching can be avoided by reducing the diffusion length. One possibility is to decrease the growth temperature and hence to reduce the residence time of a group-III adatom on the surface (series 2-IV). An alternative at a growth condition is to reduce miscut angle to increase terrace width (series 2-V).

#### 4.4.3.1 Experimental details

All the AlN epitaxial layers in this section were grown on three orientations of c-plane sapphire substrates. The miscut angles of substrates were  $0.08^\circ \pm 0.02^\circ$ ,  $0.25^\circ \pm 0.04^\circ$  and  $0.36^\circ \pm 0.04^\circ$  towards the m-plane. Sapphire substrate miscut angle defines the width and density of surface step, because the usage of intentionally inclined surface causes a finite step width that is terminated with a surface step, see sapphire sample surface in Figure 4.14.

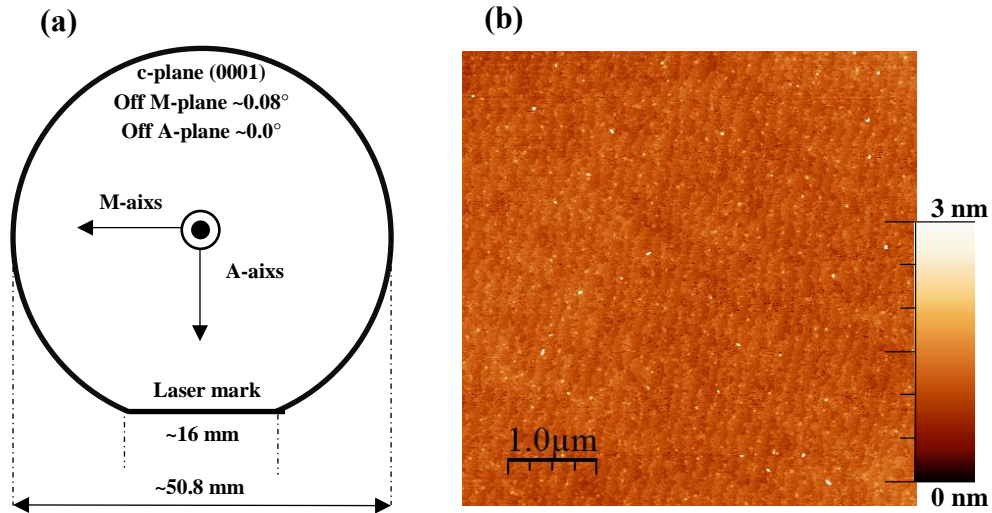


Figure 4.14: (a) schematic of the 2 inch sapphire substrate and (b) its  $5 \times 5 \mu\text{m}^2$  AFM image.

Prior to deposition, thermal cleaning of the sapphire substrates was performed in a  $\text{H}_2$  atmosphere at  $1180^\circ\text{C}$  for 10 min. The wafers were then cooled to  $800^\circ\text{C}$  for a 40 seconds Al pre-treatment step followed by a thin LT-AlN layer with a V/III ratio of 10000 at 100 mbar.

Three growth runs were made as described in Table 4.2. Three different miscut substrates were simultaneously loaded in the reactor. In each case after the LT-AlN, the TMAI supply

was interrupted and wafer temperature increased to either 1110, 1160 or 1260 °C under an NH<sub>3</sub> flow. 1.5 µm thick AlN layers were subsequently grown on the LT-AlN with a V/III ratio of 50 at 50 mbar.

<b>T (°C) of main AlN</b>	<b>0.08°±0.02°</b>	<b>0.25°±0.04°</b>	<b>0.36°±0.04°</b>
<b>1110</b>	NT0452a	NT0452b	NT0452c
<b>1160</b>	NT0467a	NT0467c	NT0467b
<b>1260</b>	NT0454a	NT0454b	NT0454c

**Table 4.2:** Growth conditions for AlN epilayers of 1.5 µm thickness with AlN nucleation layers of 0.75 nm thickness grown.

#### 4.4.3.2 Results

Growth was monitored using the data provided by a LayTec reflectometer and Epicurve system. Figure 4.15 shows the in-situ transients measured by the 633 nm LED and the wafer curvature for the growth of AlN layer grown on 0.08° miscut angle of c-plane sapphire with different growth temperature. Firstly, the Fabry-Perot oscillations of the AlN layers show almost no damping in amplitude indicating that all AlN layers adopted a planar growth mode from the beginning in Figure 4.15 (a). The similar oscillation behaviours were also found in other samples grown on 0.25° and 0.36° c-plane sapphire substrates.

Secondly, the wafers became more concave as increasing AlN thickness [Figure 4.15 (b)], which suggested that our Al-polar oriented growth method had a tendency to enhance wafer bowing and film tensile strain. The variation in wafer curvature could be caused by several potential processes. One phenomenon which could be causing the wafer bowing is vertical temperature gradient within a sample as well as the thermal stress resulting from a temperature change with a difference in thermal expansion coefficient between AlN and sapphire. Since the layer was grown at constant temperature, the thermal mismatch can be ignored. Another source of strain for growth of III-nitrides is the hetero-epitaxial lattice mismatch. For AlN on c-sapphire, it rotates 30° about its c-axis with respect to that of sapphire, this results in a tensile stain of about 13% [33].

The growth rate of AlN was found to decrease with increasing growth temperature over the range studied in Figure 4.16, which indicate that the mean residence time of Al adatoms is larger on the surface as temperature rise. The decrease of the growth rate with increasing



growth temperature may be attributed to increase parasitic pre-reactions in the gas phase. This was found to be irrespective of the sapphire substrate miscut angle. However, the growth rate of AlN was found to be subtly different for each of the three simultaneously grown samples, with the small thickness changes ( $\sim 2\%$ ) between sample types being consistent, though the variation is not consistent with the miscut angle, nor susceptor pocket selection. This may be due to slight differences in the temperature of the growing surface caused by variation of the thickness (all nominally the same), backside polish of sapphire which were provided by different manufacturers or the error of growth rate estimation (error bar of  $1\text{ }\mu\text{m}$  thick is about  $\pm 40\text{ nm}$ ).

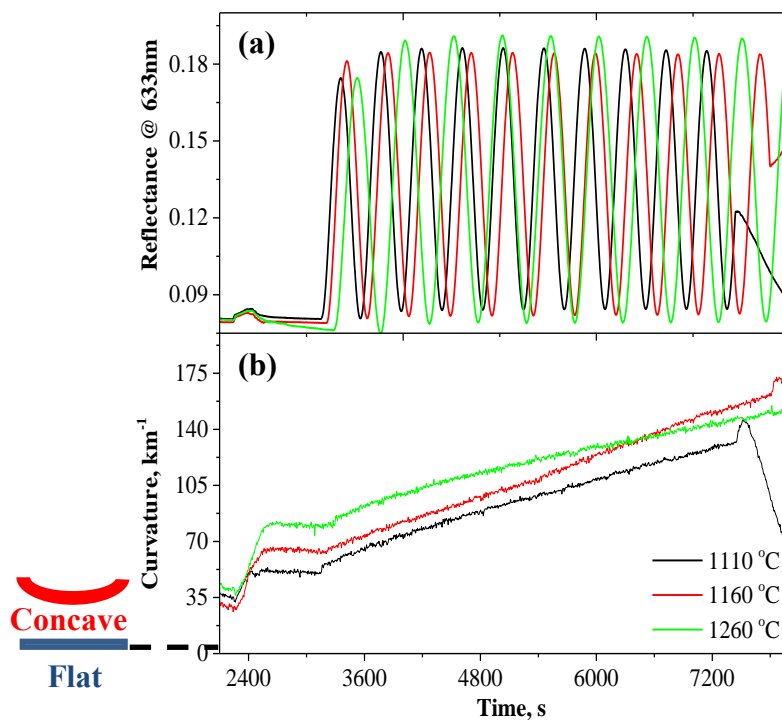


**Figure 4.15: Wafer curvature and the 633 nm reflectance measured in-situ during growth of AlN layers on  $0.08^\circ$  miscut of c-plane sapphire.**

The surface morphologies of AlN samples grown on different miscut substrates at different temperatures are shown in Figure 4.17 and Figure 4.18. Monoatomic layer steps are clearly observed at the lowest growth temperature ( $1110\text{ }^\circ\text{C}$ ). The surface was found to be atomically flat with irregularly ordered steps. At small miscut these adopt a rather random pattern, which is modified with a clear orientation for the larger miscut angles. There is evidence of pinning in the samples. The AFM images indicate that this may be attributed to screw dislocations threading through the material, which has been confirmed by analysis on smaller AFM scan areas, see Figure 4.18.

For the two larger substrate miscuts ( $0.25^\circ$  and  $0.36^\circ$ ) at  $1250^\circ\text{C}$ , a dramatic change in morphology is observed, with large jumps in surface height occurring, separated by relatively broad smooth terraces. The step edges are fairly straight on a macroscopic, with jagged features and align along the m-plane direction, normal to the misorientation. This is indicative of strong step bunching in the sample. In the case of the on  $0.08^\circ$  substrate the RMS roughness was significantly reduced though it is noticeable that the surface is significantly rougher than that for the equivalent sample grown at  $1110^\circ\text{C}$  [see Figure 4.19 (a)], and as can be observed from the smaller atomic layer terrace widths in the AFM image. The step bunching leads to a clear jump in the RMS roughness values observed in Figure 4.19 (a). This type of roughness degradation is more of an issue as the large relatively sudden height differences (of the order of 5-8 nm) would potentially lead to rather discontinuous quantum wells if used as a template for LED overgrowth.

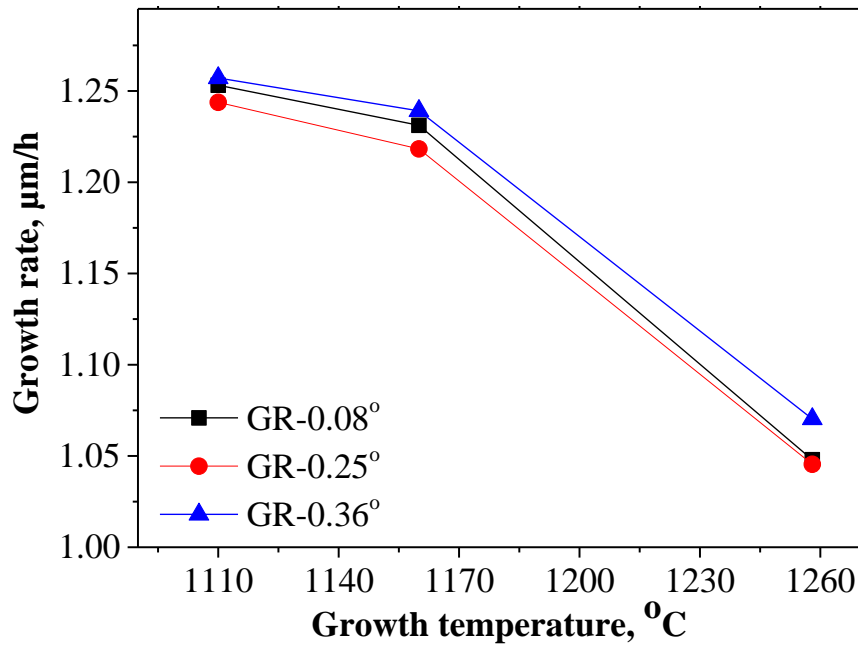


**Figure 4.16: Change in growth rate with respect to growth temperature and miscut angle**

For the  $1160^\circ\text{C}$  sample an intermediate result was observed, with some evidence of slight step bunching at the highest miscut angle.

It can be seen that the type of morphology strongly depends on both growth temperature and miscut angle. When the growth temperature is enhanced, a transition from step-flow mode to step bunching is observed [Figure 4.17 (b)-(e)-(h) and (c)-(f)-(i)]. A similar transition is also found when increasing miscut angle [Figure 4.17 (d)-(e)-(f) and (g)-(h)-(i)].

The variation of the (0002) and (10 $\bar{1}1$ ) XRD  $\omega$ -scan FWHM of the AlN layers grown with different temperature and miscut is shown in Figure 4.19 (b). There is a gradual decrease in screw type dislocation with increasing growth temperature. The temperature trend from the (10 $\bar{1}1$ ) FWHMs is less clear though grown at the lowest temperature growth has the lowest quality. In general the samples with highest sapphire miscut have the lowest XRD FWHM though there is not consistent trend. It is possible that the step bunching and induced dislocation motion may lead to enhanced annihilation, though the possibility of the different manufacturer final surface polish cannot be discounted.

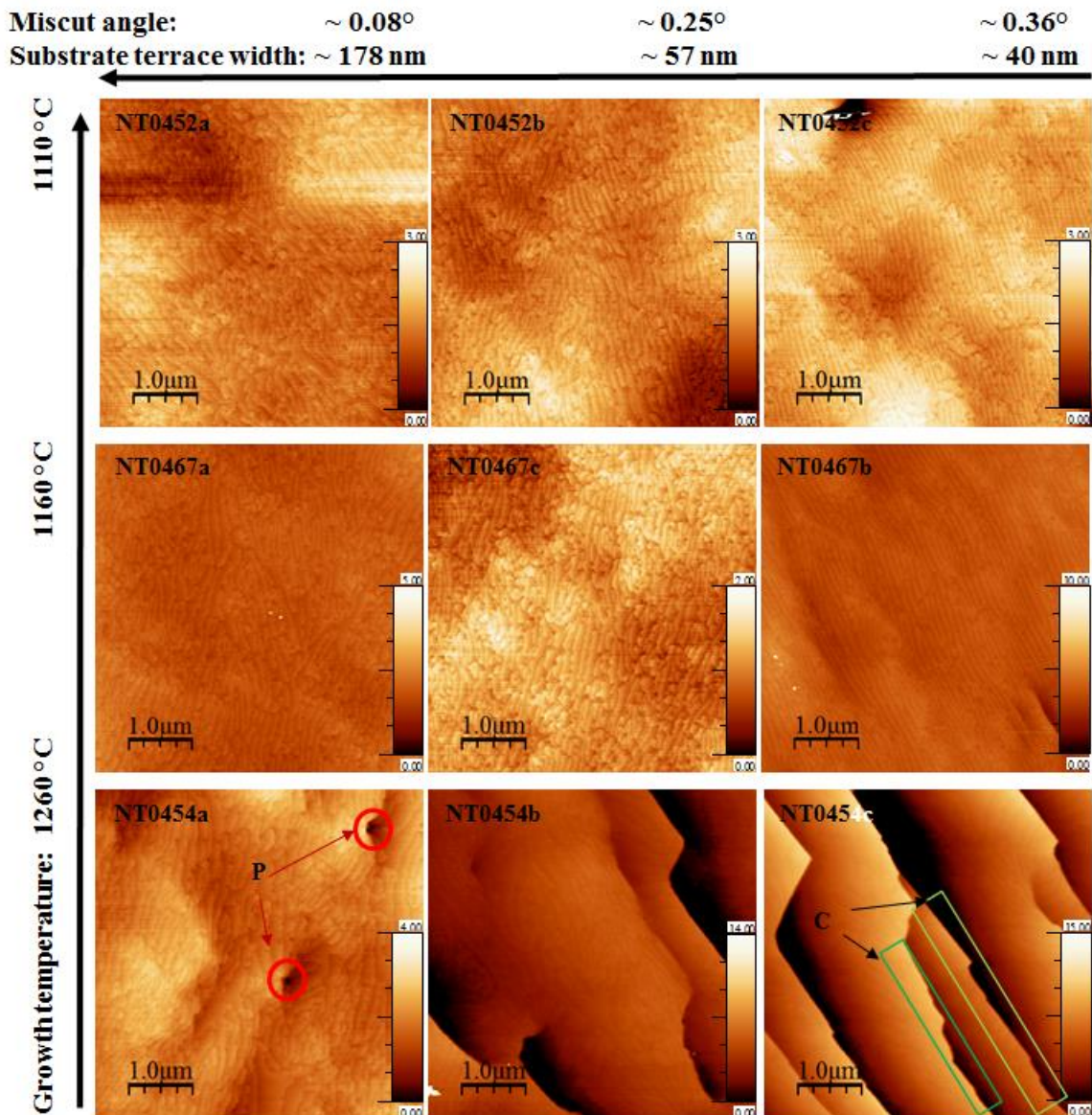


Figure 4.17: (a-i)  $5 \times 5 \mu\text{m}^2$  AFM images of AlN surface morphologies grown on three orientations of ‘c-plane’ sapphire substrates under different growth temperature. Abbreviation for the observed morphology: cliffs (C) and pits (P). The unit of Z scale bars are nanometer



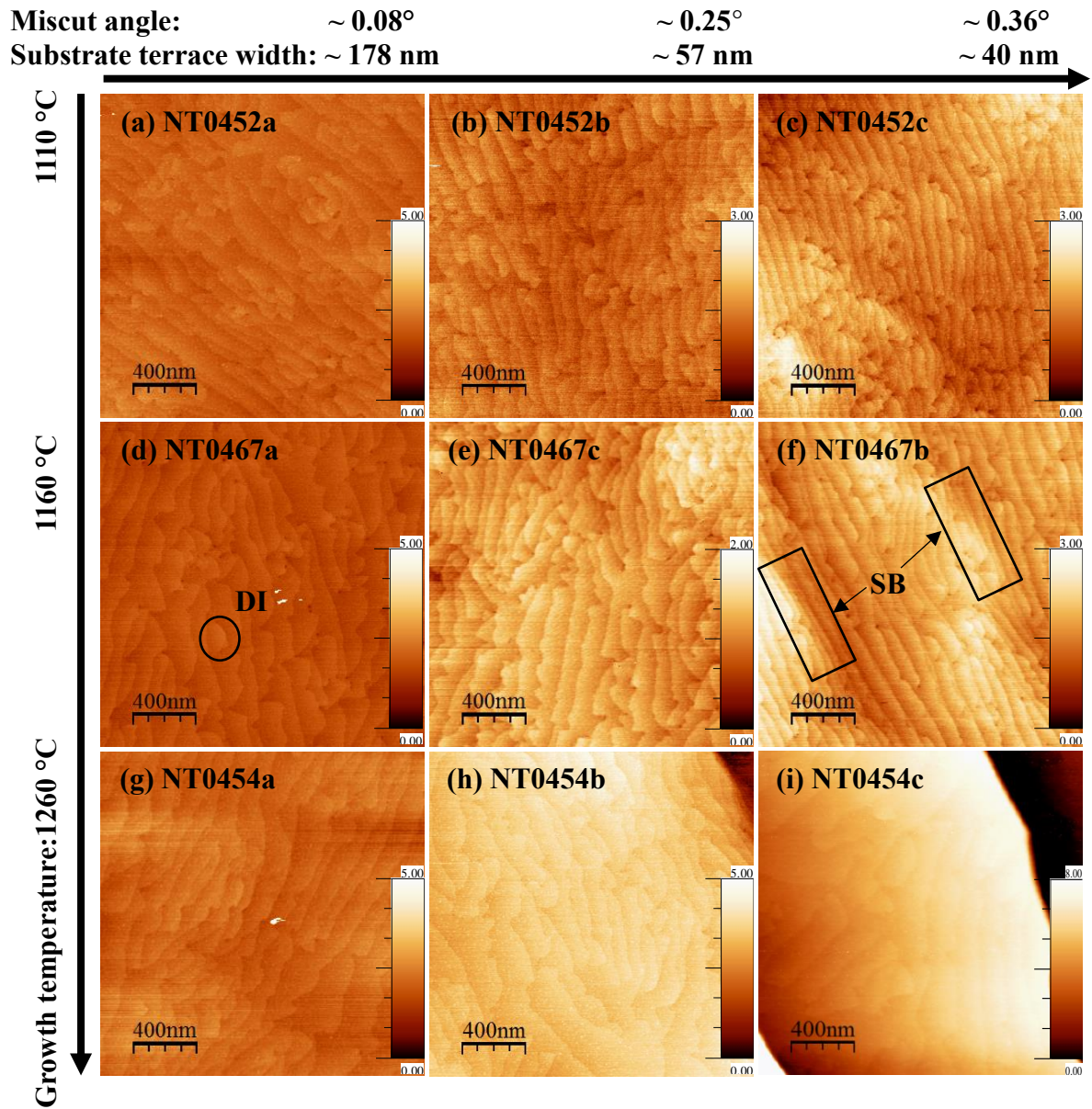


Figure 4.18: (a-i)  $2 \times 2 \mu\text{m}^2$  AFM images of AlN surface morphologies grown on three orientations of ‘c-plane’ sapphire substrates under different growth temperature. Abbreviation for the observed morphology: diffuse islands (DI) and step bunching (SB). The unit of Z scale bars are nanometer

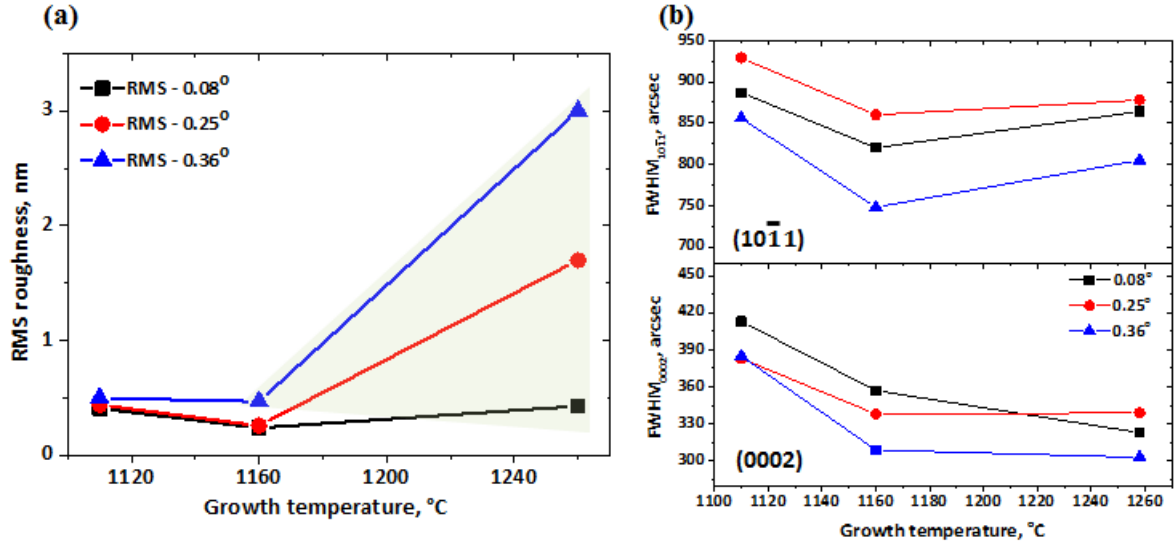


Figure 4.19: (a) RMS surface roughness of AlN from  $5 \times 5 \mu\text{m}^2$  which were grown on miscut angle  $0.08^\circ$ ,  $0.25^\circ$  and  $0.36^\circ$  sapphire substrate under difference growth temperatures, respectively. Step bunching features are observed green region. (b) X-ray diffraction full-width at half-maximum (FWHM) values of the AlN buffers grown at different growth temperatures on different substrate misorientations.

#### 4.4.3.3 Discussion and conclusion

The role of substrate miscut angle in the III-V system for samples grown by MOVPE has been reported by others [31, 35], including by Nagamatsu et al [36] for AlN who reported both a bunching effect and improved crystal quality for growth on higher sapphire miscut. In contrast, our results indicate that crystal quality is largely independent of the miscut, though the reduction of step bunching features is obtained.

Meanwhile, the variation of growth temperature has a significant influence on the kinetics of the adsorption and surface diffusion processes for AlN. The mean surface diffusion length of Al atoms ( $L_A$ ) is obtained by the Einstein relation [37],

$$L_A = \sqrt{D_A \tau_A} \quad (4.5)$$

where  $D_A$  is the surface diffusion coefficient and  $\tau_A$  is the mean diffusion time of an adatom at the surface before being incorporated. The dependence of the diffusion coefficient  $D_A$  and  $\tau_A$  on the temperature are determined by a simple activation energy approach [37],

$$D_A = D_0 \exp\left(-\frac{E_A}{\kappa_B T}\right) \quad (4.6)$$

$$\frac{1}{\tau_A} = \frac{1}{\tau_0} \exp\left(-\frac{E_{Des}}{\kappa_B T}\right) \quad (4.7)$$

Using (4.6) and (4.7), (4.5) becomes

$$L_A = \sqrt{D_0 \tau_0} \exp\left(\frac{E_{Des} - E_A}{2kT}\right) \quad (4.8)$$

Where  $E_A$  is the surface diffusion activation energy for an isolated adatom,  $D_0$  and  $\tau_0$  are the activation frequency factor,  $E_{Des}$  is the activation energy for desorption from the surface to the vapour,  $T$  is the growth temperature, and  $\kappa_B$  is the Boltzmann constant. Therefore,  $D_A$  and  $\tau_A$  increase with increasing the growth temperature, eventually increasing the diffusion length, when  $E_{Des}$  is smaller than  $E_A$ . Otherwise, if  $E_{Des}$  is larger than  $E_A$ , it means that the desorption of adatoms will be dominant instead of diffusion on the surface.

During growth, atoms reach the growth surface which can be adsorbed on the terrace (atom C), atomic ledges (atom B) or atomic kinks (atom A). The binding energies of the atoms increase with decreasing number of the dangling bonds ( $E_C < E_B < E_A$ ) on these sites. Therefore, atom A has the highest binding energy among atoms A, B and C. The classical step flow growth mode takes place when all the atoms finally incorporated into the atomic kinks (like atom A) and the probabilities of absorption to step edges from the upper or the lower step are equal, while those did not reach the atomic kinks are desorbed from the growth surface as shown in Figure 4.20 (a). These steps propagate perpendicularly to the growth direction with an atomic layer height [one monolayer (ML) height]. However, surface morphology may also suffer three basic deterministic instabilities: island, meandering and bunching. It is observed that the reflectance at 405 and 633 nm from LayTec stays constant even after 30 mins of annealing for AlN at 1260 °C. This indicates that the decomposition rate of AlN is negligible at our typical growth conditions. Therefore, only the adsorption, surface diffusion and incorporation process have major impact on surface dynamics for AlN growth.

An analytical description for the morphological evolution from 2D island nucleation growth to step-flow growth was found by Burton, Cabrera and Frank, namely BCF-theory [37]. If the diffusion length is much smaller than half step terrace width ( $L_A \ll L/2$ ), incorporation of adatoms in the terrace is high before they incorporate to a step edge. As a consequence, island formation [Figure 4.20 (c)] occurs.

If  $L_A > L$ , then most of adatoms may tend to incorporate into the steps and kink sites that on either side of the terrace, keeping the stable step morphology. However the BCF-theory does not distinguish between adatoms that arrive at the step from the upper ( $L_{n-1}$ ) or lower ( $L_{n+1}$ ) terrace. It also cannot explain other two unstable morphology features: step meandering and step bunching. Schwoebel first pointed out that the change of the diffusion potential for an

adatom due to an energy barrier, which is known as Ehrlich-Schwöbel barrier (ES barrier or ESB) [38, 39]. There are two types of ESBs: (I) kink Ehrlich-Schwöbel barrier (KESB), which is 1D effect along the step, and (II) step Ehrlich-Schwöbel barrier (SESB), which is a 2D effect as the asymmetry at a step-edge.

If the growth is in  $L \geq L_A \geq L/2$  regime, a surface transition between the 2D regime and island form will occur. It means that the strength of SESB is high in regard to the energy of the diffusing adatoms, so adatoms attached to a step-edge diffuse along it until they find a kink to incorporate [40]. 1D bumps or hillocks along the step-edge can lead to a mound formation if a KESB exists, which will eventually result in a step meandering morphology [Figure. 4.20 (d)] [41, 42]. This instability leads to the formation of ripples in the direction of the step train.

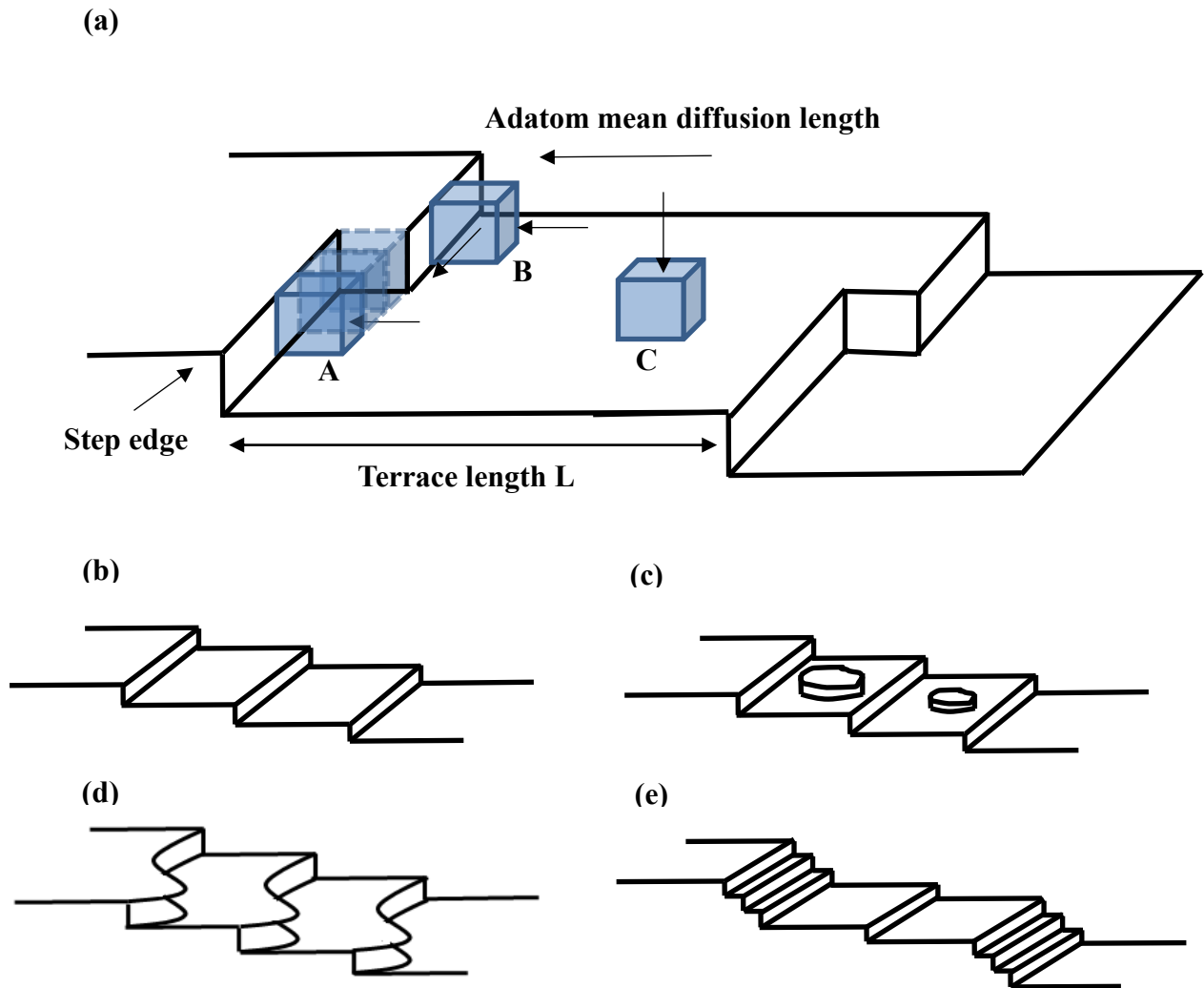


**Figure 4.20: (a) Schematic view of the 2D step flow growth mode. Three morphological instabilities that can occur during epitaxial growth. (b) A vicinal surface may be unstable with respect to (c) island formation, (d) step meandering and (e) step bunching.**

In the  $L_A \geq L$  regime, adatom can diffuse further from one terrace to another. It faces an energy barrier which might form at the step-edge, hindering either adatoms from the upper terrace to incorporate at the step and make it more easy for adatoms arriving from the lower terrace [defined as positive SESB, as shown Figure 4.21 (b)] or vice versa [negative SESB, as shown Figure 4.21 (c)].

$X_n$  and  $X_{n+1}$  denote the position of steps  $n$  and  $n+1$ , respectively. The terrace width ( $L$ ) is bounded by two steps, while  $L_{n+1}$  and  $L_{n-1}$  are the terrace widths in front of and behind the step  $n+1$  and  $n$  as shown in Figure 4.21 (a), respectively, then the speeds of motion of the steps can be described as one dimension model [37],

$$\frac{dX_n}{dt} = k_{X_n}^- L_{n-1} + k_{X_n}^+ L_n \quad (4.9)$$

$$\frac{dX_{n+1}}{dt} = k_{X_{n+1}}^- L_n + k_{X_{n+1}}^+ L_{n+1} \quad (4.10)$$

Where  $k_{n,n+1}^\mp$  are adatom incorporation coefficients to steps from their respective upper (-) and lower (+) terraces, respectively,  $L_n = X_{n+1} - X_n$  is the length of the  $n$ th terrace. Subtracting the equations (4.9) and (4.10) gives,

$$\frac{dL_n}{dt} = \frac{dX_{n+1}}{dt} - \frac{dX_n}{dt} = (k_{X_{n+1}}^+ L_{n+1} - k_{X_n}^- L_{n-1}) - (k_{X_n}^+ - k_{X_{n+1}}^-) L_n \quad (4.11)$$

When step pairing has occurred (i.e., the step  $X_n$  has caught up with the step  $X_{n+1}$ ) and so the terrace  $L_n$  should be equal to zero. Therefore,

$$\frac{dL_n}{dt} = k_{X_{n+1}}^+ L_{n+1} - k_{X_n}^- L_{n-1} \quad (4.12)$$

In order to maintain the step pairing during growth,  $\frac{dL_n}{dt} \leq 0$ , which results in  $k_{X_{n+1}}^+ \leq k_{X_n}^-$ , assuming  $L_{n+1} = L_{n-1}$ . This means that the incorporation rate of adatoms from upper terrace (-) is higher than that from the lower terrace (+), continued growth will cause to further step bunching. This asymmetric incorporation can be explained by negative ESB as shown in Figure 4.21(c). The step bunching is initiated by the pairing of adjacent steps, so the system is keeping unstable when  $k_{X_n}^-$  is dominant and much larger than  $k_{X_{n+1}}^+$ .

On the other hand, when the adatom faces a positive ESB ( $k_{X_{n+1}}^+ > k_{X_n}^-$ ) at a step downwards [Figure 4.21(b)], it will reflect and not diffuse downwards. It will result in  $\frac{dL_n}{dt} > 0$  and lead to a stabilization of terrace width, keeping a step-flow growth mode. However, our experimental results indicate that such a terrace width stabilisation is not favoured.



The result can be summarized by considering the ratio of the mean diffusion length of adatoms over the step width ( $L_A/L$ ) and the mean direction of adatoms flow on the surface. The step bunching is triggered by a long diffusion length of adatoms and downhill diffusion with the presence of negative SESB.

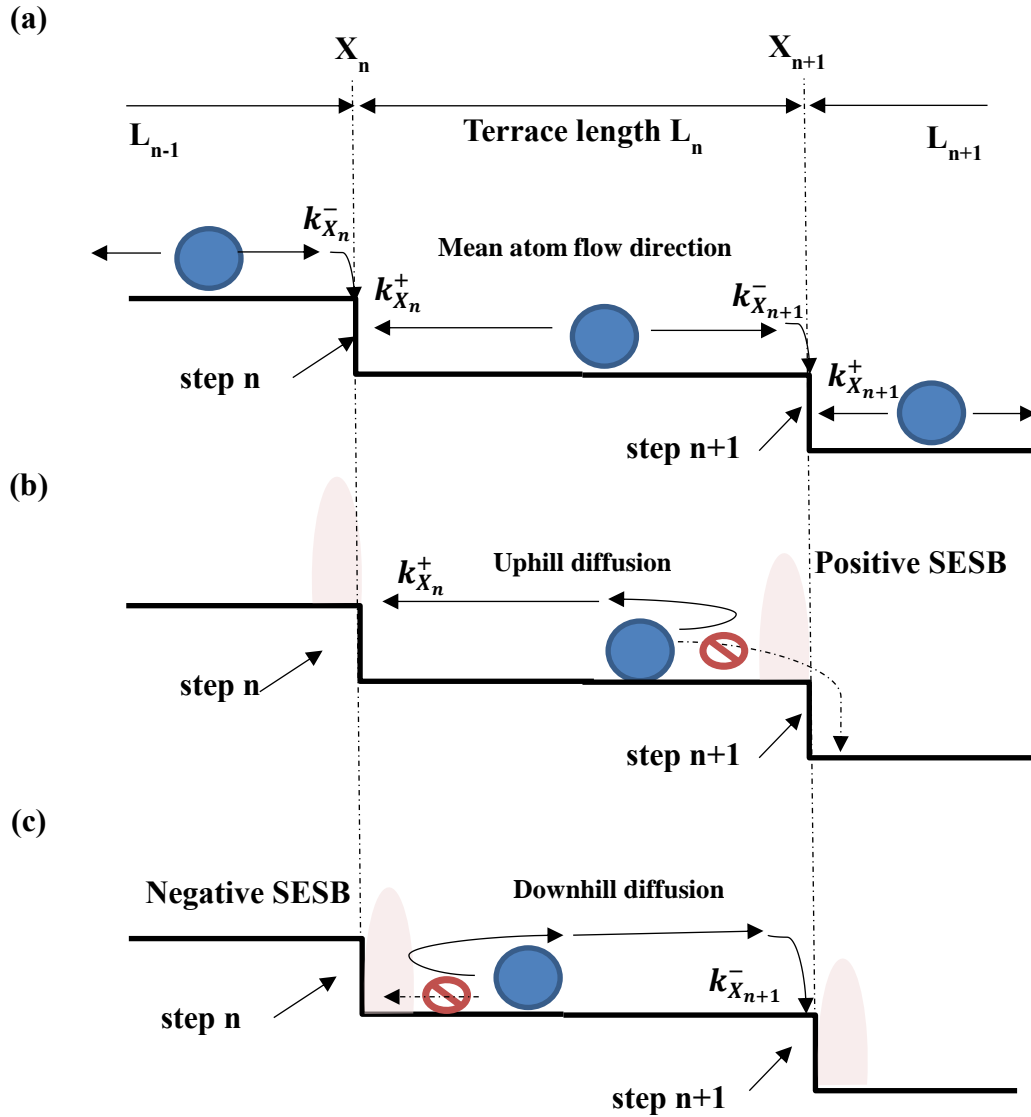
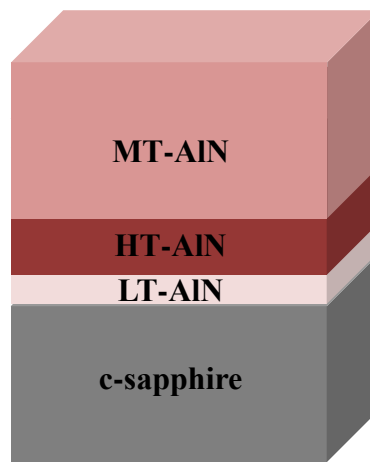


Figure 4.21: illustration of impact of without (a) and with ESB (b and c) on surface morphology.

## 4.5 Three-step process

In order to realize both an ultra-flat surface and improved crystal quality for high efficiency UV optoelectronic devices, a three-step process was employed. As illustrated in Figure 4.23, after thermal cleaning approximately 0.75 nm LT-AlN was deposited at 800 °C. HT-AlN was then grown as described in series 2-III and series 2-IV (section 4.4), which was followed by AlN growth at intermediate temperature of 1110 °C. A V/III ratio of 50, reactor pressure of 50 mbar and a flow of H<sub>2</sub> carrier gas of 8000 sccm at this stage were used to reduce the parasitic pre-reactions between NH<sub>3</sub> and TMAI and to reach a uniform growth rate across the entire 2-in diameter wafer.



**Figure 4.23: Schematic structures of the AlN epilayers grown on sapphire using three-step recipe.**

In series 3-I, the same layer stack consisting of a 0.75 nm LT-AlN and a 1 µm MT-AlN was used. To address the morphology and crystal quality of the AlN, the thickness of HT-AlN was modified from 20, 50, 100 to 160 nm. In a further study (series 3-II) the substrate miscut was varied to investigate its impact for a fixed thickness of the AlN layers, including a 0.75 nm LT-AlN, 100 nm HT-AlN and 2.2 µm MT-AlN layer in this case. In series 3-III, the impact of the thickness of the MT-AlN was investigated. A growth condition overview is summarized in Table 4.3. Finally, AlN was grown on commercially provided AlN nucleation layer grown on a sapphire substrate via physical vapour deposition PVD technique [43] to compare with our internal AlN template growth recipe.

Growth Parameters	LT-AlN	HT-AlN	MT-AlN
Growth (°C)	800	1250	1110
Growth Pressure (mbar)	100	100	50
V/III Ratio	1000	100	50
TMAI (umol/min)	5	20	20
NH <sub>3</sub> (umol/min)	5000	2000	1000
Growth Thickness (nm)	0.75	? (3-I)	? (3-III)
Total Flow (sccm)	8000	8000	8000

**Table 4.3: Growth condition overview of three-step process.**

#### 4.5.1 Series 3-I: HT-AlN interlayer thickness

In this series, c-plane sapphire with  $0.36^\circ \pm 0.04^\circ$  miscut towards m-plane was used for the growth of AlN layers. Based on the evolution of the previous surface morphology, a MT-AlN epilayer was introduced to maintain a smooth surface and eliminate bunching, by reducing the Al adatom effective diffusion length. The HT-AlN interlayer was deposited on LT-AlN before the main layer of 1  $\mu\text{m}$  MT-AlN. The studied HT-AlN interlayer thickness was varied from 20 to 160 nm and the XRD FWHM values of  $\omega$ -scans were compared, as shown in Figure 4.24. There is no major difference in the values of the (0002) FWHM, the minimum is  $\sim 350$  arcsec. However, the FWHM of the skew-symmetric ( $10\bar{1}1$ ) plane was reduced to  $\sim 760$  arcsec using 100 nm thick HT-AlN.

Figure 4.25 shows the surface morphology of the samples in series 3-I. When only a 20 nm HT-AlN is used [Figure 4.25 (a) and (e)], the surface is rough with many large pits attributed to incomplete island coalescence. The samples with thicker HT-AlN layers do not have these large pits and the most of large step bunches are eliminated, although some 2-3 nm high macro steps are found in Figure 4.25 (d). Previous studies (Figure 4.12) have demonstrated that macro steps majorly formed in the HT-AlN layer growth at certain thickness. In a  $1 \times 1 \mu\text{m}^2$  scan, atomic stepped terraces are clearly visible for all samples, and the RMS surface roughness of three-stage AlN with 100 nm thick HT-AlN interlayer is around 0.6 nm, derived from multiple  $5 \times 5 \mu\text{m}^2$  scans.

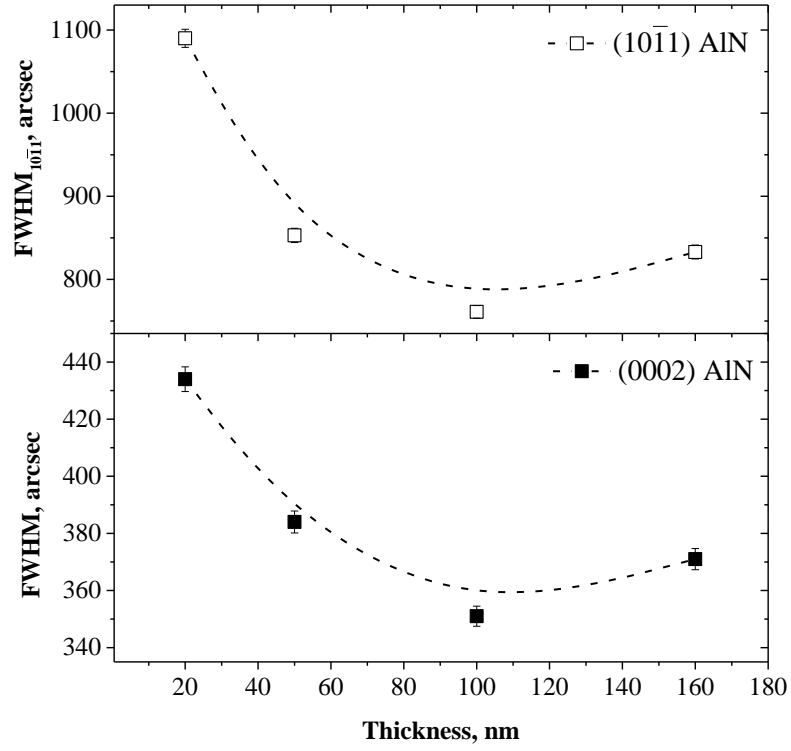


Figure 4.24: XRD FWHM values for three-step recipe with various thickness of HT-AlN interlayer. Solid lines are guidelines for the eye only.

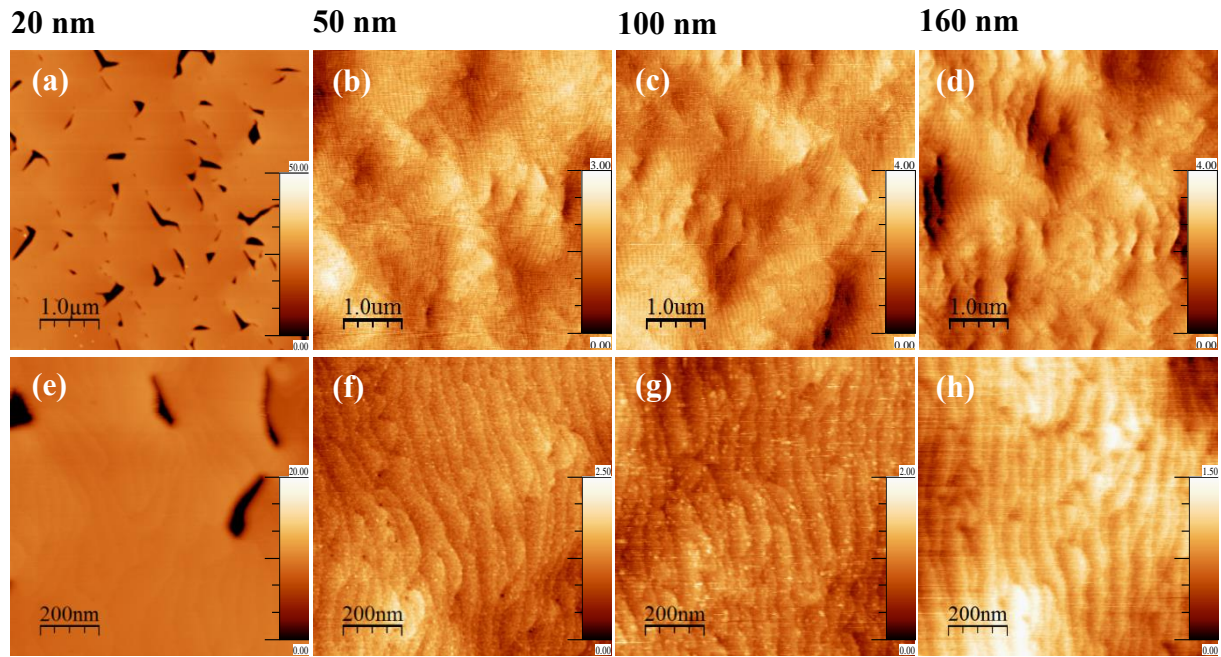


Figure 4.25: (a-d)  $5 \times 5 \mu\text{m}^2$  and (e-h)  $1 \times 1 \mu\text{m}^2$  AFM images for samples with 20 nm [(a) and (e)], with 50 nm [(b) and (f)], 100 nm [(c) and (g)] and 160 nm [(d) and (h)] thick HT-AlN interlayer. The unit of Z scale bars are nanometer.

### 4.5.2 Series 3-II: impact of miscut angle

The AlN epilayers (including ~0.75 nm LT-AlN, ~100 nm HT-AlN and ~2.2  $\mu\text{m}$  MT-AlN layer) in series 3-II were grown on three miscut angles of c-plane sapphire substrates. The miscut angles of substrates were  $0.08^\circ$ ,  $0.25^\circ$  and  $0.36^\circ$  towards the m-plane, respectively. The step bunches were found to be largely eliminated on all three misorientations in Figure 4.26 (a), (b) and (c). The mean AlN terrace length are  $155\pm 10$ ,  $100\pm 10$  and  $80\pm 10$  nm with respect to the miscut angle of  $0.08^\circ$ ,  $0.25^\circ$  and  $0.36^\circ$  c-plane sapphire [Figure 4.25 (d), (e) and (f)]. Each Al terrace length data point was measured across four  $2\times 2\ \mu\text{m}^2$  AFM scans. The classic step-flow growth mode is observed for AlN grown on  $0.36^\circ$  miscut c-sapphire [Figure 4.26 (c) and (f)]. A mixture surface morphology between island (small hillock) and step-flow is found for AlN grown on  $0.08^\circ$  and  $0.25^\circ$  miscut c-sapphire [Figure 4.26 (a), (b), (d) and (e)].

Figure 4.27 (a) shows the RMS surface roughness of the AlN epilayers with different miscut angles measured by multiple  $2\times 2\ \mu\text{m}^2$  (circle) and  $5\times 5\ \mu\text{m}^2$  (square) AFM scans. The RMS roughness tends to increase with increase in the miscut angle of c-plane sapphire. These results indicate that misorientation of the substrate has influence on the surface roughness due to change of surface growth mode by varying  $L_A/L$ . In addition, the three-step growth process also has a greater resilience to tensile cracking at higher thickness than the simple two-step growth process. The critical thickness of AlN is ~2  $\mu\text{m}$  by 2-step process and ~2.5 by 3-step process, respectively, beyond which cracking of AlN occurs.

Figure 4.27 (b) shows the FWHM values of the XRD. It is clear to see that a large miscut in the c-plane sapphire substrate slightly improved the crystal quality of AlN. The minimum (0002) and (10 $\bar{1}$ 1) XRD FWHM values were around 270 arcsec and 460 arcsec for AlN grown on  $0.36^\circ$  miscut c-sapphire, respectively. Similar results were observed for the two-step process (section 4.4.3.2).

In summary, the use of 3-step growth process can lead to improve crystal quality whilst avoiding the formation of step bunches which were previously found to be highly sensitive to small changes in sapphire miscut angle. Unfortunately, it should be note that the step bunching issue was found to reoccur on both  $0.25^\circ$  and  $0.36^\circ$  miscut angle samples for AlGaIn growth, which will be discussed in the next chapter.

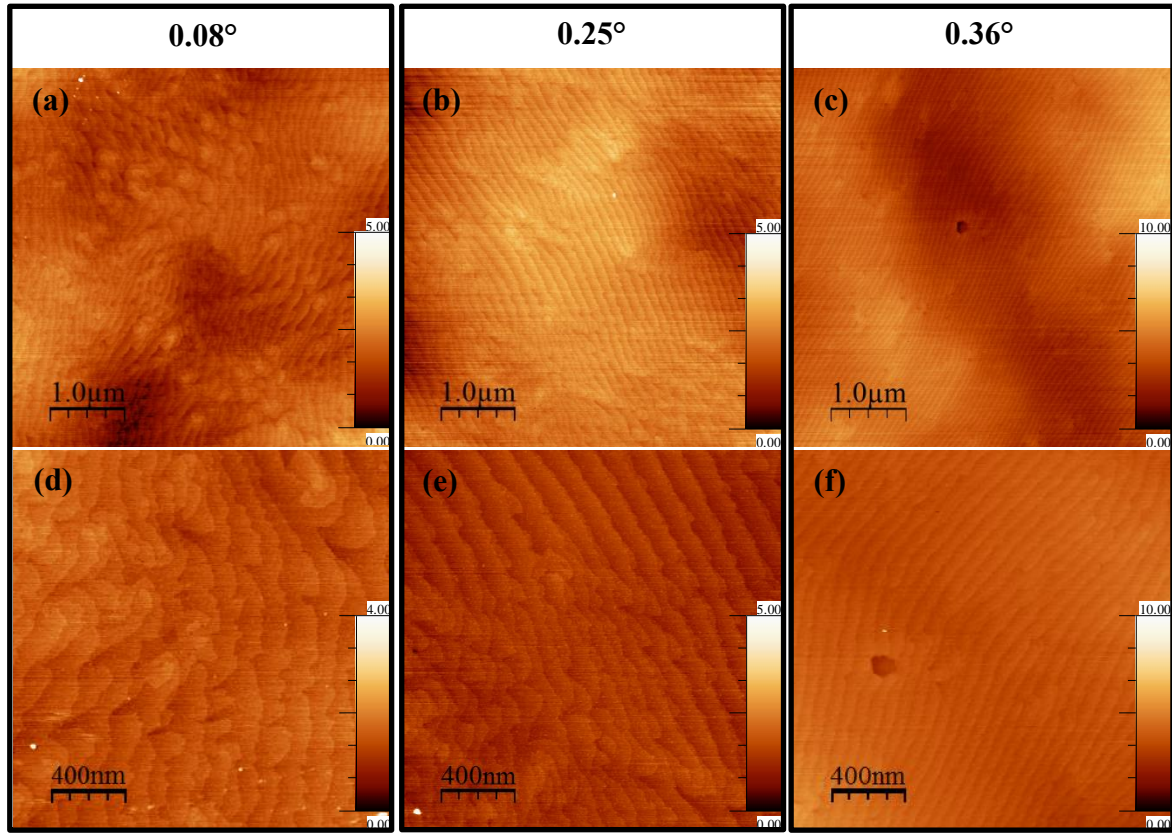


Figure 4.26:  $5 \times 5 \mu\text{m}^2$  and  $2 \times 2 \mu\text{m}^2$  AFM images of samples (a) with  $0.08^\circ$ , (b) with  $0.25^\circ$  and (c)  $0.36^\circ$  miscut angle. The unit of Z scale bars are nanometer.

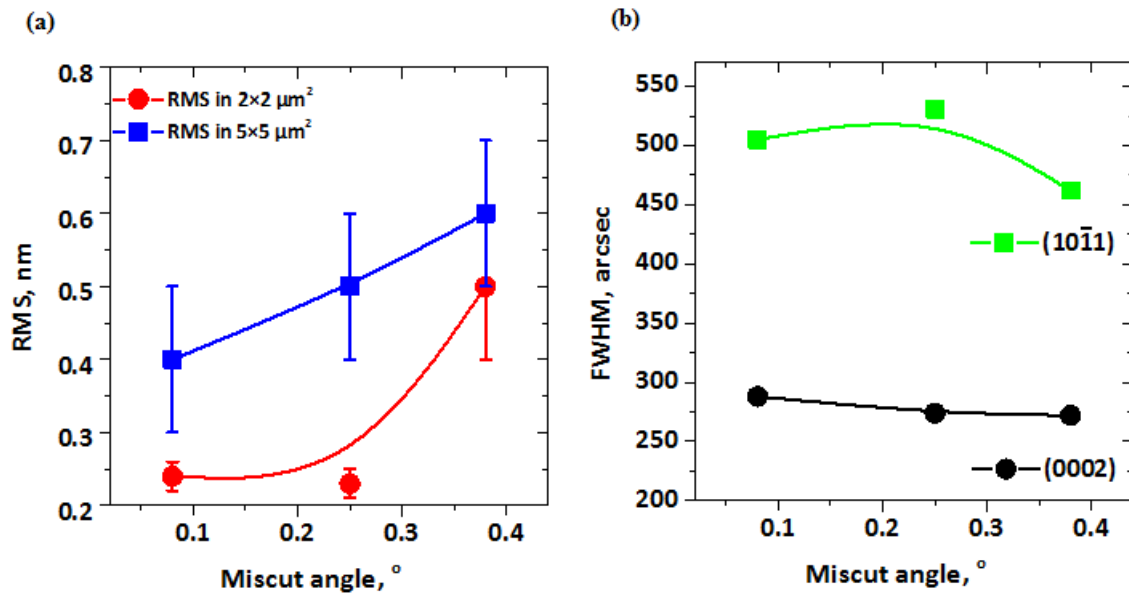


Figure 4.27: (a) RMS surface roughness of AlN and (b) XRD FWHM values for (0002) and (10 $\bar{1}1$ )  $\omega$ -scans for three-step recipe with various substrate miscut angle.

### 4.5.3 Series 3-III: Impact of AlN epilayer thickness

In series 3-III, AlN epilayers were grown on c-plane sapphire with a miscut angle of  $0.08^\circ$  using three-step process, where MT-AlN epilayer thicknesses of 1, 1.6, 2, 2.6, and 3  $\mu\text{m}$  were used.

Unfortunately, cracks were observed to form when the thickness of sample was greater than 2.6  $\mu\text{m}$ , and this crack density increased with the increasing of thickness. Eventually, some parts of epilayer delaminate as shown in Figure 4.27 (b). This cracking is one of the severe problems for thicker layer growth of AlN. Therefore, a so-called critical thickness for cracking limits the increase of the layer thickness at least on sapphire substrate depending on growth method. The critical thickness is  $2.5 \pm 0.1 \mu\text{m}$  from our experimental results with 3-step process.

As successfully optimizing the growth parameters and developing a 3-step process for the AlN epilayers on sapphire substrate, we also attempted to grow AlN on commercial substrates as mentioned previously with the same growth parameters. It was observed that the AlN thickness achievable before cracking was reduced to about 1.2  $\mu\text{m}$  after which more severe delamination could occur [see Figure 4.27 (c)]. This indicates that the commercially produced AlN layer leads to a much higher degree of tensile strain in the epitaxial growth.

Figure 4.28 (a) shows the XRD FWHM values as a function of the MT-AlN thickness for (0002),  $(10\bar{1}2)$  and  $(10\bar{1}1)$  reflections. The XRD FWHM values decreases steadily with increasing the thickness of AlN. It was also observed that the regular and parallel atomic steps start to appear as thickness increasing [Figure 4.28 (b) and (c)]. Indeed, a pinned step will form when a threading dislocation with a screw component intersects the surface: the pinning of the step causes a surface displacement equal to the Burger vector normal to the surface, which manifests in steps connecting two dislocations of opposite sign [44]. Therefore, dislocation pinning affects the evolution of the steps during growth, and the density of pinning step can be reduced by decreasing screw type dislocation.

Figure 4.29 shows AFM images of AlN epilayer grown on commercial substrates. The surface is atomically flat having jagged step-edge with atomic step heights. The average terrace width is about  $100 \pm 10 \text{ nm}$ . The XRD FWHM value of the (0002) and  $(10\bar{1}1)$  are around 34 and 800 arcsec for subsequent AlN epilayer, respectively.



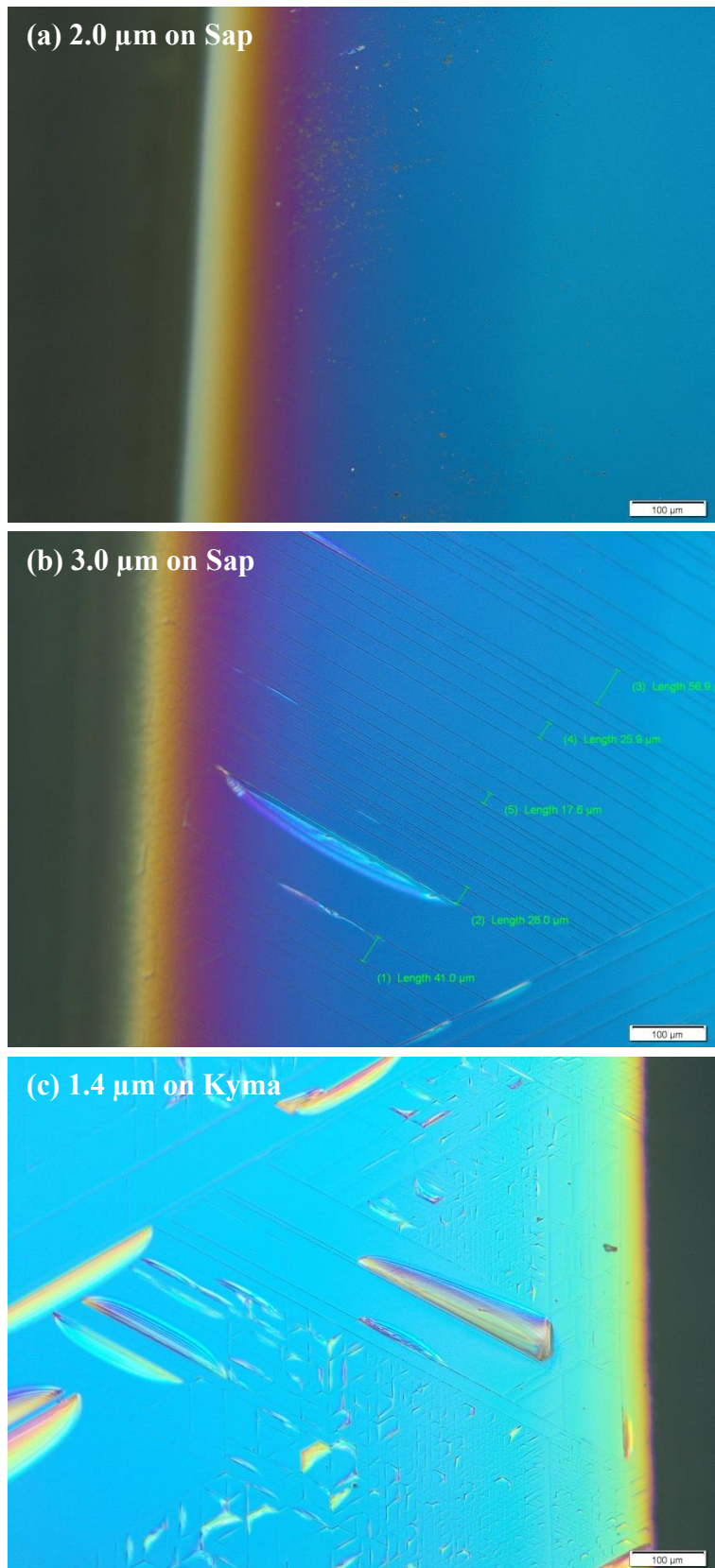


**Figure 4.27: Nomarski optical contrast micrograph of (a) a crack-free and (b) cracked AlN epilayer with 2 and 3  $\mu\text{m}$  thick, respectively. (c) a heavily cracked AlN grown on commercial substrate.**



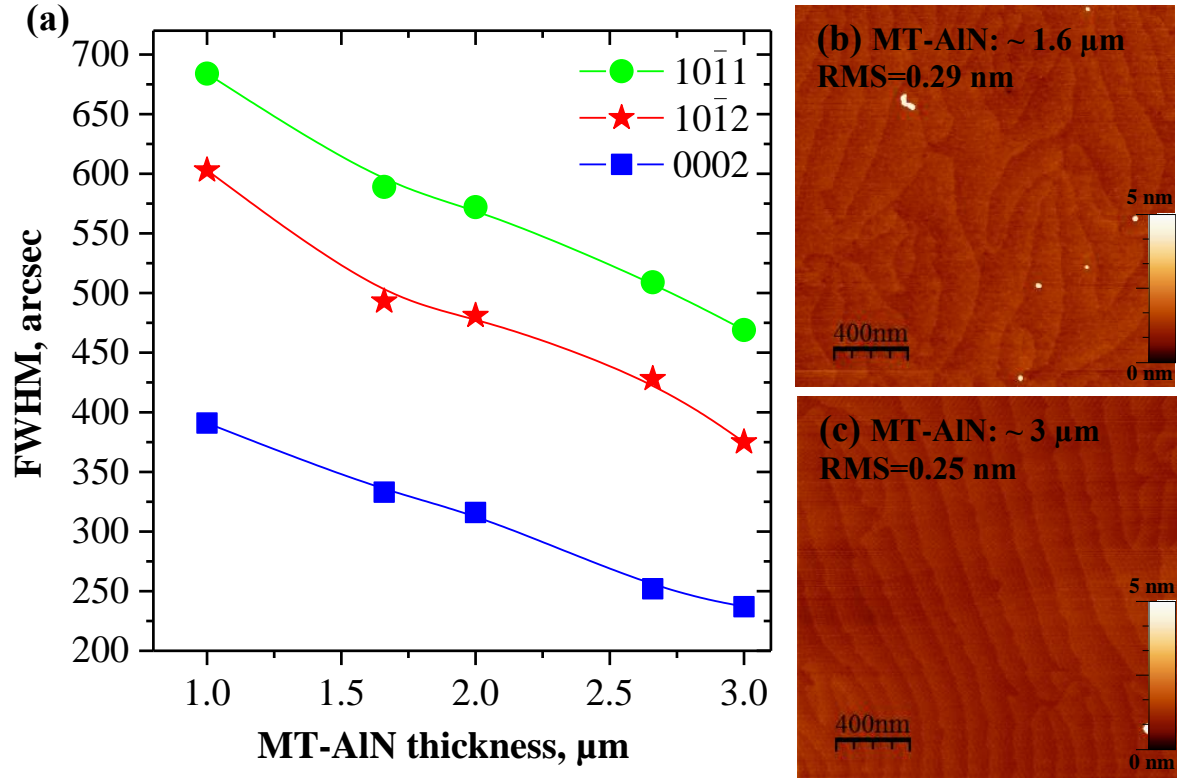


Figure 4.28: (a) XRD FWHM values of the AlN samples grown on c-sapphire as a function of MT-AlN thickness.  $2 \times 2 \mu\text{m}^2$  AFM images of (b) 1.6 and (c) 3  $\mu\text{m}$  thick MT-AlN samples, respectively. Solid lines are guidelines for the eye only.

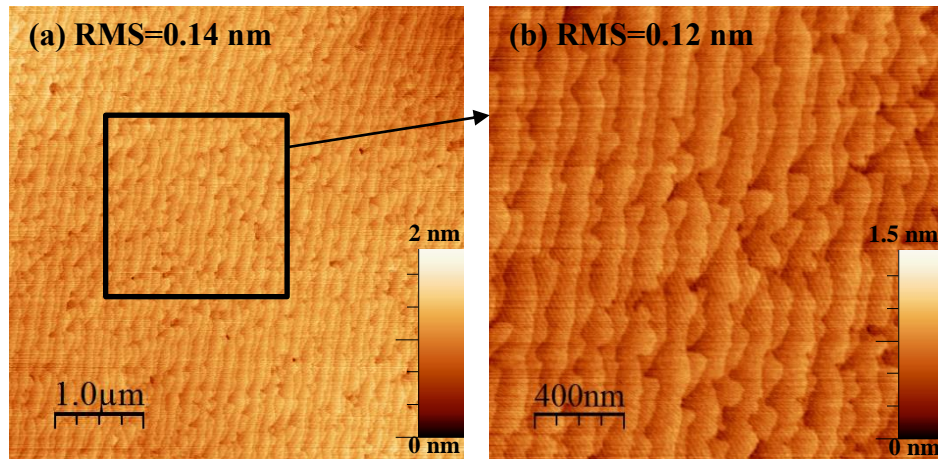


Figure 4.29: AFM image of (a)  $5 \times 5 \mu\text{m}^2$  and (b)  $2 \times 2 \mu\text{m}^2$  scanned AlN epilayer on commercial substrate exhibiting atomically flat and clearly resolved terrace width with atomic step height on the surface.

Generally, the XRD  $\text{FWHM}_{0002}$  value is broadened by screw and mixed TDs, and the XRD  $\text{FWHM}_{10\bar{1}1}$  value is broadened by all TDs (screw, edge and mixed type), then the screw and edge type TDDs ( $N_S$  and  $N_E$ ) in AlN can be roughly estimated from XRD FWHM results using the following equation [45]:

$$\beta_{hkl} = \sqrt{\beta_{\text{tilt}} \cos \chi + \beta_{\text{twist}} \sin \chi} \quad (4.13)$$

$$N_S = \beta_{tilt}^2 / 4.35 b_c^2 \quad (4.14)$$

$$N_E = \beta_{twist}^2 / 4.35 b_a^2 \quad (4.15)$$

Where  $\beta_{hkl}$  is the measured XRD FWHM,  $\chi$  is the angle between the reciprocal lattice vector ( $K_{hkl}$ ) and the (001) surface normal,  $\beta_{tilt}$  and  $\beta_{twist}$  are the tilt (out-of-plane rotation) and the twist (in-plane rotation) spreads,  $b_c$  and  $b_a$  are the Burgers vectors of the screw ( $b_c=0.4982$  nm) and edge ( $b_a=0.3112$  nm) components, respectively. The estimated values of  $N_S$  and  $N_E$  for AlN epilayers are presented in Table 4.4.

To further to investigate the dislocation behavior, TEM investigations on  $\sim 2.5$   $\mu\text{m}$  thick AlN epilayer grown on c-plane sapphire with  $\sim 0.08^\circ$  miscut angle towards m-plane) was carried out by Kevin Kahn of Imperial College London. Cross-sectional weak beam dark field (WBDF) TEM images can be used to identify changes in the densities and the relative proportions of these dislocations using  $g=\langle 0002 \rangle$  [Figure 4.30 (a)] and  $g=\langle 11\bar{2}0 \rangle$  [Figure 4.30 (b)] diffraction conditions, in which individual dislocations with screw type and edge type, respectively. In these images, TDs correspond to white lines.

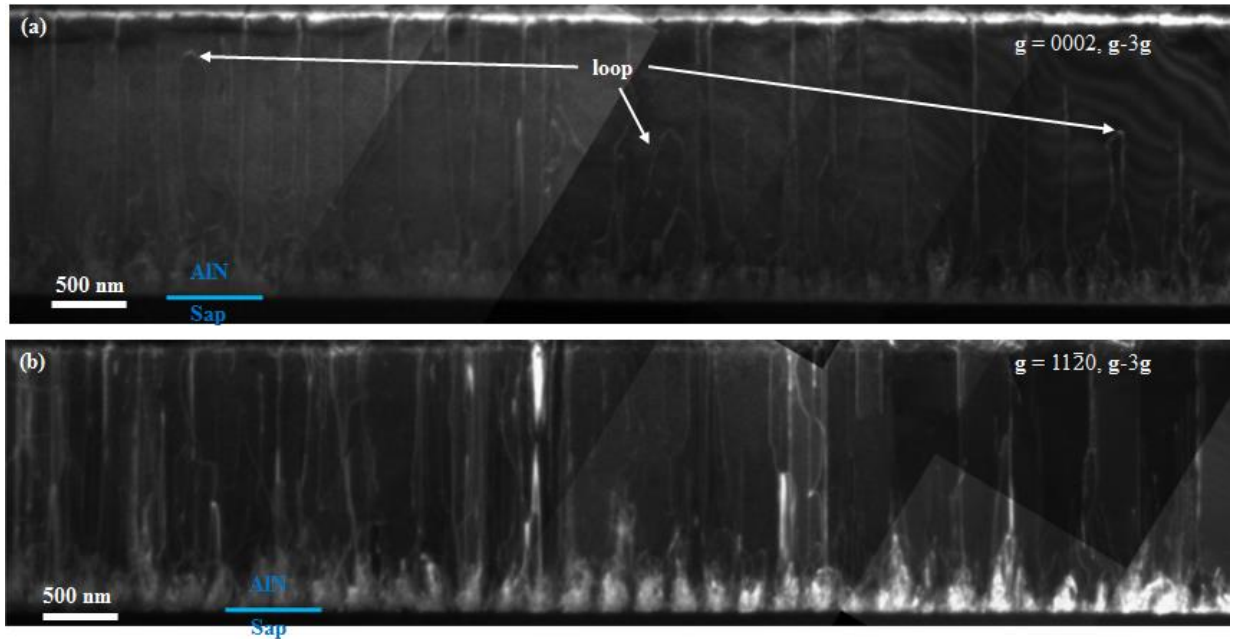


**Figure 4.30:** WBDF cross-sectional TEM images of Sample  $\alpha$  (a)  $g=0002$  showing only c-type and (a+c)-type TDs, (b)  $g=11\bar{2}0$  showing both a-type and (a+c)-type TDs.

It is clearly shown that large numbers of TDs were created at the AlN/sapphire interface, and dislocations decreased as the epilayer thickness increased. Some of the screw and edge TDs were bent with increasing epilayer thicknesses and annihilated by loop formation. Imura et al. [46] also observed similar results and reported that the transition of the growth mode by

thickness variation can reduce the number of dislocations, as these dislocations of opposite signs are forced to redirect towards each other resulting in dipole half-loop formation. Furthermore, it is found that the dense edge-type dislocations starting at the nucleation site thread the entire epilayer thickness and terminate at the surface. The screw and edge type TDDs estimated from TEM analysis are presented in Table 4.4.

Parameters	$\alpha$ -AlN	$\beta$ -AlN
Total thickness	$\sim 2.5 \mu\text{m}$	$\sim 1.5 \mu\text{m}$
AFM RMS surface roughness ( $5 \times 5 \mu\text{m}^2$ )	0.3 nm	$\sim 0.14 \text{ nm}$
FWHM of XRD (0002) reflection	$\sim 250 \text{ arcsec}$	$\sim 34 \text{ arcsec}$
FWHM of XRD ( $10\bar{1}1$ ) reflection	$\sim 500 \text{ arcsec}$	$\sim 800 \text{ arcsec}$
Screw type TDs from XRD	$\sim 1.4 \times 10^8 \text{ cm}^{-2}$	$\sim 2.5 \times 10^6 \text{ cm}^{-2}$
Edge type TDs from XRD	$\sim 1.7 \times 10^9 \text{ cm}^{-2}$	$\sim 4.6 \times 10^9 \text{ cm}^{-2}$
Screw type TDs from TEM	$\sim 2.2 \times 10^8 \text{ cm}^{-2}$	
Edge type TDs from TEM	$\sim 1.3 \times 10^9 \text{ cm}^{-2}$	

**Table 4.4:** Measured characterization results of optimized 3-step process AlN epilayers grown on c-plane sapphire ( $\alpha$ -AlN) and Kyma substrate ( $\beta$ -AlN), respectively.

## 4.6 Conclusion

Despite the rapid progress made in Group-III nitride materials growth, AlN is still typically grown on sapphire, which is cheaper but has a large lattice mismatch with the nitride based films. In this chapter different growth methods of AlN have been described and discussed. A growth window for Al-polar film was found.

The reproducibility of AlN is more complicated than expected. AlN recipes are particularly difficult to transfer between reactors, even those from the same design family, and recipes often need extensive modification and do not give the material of the same quality. AlN growth is extremely sensitive to the initial chemical condition of the reactor, and that small changes can have significant effects on growth. In a “dirty” and improper coating reactor condition, polarity and defect density turned out to be highly non-reproducible. A nitridation of the sapphire surface was taking place, because nitrogen containing impurities left over from the previous growth run. This unintended nitridation led to growth of N- or mixed-polar AlN with inversion domains and a high surface roughness. In order to avoid unwanted nitridation, by a H<sub>2</sub> bake and proper TMAI pre-treatment, reproducibility was achieved.

For a high miscut angle, in combination with a high growth temperature, step bunching occurred and explained by a negative ESB. The step bunching disappeared when lowering the miscut angle of the substrate or reducing the growth temperature resulting in an atomically smooth surface.

It is also observed that a high quality AlN layers exhibited decreasing TDDs with increasing layer thickness due to dislocation climbing, bending and annihilation, verifying by XRD and TEM measurements. By successfully optimizing all parameters of each growth series, the (0002) and (10 $\bar{1}$ 1) XRD FWHM values were finally reduced to around 280 arcsec and 500 arcsec with three-step growth on 0.08°±0.02° miscut angle of sapphire with smooth and crack-free surface.

## 4.7 Reference:

- [1] H. Li, T. C. Sadler, P. J. Parbrook, *J. Cryst. Growth*, 72, 383 (2013).
- [2] Y. Feng, H. Wei, S. Yang, Z. Chen, L. Wang, S. Kong, G. Zhao and X. Liu, *Scientific Reports* 4, 6416 (2014).
- [3] H. Behmenburg, C. Giesen, R. Srnanek, J. Kovac, H. Kalisch, M. Heuken, R.H. Jansen, *J. Cryst. Growth*, 42, 316 (2011).
- [4] S. Keller and S. P. DenBaars, *J. Cryst. Growth* 248, 479 (2003).
- [5] A.V. Lobanova, K.M. Mazaev, R.A. Talaev, M. Leys, S. Boeykens, K. Cheng and S. Degroote, *J. Cryst. Growth*. 287, 601 (2006).
- [6] N. Fujimoto, T. Kitano, G. Narita, N. Okada, K. Balakrishnan, M. Iwaya, S. Kamiyama, H. Amano, I. Akasaki, K. Shimono, T. Noro, T. Takagi and A. Bandoh, *Phys. Stat. Sol. c*3, 1617 (2006).
- [7] F. Brunner, H. Protzmann, M. Heuken, A. Knauer, M. Weyers and M. Kneissl, *Phys. Stat. Sol. c*5, 1799 (2008).
- [8] M. Imura, K. Nakano, G. Narita, N. Fujimoto, N. Okada, K. Balakrishnan, M. Iwaya, S. Kamiyama, H. Amano, I. Akasaki, T. Noro, T. Takagi and A. Bandoh, *J. Cryst. Growth* 298, 257 (2007).
- [9] A. Kakanakova-Georgieva, R. R. Ciechonski, U. Forsberg, A. Lundskog and E. Janze, *Cryst. Growth Des.* 9, 880 (2009).
- [10] F. Brunner, H. Protzmann, M. Heuken, A. Knauer, M. Weyers and M. Kneissl, *Phys. Stat. Sol. c*5, 1799 (2008).
- [11] Y. Ohba, H. Yoshida and R. Sato, *Jpn. J. Appl. Phys.* 36, L1565 (1997).
- [12] M. Kneissl, T. Kolbe, C. Chua, V. Kueller, N. Lobo, J. Stellmach, A. Knauer, H. Rodriguez, S. Einfeldt, Z. Yang, N. M. Johnson and M. Weyers, *Semicond. Sci. Technol.* 26, 014036 (2011).
- [13] V. Kueller, A. Knauer, F. Brunner, U. Zeimer, H. Rodriguez, M Kneissl and M. Weyers, *J. Cryst Growth*. 315, 200 (2011).
- [14] M. Imura, N. Fujimoto, N. Okada, K. Balakrishnan, M. Iwaya, S. Kamiyama, H. Amano, I. Akasaki, T. Noro, T. Tagaki and A. Bandoh, *J. Cryst Growth*. 300,136 (2007).
- [15] N. Okada, N. Kato, S. Sato, T. Sumii, T. Nagai, N. Fujimoto, M. Imura, K. Balakrishnan, M. Iwaya, S. Kamiyama, H. Amano, I. Akasaki, H. Maruyama, T. Tagaki, T. Noro and A. Bandoh, *J. Cryst Growth*. 298, 349 (2007).
- [16] T. G. Mihopoulos, V. Gupta and K. F. Jensen, *J. Cryst. Growth* 195, 733 (1998).
- [17] D. G. Zhao, J. J. Zhu, D. S. Jiang, H. Yang, J. W. Liang, X. Y. Li and H. M. Gong, *J. Cryst. Growth* 289, 72 (2006).

- [18] A. V. Lobanova, A. S. Segal, E. V. Yakovlev and R. A. Talalaev, J. Cryst. Growth, 352, 199 (2012).
- [19] J. Stellmach, M. Pristovsek, O. Savas, J. Schlegel, E. V. Yakovlev and M. Kneissl, J. Cryst. Growth. 315, 229 (2011).
- [20] J. R. Creighton, G. T. Wang, W. G. Breiland and M.E. Coltrin, J. Cryst. Growth. 261, 204 (2004).
- [21] T. G. Mihopoulos, V. Gupta and K. F. Jensen, J. Cryst. Growth. 195, 733 (1998).
- [22] T. Uchida, K. Kusakabe and K. Ohkawa, J. Cryst. Growth. 304, 133 (2007).
- [23] J. R. Creighton, G. T. Wang and M. E. Coltrin, J. Cryst. Growth. 298, 7 (2007).
- [24] T. Wang, J. Bai, P. J. Parbrook and A. G. Cullis, Appl. Phys. Lett. 87, 151906 (2005).
- [25] T. Akiyama, Y. Saito, K. Nakamura and T. Ito, Surf Sci, 606, 221 (2012).
- [26] T. Y. Chang, *Characterisation of polar (0001) and non-polar (11-20) Ultraviolet nitride semiconductors*, PhD Thesis, University of Cambridge (2013).
- [27] M. A. Moram and M.E. Vickers, Rep. Prog. Phys. 72, 036502 (2009).
- [28] H. Amano, N. Sawaki, I. Akasaki and Y. Toyoda, Appl. Phys. Lett. 48, 353 (1986).
- [29] S. Nakamura, Jpn. J. Appl. Phys. 30, L1705 (1991).
- [30] H. Amano, M. Iwaya, T. Kashima, M. Katsuragawa, I. Akasaki, J. Han, S. Hearne, J.A. Floro, E. Chason, J. Figiel, Jpn. J. Appl. Phys. 37 (1998) L1540.
- [31] A. Gocalinska, M. Manganaro, D. D. Vedensky and E. Pelucchi, Phys. Rev. B86, 165307 (2012).
- [32] M. Kasu and N. Kobayashi, J. Appl. Phys. 78, 3026 (1995).
- [33] C. J. Sun, P. Kung, A. Saxler, H. Ohsato, K. Haritos, and M. Razeghi, J. Appl. Phys., 75, 3964 (1994).
- [34] A. Gocalinska, M. Manganaro, D. D. Vedensky, E. Pelucchi, Phys. Rev. B86 165307 (2012).
- [35] M. Kasu and N. Kobayashi, J. Appl. Phys. 78, 3026 (1995).
- [36] K. Nagamatsu, N. Okada, N. Kato, T. Sumii, A. Bandoh, M. Iwaya, S. Kamiyama, H. Amano, I. Akasaki, Physica Status Solidi (C) 9 (2008) 3048.
- [37] W. Burton, N. Cabrera, and F. Frank, Phil. Trans. Roy. Soc. Ldn A 243, 299 (1951).
- [38] G. Ehrlich and F. G. Hudda, J. Chem. Phys. 44, 1039 (1966).
- [39] R. L. Schwoebel and E. J. Shipsey, J. Appl. Phys. 37, 3682 (1966).
- [40] C. Misbah, O. Pierre-Louis, and Y. Saito, Rev. Mod. Phys. 82, 981 (2010).
- [41] J. Villain, J. Phys. I France, 1, 19 (1991).

- [42] P. Politi and J. Villain, Phys. Rev. B 54, 5114 (1996)
- [43] AlN nucleation layers grown via PVD by Kyma Technologies, 8829 Midway West Road, Raleigh, NC 27617.
- [44] F. C Frank, The influence of dislocations on crystal growth, Discuss. Faraday Soc. 5, 48 (1949).
- [45] C. G. Dunn, E. F. Koch, Acta Metall. 5, 548 (1957).
- [46] M. Imura, K. Nakano, N. Fujimoto, N. Okada, K. Balakrishnan, M. Iwaya, S. Kamiyama, H. Amano, I. Akasaki, T. Noro, T. Takagi and A. Bandoh, Jpn. J. Appl. Phys. 45, 8639 (2006).

# MOVPE Growth of Planar Undoped AlGa<sub>N</sub> on AlN Template

---

## 5.1 Introduction

In recent years, high Al content AlGa<sub>N</sub> alloys have attracted great interest as an important photonics and electronic material due to their applications in ultraviolet (UV) light emitting diodes (LEDs), laser diodes (LDs), solarblind photodetectors (PDs) and high electron mobility transistors (HEMTs) [1, 2, 3, 4]. The direct growth of a thick ( $\geq 1 \mu\text{m}$ ) AlGa<sub>N</sub> (Al $\geq 10\%$ ) layer on a pseudo Ga<sub>N</sub> substrate is extremely difficult, because tensile stress generated in the AlGa<sub>N</sub> layer leading to cracks, thus degrading the quality of the film [5]. The use of low-temperature interlayers and short period superlattice layers have been demonstrated to be available method to avoid this problem and allow crack-free growth of thicker and higher Al content AlGa<sub>N</sub> layers on Ga<sub>N</sub> [6, 7, 8]. Meanwhile, high crystalline quality Al<sub>0.2</sub>Ga<sub>0.8</sub>N have been realized by the SiN<sub>x</sub> nanomask deposition process [9, 10]. However, the use of Ga<sub>N</sub> template drastically decreases the light extraction efficiency in LEDs with emission wavelength  $\leq 360 \text{ nm}$  due to strong UV light absorption. Hence, low Al content AlGa<sub>N</sub> grown on Ga<sub>N</sub> template have only been used in limited applications, mainly for HEMTs [4] and near UV LEDs above 365 nm [11].

As an alternative, the growth of high ( $x \geq 50\%$ ) Al content Al<sub>x</sub>Ga<sub>1-x</sub>N on AlN-on-sapphire “templates” with low dislocation density should be considered for UV LEDs [12, 13, 14, 15, 16, 17, 18]. Growth of AlGa<sub>N</sub> on AlN is preferred over Ga<sub>N</sub> as the compressive strain introduced into the AlGa<sub>N</sub> eliminates the risk of cracking, in addition to offering the benefits of transparency in obtaining good light extraction efficiency. However, on the c-plane, the accommodation of the lattice misfit between AlN and AlGa<sub>N</sub> is a large issue: it induces additional dislocations at the AlN/AlGa<sub>N</sub> interface, which only partially relax the film. This incomplete relaxation means there is a large residual compressive strain in the overgrown



material. For UV LEDs the increase in dislocation density must be minimized, the residual compressive strain reduced and the effect on the surface morphology addressed.

In this chapter, the growth and characterization of undoped  $\text{Al}_x\text{Ga}_{1-x}\text{N}$  epilayers by employing different growth conditions and templates will be described.

## 5.2 Experimental details

Trimethylgallium (TMGa) and Trimethylaluminium (TMAI) were used as group-III precursors, while ammonia ( $\text{NH}_3$ ) was the group-V precursor for the growth of  $\text{Al}_x\text{Ga}_{1-x}\text{N}$  epilayers. All samples were prepared on pre-grown AlN templates on sapphire. The AlN templates were reintroduced in the reactor and were overgrown with  $\text{Al}_x\text{Ga}_{1-x}\text{N}$  films on a thin AlN connecting layer. AlN template: type  $\alpha$  was prepared by a three-step temperature process on c-plane sapphire ( $\text{FWHM}_{002}=280$  arcsec and  $\text{FWHM}_{101}=550$  arcsec), while type  $\beta$  was prepared through AlN overgrowth on c-plane sapphire with a thin 50 nm AlN nucleation layer prepared commercially ( $\text{FWHM}_{002}=35$  arcsec and  $\text{FWHM}_{101}=850$  arcsec). 6 sets of samples have been grown with a typical structure and growth sequence as illustrated in Figure 5.1(a) and (b). The overview of growth condition is given in Table 5.1.

The reactor was maintained at 50 mbar for all series. The total MO precursors (TMGa+TMAI) were maintained at 30  $\mu\text{mol}/\text{min}$ , and samples were grown at 1110 °C in first three sets (I, II, and III). In the first set (I), the V/III ratio was changed from 100 to 2343 keeping with a constant TMGa/TMAI ratio of 2. The  $\text{NH}_3$  flow rate was changed from 3 mmol/min (67.2 sccm) to 70.3 mmol/min (1575 sccm). In the second set (II), the TMGa/TMAI ratio was varied from 0 to 6 with a V/III ratio of 781. In the third set (III), the TMGa/TMAI ratio was varied from 1 to 5 with a constant V/III ratio of 100 grown on two different kinds of AlN templates (three-step process of AlN on c-plane sapphire templates  $\alpha$  and AlN Kyma templates  $\beta$ ). In the last three sets (IV, V and VI), the V/III and TMGa/TMAI ratio were maintained at 781 and 2, respectively. The MO and  $\text{NH}_3$  flow rate were changed proportionally, and growth temperature was adjusted between 1110 and 1245 °C.

The main targets of this section include: Section 5.3.1 is to investigate the control of AlN content in  $\text{Al}_x\text{Ga}_{1-x}\text{N}$  by varying V/III ratio, TMGa/TMAI ratio, growth rate and growth temperature, and then determine Al content by XRD and PL measurements. Section 5.3.2 is to study the microstructural properties of samples using XRD and in-situ curvature measurement. Section 5.3.3 is to investigate the surface morphology, which was assessed by

Nomarski interference light microscopy using an Olympus BX51M and atomic force microscopy (AFM) using a Multimode<sup>TM</sup> Veeco with analysis using WSxM freeware [19]. Additionally, cathodoluminescence (CL) in a secondary electron microscope (SEM) enables information to be obtained on the surface morphology and the optical properties at the same time for studying the distribution of Al content on the surface (All the SEM-CL images are taken by Gunnar Kusch at the University of Strathclyde).

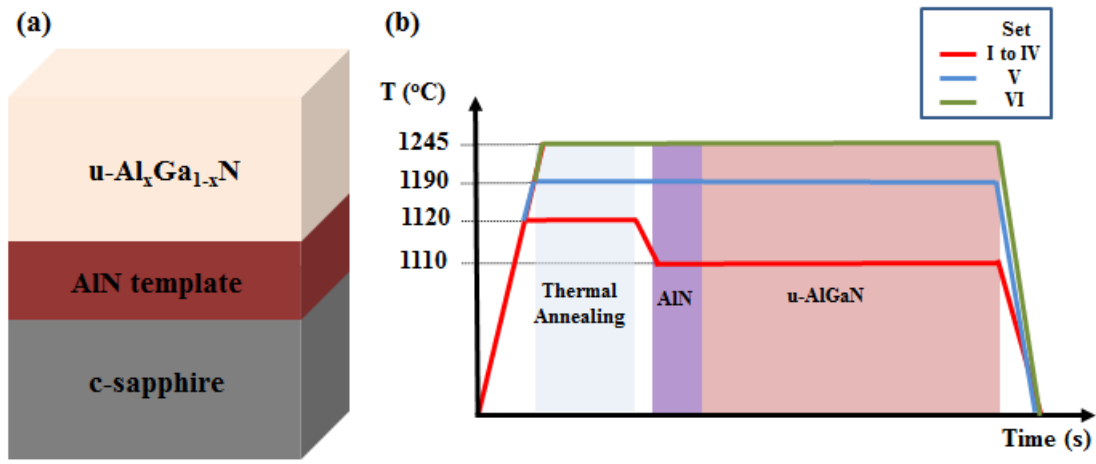


Figure 5.1: (a) Schematic of the undoped Al<sub>x</sub>Ga<sub>1-x</sub>N structure and (b) growth sequence on AlN/sapphire template.

Set	V/III ratio	TMGa/TMAI	MO (μmol/min)	GT (°C)	Thickness (μm)	Template
(I)	100-2343	2	30	1110	1	(α)
(II)	781	0-6	30	1110	1	(α)
(III)	100	1-5	30	1110	1	(α) and (β)
(IV)	781	2	15-60	1110	1.5	(α) and (β)
(V)	781	2	60-150	1190	1.5	(α) and (β)
(VI)	781	2	60-180	1245	1.5	(α) and (β)

Table 5.1: Sample overview for variation of V/III ratio, TMGa/TMAI ratio, metal-organic (MO) flow rate (TMGa+TMAI), growth temperature (GT) and template for Al<sub>x</sub>Ga<sub>1-x</sub>N epilayers growth.

## 5.3 Results and discussion

### 5.3.1 Control of Al content in $\text{Al}_x\text{Ga}_{1-x}\text{N}$

To measure the Al content of the isotropic strained state of  $\text{Al}_x\text{Ga}_{1-x}\text{N}$  epilayers in the c-plane, equations (3.17) and (3.18) were solved to determine the Al content,  $x$ :

$$\frac{c_{\text{AlGa}}^{\text{meas}} - [xc_{\text{AlN}} + (1-x)c_{\text{Ga}}]}{xc_{\text{AlN}} + (1-x)c_{\text{Ga}}} = -\frac{2[xv_{\text{AlN}} + (1-x)v_{\text{Ga}}]}{1 - [xv_{\text{AlN}} + (1-x)v_{\text{Ga}}]} \times \frac{a_{\text{AlGa}}^{\text{meas}} - [xa_{\text{AlN}} + (1-x)a_{\text{Ga}}]}{xa_{\text{AlN}} + (1-x)a_{\text{Ga}}} \quad (5.1)$$

It is easy to obtain a solution for  $x$  in following cubic equation,

$$Ax^3 + Bx^2 + Cx + D = 0 \quad (5.2)$$

where

$$A = -(v_{\text{AlN}} - v_{\text{Ga}})(a_{\text{AlN}} - a_{\text{Ga}})(c_{\text{AlN}} - c_{\text{Ga}})$$

$$B = -[(1 + v_{\text{Ga}})(a_{\text{AlN}} - a_{\text{Ga}})(c_{\text{AlN}} - c_{\text{Ga}})] - (v_{\text{AlN}} - v_{\text{Ga}})[(a_{\text{AlN}} - a_{\text{Ga}})(c_{\text{Ga}} + c_{\text{AlGa}}^{\text{meas}}) + (a_{\text{Ga}} - 2a_{\text{AlGa}}^{\text{meas}})(c_{\text{AlN}} - c_{\text{Ga}})]$$

$$C = (a_{\text{AlN}} - a_{\text{Ga}})[(1 - v_{\text{Ga}})c_{\text{AlGa}}^{\text{meas}} - (1 + v_{\text{Ga}})c_{\text{Ga}}] + (c_{\text{AlN}} - c_{\text{Ga}})[2v_{\text{Ga}}a_{\text{AlGa}}^{\text{meas}} - (1 + v_{\text{Ga}})a_{\text{Ga}}]$$

$$D = a_{\text{Ga}}c_{\text{AlGa}}^{\text{meas}}(1 - v_{\text{Ga}}) - (1 + v_{\text{Ga}})c_{\text{Ga}}a_{\text{Ga}} + 2v_{\text{Ga}}a_{\text{AlGa}}^{\text{meas}}c_{\text{Ga}}$$

The measured lattice parameters  $c_{\text{AlGa}}^{\text{meas}}$  and  $a_{\text{AlGa}}^{\text{meas}}$  were determined from the peak positions on the (0002), (0004) and  $(10\bar{1}5)$  reflections, found using  $\omega$ -2 $\theta$  scans and  $\omega/\omega$ -2 $\theta$  reciprocal space maps, respectively. We used literature values for the lattice parameters and Poisson's ratios of GaN and AlN [20, 21, 22], which are summarized in Table 5.2. These lattice parameters were then used to calculate the epilayer compositions and equivalent relaxed lattice parameters assuming that Vegard's Law holds for AlGa.

	Poisson ratio $\nu$	$a$ (Å)	$c$ (Å)
GaN [20]	0.203	3.1884	5.1850
AlN [21,22]	0.225	3.111	4.981

**Table 5.2:** The lattice parameters and Poisson ratio of GaN and AlN [20, 21, 22].

The DUV PL spectroscopy (244 nm, cw Ar-ion laser) has been employed to measure the near-band-edge (NBE) emission of  $\text{Al}_x\text{Ga}_{1-x}\text{N}$  peak at room temperature (RT), so the NBE

emission below 244 nm (5.082 eV) cannot be detectable. The Al content was calculated by using Equation [23],

$$E_g = (1 - x)E_g(\text{GaN}) + xE_g(\text{AlN}) - bx(1 - x) \quad (5.3)$$

Where the bowing parameter  $b$  is 1 eV [23], the energy gaps for GaN and AlN were assumed to be 3.42 eV [24] and 6.1 eV [25], respectively at RT. The accuracy is affected by the derivation of the NBE emission as well as the evaluation implying simplifications (strain state, single bowing parameter in spite of valence band crossing) leading to an estimated uncertainty of  $\pm 2\%$ . For the XRD and PL measurements, the analysis was carried out for the highest intensity peak which was likely to be most representative of the samples. It is also worth mentioning that the deviation between XRD and PL results may lie in the detectable area (size and depth) as well as selection of calculation parameters.

In Set (I), the Al composition of the epilayers were calculated from the lattice parameters measured in XRD and NBE emission in PL against V/III ratio [Figure 5.2 (a)]. Figure 5.2 (b) shows the growth rates of AlN and GaN in  $\text{Al}_x\text{Ga}_{1-x}\text{N}$  against V/III ratio.

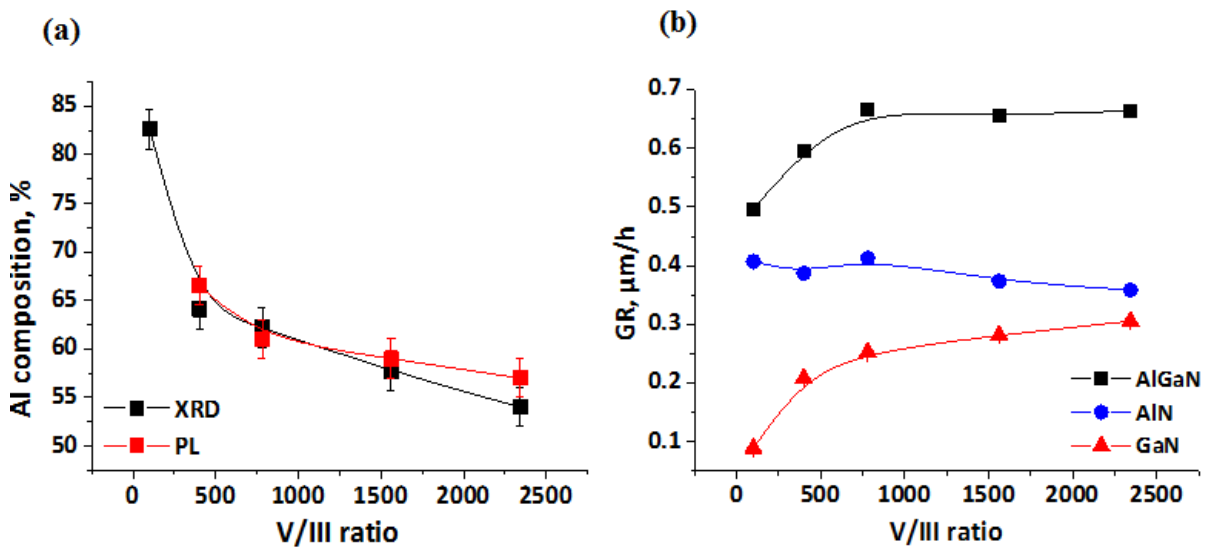


**Figure 5.2:** (a) Al composition in AlGaIn layers determined from XRD and PL against the V/III ratio. (b) Growth rates of AlN and GaN in AlGaIn layers and the growth rate of AlGaIn against the V/III ratio for set (I).

It is observed that Al composition drops with increasing V/III ratio as shown in Figure 5.2 (a). The AlGaIn growth rate was constant when V/III ratio is above 781 in Figure 5.2 (b). However, a pronounced impact of high V/III ratio on the partial growth rate of GaN in contrast to the respective AlN component [see Figure 5.3 (b)]. The effect of V/III ratio on the

AlGaN growth rate is mainly caused by two processes. Firstly, the incorporation rate of Al slightly decreases with increasing V/III ratio, which can be explained by increase of parasitic reactions due to increasing of the  $\text{NH}_3$  concentration [26]. Lower V/III ratios can help reduce the rate of losses by formation of larger oligomeric species and by gas phase nano-particle formation [27].

Secondly, at high temperature above 950 °C, GaN is known to be subject to the interaction with hydrogen ( $\text{H}_2$ ), which is also referred to as “GaN etching” , but not observed in a nitrogen ( $\text{N}_2$ ) ambient at comparable conditions [27, 28]. Hence, the resulting effective growth rate of GaN with the  $\text{H}_2$ - $\text{NH}_3$  ambient is equal to the transport limited incorporation rate minus the decomposition (etching) rate ( $\text{GaN}_{\text{GR}} = \text{GaN}_{\text{IR}} - \text{GaN}_{\text{DR}}$ ). The effective growth rate of Ga significantly increases with increasing V/III ratio from 100 to 781, which could be contributed from two reasons: (1) the suppression of decomposition of GaN through enforcing the reaction of liquid Ga ( $\text{Ga}_{\text{liq}}$ ) to GaN by increasing  $\text{NH}_3$  concentration ( $\text{NH}_3 + \text{Ga}_{\text{liq}} \leftrightarrow \text{GaN} + 3/2\text{H}_2$ ) [29], and (2) perhaps insufficient  $\text{NH}_3$  precursor can react with TMGa precursor during growth under low V/III condition, because  $\text{NH}_3$  is decomposed only up to 4% at 950 °C (at this temperature ammonia gets cracked catalytically at the growing surface,  $\text{NH}_3 \leftrightarrow 1/2\text{N}_2 + 3/2\text{H}_2$ ) [30, 31]. In addition, XRD and PL show that broader  $\text{Al}_x\text{Ga}_{1-x}\text{N}$  peaks appear as Al content decreases due to inhomogeneous distribution of strain state and/or composition as shown in Figure 5.3 (a) and (b).

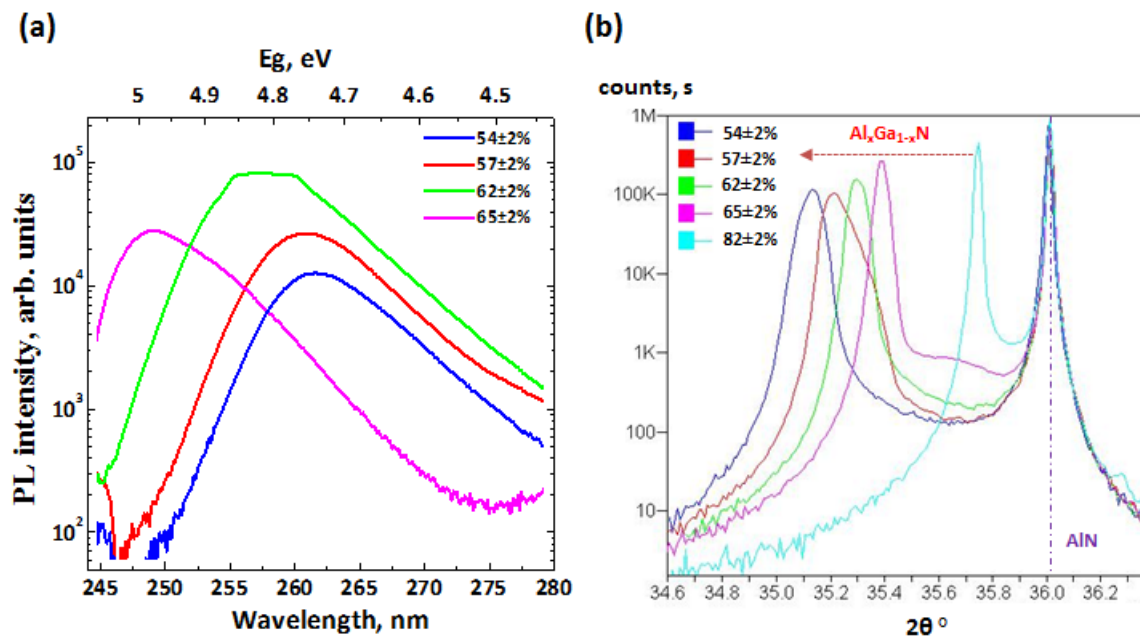


Figure 5.3: (a) PL spectra and (b) XRD measurement of the  $\omega$ -2 $\theta$  scan (0002) reflections of  $\text{Al}_x\text{Ga}_{1-x}\text{N}$  for set (I).

Another efficient way to vary Al content is changing TMGa/TMAI ratio in  $\text{Al}_x\text{Ga}_{1-x}\text{N}$ , because Al (or Ga) contents are expected to be stable against phase segregation under common growth conditions. Generally, for 100% incorporation efficiency of Al (or Ga) without the presence of parasitic reactions for  $V/\text{III} \gg 1$ , the Al composition  $X_{\text{Al}}$  of an alloy  $\text{Al}_x\text{Ga}_{1-x}\text{N}$  can be expressed as a linear dependence as the same content of the precursors in gas phase [ $X_{\text{Al}} = 2\text{TMAI}/(\text{TMGa} + 2\text{TMAI})$ ]. The factor of 2 in the TMAI flow is due to TMAI being a dimer (i.e., every molecule in the vapour contains two Al atoms) in the gas phase at room temperature [32]. In Sets (II) and (III),  $\text{NH}_3$  flow rate,  $V/\text{III}$  ratio and total MO flow rate were maintained the same, but only varying TMGa/TMAI ratio during experiments. Figure 5.4 (a) shows a plot of the Al content against the  $2\text{TMAI}/(\text{TMGa} + 2\text{TMAI})$  ratio for the samples grown at the  $V/\text{III}$  ratio of 781 and 100, respectively. It is clear to show that the Al content decreases with dropping  $2\text{TMAI}/(\text{TMGa} + 2\text{TMAI})$  ratio. On the other hand, an increase in Al incorporation rate while maintaining the same  $2\text{TMAI}/(\text{TMGa} + 2\text{TMAI})$  ratio can be achieved by simply reducing the  $\text{NH}_3$  flow rate, which was also observed and explained in Set (I). Figure 5.4 (b) shows a comparison between the effective growth rates of the AlN and GaN,  $\text{Al}_x\text{Ga}_{1-x}\text{N}$  against the  $2\text{TMAI}/(\text{TMGa} + 2\text{TMAI})$  ratio. No significant amounts of Al are being lost for pre-reactions (PRs) in set (II) and (III), and the change in composition between the two series is mainly controlled by the Ga decomposition process described previously.

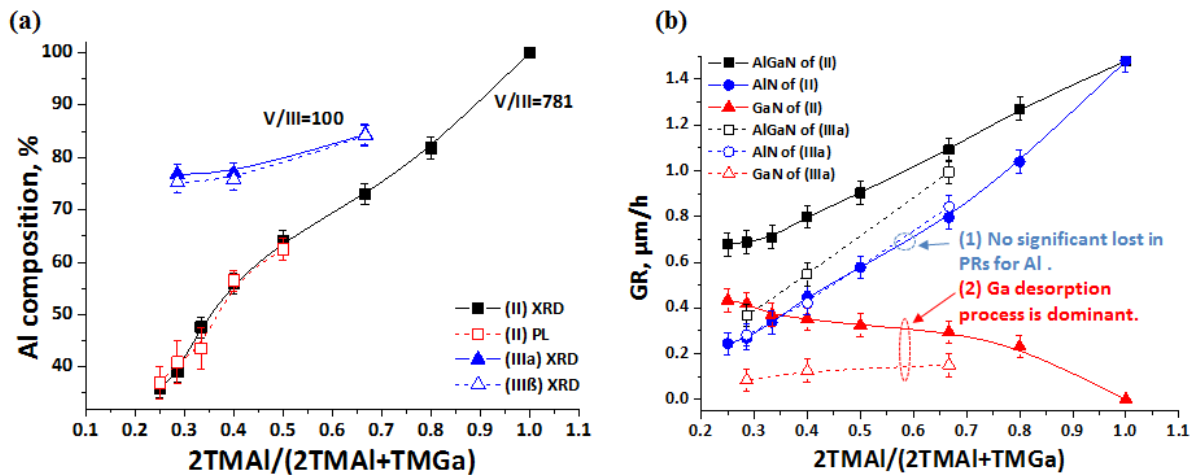
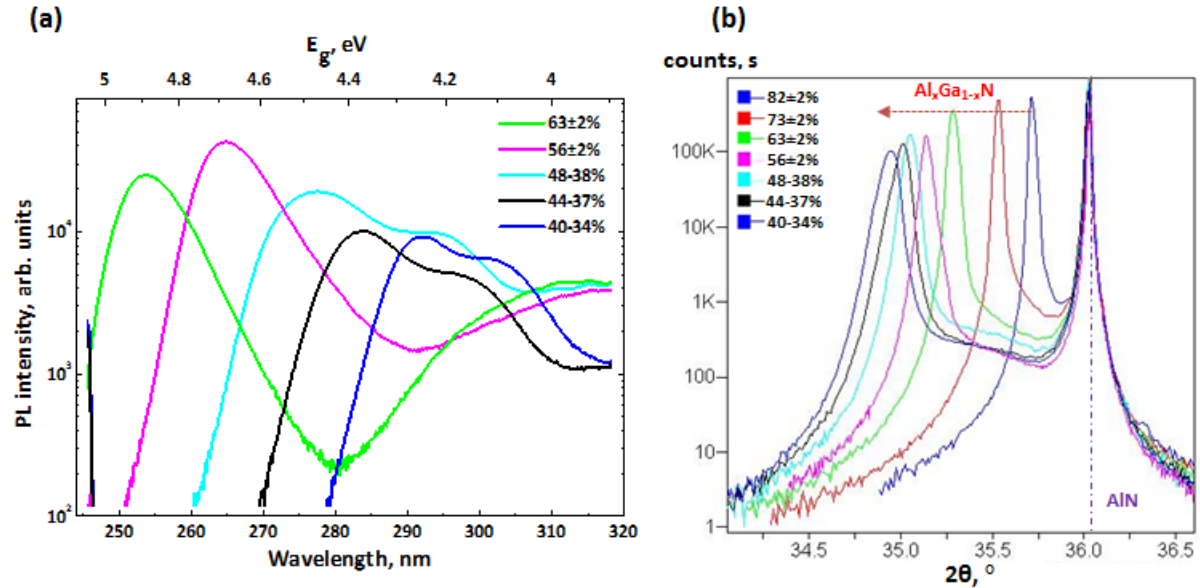


Figure 5.4: (a) Al composition against the TMGa/TMAI ratio for set (II), (IIIa) and (IIIβ). (b) Growth rates of AlN and GaN and the growth rate of AlGaN against TMGa/TMAI ratio for set (II) and (IIIa).

PL shows that the  $\text{Al}_x\text{Ga}_{1-x}\text{N}$  layers of Set (II) have shoulder peak emission, when Al composition is below 50% as shown in Figure 5.5 (a). The shoulder emission at longer wavelengths indicates the significantly inhomogeneous distribution of composition and/or

strain state. The  $\omega/2\theta$  (0002) peak of  $\text{Al}_x\text{Ga}_{1-x}\text{N}$  also became broader as decreasing Al composition same as Set (I) [Figure 5.5 (b)]. This inhomogeneous distribution feature will be confirmed in the next section.



**Figure 5.5: (a) PL spectra and (b) XRD measurement of the  $\omega$ - $2\theta$  scan (0002) reflections of  $\text{Al}_x\text{Ga}_{1-x}\text{N}$  for set (II).**

Figure 5.6 (a) shows a plot of the Al content (measured by XRD) against the total MO and  $\text{NH}_3$  flow rate grown at the constant V/III ratio of 781 for Set (IV), (V) and (VI). The Al content decreases as MO flow rate increases as the GaN incorporation rate into the film rises but the decomposition rate of GaN is not expected to change too much when growth temperature, pressure, TMGa/TMAI ratio and the V/III ratio are maintained. Additionally, noticeable differences between the two template types are observed. In all cases, the Ga incorporation is higher on samples prepared on  $\beta$  templates, which can be explained by a strain based composition pulling effect [33, 34]. This effect causes the gradual compositional to change in the epilayer due to any compressive strain caused by lattice mismatch between epilayer and the underlying template. In Section 5.3.2, it is shown that the relaxation value of samples grown on  $\beta$  templates is higher than that for samples grown on  $\alpha$  templates measured by  $(10\bar{1}5)$  XRD reciprocal space mapping (RSM).

Figure 5.6 (b), (c) and (d) show a comparison between the growth rates of the  $\text{Al}_x\text{Ga}_{1-x}\text{N}$ , AlN and GaN against the MO flow rate. It is clear to see that the growth rate of GaN decreases with increasing growth temperature due to higher decomposition rate of GaN, and results in increasing Al content, while the MO flow rate and V/III ratio are maintained.

However, The Al content can be increased via raising the MO flow rate at higher temperature. The growth rate of Al didn't change linearly with increasing MO flow rate at higher temperature maybe due to the pre-reaction of TMAI at gas phase.

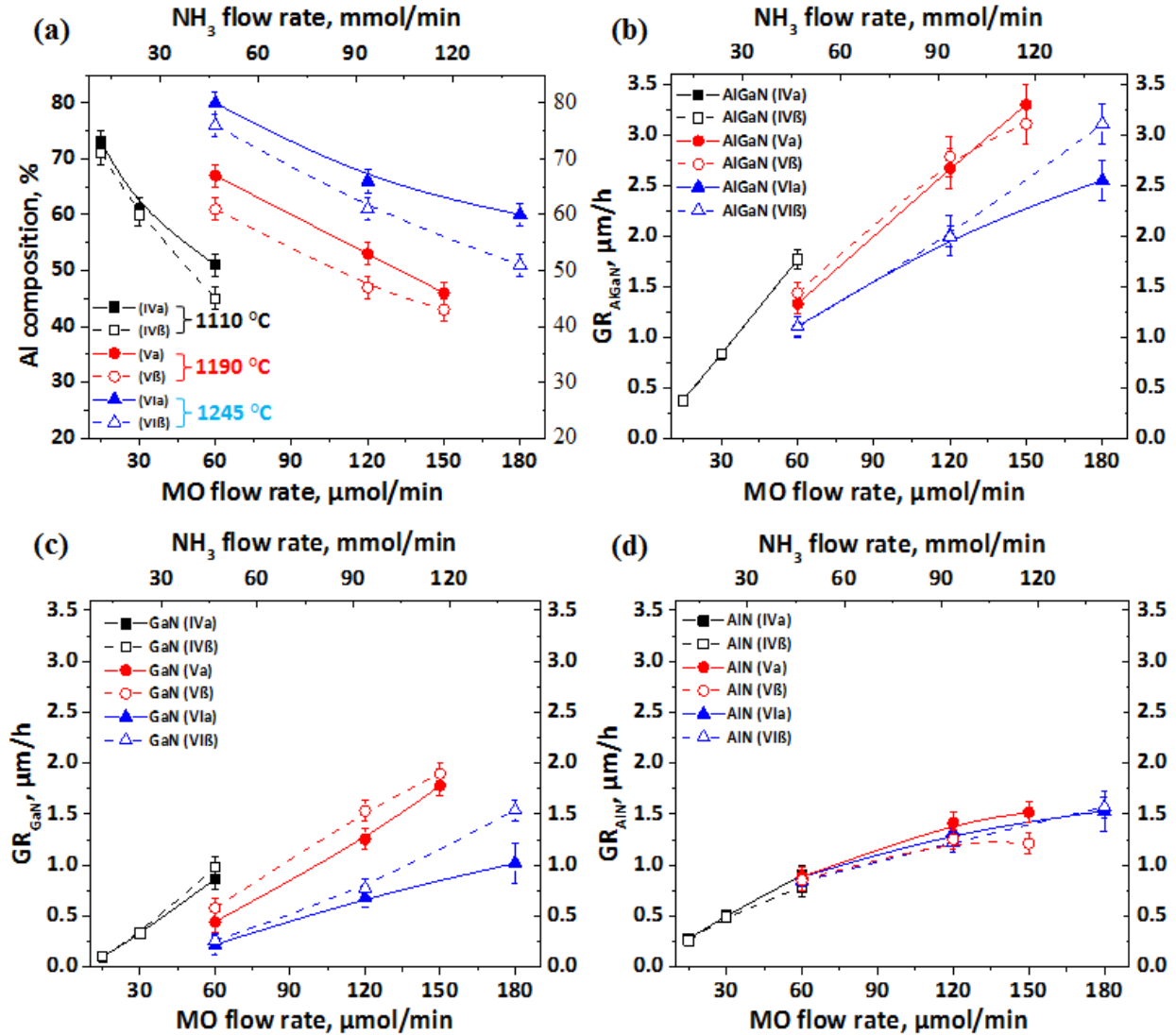


Figure 5.6: (a) Al composition, growth rates of (b)  $\text{Al}_x\text{Ga}_{1-x}\text{N}$ , (c) AlN and (d) GaN against the MO and  $\text{NH}_3$  flow rate for set (IV), (V) and (VI).

In summary, it is clear to see that the Al and Ga incorporation rate are different via changing growth condition and template. Using kinetic model of Xi et al [35], as expressed in Equation 5.3, it has be proposed to explain the bowing relationship between the Al content in solid phase and the group-III precursors molar flow rate ratio in gas phase within  $X_{\text{Al}}=0\text{-}100\%$  when keeping the total group-III flow rate constant by taking into account the molar growth rate at unit molar flow rate ratio between AlN and GaN ( $\gamma=G_{\text{AlN}}/G_{\text{Ga}}N$ ),

$$X_{\text{Al}} = \frac{G_{\text{AlN}} \times 2F_{\text{AlN}}}{G_{\text{AlN}} \times 2F_{\text{AlN}} + G_{\text{Ga}}N \times F_{\text{Ga}}N} = \frac{2\gamma F_{\text{AlN}}}{2\gamma F_{\text{AlN}} + F_{\text{Ga}}N} \quad (5.3)$$



Where  $F_{AlN}$  and  $F_{GaN}$  are molar flow rates of TMAI and TMGa precursors ( $\mu\text{mol}/\text{min}$ ),  $G_{AlN}$  and  $G_{GaN}$  are the growth rate at unit molar flow rate of TMAI and TMGa ( $\text{nm}/\mu\text{mol}$ ), respectively. Figure 5.7 shows a group of theoretical calculation curves with different  $\gamma$  plotted with our experimental results from Series (I), (II) and (III). Firstly, pre-reactions are a well-known problem and expected for Al and  $\text{NH}_3$  in the gas phase for MOVPE growth, since it is a spontaneous and strongly exothermic reaction. This depletes the source flow of the Al content, artificially increasing the Ga content within the alloy [31]. However, a  $\gamma$  factor greater than 1 (convex bowing) implies that no significant amount of Al is being lost to pre-reactions in our experimental Sets (I), (II) and (III) (Figure 5.7). Secondly, the effective incorporation of Ga is increased by increasing  $\text{NH}_3$  flow rate due to the suppression of GaN decomposition in set (I) [Figure 5.7 (a)]. Finally, when the total MO flow rate is fixed at  $30 \mu\text{mol}/\text{min}$  in sets (II) and (III), an increasing TMAI flow rate is equivalent to reduce TMGa proportionally ( $\text{TMGa}^\downarrow = \text{MO}_{\text{Total}} - \text{TMAI}^\uparrow$ ) and results in higher  $\text{NH}_3/\text{Ga}$  ratio. Therefore, an increasing of  $2\text{TMAI}/(2\text{TMAI}+\text{TMGa})$  ratio results in a lower  $\gamma$  value, this implies that effective Ga incorporation rate is also increased.

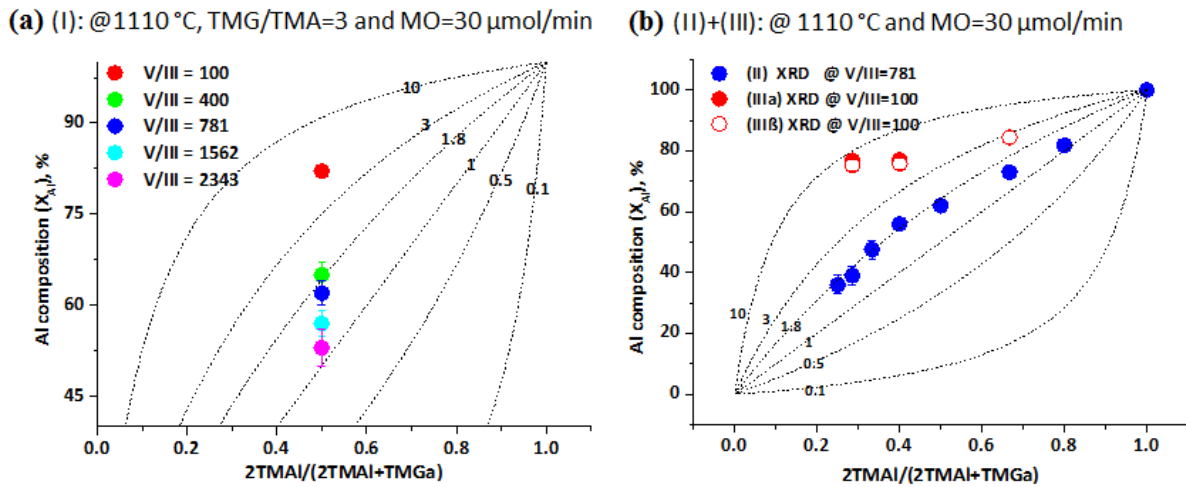


Figure 5.7: The relation of the Al composition of  $\text{Al}_x\text{Ga}_{1-x}\text{N}$  in solid phase and the ratios of  $2\text{TMAI}/(2\text{TMAI}+\text{TMGa})$  in gas phase with theoretical curves in dashed lines as given by equation (5.3), image (a) for series (I) and (b) for series (II) and (III).

Figure 5.8 shows a group of calculation curves with different  $\gamma$  factor and inserts experimental results of series (IV $\alpha$ ), (V $\alpha$ ) and (VI $\alpha$ ). It is clear to see that at high growth temperature Ga desorption is found to be an issue leading to high Al content films and high  $\gamma$  factor (inserted arrows indicate that the Al composition change as a function of growth temperature with same MO flow rate). In order to suppress this effect, increasing the MO flow rate can improve the incorporation efficiency of TMGa.

In summary, the  $\gamma$  factor depends on particularities of the process, specifically on V/III ratio, TMAI/TMGa ratio, precursor flow rate and growth temperature. These parameters influence two parts: pre-reaction rate of TMAI precursor and Ga desorption rate, which ultimately determines the net incorporation rate. Certain conditions, like high growth temperature (above 1110 °C), low V/III ratio (low  $\text{NH}_3$  flow rate) and strong compressive strain may lead to low Ga supersaturation and high Al supersaturation during AlGa<sub>x</sub>N growth.

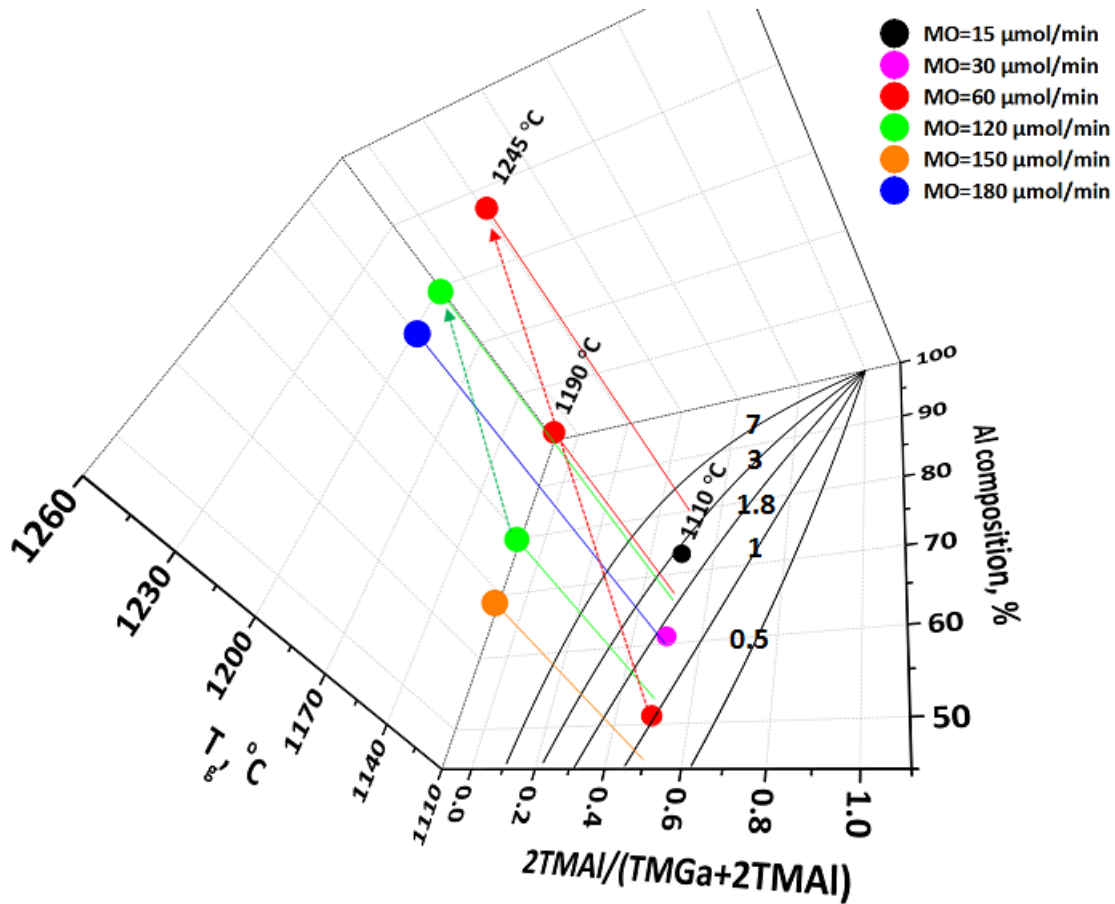


Figure 5.8: The relation of the Al composition of  $\text{Al}_x\text{Ga}_{1-x}\text{N}$  in solid phase against growth temperature and the ratios of  $2\text{TMAI}/(2\text{TMAI}+\text{TMGa})$  in gas phase with theoretical curves in straight lines with different  $\gamma$  value as given by equation (5.3) for series (IVa), (Va) and (VIa).

### 5.3.2 Structural Properties

#### XRD measurements

Figure 5.9 shows the FWHM values of XRD (0002) and (10 $\bar{1}1$ ) reflections of the AlGa $_x$ N epilayers against Al content for all series. The FWHM<sub>0002</sub> values of Al $_x$ Ga $_{1-x}$ N epilayers indicated that the crystal quality due to lattice tilt (dislocations with a screw component) degrades as the Ga content increases in all sample sets [Figure 5.9 (a)] as expected due to the increased lattice mismatch to the AlN templates. However, the Al $_x$ Ga $_{1-x}$ N FWHM<sub>10 $\bar{1}1$</sub>  values do not follow this trend, as shown in Figure 5.9 (b), suggesting that the higher density of edge dislocation is more invariant. Indeed for the highest Ga content layers grown on template  $\beta$  the FWHM<sub>10 $\bar{1}1$</sub>  reduces, suggesting some dislocation annihilation in this case. In this direct epitaxy method without any interlayer or short period superlattices, the material quality is highly dependent on the template quality and independent of the growth conditions.

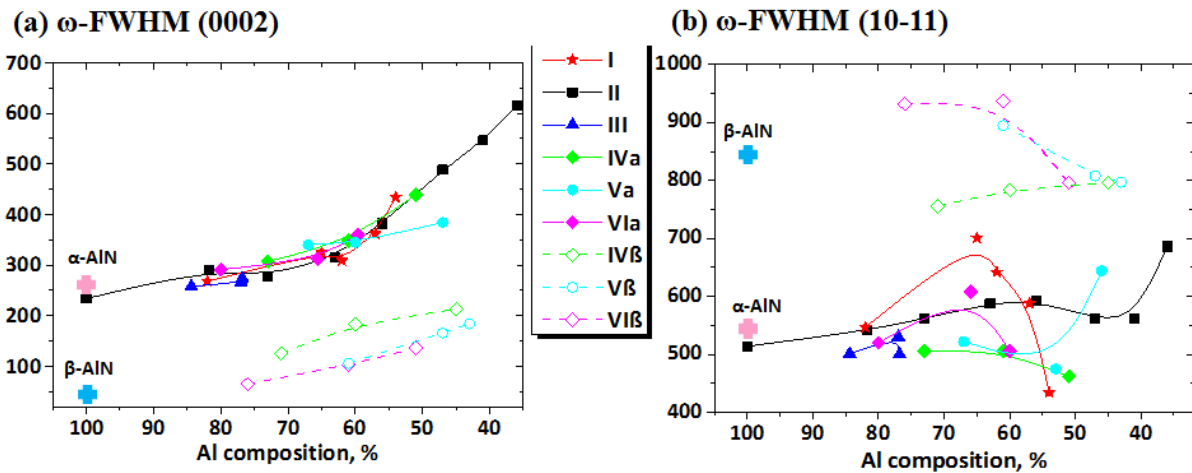
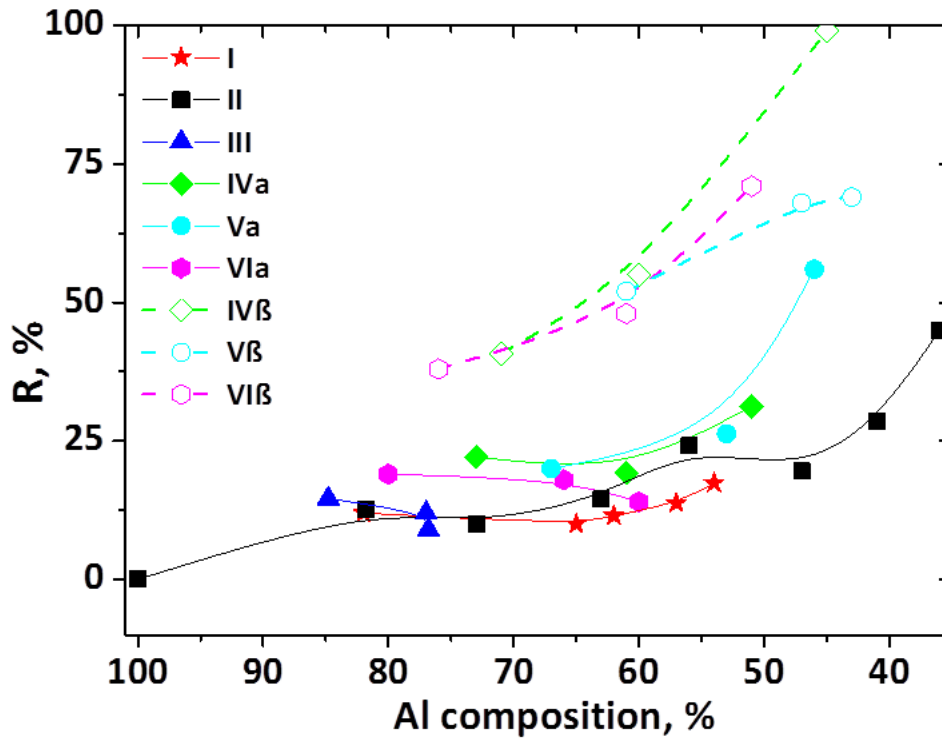


Figure 5.9: FWHM values of (a) (0002) and (b) (10 $\bar{1}1$ ) XRD rocking curves in all series of samples, the FWHM values of  $\alpha$  and  $\beta$  type template are also inserted in figures.

The primary source of strain affecting AlGa $_x$ N epilayer is the difference of in-plane ( $a$ ) and out-of plane ( $c$ ) lattice parameters that exists between the epilayer and template. The distances between the surface atoms of our AlN template to which the AlGa $_x$ N adatoms conform in binding to the surface induce compressive strain. This initial strain due to lattice mismatch in AlGa $_x$ N epilayers is modified by strain relaxation mechanisms, which results in non-coherent pseudomorphic growth after some critical thickness.

Figure 5.10 shows the Al $_x$ Ga $_{1-x}$ N epilayers relaxation as a function of the Al content for all series by XRD. It is found that strain relaxation value rises with increasing Ga content. The

strain relaxation value is consistently higher for epilayers grown on  $\beta$  template, maybe attributed to the high edge type dislocation density in  $\beta$  template.



**Figure 5.10:**  $\text{Al}_x\text{Ga}_{1-x}\text{N}$  relaxation as a function of the Al content for (a) Series (I) to (III) and (b) Series (IV) to (VI).

The RSMs of the  $10\bar{1}5$  reflections were carried out in order to visually contrast the lattice mismatch between AlN and  $\text{Al}_x\text{Ga}_{1-x}\text{N}$  peaks in one map. The  $(10\bar{1}5)$  RSMs of series (II)  $\text{Al}_x\text{Ga}_{1-x}\text{N}$  selected samples with various Al composition from  $x=1$  to  $x=0.36$  on the  $\alpha$  template grown at  $1110^\circ\text{C}$  are shown in Figure 5.11, where  $Q_x$  and  $Q_z$  indicate the directions parallel and perpendicular to the interface of template, respectively (rlu means the reciprocal lattice unit). The vertical and inclined lines represent the positions of a fully strained and fully relaxed layer grown on AlN template, respectively. The red line cross the centre of AlGa<sub>N</sub> ellipse starting from fully strained to relaxed line means that the position of AlGa<sub>N</sub> grown on AlN start from fully strained to fully relaxed.

It is observed that a broadening of  $\text{Al}_x\text{Ga}_{1-x}\text{N}$  peak is visible as the Al content decreasing by comparing the ellipses, which suggests that material quality degrades. Simultaneously, maximum position of the  $\text{Al}_x\text{Ga}_{1-x}\text{N}$  layers did not perpendicularly align to the AlN templates with respect to the different arrangement in their in-plane directions and moved closer to fully relaxed line. This indicates that  $\text{Al}_x\text{Ga}_{1-x}\text{N}$  layers grown on the AlN templates are not pseudomorphically grown and the mismatch strain is higher with lower Al contents.

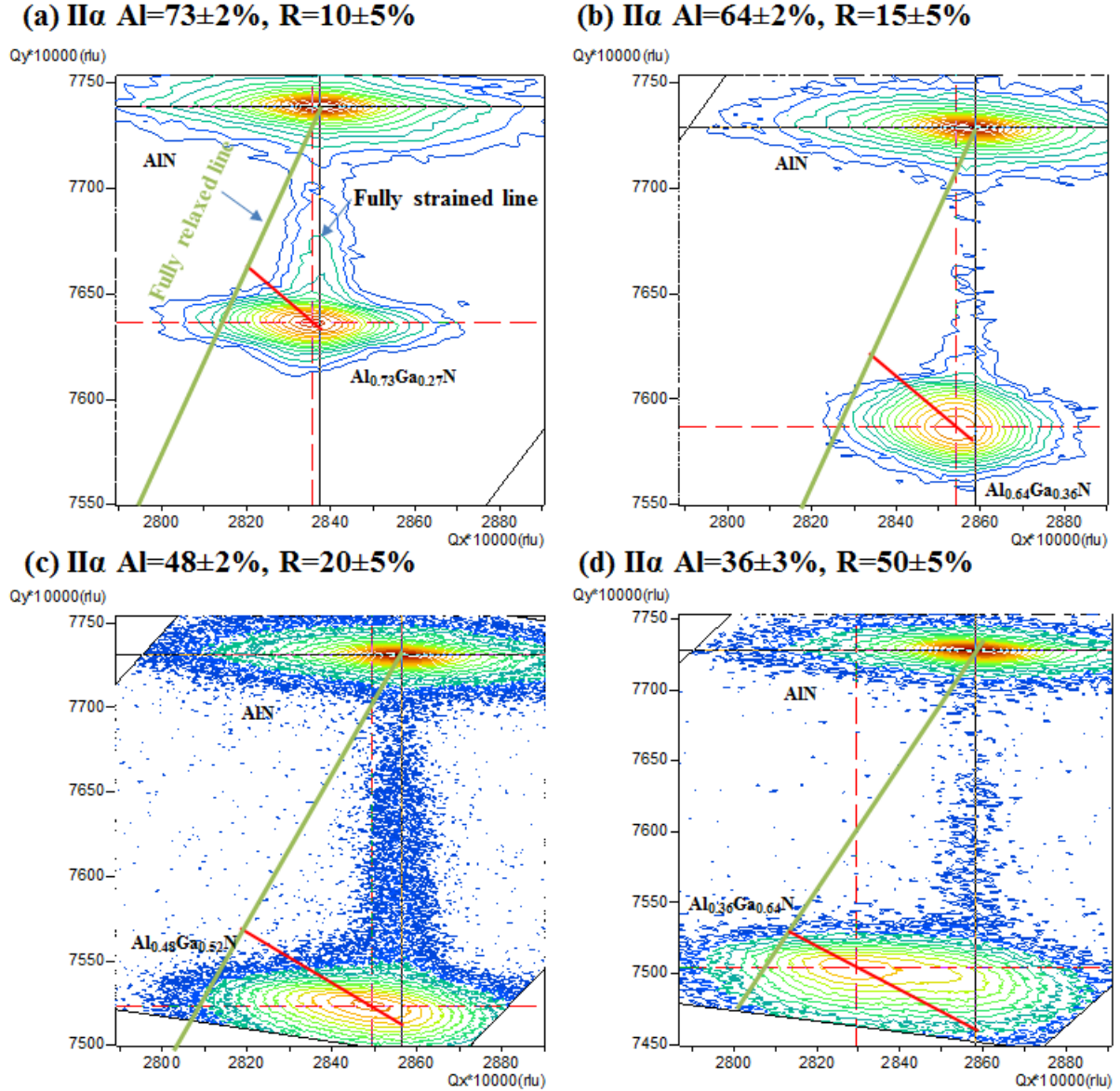


**Figure 5.11:** RSM of  $(10\bar{1}5)$  reflection of selected samples (a)  $\text{Al}=73\pm2\%$ , (b)  $\text{Al}=64\pm2\%$ , (c)  $\text{Al}=48\pm2\%$  and (d)  $\text{Al}=36\pm3\%$  grown on  $\alpha$  template from series (II). Green line is fully relaxed line, black line is fully strained line and red line corresponds to certain composition from fully strained to fully relaxed. Acronym R is relaxation value.

For investigations of the strain state of  $\text{Al}_x\text{Ga}_{1-x}\text{N}$  ( $x=0.61\pm0.02$ ) grown at different temperatures and on two different template types (Figure 5.12), asymmetric RSMs were created around the  $(10\bar{1}5)$  reflection. Firstly, comparing Figure 5.12 (a) and (b), (c) and (d), the peak position of AlGa $\text{N}$  grown on  $\beta$  template is closer to fully relaxed line than sample grown on  $\alpha$  template. This indicates that the AlGa $\text{N}$  layers grown on the  $\beta$  template are more relaxed. The major difference between  $\alpha$  and  $\beta$  template is dislocation density, which has been revealed in Chapter 4. This suggests that the high density of pure edge type dislocations can relieve much of the in-plane compressive strain during u-AlGa $\text{N}$  growth. Secondly, there

is a slight difference in strain state when the sample is grown at 1110 °C and 1245 °C on the same template, which may suggest that the layer relaxed more slowly at higher growth temperature with higher growth rate.

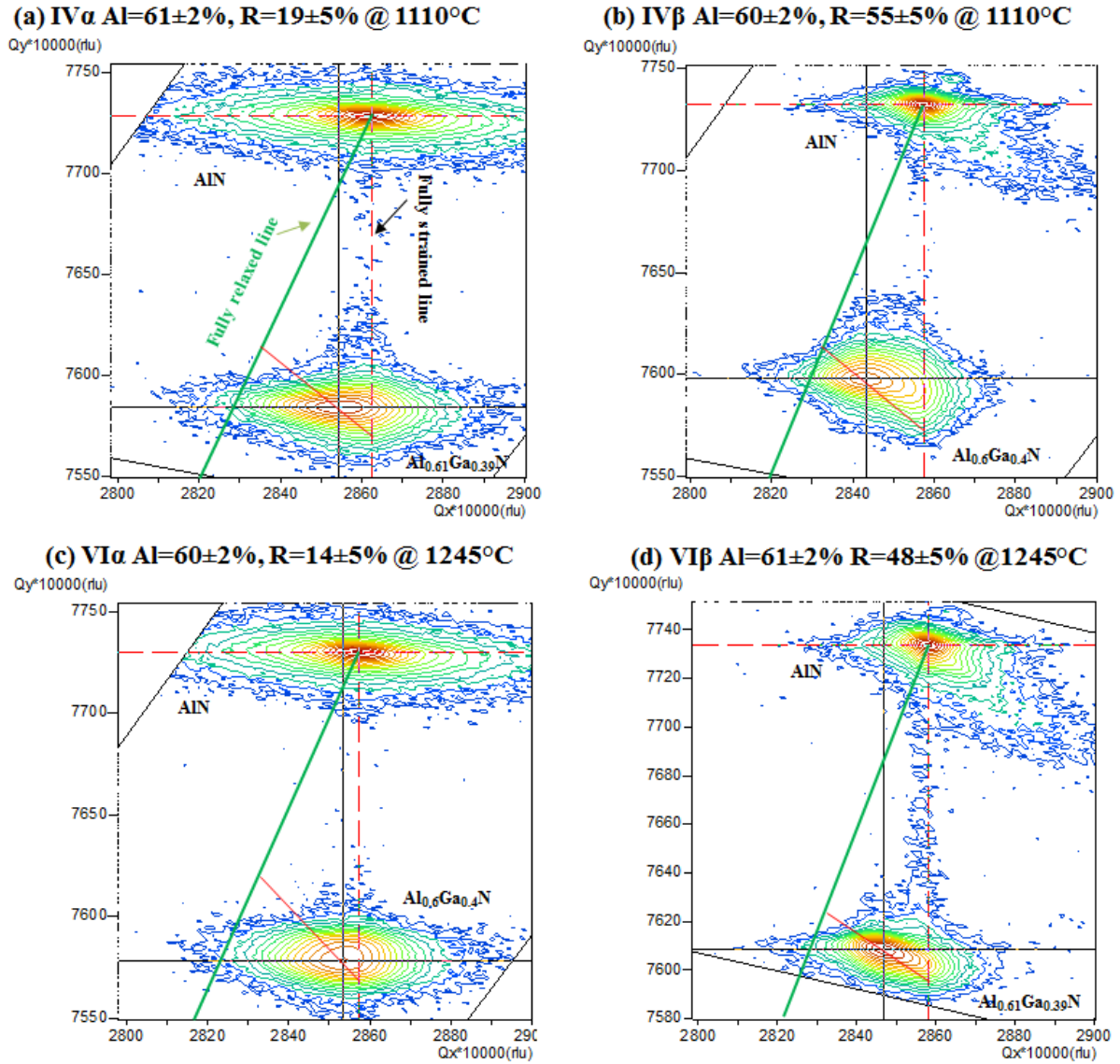


**Figure 5.12: Asymmetrical RSM of (10 $\bar{1}$ 5) reflection of selected samples with Al composition around 60% grown on  $\alpha$  and  $\beta$  template from series (IV) and (VI). Acronym R is relaxation value.**

## In-situ optical measurements

Relaxation measurement in XRD averages the strain across the entire AlGa<sub>0.4</sub>N epilayer due to deep penetration depth of X-rays, where the determined strain state is measured at post-growth stage. In-situ wafer curvature measurement has the benefit to determine the strain at a specific thickness of the growing sample at the growth temperature. If the surface strain state of AlGa<sub>0.4</sub>N epilayer doesn't change (no introduction of extrinsic and/or intrinsic strain) with increasing layer thickness, the wafer curvature value will stay constant. In practice, some



relaxation occurs by generation of dislocations and/or bending of existing dislocations for AlGa<sub>x</sub>N growth. This process relieved some fraction of the strain and therefore rate of change of wafer curvature can change as a result.

Figure 5.13 shows the wafer curvature measured during growth and cooling down to RT for selected samples in series (II), which was extracted by the Laytec in-situ curvature monitor system. The Al composition of selected samples is from 82±2% to 40±3%. It is noted that periodic oscillations in samples with 82±2% and 73±2% Al content arise from laser interference effects and are not due to epilayer stress.

During temperature ramp up the concave curvature increased rapidly, primarily in this case due to the different thermal expansion of sapphire substrate and the AlN epilayer on the template. The vertical temperature gradient effect on the template also led to a different thermal expansion of the upper and lower surfaces, respectively. Furthermore, the wafer edges can cool more effectively than the centre leading to differing expansion across the surface laterally.

During AlN connecting layer growth further tensile strain AlN increased the concave curvature value slightly more.

The Al<sub>x</sub>Ga<sub>1-x</sub>N epilayers grown on the AlN templates are under compressive stress due to the larger in-plane lattice parameter of Al<sub>x</sub>Ga<sub>1-x</sub>N, and therefore the wafer curvature value decreases and bows toward the original flat wafer condition and even convex values. As expected, all of the samples showed decreasing curvature as the AlGa<sub>x</sub>N epilayer thickness increased. The respective Al<sub>x</sub>Ga<sub>1-x</sub>N epilayers have inherently different degrees of compressive strain due to the Al composition, as evidenced by the larger slope corresponding to the lower Al content at the start of the Al<sub>x</sub>Ga<sub>1-x</sub>N growth step, attributed to the higher lattice mismatch with the AlN template. With further growth, the gradient of curvature was observed to decrease gradually, suggesting that the relaxation of compressive strain appeared during growth.

The in-situ measurements of emissivity-corrected temperature, 633 nm reflectance and in-situ curvature data as a function of time for selected AlGa<sub>x</sub>N growth runs of series (IV) and (VI), are shown in Figure 5.14. Note that the VIα Al=60±2% and VIβ Al=61±2% are not from same growth run, but they have similar Al content. In the reflectance measurement at 633 nm, the reflectance intensity-maxima and minima of AlGa<sub>x</sub>N grown on both templates approached the constant value with increasing layer thickness, and their curves were almost horizontally

aligned in Figure 5.14 (c) and (d). This suggested that epilayer thickness fluctuations were only on a nanometre scale. The RMS surface roughness of these samples was less than 5 nm, as measured by  $20 \times 20 \mu\text{m}^2$  AFM scans as shown in Section 5.3.3.

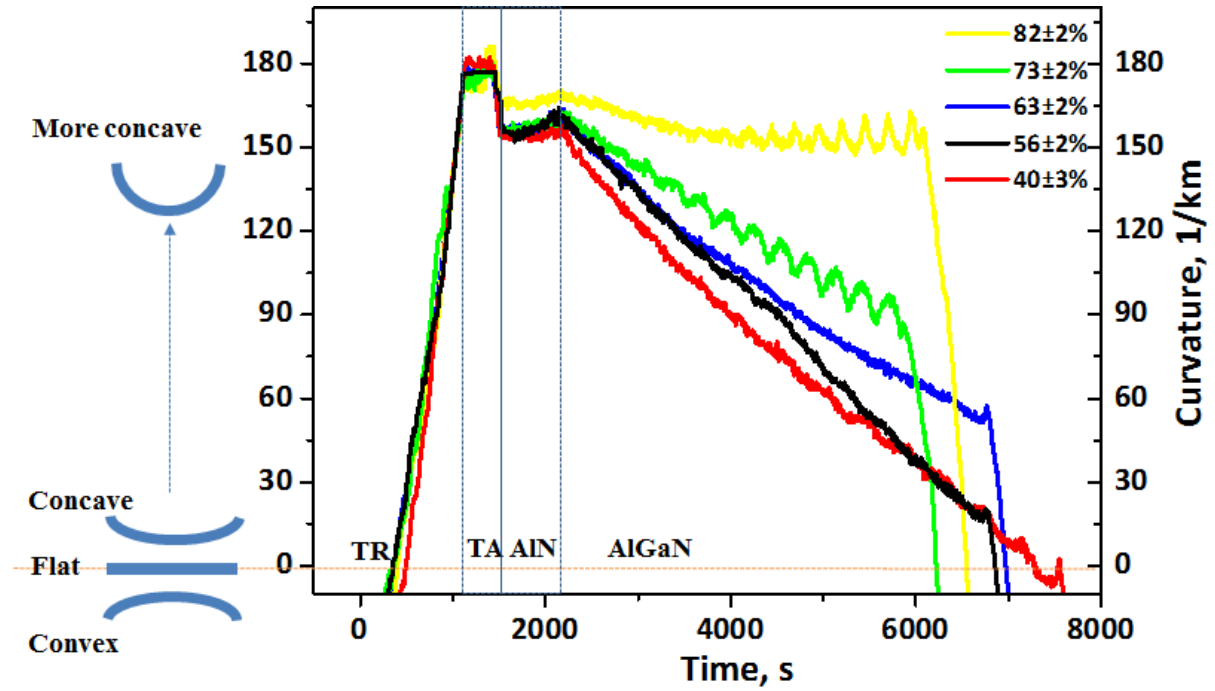


**Figure 5.13:** wafer curvature measurements during growth for selected samples in series (II). Growth sequence included temperature ramp up (TR), thermal annealing (TA), AlN connecting layer and AlGaIn overgrowth.

The in-situ measurements of emissivity-corrected temperature, 633 nm reflectance and in-situ curvature data as a function of time for selected AlGaIn growth runs of series (IV) and (VI), are shown in Figure 5.14. Note that the VI $\alpha$  Al=60 $\pm$ 2% and VI $\beta$  Al=61 $\pm$ 2% are not from same growth run, but they have similar Al content. In the reflectance measurement at 633 nm, the reflectance intensity-maxima and minima of AlGaIn grown on both templates approached the constant value with increasing layer thickness, and their curves were almost horizontally aligned in Figure 5.14 (c) and (d). This suggested that epilayer thickness fluctuations were only on a nanometre scale. The RMS surface roughness of these samples was less than 5 nm, as measured by  $20 \times 20 \mu\text{m}^2$  AFM scans as shown in Section 5.3.3.

Distinct differences were apparent from the in-situ wafer curvature measurements for samples grown on  $\alpha$  and  $\beta$  template as shown in Figure 5.14 (e) and (f). The curvature value continually decreased with increasing layer thickness for AlGaIn grown on  $\alpha$  template, but the curvature value approached constant for AlGaIn grown on  $\beta$  template. As mentioned in asymmetric (10 $\bar{1}$ 5) RSM XRD measurements, the relaxation value of these AlGaIn grown on  $\alpha$  and  $\beta$  template is around 15 and 50 %, respectively. These results indicated that most of



strain has been relieved initially by dislocations, and less relaxation then took place as further growth for sample grown on  $\beta$  template. The reason for that could be a high density of pure edge type dislocation in  $\beta$  template.

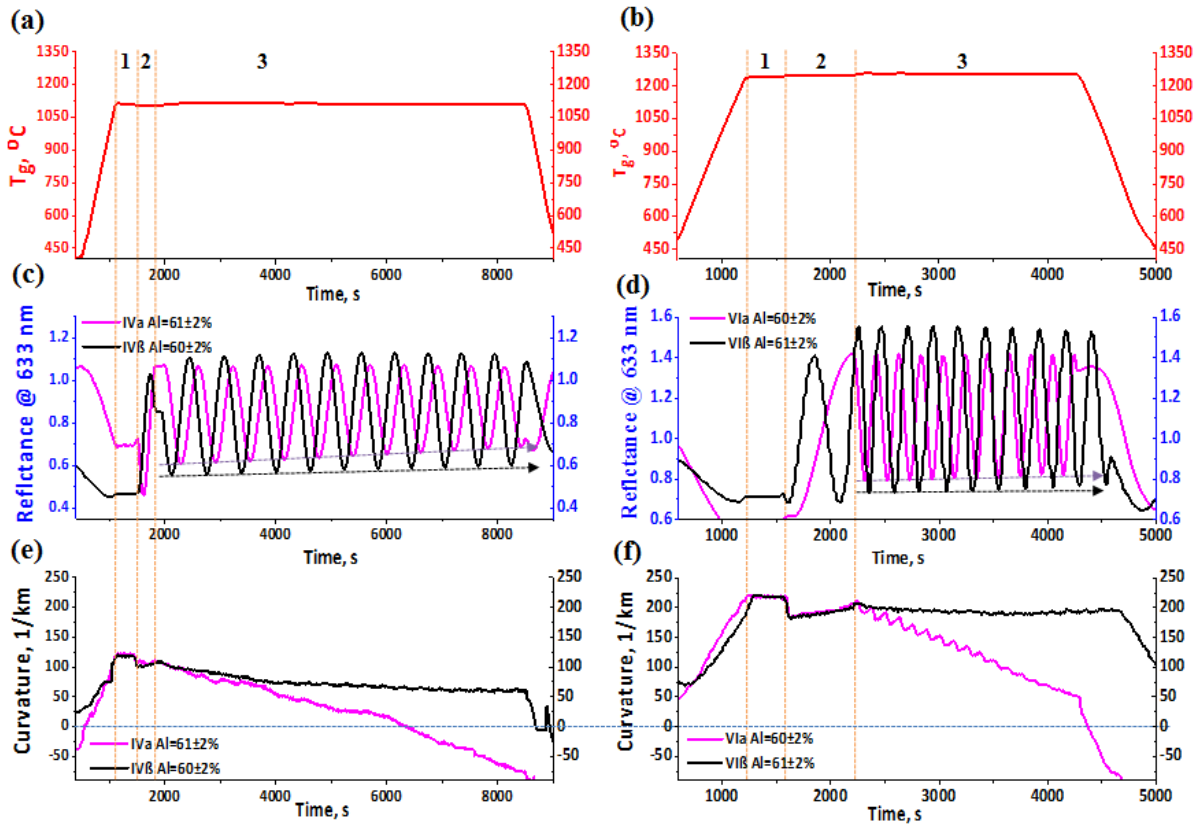


**Figure 5.14** In-situ LayTec measured (a) & (b) growth temperature, (c) & (d) reflectance at 633 nm and (e) & (f) wafer curvature during AlGaIn for series (IV) and (VI), respectively. Steps “1”, “2” and “3” denote thermal annealing, AlN connecting layer growth and AlGaIn overgrowth, respectively. The reflectance of gradient is marked by arrows.

The strain relaxation in the growth of AlGaIn on AlN has been discussed by many groups [36, 37, 38, 39, 40, 41, 42]. The relaxation of in-plane compressive strain has been reported to correlate with point defect (group-III vacancies) concentration, misfit dislocations (MDs) and the inclination of pure edge type threading dislocations (TDs). Several contrasting models have been proposed to describe the relaxation process, involving bulk-energy balancing [36, 37], surface-mediated climb [38, 39, 40] and “pinning” of dislocation [41, 42]. More details about strain relaxation will be discussed in Section 6.3.1.

In summary, despite many arguments in the strain relaxation model, it is generally accepted that the strain relaxation process occurs by defects (point defects and dislocations). Ideally, strain engineering and prevention of relaxation is important for obtaining AlGaIn layers with a similar dislocation density as the underlying AlN template.

### 5.3.3 Control of the surface morphology

Root-mean squared (RMS) surface roughness of undoped  $\text{Al}_x\text{Ga}_{1-x}\text{N}$  was estimated by multiple  $20 \times 20 \mu\text{m}^2$  AFM scans for series (I), (II) and (III) as shown in Figure 5.15 (a). It is observed that the surface RMS roughness is higher with an increasing Ga content. Figure 5.15 (b) and (c) reveal that the morphology on the micrometre scale drastically worsens with decreasing Al content.

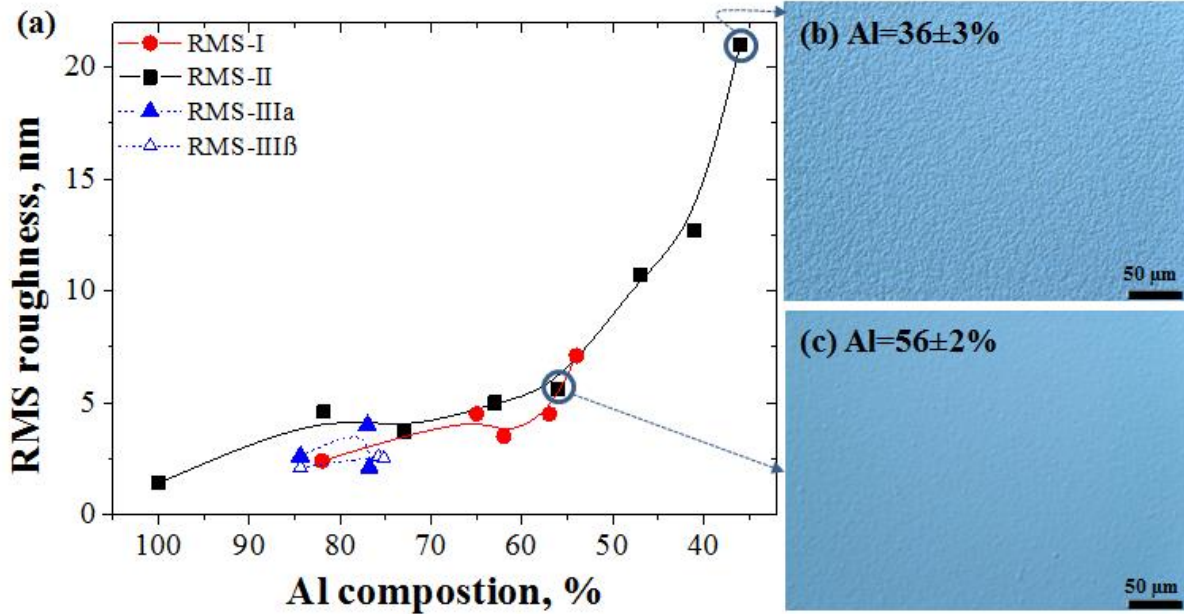


**Figure 5.15:** (a) the RMS roughness of the  $\text{Al}_x\text{Ga}_{1-x}\text{N}$  epilayers as a function of Al composition for series I, II and III. (b) and (c) Nomarski optical microscope images of selected samples from series II.

The  $\text{Al}_x\text{Ga}_{1-x}\text{N}$  with a various Al composition obviously exhibits a morphology evolution in series (II) from AFM scans [Figure 5.16 (a-h)]. Generally, the AlN template is grown under a low V/III ratio ( $\leq 100$ ) condition as shown in Chapter 4, which leads to a smooth step-flow mode surface morphology with pinned steps and an RMS roughness of around 0.4 nm. These pinned steps are associated with the screw-type threading dislocations causing surface displacements normal to the surface as shown in Figure 4.28 (b). With a high V/III ratio ( $\geq 781$ ), the effective Al adatom diffusion length becomes shorter, which leads to spiral hillock growth around screw-type dislocation as shown in Figure 5.16 (a). The dislocation line is normal to the surface. A high density of Al(Ga)N spiral hillocks became less when Al composition decreases from 100% to 60 % [Figure 5.16 (a-d) and (i-l)]. Surface bunched steps appeared and turned into flat topped islands when Al composition continually decreased from 56 to 37% as shown in Figure 5.16 [Figure 5.16 (e-h) and (m-p)].

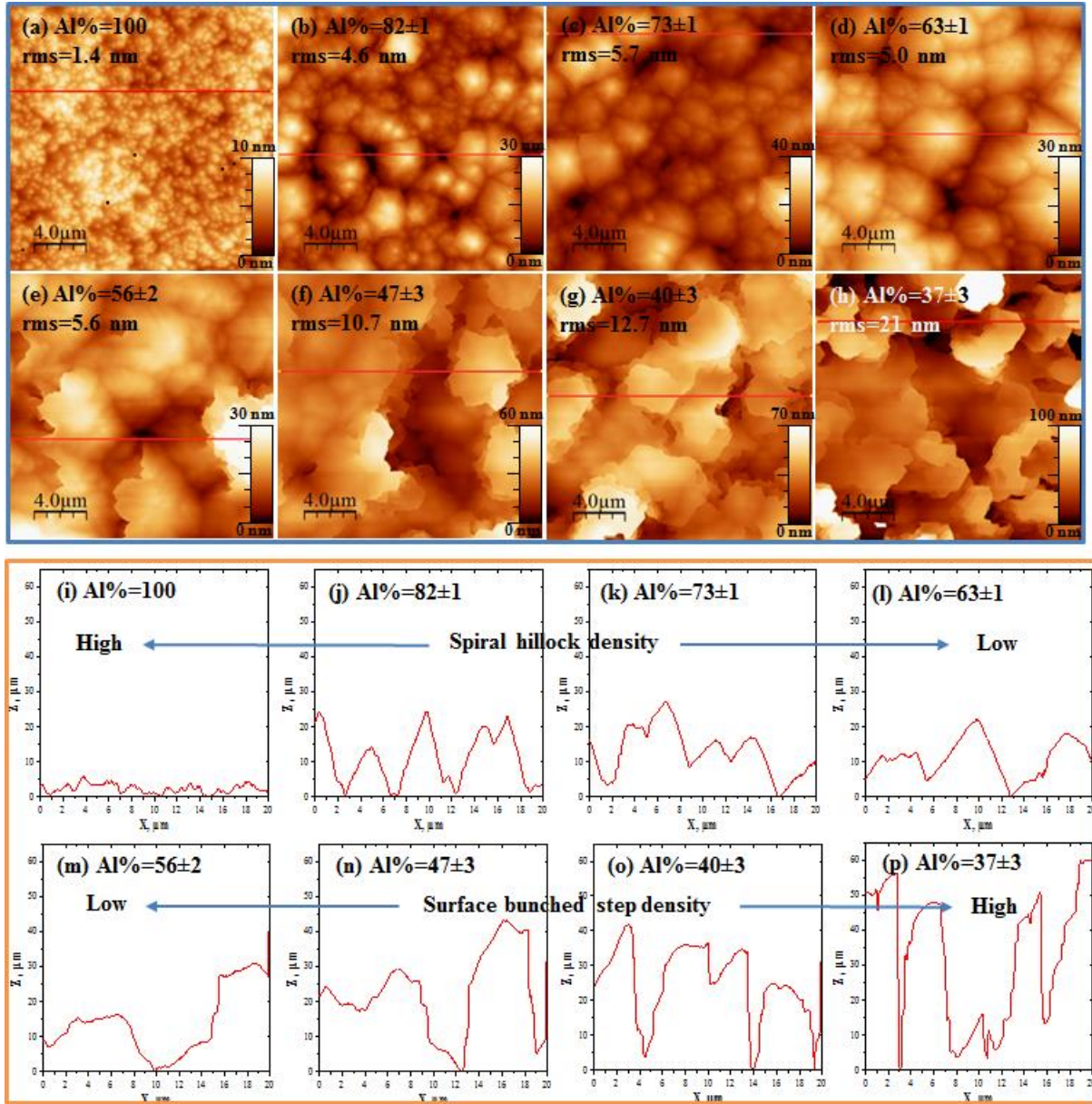


**Figure 5.16:** (a)  $20 \times 20 \mu\text{m}^2$  AFM images of  $\text{Al}_x\text{Ga}_{1-x}\text{N}$  from series II. (b) Extracted line scans from locally plane fitted AFM scans of series II [corresponding to red line in (a)].

In order to investigate the uniformity of Al and Ga distribution on the large scale surface morphology and probe the luminescence properties of the AlGaN epilayer, the combination of SE and CL hyperspectral imaging were conducted. The SE images of  $\text{Al}_x\text{Ga}_{1-x}\text{N}$  ( $x=0.56 \pm 0.02$  and  $=0.40 \pm 0.03$ ) in Figure 5.17 (a) and 5.18 (a) reflect the topography in the corresponding AFM measurement in Figure 5.16(a). Figure 5.17 (b&d) and (c&e) show the  $10 \times 10 \mu\text{m}^2$  maps of the fitted CL peak energy and intensity, respectively, of the  $\text{Al}_{0.56}\text{Ga}_{0.44}\text{N}$  near band edge (NBE) peak, which were acquired from the centre of the SE image in Figure 5.17 (a). The energy map in Figure 5.17 (b) shows planar regions with a peak centred on  $4.60 \pm 0.02$  eV. The intensity of the  $4.60 \pm 0.02$  eV peak is mostly constant over the measured



planar area, while there is a large drop in intensity along the step edges seen in the Figure 5.17 (c). The  $4.34 \pm 0.04$  eV luminescence [Figure 5.17 (d)] is highly localized and only occurs along the step edges with a 20 times lower intensity than the intensity of planar regions. This indicates that along step edges the growth conditions of AlGaN are different than on the otherwise smooth sample surface. In addition, the average height of bunched step edges is around  $15 \pm 5$  nm, the vertical range of the  $\text{Al}_{0.56}\text{Ga}_{0.44}\text{N}$  surface is shown in Figure 5.16 (m).

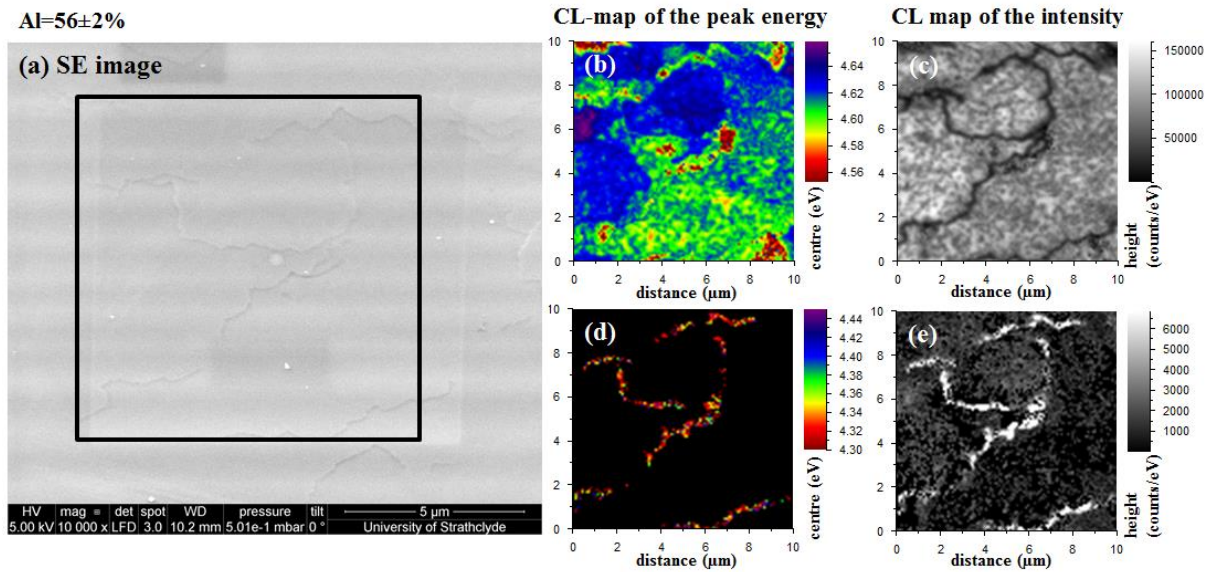


**Figure 5.17:** SE image (a) and fitted  $10 \times 10 \mu\text{m}^2$  CL-maps of the peak energy [(b) and (d)] and intensity [(c) and (e)] of  $\text{Al}_{0.56}\text{Ga}_{0.44}\text{N}$  from Series II.

The plan-view SE image [Figure 5.18 (a)] illustrates a very rough surface as expected due to large relaxation from XRD data, which has the Al content of  $40 \pm 3\%$ . Hyperspectral CL imaging of a  $10 \times 10 \mu\text{m}^2$  area in the centre of the SE images reveals two NBE AlGaN peaks at  $4.34 \pm 0.02$  eV for planar regions [Figure 5.18 (b)] and  $4.15 \pm 0.05$  eV for step edges [Figure 5.18 (d)]. The emission intensity is nearly same for planar regions [Figure 5.18 (c)] and step edges [Figure 5.18 (e)], which suggests large lateral compositional variation, and also identify the origin of the PL shoulder in the corresponding RT-PL measurement in Figure 5.5 (a). Its average height of step edges is approximately  $35 \pm 5$  nm, the vertical range of the  $\text{Al}_{0.4}\text{Ga}_{0.6}\text{N}$  surface is shown in Figure 5.16 (o).

In both cases the CL shows a red shift in emission energy (longer emission wavelength) on the step edges, which has been also observed by others [43, 44, 45, 46, 47]. These variations in the emission energy could be caused by the combination of two effects based on strain relaxation and the difference of mobility of the Ga and Al adatoms.

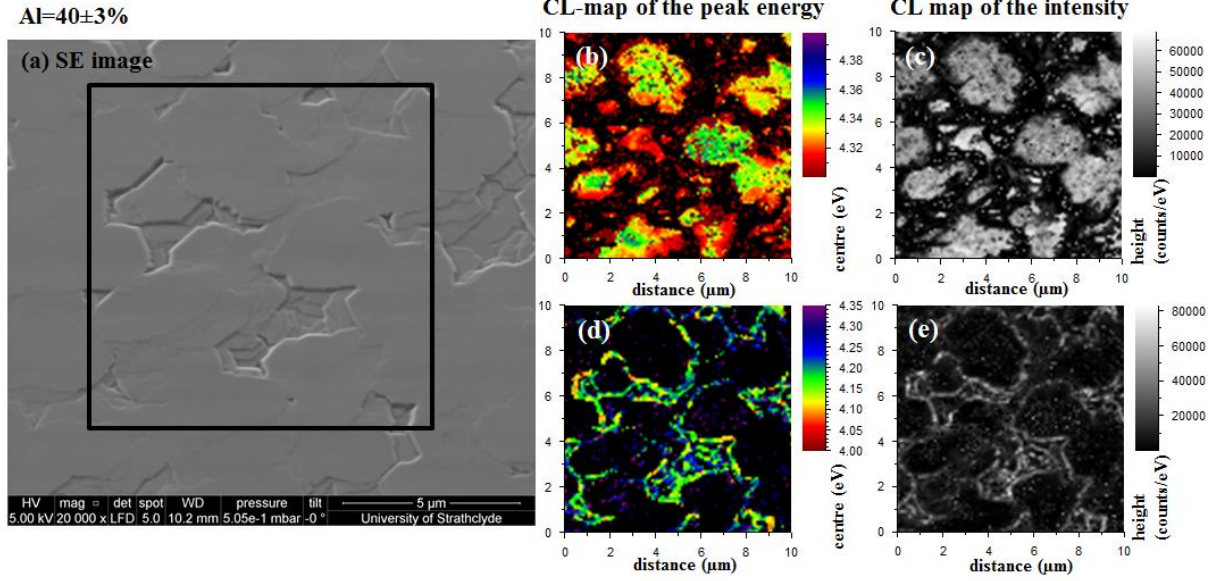


**Figure 5.18:** SE image (a) and fitted  $10 \times 10 \mu\text{m}^2$  CL-maps of the peak energy [(b) and (d)] and intensity [(c) and (e)] of  $\text{Al}_{0.4}\text{Ga}_{0.6}\text{N}$  from Series II.

As mentioned in the previous Section 5.3.1, I observed a strain based composition pulling effect, which leads to compositional variation in the epitaxial layer due to compressive biaxial strain. This can also occur locally on the surface, as well as on the macroscopic scale. Chang et al. [43] and A. Knauer et al. [44] both observed that the region around the inclined threading dislocations in the AlGaIn epilayer had lower Al content. They also found that the bunched steps terminated at the AlGaIn surface were associated with the inclined arrays of threading dislocations, which could provide strain relaxation on the step edges. The Ga atoms have the tendency to segregate to these relaxed areas, which leads to a higher Ga incorporation.

On the other hand, as described in the Section 4.4.3.3, the step bunching feature in AlN growth is caused by the presence of a negative step Ehrlich-Schwoebel barrier (SESB) on the step edges and long enough diffusion length of Al adatoms. In low Al content  $\text{Al}_x\text{Ga}_{1-x}\text{N}$  ( $x < 0.5$ ) growth, Ga adatoms are the dominating diffusing species in the AlGaIn surface formation. The negative SESB increases the adatom downhill diffusion which can result in the formation of a Ga-rich cluster at upper step edge with the subsequent formation of a new side facet. Meanwhile, the higher diffusion length of Ga adatoms has been reported to lead to enhanced Ga incorporation on these new side facets while Al adatoms are incorporated more randomly on the planar terraces [45, 47]. Eventually, the different incorporation rates of Al and Ga on the step edges and flat area result in rough surface and significant compositional inhomogeneity.

A rough surface can lead to poor epilayer quality and ultimately affects the device performance. A large density of bunched steps can cause variations in surface height that may lead to a non-uniform quantum well thickness and the spiral structure may lead to fluctuations in the composition of III-nitride alloys and dopant concentration. Beside the low Al content ( $\leq 50\%$ ) region, it is necessary to control surface roughness while growing epilayers at a desired range of thicknesses with high Al content ( $\geq 50\%$ ) for near and deep UV  $\text{Al}_x\text{Ga}_{1-x}\text{N}$ -based devices. Figure 5.19 (a) shows the surface RMS roughness by averaging multiple  $20 \times 20 \mu\text{m}^2$  AFM scans each sample of Series (IV), (V) and (VI). Hexagonal pyramid defects can be observed in Nomarski microscope [Figure 5.19 (b) and (c)], which may be associated with the existing v-pit defects on the underlying AlN templates [47]. Meanwhile, the surface morphology is getting smoother as increases the growth temperature from 1110 to 1245 °C [Figure 5.19 (b)-(f)].

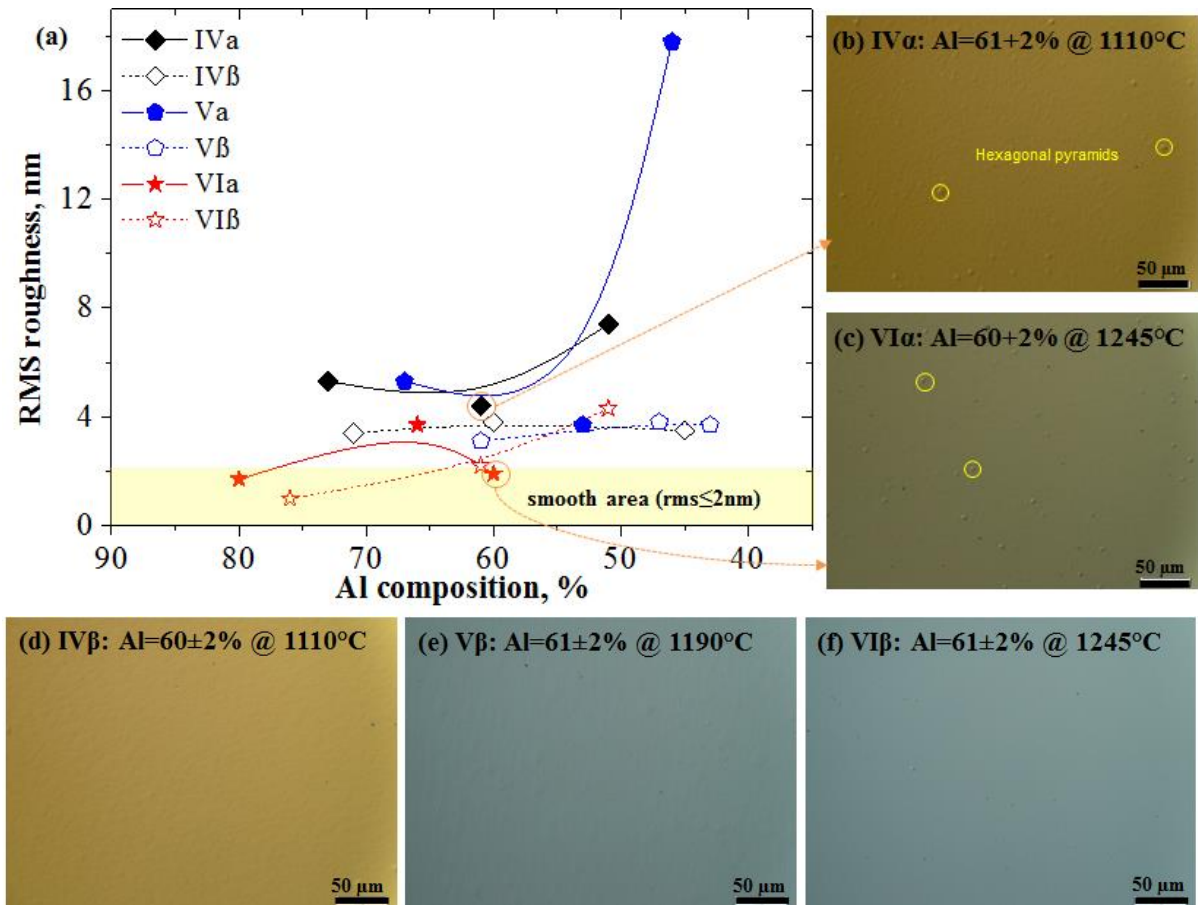


**Figure 5.19:** (a) the RMS roughness of the  $\text{Al}_x\text{Ga}_{1-x}\text{N}$  epilayers as a function of Al composition for series (IV), (V) and (VI). (b)-(f) Nomarski optical microscope images of selected samples from series (IVa), (VIa), (IVβ), (Vβ) and (VIβ) when Al composition is around 60% against growth temperature.



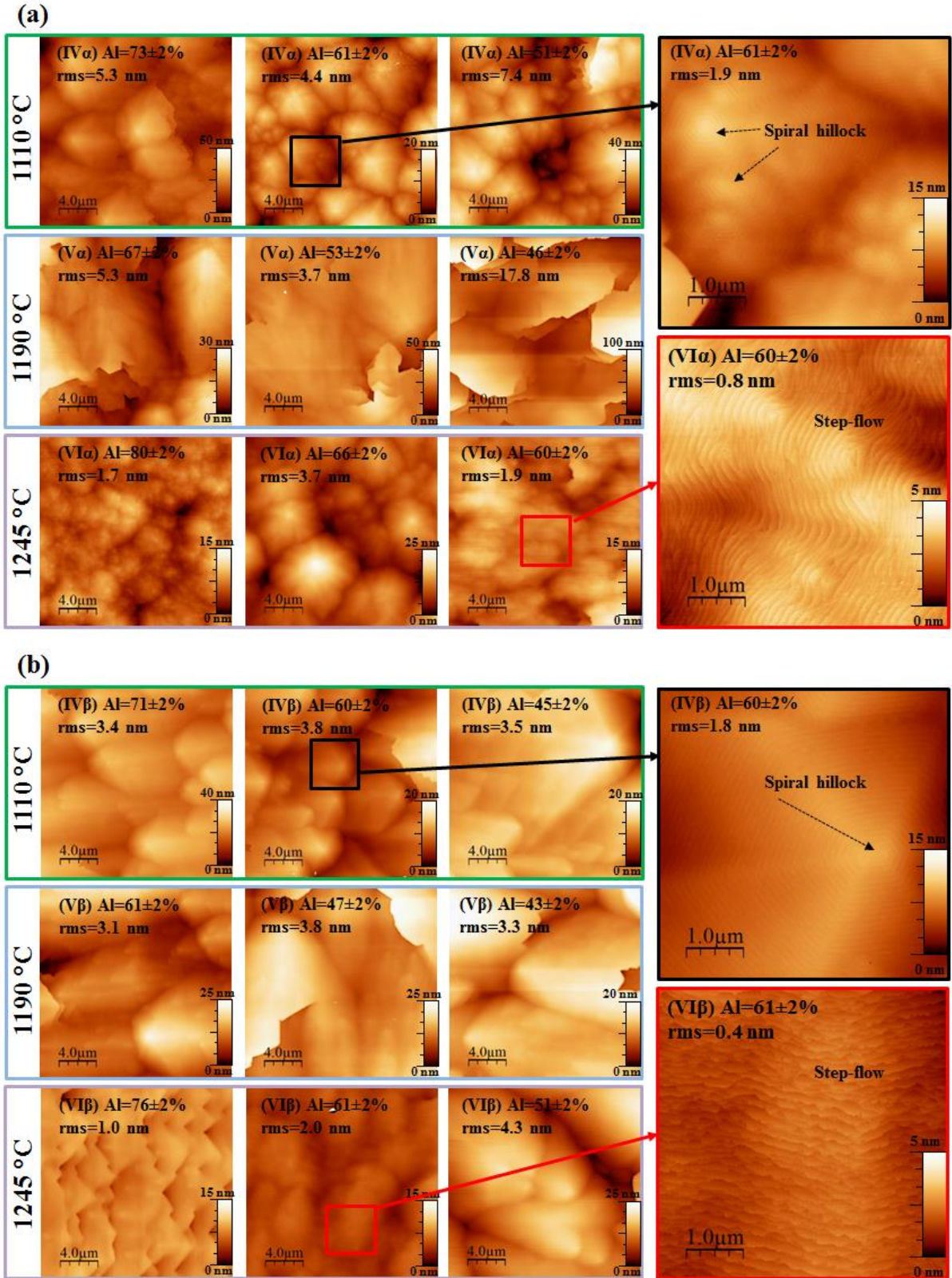
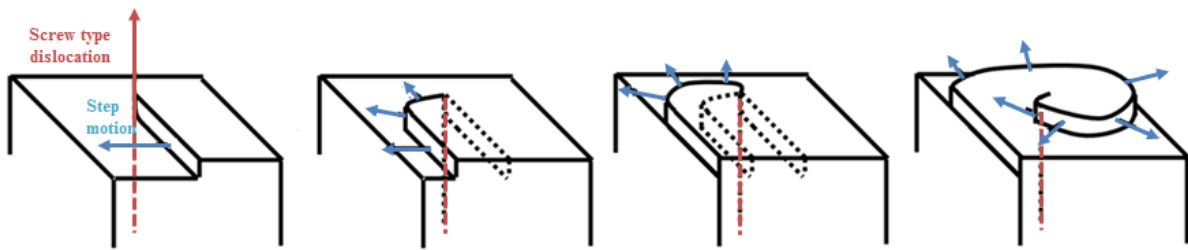


Figure 5.20: 20 × 20 μm<sup>2</sup> AFM images of Al<sub>x</sub>Ga<sub>1-x</sub>N for series IV, V and VI grown on (a) α template and (b) β template (Right). (Left) 5 × 5 μm<sup>2</sup> AFM images of Al<sub>x</sub>Ga<sub>1-x</sub>N for selected samples.

Figure 5.20 shows AFM images of the Al<sub>x</sub>Ga<sub>1-x</sub>N epilayers growth at different temperature (1110 to 1245 °C) with a various MO flow rate (15 to 180 μmol/min) for series (IV), (V) and

(VI). It is clear to see that hexagonal spiral hillocks originating from screw dislocations dominate the surface morphology at 1110 °C grown on both templates. These hexagonal pyramids are 6-sided polygons with same orientations. As the growth temperature increasing to 1245 °C, the step-flow mode is visible when Al composition is around 60% on both templates. These results indicate a change of the surface diffusion of the adatoms, which can lead to a change in the growth mode.

In the classical BCF theory of surface growth, atoms are first adsorbed to the crystal surface (“adatoms”) and then diffuse along the surface until they are either incorporated into the crystal a step or desorb from the surface [48]. The origins of steps are from screw type dislocations and the misorientation of the substrate. These screw component dislocations on a crystal surface continually extrude steps. In certain growth conditions, the continuous growth of a pinned step can result in a spiral hillock as shown in Figure 5.21.



**Figure 5.21: Schematic surface evolution of growth spirals at the intersection of a screw dislocation.**

Figure 5.22 shows AFM images of spiral hillocks which have a dislocation core at centre and atomic steps originating from the dislocation core cover the entire surface. It is also clear to see that a growth spiral exhibits a double-spiral (a pair of growth spirals starting from a dislocation core) structure, attributed to the component of the Burger vector of pure screw type dislocation along the c-axis.

As described in Chapter 4, high growth temperature promoted surface diffusion length of Al adatoms. With increasing growth temperature, hexagonal hillock dominant surface turned to be step-flow mode surface as shown in Figure 5.23. This suggests that a transition between 2D and 3D growth mode is dominated by Al adatoms for high Al content  $\text{Al}_x\text{Ga}_{1-x}\text{N}$  growth ( $x > 0.5$ ). Therefore, a step-flow mode surface feature can be obtained under optimal high growth temperature.



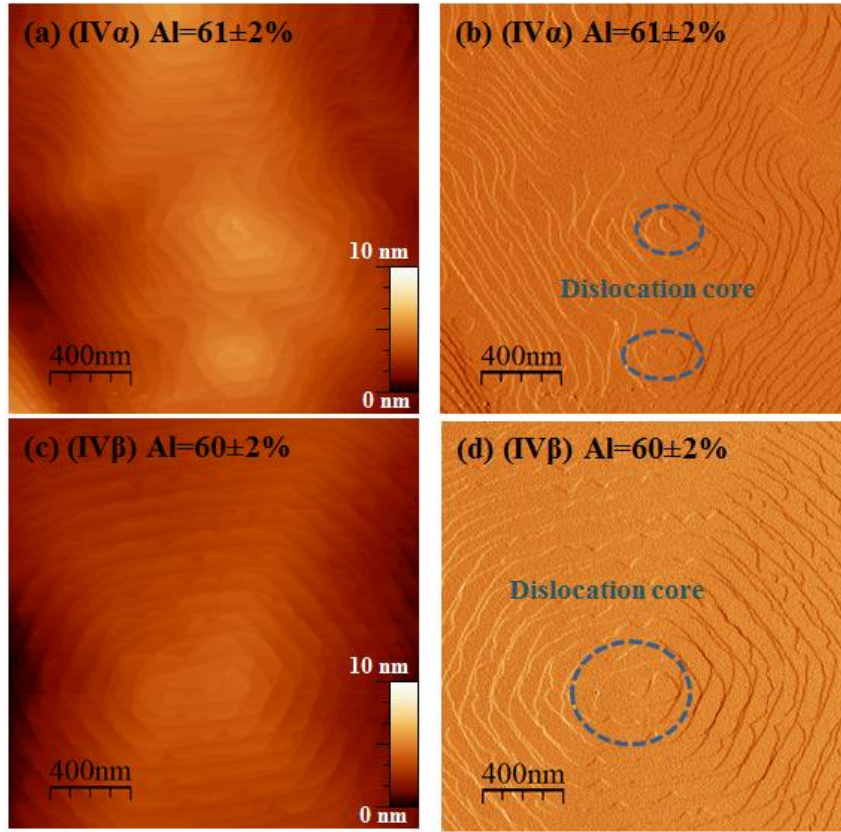


Figure 5.22: 2×2 μm<sup>2</sup>AFM images [(a) and (b)] and signal amplitudes [(c) and (d)] of samples from series IVα and IVβ, respectively.

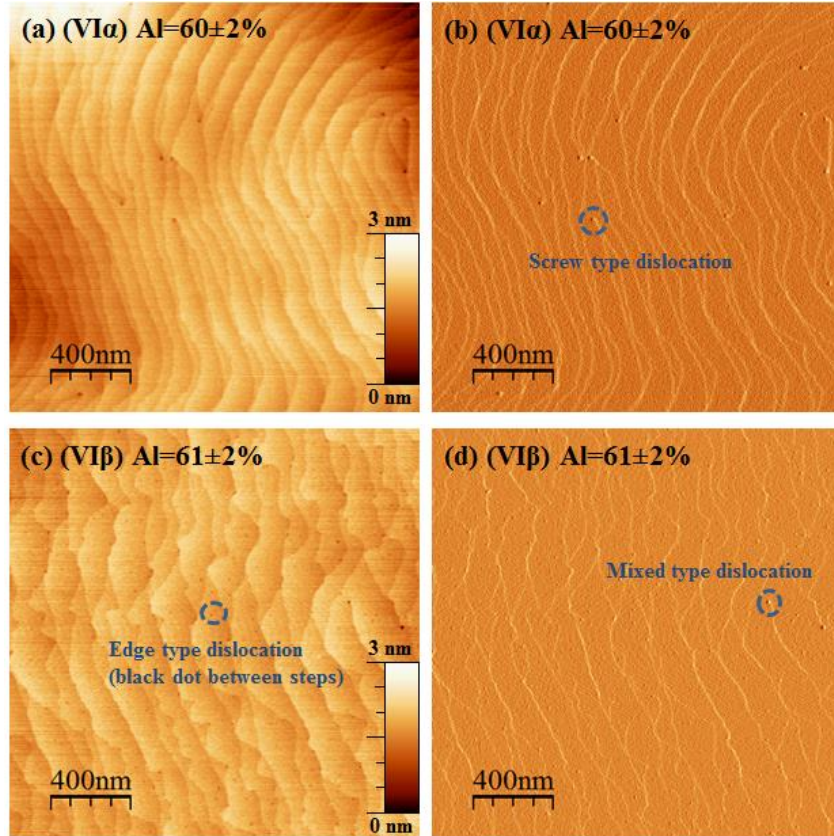


Figure 5.23: 2×2 μm<sup>2</sup>AFM images [(a) and (b)] and signal amplitudes [(c) and (d)] of samples from series VIα and VIβ, respectively.

## 5.4 Summary

In this chapter, the control of Al content in  $\text{Al}_x\text{Ga}_{1-x}\text{N}$  by varying growth condition has been demonstrated and discussed. Optimal growth parameters can be chosen to avoid or at least minimise the effect of gas phase processes that could further influence the ratio of Al and Ga incorporation. At low V/III ratio and high growth temperature, Ga desorption was found to be an issue leading to high Al content films. This effect can be suppressed by increasing  $\text{NH}_3$  and the MO flow rate.

For the direct epitaxial method without interlayers or superlattice buffer layers, it is observed that the crystal quality is highly depending on the template quality and independent in the range of our growth conditions. The  $\text{FWHM}_{0002}$  values of  $\text{Al}_x\text{Ga}_{1-x}\text{N}$  epilayers also indicated that the crystal quality degrades as the Ga content increases in all sample sets, as expected due to the increased lattice mismatch to the AlN templates.

It is found that strain relaxation value arises with increasing Ga content. The strain relaxation value is consistently higher for epilayers grown on the  $\beta$  template, attributed to the high pure edge type and mixed type threading dislocation density in the  $\beta$  template. The increased relaxation in the material grown on  $\beta$  template is also clear from a reduced buildup in compressive strain in the epitaxial layers, as measured using a LayTec in-situ curvature monitoring tool.

A red shift has been observed on the bunched step edges by the plan-view CL data. This phenomenon is attributed to the strain relaxation and the different surface mobility of Ga and Al adatoms, which lead to a different incorporation rate of Ga and Al in the planar region and step edges. Furthermore, the surface morphology evolution is depended on the adatoms surface diffusion length to the original effective terrace width ratio ( $L_A/L$ ). The transition between 2D and 3D growth mode can be controlled by increasing growth temperature, which promotes surface diffusion of adatoms.

## 5.5 Reference:

- [1] S. Fujikawa, T. Takano, Y. Kondo and H. Hirayama, J. Appl. Phys. 47, 2941 (2008).
- [2] T. Takano, Y. Narita, A. Horiuchi and H. Kawanishi, Appl. Phys. Lett. 84, 3567 (2004).
- [3] T. Tut, T. Yelboga, E. Ulker and E. Ozbay, Appl. Phys. Lett. 92, 103502 (2008).
- [4] O. Ambacher, B. Foutz, J. Smart, J.R. Shealy, N.G. Weimann, K. Chu, M. Murphy, A.J. Sierakowski, W.J. Schaff, L.F. Eastman, R. Dimitrov, A. Mitchell, and M. Stutzmann, J. Appl. Phys. 87, 334 (2000).
- [5] J. Han, M. H. Crawford, R. J. Shul, S.J. Hearne, E. Chason, J. J. Figiel and M. Banas, MRS Internet J. Nitride Semicond. Res. 4S1, G7.7 (1999).
- [6] T. Kashima, R. Nakamura, M. Iwaya, H. Katoh, S. Yamaguchi, H. Amano and I. Akasaki, Jpn. J. Appl. Phys. 38, L1515 (1999).
- [7] S. Kamiyama, Motoaki Iwaya, N. Hayashi, T. Takeuchi, H. Amano, I. Akasaki, S. Watanabe and Y. Kaneko, J. Cryst. Growth. 223, 83 (2001).
- [8] J. Han, K. E. Waldrip, S. R. Lee, J. J. Figiel, S. J. Hearne, G. A. Petersen and S. M. Myers, Appl. Phys. Lett. 78, 67 (2001).
- [9] O. Klein, J. Biskupek, U. Kaiser, K. Forghani, S.B. Thapa and F. Scholz, J. Phys.: Conf. Ser. 209, 012018 (2010).
- [10] K. Forghani, M. Klein, F. Lipski, S. Schwaiger, J. Hertkorn, R. A. R. Leute, F. Scholz, M. Feneberg, B. Neuschl, K. Thonke, O. Klein, U. Kaiser, R. Gutt and T. Passow, J. Cryst. Growth 315, 216 (2011).
- [11] D. Morita, M. Sano, M. Yamamoto, T. Murayama, S. Nagahama and T. Mukai, Jpn. J. Appl. Phys. 41, L1434 (2002).
- [12] H. Hirayama, T. Yatabe, N. Noguchi, T. Ohashi and N. Kamata, Appl. Phys. Lett. 91, 071901 (2007).
- [13] W. Sun, M. Shatalov, J. Deng, X. Hu, J. Yang, A. Lunev, Y. Bilenko, M. Shur and R. Gaska, Appl. Phys. Lett. 96, 061102 (2010).
- [14] S. Fujikawa, H. Hirayama, T. Takano and K. Tsubak, Phys. Status Solidi C 6, S784 (2009).
- [15] A. Fujioka, T. Misaki, T. Murayama, Y. Narukawa and T. Mukai, Appl. Phys. Express. 3, 041001 (2010).
- [16] M. Shatalov, W. Sun, A. Lunev, X. Hu, A. Dobrinsky, Y. Bilenko and J. Yang, Appl. Phys. Express. 5, 082101 (2012).
- [17] M. Ippommatsu, Optronics. 2, 71 (2014).
- [18] H. Hirayama, N. Maeda, S. Fujikawa, S. Toyoda and N. Kamata, Optronics, 2, 58 (2014).

- [19] I. Horcas, R. Fernandez, J.M. Gomez-Rodriguez, J. Colchero, J. Gomez-Herrero and A.M. Baro, Review of Scientific Instruments. 78, 013705 (2007).
- [20] M. Moram, Z. Barber, and C. Humphreys, J. Appl. Phys. 102, 023505 (2007).
- [21] A. F. Wright, J. Appl. Phys. 82, 2833 (1997).
- [22] M. Moram and M. Vickers, Rep. Prog. Phys. 72, 036502 (2009).
- [23] K. B. Nam, J. Li, M. L. Nakarmi, J. Y. Lin and H. X. Jiang, Appl. Phys. Lett. 84, 5264 (2004).
- [24] N. Nepal, J. Li, M. L. Nakarmi, J. Y. Lin and H. X. Jiang, Appl. Phys. Lett. 87, 242104 (2005).
- [25] J. Li, K. B. Nam, M. L. Nakarmi, J. Y. Lin, H. X. Jiang, P. Carrier and S. H. Wei, Appl. Phys. Lett. 83 (25), 5163 (2003).
- [26] A. V. Lobanova, K. M. Mazaev, R. A. Talalaev, M. Leys, S. Boeykens, K. Cheng, S. Degroote, J. Cryst. Growth. 287, 601 (2006).
- [27] M. Dauelsberg, D. Brien, H. Rauf, F. Reiher, J. Baumgartl, O. Häberlen, A. S. Segal, A. V. Lobanova, E. V. Yakovlev, R. A. Talalaev, J. Cryst. Growth 393, 103 (2014).
- [28] E. V. Yakovlev, R.A. Talalaev, A.S. Segal, A.V. Lobanova, W.V. Lundin, E.E. Zavarin, M.A. Sinitsyn, A.F. Tsatsulnikov, A.E. Nikolaev, J. Cryst. Growth 310, 4862 (2008).
- [29] J. Karpinski, J. Jun, and S. Porowski, J. Cryst. Growth. 66, 1 (1984).
- [30] V. S. Ban, J. Electrochem. Soc. 119, 761 (1972).
- [31] M. Kamp, M. Mayer, A. Pelzmann, and K. J. Ebeling, MRS Internet J. Nitride Semicond. Res. 2(26) (1997).
- [32] G. B. Stringfellow, *Organometallic Vapor-Phase Epitaxy: Theory and Practice*, Academic Press Inc, 2nd Edition, San Diego (1999).
- [33] H. Lin, Y. Chen, T. Lin, C. Shih, K. Liu, and N. Chen, J. Cryst. Growth. 290, 225 (2006).
- [34] J. Gong, W. Liao, S. Hsieh, P. Lin, and Y. Tsai, J. Cryst. Growth. 249, 28 (2003).
- [35] Y. A. Xi, K. X. Chen, F. W. Mont, J. K. Kim, W. Lee, E. F. Schubert, W. Liu, X. Li, and J. A. Smart, Appl. Phys. Lett. 90, 051104 (2007).
- [36] P. Cantu, F. Wu, P. Waltereit, S. Keller, A. E. Romanov, U. K. Mishra, S. P. DenBaars, and J. S. Speck, Appl. Phys. Lett. 83, 674 (2003).
- [37] A. E. Romanov, and J. S. Speck, Appl. Phys. Lett. 83, 13 (2003).
- [38] D. M. Follstaedt, S. R. Lee, A. A. Allerman, and J. A. Floro, J. Appl. Phys. 105, 083507 (2009).
- [39] J. Xie, S. Mita, A. Rice, J. Tweedie, L. Hussey, R. Collazo, and Z. Sitar, Appl. Phys. Lett. 98, 202101 (2011).

- [40] S. Kurai, K. Shimomura, H. Murotani, Y. Yamada, H. Miyake, and K. Hiramatsu, J. Appl. Phys. 112, 033512 (2012).
- [41] M. Moram, M. Kappers, F. Massabuau, R. Oliver, and C. Humphreys, J. Appl. Phys. 109, 073509 (2011).
- [42] M. Moram, M. Kappers, F. Massabuau, R. Oliver, and C. Humphreys, J. Appl. Phys. 110, 096102 (2011).
- [43] T. Y. Chang, M. A. Moram, C. McAleese, M. J. Kappers, and C. J. Humphreys, J. Appl. Phys. 108, 123522 (2010).
- [44] A. Knauer, U. Zeimer, V. Kueller, and M. Weyers, Phys. Stat. Sol. C. 11, 377 (2014).
- [45] G. Kusch, H. Li, P. R. Edwards, J. Bruckbauer, T. C. Sadler, P. J. Parbrook, and R. W. Martin, Appl. Phys. Lett. 104, 092114 (2014).
- [46] S. Kurai, F. Ushijima, H. Miyake, K. Hiramatsu, and Yamada Y J. Appl. Phys. 115, 053509 (2014).
- [47] A. Mogilatenko, J. Enslin, A Knauer, F. Mehnke, K. Bellmann, T. Wernicke, M. Weyers, and M. Kneissl, Semicond. Sci. Technol. 30, 114010 (2015).
- [48] W. K. Burton, N. Cabrera and F. C. Frank, Philos. Trans. R. Soc. London, Ser. A 243, 299 (1951).

# MOVPE Growth of Si-doped $\text{Al}_x\text{Ga}_{1-x}\text{N}$ on AlN Template

---

## 6.1 Introduction

LED device structures emitting in the ultraviolet region ( $\lambda \leq 340$  nm) are generally based on the wide bandgap  $\text{Al}_x\text{Ga}_{1-x}\text{N}$  alloy system. For fabrication of these AlGa<sub>N</sub>-based optoelectronic devices, the effective control of conductivity in n-type Si-doped  $\text{Al}_x\text{Ga}_{1-x}\text{N}$  becomes one of vital issues. For n-type GaN, good conductivity is easily obtained by substituting a group-IV atom (e.g., Si and Ge) as a donor on the cation site [1]. The activation energy for the ionization of Si donors ( $\Delta E_d = E_C - E_D$ ) in GaN is determined to ~30 meV by using the photoluminescence spectroscopy [2]. On the other hand, for Si-doped AlN, there is no agreement on the ionization energy, with values for the ionization energy ranging from 63 to 255 meV using photoluminescence spectroscopy [3, 4, 5]. However, it is certain that it will be more challenging to obtain high conductivity in n-type  $\text{Al}_x\text{Ga}_{1-x}\text{N}$  epilayers with an Al content higher 50%, because the ionization energy of the dopants increases with increasing Al content.

In addition to the large  $\Delta E_d$  of high Al content AlGa<sub>N</sub>, the doping process can be affected by the spontaneous creation of intrinsic defects (the formation of cation vacancies  $V_{Al}$ ) and unintentional introduction of impurities (O and C) which may cause a self-compensation during the doping process [6, 7, 8, 9]. Normally, the impurity O may come from ammonia ( $\text{NH}_3$ ), the group-III precursors, sapphire substrate or reactor furniture. The impurity C could be generated from the group-III precursors and SiC coating on the graphite susceptor. Higher impurity concentrations of O, C and Si can easily form a donor complex (DX) transferring a shallow donor to a deep donor level so that intentional donors of Si atoms will undergo with a higher ionization energy resulting in much more difficult to donate free electrons at high Al content ( $x > 0.5$ )  $\text{Al}_x\text{Ga}_{1-x}\text{N}$  [10, 11, 12, 13]. Si substitutes Al becoming a shallow donor

[Figure 6.1(a)], and then the shallow Si donor compensated by acceptorlike electron traps form a stable deep localised DX centre ( $DX_1$  or  $DX_2$ ) shown in Figure 6.1 (b) and (c) [12]. The distorted donors ( $DX_1$  and  $DX_2$ ) are formed by breaking one of the tetrahedral bonds and trapping of one additional electron. Hence, it undergoes a large lattice relaxation. In the following parts, the influence of Al content, Si/(Ga+Al) [Si/III] ratio and different template during growth on the structural, electrical and optical properties of Si-doped  $Al_xGa_{1-x}N$  epilayers are investigated.

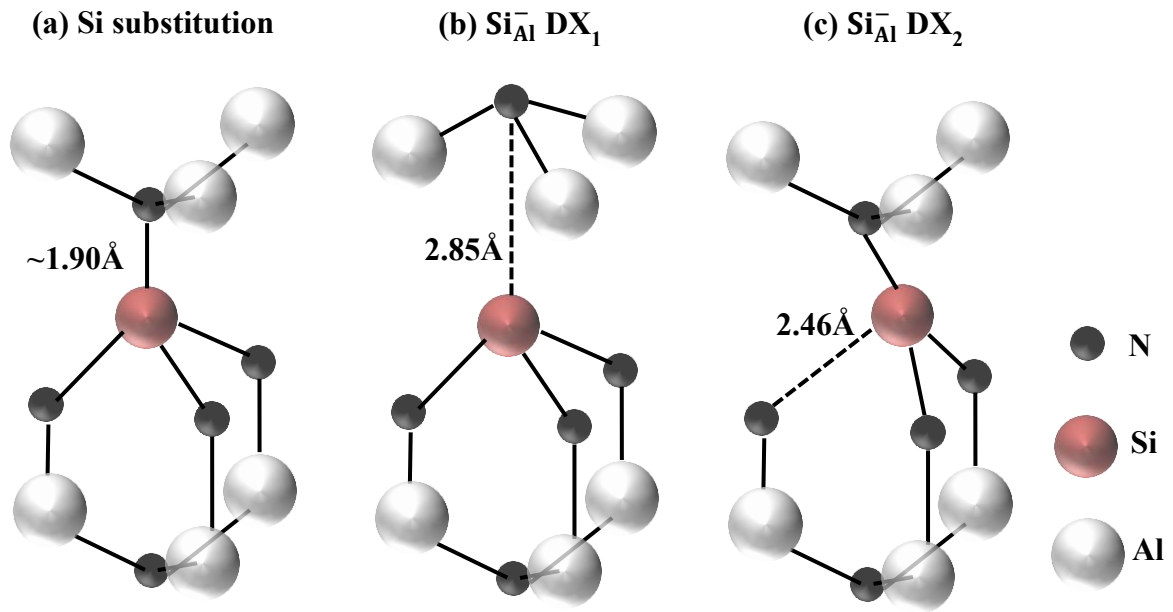


**Figure 6.1:** Schematic view of (a) the substitution Si donor, DX centres for Si: (b)  $Si_{Al}^- (DX_1)$  and (c)  $Si_{Al}^- (DX_2)$ . The length of the broken bond is shown as dashed line in  $\text{\AA}$  [12].

## 6.2 Experimental details

Two series of approximately  $1 \text{ }\mu\text{m}$  thick Si-doped  $Al_xGa_{1-x}N$ , with a nominal Al composition of 48% and 60 %, were deposited on two AlN template types ( $\alpha$  and  $\beta$ ) grown by metalorganic vapour phase epitaxy (MOVPE). AlN template: type  $\alpha$  was prepared by a three-step temperature process on c-plane sapphire ( $FWHM_{0002} = \sim 280 \text{ arcsec}$  and  $FWHM_{10\bar{1}1} = \sim 550 \text{ arcsec}$ ), while type  $\beta$  was prepared through AlN overgrowth on c-plane sapphire with a thin 50 nm AlN nucleation layer prepared commercially ( $FWHM_{0002} = \sim 35 \text{ arcsec}$  and  $FWHM_{10\bar{1}1} = \sim 850 \text{ arcsec}$ ). A schematic of the general sample structure is shown in Figure 6.2. Trimethylgallium (TMGa) and trimethylaluminium (TMAI) were used as group-III precursors, while ammonia ( $NH_3$ ) was the group-V precursor. Disilane ( $Si_2H_6$ ) was used for Si doping. During the Si-doped  $Al_xGa_{1-x}N$  growth, growth temperature and reactor pressure

were kept constant at 1110 °C and 50 mbar, respectively. By variation of the Si<sub>2</sub>H<sub>6</sub> supply, the resulting Si/(Al+Ga) [Si/III] molar ratio in the gas phase was changed between  $1.4 \times 10^{-4}$  and  $3.6 \times 10^{-4}$  in the first series, which will be referred to as I $\alpha$  or I $\beta$  depending on the templates, and between  $1.1 \times 10^{-4}$  and  $5.6 \times 10^{-4}$  in the second series (named II $\alpha$  and II $\beta$ , respectively). There is no data point at [Si/III]  $\sim 1.1 \times 10^{-4}$  in the series II $\beta$ , so the Si/III ratio is varied from  $2.0 \times 10^{-4}$  to  $5.6 \times 10^{-4}$  for II $\beta$ . The growth conditions are summarized in Table 6.1.

The Si<sub>2</sub>H<sub>6</sub> gas is diluted by double dilution channels before entering the reactor chamber, which enables us to control the Si<sub>2</sub>H<sub>6</sub> molar flow rate in a large range. The double dilution stage has been discussed in Chapter 3. The effective Si<sub>2</sub>H<sub>6</sub> volume flow rate  $V$  (sccm) can be calculated by using the equation:

$$V = \frac{V_{source}}{V_{source} + V_{dilute}} \times V_{inject} \times 50 \times 10^{-6} \quad , \quad (6.1)$$

Where  $V_{source}$  is flow through the source mass flow controller (MFC),  $V_{dilute}$  is flow through the dilution MFC,  $V_{inject}$  is flow through the Inject MFC, and the factor  $50 \times 10^{-6}$  is due to the fact that Si<sub>2</sub>H<sub>6</sub> was already diluted to 50 ppm (parts per million) inside the gas cylinder with helium (He) before entering the Si<sub>2</sub>H<sub>6</sub> source MFC. The relation between the molar flow rate  $M$  ( $\mu\text{mol}/\text{min}$ ) and the volume flow rate  $VF$  of Si<sub>2</sub>H<sub>6</sub> is:

$$M(\mu\text{mol}/\text{min}) = \frac{V(\text{cm}^3/\text{min})}{22.4 \times 10^3(\text{cm}^3/\text{mol})} \times 10^6 \quad (6.2)$$

The chemical composition and strain state of the layers were analysed by XRD. The Al composition extracted from XRD is referred to throughout this chapter. The thickness of the epilayers was determined by in-situ spectroscopic reflectance using the EpiTT system. At the same time, in-situ measurements were performed to monitor the wafer curvature during Si-doped AlGaIn growth. Nomarski and AFM were used to study the surface morphology. Van-der-Pauw Hall measurements using Ti/Al/Ti/Au metal contacts deposited by e-beam evaporation with layer thickness of 20/170/5/100 nm were carried out at room temperature (RT) to determine resistivity, carrier concentration and mobility of the carriers. In order to obtain ohmic contacts, rapid thermal annealing (RTA) was employed for 60 s at a temperature of 600°C. RT PL was used to study the optical properties of these samples.



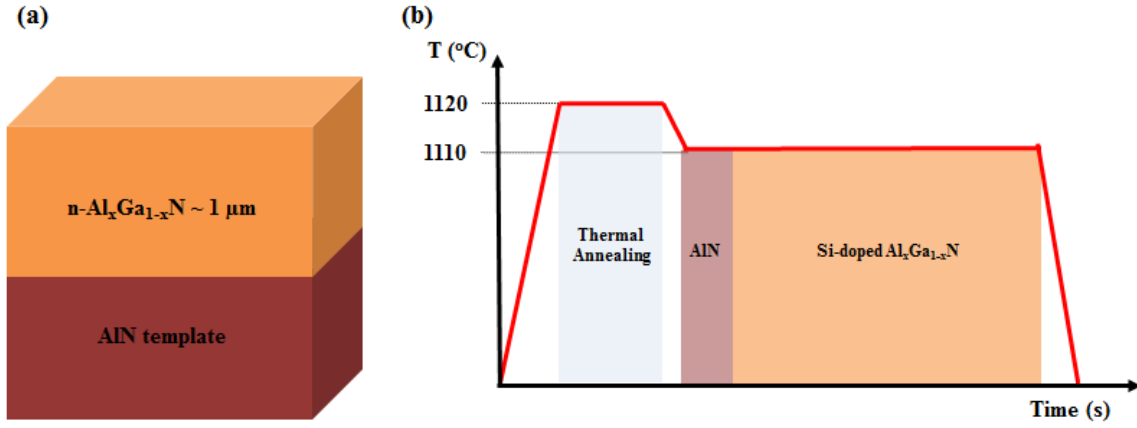


Figure 6.2: (a) schematic of Si-doped  $\text{Al}_x\text{Ga}_{1-x}\text{N}$  epilayers deposited on AlN template/sapphire and (b) growth sequence.

Series	Al_XRD (%)	TMGa / TMAI ( $\mu\text{mol}/\text{min}$ )	$\text{NH}_3$ ( $\text{mmol}/\text{min}$ )	$\text{Si}_2\text{H}_6$ ( $\mu\text{mol}/\text{min}$ ) $\times 10^{-3}$	Si/III in gas phase $\times 10^{-4}$	Template
(I)	$48 \pm 2$ (I $\alpha$ ) $48 \pm 2$ (I $\beta$ )	22.5 / 7.5	30	2.7-6.7	0-3.6	( $\alpha$ ) and ( $\beta$ )
(II)	$60 \pm 2$ (II $\alpha$ ) $58 \pm 2$ (II $\beta$ )	20 / 10	23.43	2.2-11.2	0-5.6	( $\alpha$ ) and ( $\beta$ )

Table 6.1: growth parameters for the Si-doped  $\text{Al}_x\text{Ga}_{1-x}\text{N}$  epilayers.

## 6.3 Results and discussion

### 6.3.1 Structural properties of n-type AlGa $\text{N}$ epilayers

Figure 6.3 shows the dependence of the X-ray rocking curve FWHM values of (0002) and (10 $\bar{1}1$ ) reflections as a function of Si/III ratio for Series I and II, respectively. When Si/III ratio increased, the  $\text{FWHM}_{0002}$  value increased and then kept constant approximately 400 and 380 arcsec for Series I and II as shown in Figure 6.3 (a) and (c), respectively. The screw type dislocation was seen to increase, when a  $\text{Si}_2\text{H}_6$  flow was added to the growth process, especially for samples grown on  $\beta$  template. On the other hand, there was no clear tendency of the  $\text{FWHM}_{10\bar{1}1}$  value for both series as shown in Figure (b) and (d). This indicated that the variation of edge type dislocation density was indifferent as to the employed Si concentration.

In order to determine the strain state of the AlGa $\text{N}$  layers, reciprocal space mapping (RSM) of asymmetric (10 $\bar{1}5$ ) reflections were carried out in Figure 6.4. Since the in-plane lattice parameter of AlGa $\text{N}$  is larger than that of AlN, the Si-doped AlGa $\text{N}$  is expected to be

compressively strained. In Series II, the  $(10\bar{1}5)$  RSM results showed that the degree of relaxation (R) of  $\text{Al}_{0.6}\text{Ga}_{0.4}\text{N}$  layers ( $\text{II}\alpha$ ) increased from  $10\pm 5\%$  when the Si/III ratio = 0 and reached to  $30\pm 5\%$  when the Si/III ratio =  $5.6\times 10^{-4}$  as shown in Figure 6.4 (a-c). A similar trend was also observed in the series  $\text{I}\alpha$ . Meanwhile, the strain relaxation values were consistently higher for epilayers grown on  $\beta$  template, attributed to the high edge type dislocation density in the  $\beta$  template as discussed in Chapter 5. The value of R increased from  $50\pm 5\%$  to  $80\pm 5\%$  when Si/III ratio increased from 0 to  $3.6\times 10^{-4}$  in  $\text{Al}_{0.48}\text{Ga}_{0.42}\text{N}$  layers ( $\text{I}\beta$ ) as shown in Figure 6.4 (d-f). The value of R varied drastically and was almost fully relaxed ( $95\pm 5\%$ ) for a Si/III ratio =  $5.6\times 10^{-4}$  in  $\text{Al}_{0.58}\text{Ga}_{0.42}\text{N}$  layers ( $\text{II}\beta$ ) as shown in Figure 6.4 (g-i). These results indicated that the degree of compressive strain was reduced by increasing Si/III ratio in the range of our doping level.

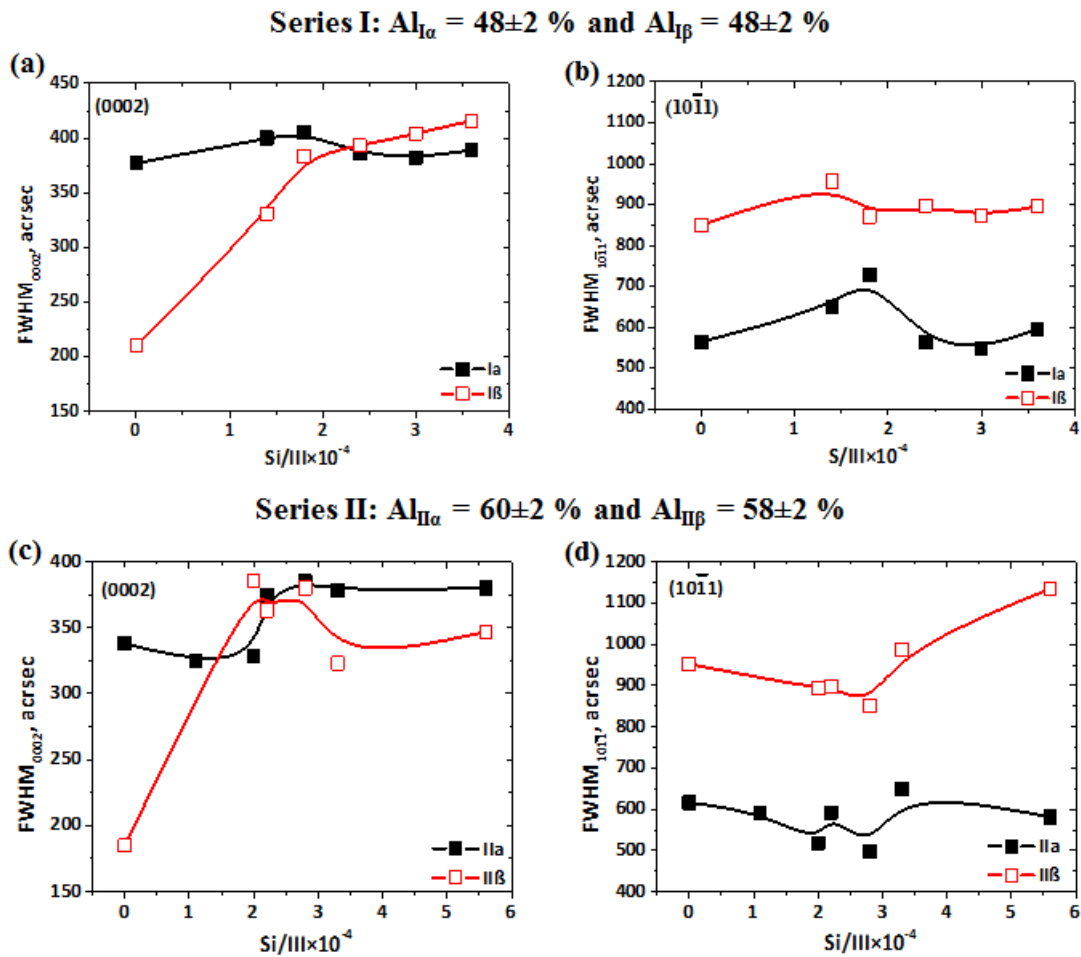
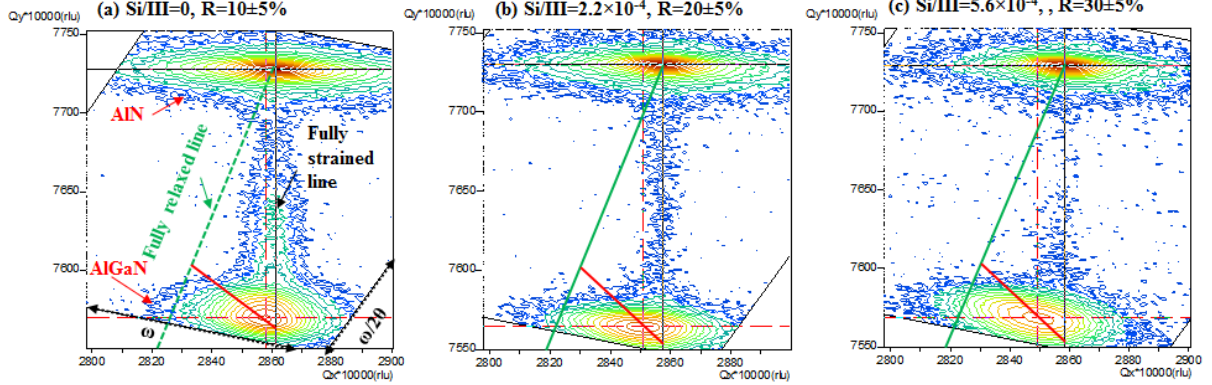
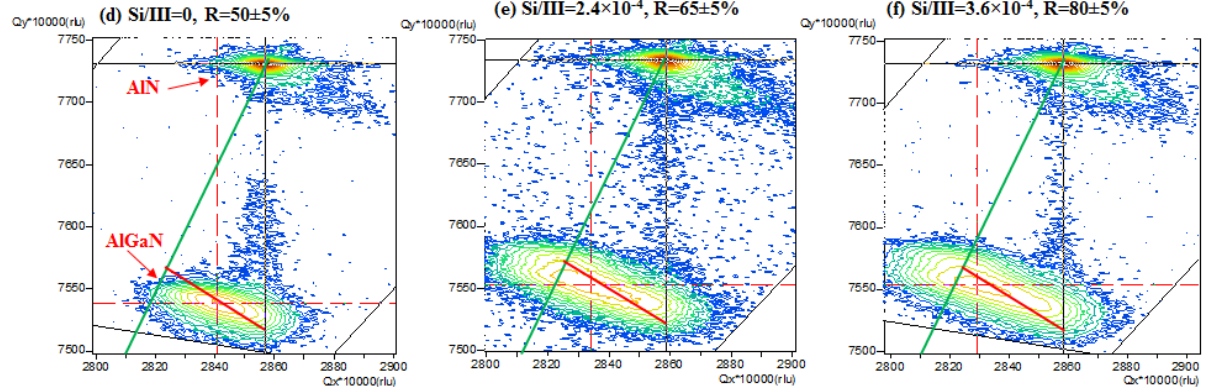


Figure 6.3: FWHM values of (a) & (c) (0002) and (b) & (d)  $(10\bar{1}1)$  XRD rocking curves for  $n\text{-Al}_x\text{Ga}_{1-x}\text{N}$  of series I and II, respectively. Solid lines are guidelines for the eye only.

### II $\alpha$ Al=60 $\pm$ 2%



### II $\beta$ Al=48 $\pm$ 2%



### II $\beta$ Al=58 $\pm$ 2%

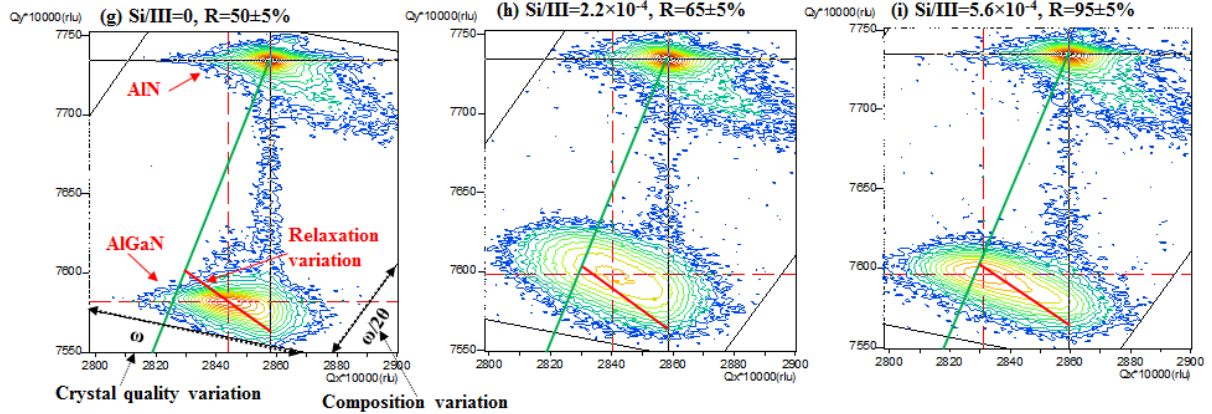


**Figure 6.4:** RSM of (10 $\bar{1}5$ ) reflection measured from the Si-doped AlGa $_x$ N layers grown on  $\alpha$  and  $\beta$  templates with different Si/III ratios for series II $\alpha$  (a-c), II $\beta$  (d-f) and II $\beta$  (g-i), respectively, where R is relaxation value. Green line is the fully relaxed line, black line is the fully strained line, and red line corresponds to certain composition from fully strained to fully relaxed. An increase of the a-lattice parameter ( $\propto 1/Q_x$ ) of the doped layers in comparison to the undoped AlGa $_x$ N is visible. The vertical axis is valid for the c-lattice parameter ( $\propto 1/Q_y$ ).

In-situ wafer curvature measurements were used to study the effect of Si doping on intrinsic strain during MOVPE growth of n-type Al $_x$ Ga $_{1-x}$ N epilayers. Figure 6.5 shows wafer curvature measurement of series II $\alpha$  and II $\beta$ . As discussed in Chapter 5, the undoped Al $_{0.6}$ Ga $_{0.4}$ N layer grown on AlN template grew under an initial compressive strain due to

lattice mismatch with the underlying template. When Si was introduced during  $\text{Al}_x\text{Ga}_{1-x}\text{N}$  growth, the degree of strain relaxation increased with respect to the undoped control samples as shown in Figure 6.5. In the case of the Series II $\beta$  [Figure 6.5 (b)], a transition from compressive to a tensile biaxial strain state is realized as the positive slopes of curvature observed for all Si-doped epilayers. For the Series II $\alpha$ , the compressive strain inherent in the Si-doped  $\text{Al}_{0.6}\text{Ga}_{0.4}\text{N}$  grown on  $\alpha$  AlN template was relaxed significantly during growth [Figure 6.5 (a)], so the biaxial surface strain of the Si-doped AlGa $\text{N}$  samples did not transition into tension as was seen for the samples grown on  $\beta$  AlN template. A similar behaviour was also observed in Series I. These preliminary results indicate that a less compressive strain is induced in the crystal structure by increasing  $\text{Si}_2\text{H}_6$  flow rate. It is also clear to see that Si-doped AlGa $\text{N}$  epilayers with higher edge type threading dislocation density (TDD) relaxed faster than these with lower edge type TDD by comparison between  $\alpha$  and  $\beta$  series, which indicates that edge type TDs are dominant in relaxation of compressive strain. These phenomena have been widely observed and proven that the introduction of Si as a common donor leads to a reduction of compressive strain or increasing tensile strain in the  $\text{Al}_x\text{Ga}_{1-x}\text{N}$  and Ga $\text{N}$  epilayers [14, 15, 16, 17, 18, 19, 20, 21, 22], while the strain relaxation mechanism is still under debate.

Several research groups have observed a strong correlation between TD inclination and both the reduction of compressive strain and the generation of tensile strain in  $\text{Al}_x\text{Ga}_{1-x}\text{N}$  epilayers, which is explained by the dislocation effective climb. Cantu et al. [14] firstly suggested that the strain relaxation was explained by dislocation inclination in Si-doped  $\text{Al}_{0.49}\text{Ga}_{0.51}\text{N}$  layers grown on top of  $\text{Al}_{0.49}\text{Ga}_{0.51}\text{N}$  buffer layers. They have found that these pure edge type dislocation (with Burgers vector  $\mathbf{b}=1/3\langle 11\bar{2}0 \rangle$ ) inclined toward the  $\langle 1\bar{1}00 \rangle$  directions [if viewed projected onto the (0001) growth plane] and had a misfit component, thus relieving misfit strain. These bent dislocations are not in their glide planes, so the bending must result from non-conservative dislocation motion and must occur either by climb or by some other mechanism. Romanov and Speck [15] developed a theoretical bulk-energy balance model to describe dislocation inclination. According to their proposal, dislocation bending occurs once a critical strained-layer thickness is exceeded and bending becomes energetically favourable. Acord et al. [16] subsequently revealed a compressive-to-tensile transition of the strain state at the n-AlGa $\text{N}$  epilayer surface upon the addition of  $\text{SiH}_4$  during growth, which correlated with a change in the average angle of inclination of edge type TDs in the epilayer. The bend angles were observed to increase as the  $\text{SiH}_4$  flow increased, and that effectively relieved

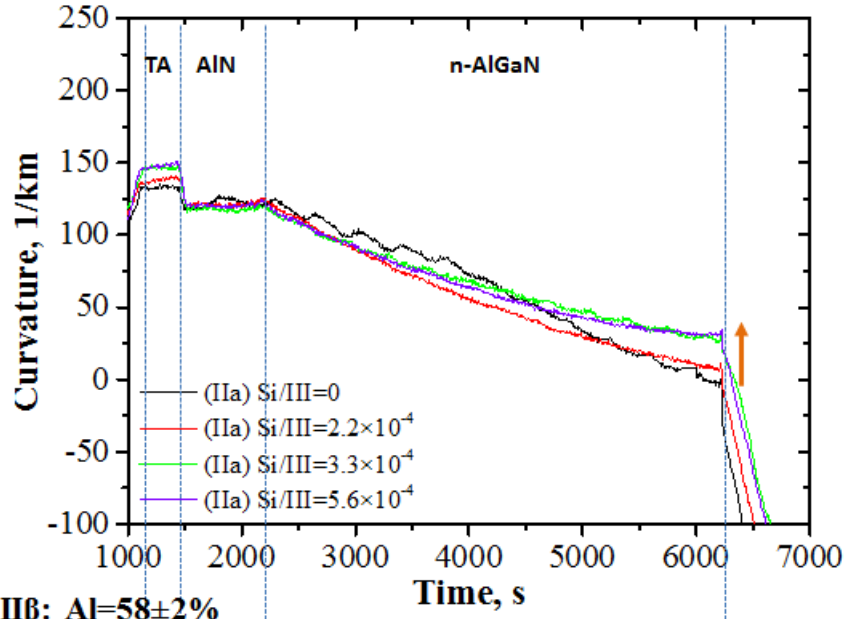
more strain. A contrasting “surface-mediate climb” model has been proposed by Follstaedt et al. [17]. They found that the initial bending dislocation occurred below the critical thickness at the growth surface, where an existing dislocation overgrew a surface vacancy without filling the vacancy due to higher the formation energy for an interstitial than for a vacancy. Xie et al. [18, 19] further explained that the surface-mediate dislocation is governed by vacancies. The Fermi level rises as free carrier concentration increases with increasing Si concentration, so the formation energy of a negatively charged vacancy decreases. Thus, the dislocations can climb being mediated at the growth surface and related with the free carrier concentration. However, the relaxation of compressive strain or generation of tensile strain could be reduced with further increasing Si concentration due to self-compensation of Si atoms (reduction of free carrier concentration).

In contrast to the dislocation climb model, Moram et al. [20, 21] have proposed that Si doping goes along with a higher dislocation density and the consequential “pinning” of dislocations, concluding that Si doping hinders dislocation climb, resulting in increased tensile stress and in reducing the probability of dislocation annihilation.

The role of misfit dislocations (MDs) at the AlGaN/AlN interface can also play an important effect in the strain relaxation process if the edge type TDD is low in the AlN template. Wu et al. [23] found that MD lines can be formed at the AlGaN/AlN interface by gliding of mixed type TDs (with Burgers vector  $\mathbf{b}=1/3\langle 11\bar{2}3 \rangle$ ) originating from the underlying AlN template along the less dominant slip planes  $\{0\bar{1}11\}$  down to the interface.

Despite many arguments in the strain relaxation model, it is certain that the compressive strain can be relaxed both by the inclination of pure edge type TDs and by bowing mixed type TDs, and which one plays a dominant role in the strain relaxation mechanism is highly dependent on the TDD.

(a) II $\alpha$ : Al=60 $\pm$ 2%



(b) II $\beta$ : Al=58 $\pm$ 2%

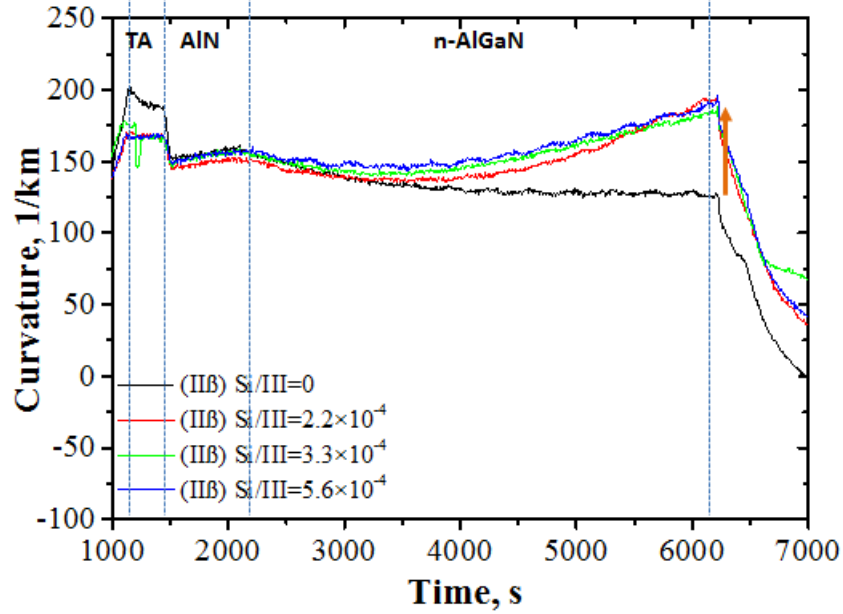


Figure 6.5: Curvature plotted with respect to time corresponding to different Si/III ratio for series II $\alpha$  (a) and II $\beta$  (b). The vertical dash lines mark different growth stages: thermal annealing (TA), AlN connecting layer and n-AlGaN growth.

### 6.3.2 Morphological properties

Root-mean squared (RMS) surface roughness of the n-AlGaN epilayers was assessed by multiple 20 $\times$ 20  $\mu\text{m}^2$  AFM scans for Series II as shown in Figure 6.6. No clear relationship between the Si/III ratio and surface roughness was observed, when the Si/III ratio is below 4 $\times 10^{-4}$ . However, the smoothest surface of n-AlGaN was obtained with highest Si/III ratio in

Series II, which has been confirmed by Nomarski images [Figure 6.7 (c) and (f)] and AFM scans [Figure 6.8 (d) and (h)]. Moreover, micro-scale morphological defects such as hexagonal turrets and pits (highlight by red circles) have been found on the surfaces in Figure 6.7, which may be associated with threading dislocations from the underlying templates.

The surface morphologies of the undoped and doped AlGaIn epilayers of Series II are compared in  $10 \times 10 \text{ } \mu\text{m}^2$  AFM scans (Figure 6.8). The surface morphology transition was observed from clear spiral hexagonal hillocks [6-sided polygons with same orientations as shown in Figure 6.8 (a)], unfolded and blurred spiral hillock [hillock shape is between hexagonal and circular spiral hillock as shown in Figure 6.8 (b)], bunched surface step [Figure 6.8 (c)], to step-flow mode [Figure 6.8 (d)] with increasing Si/III ratio in Series II $\alpha$ . Meanwhile, the surface morphology transition rate of Series II $\beta$  was faster than II $\alpha$ , the atomic steps appeared in the early stage when Si was introduced. Roughening was not seen to occur with increasing Si/III ratio, whereas the strain state was indeed observed to change. This indicates that evolution of the surface morphology is directly affected by the strain relaxation in the material with higher relaxation leading to lower probability of spiral hillock formation. This evolution can be driven by the counterbalance between the surface free energy and the bulk strain energy near the surface as reported by Xie et al for SiGe films [24], whereby a tensile strain is considered to promote a flat surface, in contrast to compressive strain.

A large density of nanopits has been observed in the series II $\beta$  for Si-doped AlGaIn samples [Figure 6.8 (i)]. Nanopits started to form at  $[\text{Si/III}] \sim 2.0 \times 10^{-4}$ , which was the lowest Si/III ratio in the series II $\beta$ . In contrast to the nanopits dominating surface morphology, a nearly pit-free surface has been found for even the highest Si/III ratio as shown in Figure 6.8 (j). AFM studies have shown that the small pits formed where threading dislocations terminate at the GaIn surface can be enlarged using this  $\text{Si}_2\text{H}_6$  treatment, allowing total dislocation densities to be determined accurately [25, 26]. However, here we only see this for the series that is nearly fully relaxed. For the Series II $\alpha$ , mostly under compressive strain the defects are unobserved, suggesting that Si treatment will not work in such cases. For sample Series II $\beta$ , the relaxation and tensile strain build up with Si doping ultimately leads to micro-cracks appearing in the surface [Figure 6.8 (h)]. This suggests that the material quality of the samples grown on  $\alpha$  template is better than the ones grown on  $\beta$  template, and this is in a good agreement with the XRD FWHM measurement (Figure 6.3). The Si-doping-induced tensile strain creates micro-

cracks as they can be seen in Figure 6.8 (h), which results in an almost fully relaxed epilayer and is confirmed by  $(10\bar{1}5)$  RSM.

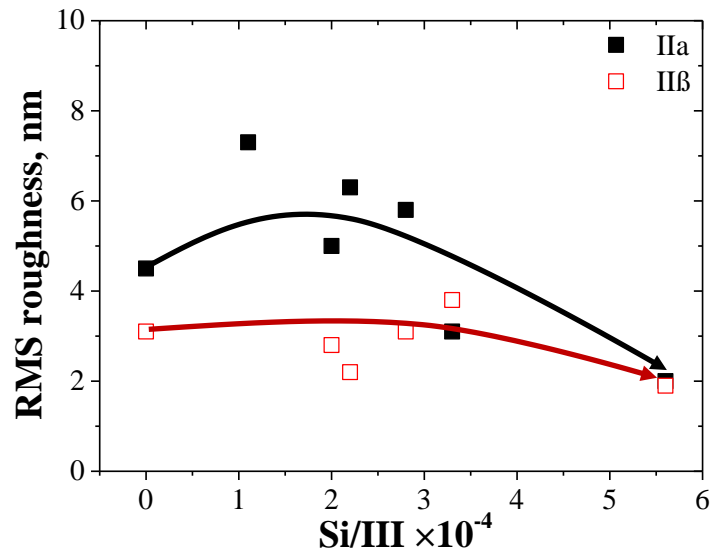
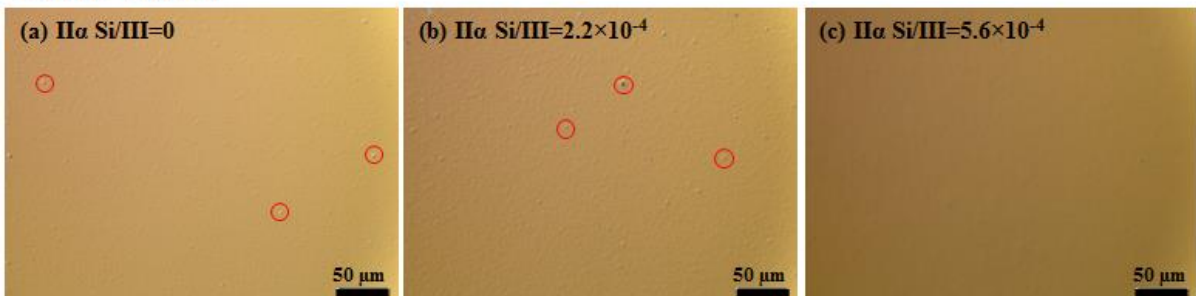


Figure 6.6: RMS surface roughness evaluations by  $20 \times 20 \mu\text{m}^2$  AFM scans for II $\alpha$  and II $\beta$  series with respect to the Si/III ratio. Solid lines are guidelines for the eye only.

#### II $\alpha$ Al=60 $\pm$ 2%



#### II $\beta$ Al=58 $\pm$ 2%



Figure 6.7: Nomarski optical microscope images of selected AlGaIn samples from Series II $\alpha$  and II $\beta$ , respectively. Micro-scale defects are indicated by red circles.



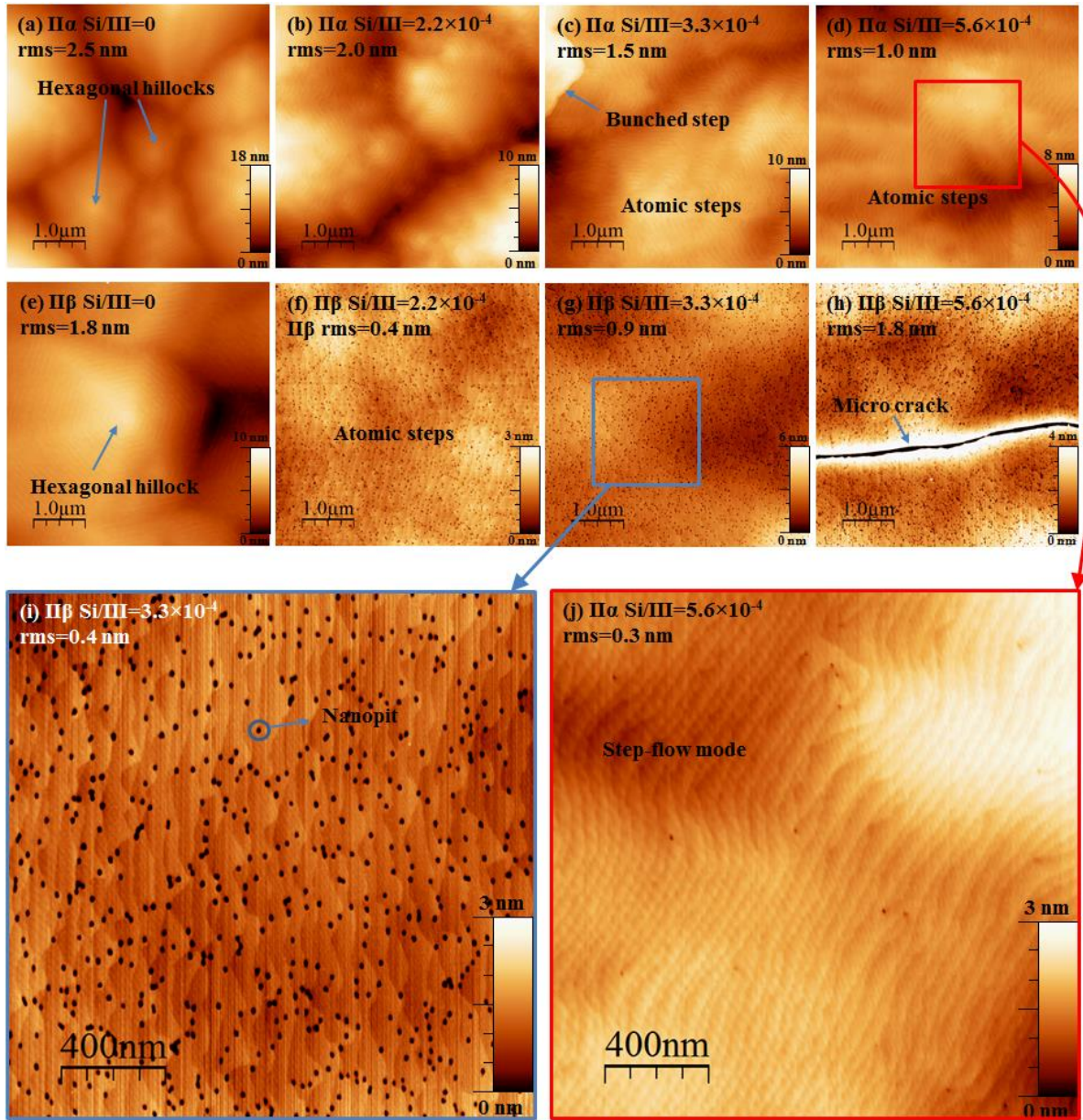
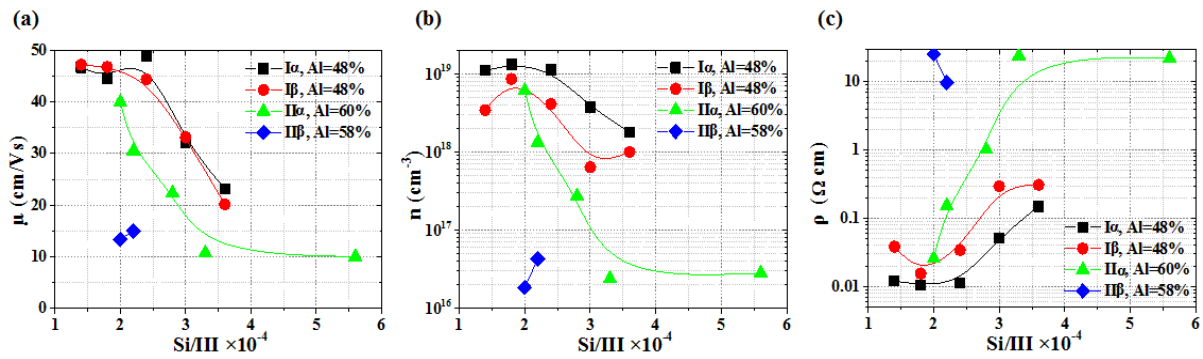


Figure 6.8: (a)-(h)  $10 \times 10 \mu\text{m}^2$  AFM images of  $\text{Al}_x\text{Ga}_{1-x}\text{N}$  for series II grown on  $\alpha$  template and  $\beta$  template. (i)-(j)  $5 \times 5 \mu\text{m}^2$  AFM images of selected samples.

### 6.3.3 Electrical properties of n-doped AlGa<sub>x</sub>N epilayers

Figures 6.9 (a) and (b) show the electron mobility and carrier concentration of the Si-doped Al<sub>x</sub>Ga<sub>1-x</sub>N layers versus Si/III ratio using 600 °C annealed Ti/Al/Ti/Au metal contacts. Unfortunately, the electron mobility and carrier concentration cannot be obtained in Series II $\beta$  due to the large resistivity, except for two data samples with the Si/III ratio of  $2.0 \times 10^{-4}$  and  $2.2 \times 10^{-4}$ . It is observed that the optimal Si/III ratio is  $2.4 \times 10^{-4}$  (Si<sub>2</sub>H<sub>6</sub> flux of 2.0 sccm) and  $2.0 \times 10^{-4}$  (Si<sub>2</sub>H<sub>6</sub> flux of 1.8 sccm) for 48% and 60% Al content grown on  $\alpha$ -AlN template, respectively. It is clear to see that electron mobility and carrier concentration both decrease as the Si/III ratio further increases in Series I $\alpha$ , I $\beta$  and II $\alpha$ , which is attributed to a higher degree of defects compensation and Si self-compensation [27]. The origin of Si self-compensating point defects is correlated with a transition of Si acting as a shallow donor to a DX centre [11, 28, 29].



**Figure 6.9:** (a) the Hall mobility ( $\mu$ ), (b) the carrier density ( $n$ ), and (c) the resistivity ( $\rho$ ) as function of Si/III ratio for series I and II. Hall measurements can only performed on two samples grown with Si/III ratio of  $2 \times 10^{-4}$  and  $2.2 \times 10^{-4}$  grown on  $\beta$  template in series II. Solid lines are guidelines for the eye only.

The resistivity of the Si-doped Al<sub>x</sub>Ga<sub>1-x</sub>N epilayers derived from hall mobility and carrier density is shown in Figure 6.9 (c). It is consistently higher for the layers grown on the  $\beta$  template than grown on the  $\alpha$  template, which could be related to the high density of edge type dislocation. Simpkins et al. [30] demonstrated that edge component dislocations behave as though negatively charged and are not highly conductive while pure screw dislocations are solely responsible for the observed leakage paths and are uncharged in GaN. Zhao et al. [31] also reported that the acceptorlike traps formed by the dangling bonds along the edge dislocation lines may compensate the Si donors and thus reduce the net free electron concentration and electron mobility. For Si-doped AlGa<sub>x</sub>N, Allerman et al. [32] and K. X. Chen et al. [33] both found a same phenomenon where the sheet resistance had a stronger dependence on edge type dislocations than on screw type dislocations, because the edge type

TDDs is usually one order of magnitude higher than screw type TDDs, and resulting in a stronger interaction between electrons and edge type dislocations.

The sheet resistance was always observed to increase for a constant Si/III ratio with increasing Al content, and Hall measurement showed this to be related to the fall in free electron concentration. Others have attributed this to the increasing ionization energy of the Si dopant [34]. However, a significant increase in the donor activation energy ( $E_d$ ) is only reported for Si-doped  $\text{Al}_x\text{Ga}_{1-x}\text{N}$  films with Al content greater than  $x=0.7-0.8$ ; below this level  $E_d$  for optimal doping remained roughly constant ( $E_d$  below  $\sim 23$  meV until  $x=0.7$  [34],  $E_d$  below  $\sim 25$  meV until  $x=0.85$  [35] and  $E_d$  below  $\sim 15$  meV until  $x=0.8$  [36]). In our experiments, Al composition was all below or equal to 60 %, with an approximately 12% difference between series I and II. Therefore, upon consideration of these findings, a rise in resistivity could be attributed to the increasing formation of compensating vacancies or vacancy-oxygen complexes with increasing Al content. This issue can be explained that the formation energy of III-vacancies and their complexes gets lowered as the bandgap increases [37].

#### 6.3.4 Optical properties of n-doped AlGa<sub>N</sub> epilayers

RT PL spectra of an undoped and Si-doped  $\text{Al}_x\text{Ga}_{1-x}\text{N}$  samples with different Si/III ratio are shown in Figure 6.10. Fabry-Perot fringes are visible in spectra due to the interference between the epilayer and template. In Series I with a constant Al content of  $48\pm 2\%$ , all samples exhibited a similar near-band-edge (NBE) luminescence at  $274\pm 2$  nm ( $4.52\pm 0.03$  eV) for  $\text{I}\alpha$  and  $278\pm 2$  nm ( $4.46\pm 0.03$  eV) for  $\text{I}\beta$ , respectively [Figures 6.10 (a) and (b)]. In series II, samples exhibit a sharp NBE luminescence at  $254\pm 2$  nm ( $4.88\pm 0.04$  eV) for  $\text{II}\alpha$  (Al= $60\pm 2\%$ ) and  $258\pm 2$  nm ( $4.80\pm 0.04$  eV) for  $\text{II}\beta$  (Al= $58\pm 2\%$ ), respectively [Figures 6.10 (c) and (d)]. These NBE luminescence will be referred to as the “UV luminescence”.

For Si-doped AlGa<sub>N</sub> samples, bright visible cyan luminescence can be seen after excitation with a 244 nm laser (excitation power density  $\sim 5$  W/cm<sup>2</sup>) (Figure 6.10 and 6.11), which originate from acceptor-like compensating defects and is noted as the “parasitic emission”. The defect-related peak positions are summarized in Table 6.2 and they have been also observed by others who identified as originating from a conduction band to deep acceptor state transition [38, 39]. The integrated parasitic peak intensity at different Si/III ratio is shown in Figure 6.13 for Series I and II, respectively. It was observed that the intensity of the

parasitic emission increased with increase of Si/III ratio in both series. These results suggest that Si-doped AlGa<sub>N</sub> films with high Si/III ratio have more compensating defects. During Si-doped AlGa<sub>N</sub> growth, the most effective compensating acceptors are the isolated cation vacancy with triply negatively charged ( $V_{III}$ )<sup>3-</sup>, and DX centres related to the O<sub>N</sub> impurity, where O substitutes for N [13, 38, 39, 40]. For example, ( $V_{III}$ )<sup>3-</sup> and ( $V_{III}-2O_N$ )<sup>1-</sup> defects capture three and one electrons, respectively, these defects act as compensation centres for Si doping, and minimizing such intrinsic defects could improve the conductivity of Si-doped AlGa<sub>N</sub> alloys.

Hybrid-exchange density functional theory (DFT) calculations indicated that the broad defect emission band could be assigned to different DX centre as marked in Figure 6.11 [13, 40, 41]. As the Fermi level increases, the ( $V_{III} - 2O_N$ )<sup>-</sup> becomes more favorable compensator. A general rise in ( $V_{III} - 2O_N$ )<sup>-</sup> related luminescence intensity with Si/III ratio in the PL spectra provides some support that the reduction in conductivity observed in the previous Hall measurements is related to such defect formation. With further calibration it may be possible to use RT PL as a rapid feedback tool for Si doping.

Generally, under n-type doping and Al-rich alloy conditions, the Fermi level is getting closer to the conduction band, which is leading to the lowering of the cation vacancy and its complex formation energies, so these point defects are easily formed during growth [42, 43]. Furthermore, the formation energy of these defects also gets lowered as the bandgap increases [43, 44]. Upon consideration of these findings, for further improvement of n-type conductivity in high Al content AlGa<sub>N</sub>, it is not a practical choice to suppress intrinsic defects by simply reducing Si/III ratio and Si doping concentration. The formation energy of these defects is lowered near a dislocation due to the presence of the associated strain field, in other words the equilibrium concentration of these defects increases near a dislocation [43, 45]. Therefore, a desirable choice to minimize the parasitic emission would be reduction of dislocations, especially edge type dislocation, which is supported by comparison between  $\alpha$  and  $\beta$  series.

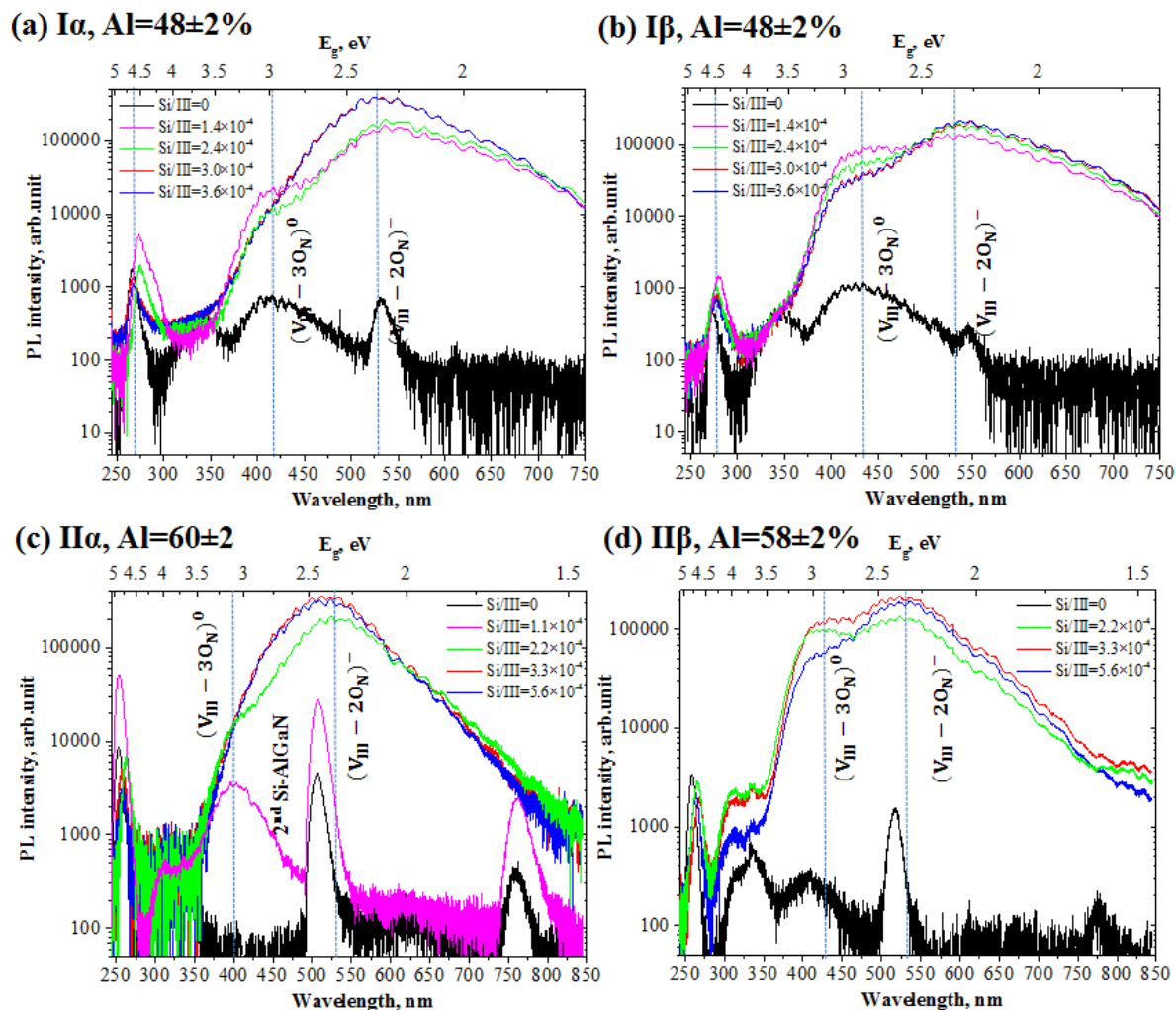


Figure 6.10: RT PL spectra corresponding to the experimental series (a) Ia, (b) Ib, (c) Ia and (d) IIb with different Si/III ratios.

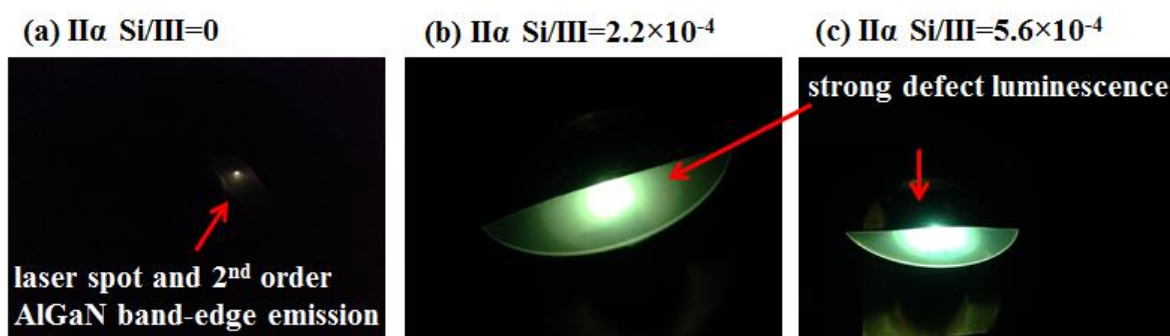


Figure 6.11: Photographs of wafers are taken under 244 nm laser light excitation for selected samples in series IIa at RT.

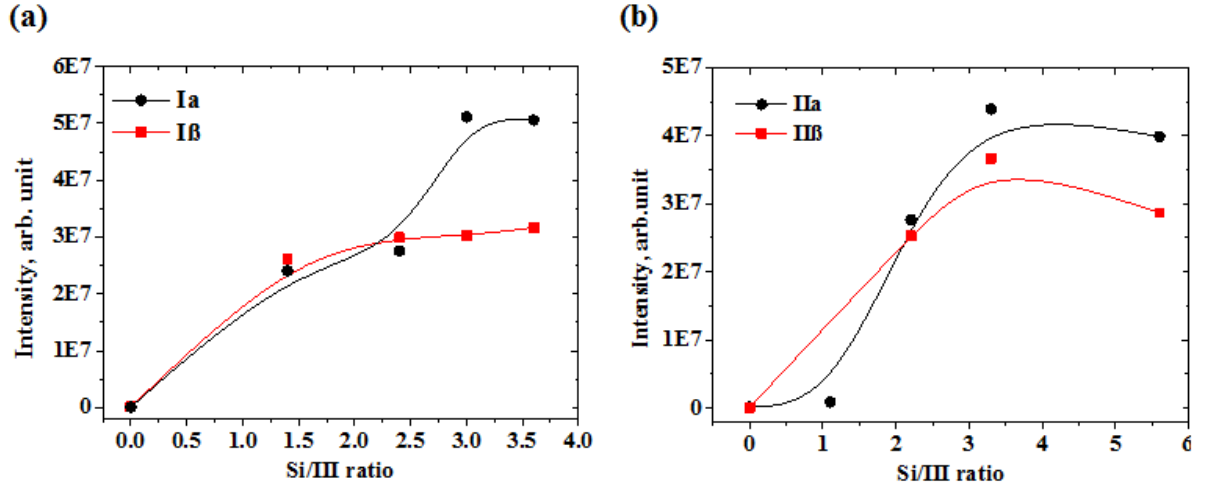


Figure 6.12: Integrated intensity of parasitic emissions of Series I (a) and series II (b) with different Si/III ratio. Solid lines are guidelines for the eye only.

Set	Al (%)	$(V_{III-3O_N})^0$ (nm)	$(V_{III-2O_N})^-$ (nm)
I $\alpha$	48 $\pm$ 2	425 $\pm$ 5 (2.92 $\pm$ 0.03 eV)	535 $\pm$ 5 (2.32 $\pm$ 0.02 eV)
I $\beta$	48 $\pm$ 2	438 $\pm$ 5 (2.83 $\pm$ 0.03 eV)	538 $\pm$ 5 (2.3 $\pm$ 0.02 eV)
II $\alpha$	60 $\pm$ 2	400 $\pm$ 5 (3.1 $\pm$ 0.03 eV)	525 $\pm$ 5 (2.36 $\pm$ 0.02 eV)
II $\beta$	58 $\pm$ 2	420 $\pm$ 5 (2.95 $\pm$ 0.03 eV)	525 $\pm$ 5 (2.36 $\pm$ 0.02 eV)

Table 6.2: Summary of defect-related peak positions for Series I and II corresponding to the different deep level transitions.



## 6.4 Conclusion

In summary, the level of Si-doping related strain was found to be strongly dependent on the edge type and mixed type dislocation density. A significant compressive-to-tensile strain transition was observed for samples grown on  $\beta$  template. At higher Si/III ratios, Si-doped AlGaIn with lower edge type dislocation densities showed a smaller change in the strain state, opposite to the case of the samples with higher densities. Hence, we can infer that the strain will be relieved in a much lower rate if using native AlN substrate with lower TDDs. The apparent relaxation of the compressive strain near the surface was reflected in the surface morphology evolution. The smoothest surface was obtained with highest Si doping, and lower compressive strain.

The electrical properties in n-type AlGaIn grown by MOVPE are investigated as a function of Si/III ratio and template type. For Series I, the sheet resistance first decreased with increasing Si/III ratio due to increase of free carriers. Further increasing Si/III ratio resulted in an increase in the sheet resistance due to strong compensation effects. In comparison between Series I and II, a drop in free carrier density with increasing Al content for a constant Si/III ratio was attributed to lower formation energies of the compensation centres. Moreover, with comparing with samples grown on the  $\alpha$  and  $\beta$  templates, the samples with high edge type TDDs were found to have a significant impact on carrier density and sheet resistance, because acceptor-like traps are formed by the dangling bonds along the edge dislocation lines. The above factors lead to a very narrow growth window for low resistivity Si-doped AlGaIn epilayers with high Al content.

All Si-doped AlGaIn samples show a sharp UV emission as well as a parasitic cyan emission. A change in parasitic luminescence was observed with variation of the Si/III ratio and Al content due to compensating native defects, and minimizing such intrinsic defects could further improve the conductivity of Si-doped AlGaIn alloys. In order to suppress the parasitic emission, an effective choice would be reducing TDDs, particularly edge type dislocations. The preliminary results indicate that the critical Si doping concentration can be judged by defect-related peak position in RT PL spectra.

## 6.5 References:

- [1] S. Fritze, A. Dadgar, H. Witte, M. Bügler, A. Rohrbeck, J. Bläsing, A. Hoffmann, and A. Krost, *Appl. Phys. Lett.* 100, 122104 (2012).
- [2] P. P. Paskov, B. Monemar, A. Toropov, J. P. Bergman, and A. Usui, *Phys. Status Solidi C* 4, 2601 (2007).
- [3] B. Neuschl, K. Thonke, M. Feneberg, R. Goldhahn, T. Wunderer, Z. Yang, N. M. Johnson, J. Xie, S. Mita, A. Rice, R. Collazo, and Z. Sitar, *Appl. Phys. Lett.* 103, 122105 (2013).
- [4] Y. Taniyasu, M. Kasu, and T. Makimoto, *Nature* 441, 325 (2006).
- [5] B. Borisov, V. Kuryatkov, Yu. Kudryavtsev, R. Asomoza, S. Nikishin, D. Y. Song, M. Holtz, and H. Temkin, *Appl. Phys. Lett.* 87, 132106 (2005).
- [6] Chris G. Van de Walle, and J. Neugebauer, *J. Appl. Phys.* 95, 3851 (2004).
- [7] M. L. Nakarmi, K. H. Kim, K. Zhu, J. Y. Lin, and H. X. Jiang, *Appl. Phys. Lett.* 85, 3769 (2004).
- [8] B. Borisov, V. Kuryatkov, Y. Kudryavtsev, R. Asomoza, S. Nikishin, D. Y. Song, M. Holtz, and H. Temkin, *Appl. Phys. Lett.* 87, 132106 (2005).
- [9] Chris G. Van de Walle, C. Stampfl, and J. Neugebauer, *J. Cryst. Growth* 189, 505 (1998).
- [10] J. Oila, V. Ranki, J. Kivioja, K. Saarinen, P. Hautiojaevi, J. Likonen, J. M. Baranowski, K. Pakula, T. Suski, M. Leszczynski, and I. Grzegory, *Phys. Rev. B.*, 63, 045205 (2001).
- [11] N. T. Son, M. Bickermann, and E. Janzén, *Appl. Phys. Lett.* 98, 092104 (2011).
- [12] L. Silvestri, K. Dunn, S. Praver, and F. Ladouceur, *Appl. Phys. Lett.* 99, 122109 (2011).
- [13] X. T. Trinh, D. Nilsson, I. G. Ivanov, E. Janzen, A. K. Georgieva, and N. T. Son, *Appl. Phys. Lett.* 105, 162106 (2014).
- [14] P. Cantu, F. Wu, P. Waltereit, S. Keller, A. E. Romanov, U. K. Mishra, S. P. DenBaars, and J. S. Speck, *Appl. Phys. Lett.* 83, 674 (2003).
- [15] A. E. Romanov, and J. S. Speck, *Appl. Phys. Lett.* 83, 13 (2003).
- [16] J. D. Acord, I. C. Manning, X. Weng, D. W. Snyder, and J. M. Redwing, *Appl. Phys. Lett.* 93, 111910 (2008).
- [17] D. M. Follstaedt, S. R. Lee, A. A. Allerman, and J. A. Floro, *J. Appl. Phys.* 105, 083507 (2009).
- [18] J. Xie, S. Mita, A. Rice, J. Tweedie, L. Hussey, R. Collazo, and Z. Sitar, *Appl. Phys. Lett.* 98, 202101 (2011).
- [19] J. Xie, S. Mita, L. Hussey, A. Rice, J. Tweedie, J. LeBeau, R. Collazo, and Z. Sitar, *Appl. Phys. Lett.* 99, 141916 (2011).



- [20] M. Moram, M. Kappers, F. Massabuau, R. Oliver, and C. Humphreys, *J. Appl. Phys.* 109, 073509 (2011).
- [21] M. Moram, M. Kappers, F. Massabuau, R. Oliver and C. Humphreys, *J. Appl. Phys.* 110, 096102 (2011).
- [22] I. C. Manning, X. Weng, M. A. Fanton, D. W. Snyder, and J. M. Redwing, *J. Cryst. Growth* 312, 1301 (2010).
- [23] Z. Wu, K. Nonaka, Y. Kawai, T. Asai, F. A. Ponce, C. Chen, M. Iwaya, S. Kamiyama, H. Amano, and I. Akasaki: *Appl. Phys. Express.* 3, 111003(2010).
- [24] Y. H. Xie, G. H. Gilmer, C. Roland, P. J. Silverman, S. K. Buratto, J. Y. Cheng, E. A. Fitzgerald, A. R. Kortan, S. Schuppler, M. A. Marcus, and P. H. Citrin, *Phys. Rev. Lett.* 73, 3006 (1994).
- [25] R. A. Oliver, M.J. Kappers, J. Sumner, R. Datta, and C.J. Humphreys., *J. Cryst. Growth.* 289, 506 (2006).
- [26] K. Cheng, M. Leys, S. Degroote, M. Germain, and G. Borghs, *Appl. Phys. Lett.* 92, 192111 (2008).
- [27] Chris G. Van de Walle, C. Stampfl, J. Neugebauer, M. D. McCluskey, and N. M. Johnson, *MRS Internet J. Nitride Semicond. Res.* 4S1, G10.4 (1999).
- [28] R. Zeisel, M. W. Bayerl, S. T. B. Goennenwein, R. Dimitrov, O. Ambacher, M. S. Brandt, and M. Stutzmann, *Phys. Rev. B* 61, R16283 (2000).
- [29] F. Mehnke, T. Wernicke, H. Pingel, C. Kuhn, C. Reich, V. Kueller, A. Knauer, M. Lapeyrade, M. Weyers, and M. Kneissl, *Appl. Phys. Lett.* 103, 212109 (2013).
- [30] B. S. Simpkins, E. T. Yu, P. Waltereit and J. S. Speck, *J. Appl. Phys.* 94 1448 (2003).
- [31] D. G. Zhao, H. Yang, J. J. Zhu, D. S. Jiang, Z. S. Liu, S. M. Zhang, Y. T. Wang, and J. W. Liang, *Appl. Phys. Lett.* 89, 112106 (2006).
- [32] A. A. Allerman, M. H. Crawford, A. J. Fischer, K. H. A. Bogart, S. R. Lee, D. M. Follstaedt, P. P. Provencio, and D. D. Koleske, *J. Cryst. Growth* 272, 227 (2004).
- [33] K. X. Chen, Q. Dai, W. Lee, J. K. Kim, E. F. Schubert, J. Grandusky, M. Mendrick, X. Li, and J. A. Smart. *Appl. Phys. Lett.* 93, 192108 (2008).
- [34] M. L. Nakarmi, K. H. Kim, K. Zhu, J. Y. Lin, and H. X. Jiang, *Appl. Phys. Lett.* 85, 3769 (2004).
- [35] B. Borisov, V. Kuryatkov, Yu. Kudryavtsev, R. Asomoza, S. Nikishin, D. Y. Song, M. Holtz, and H. Temkin, *Appl. Phys. Lett.* 87, 132106 (2005).
- [36] R. Collazo, S. Mita, J. Xie, A. Rice, J. Tweedie, R. Dalmau, and Z. Sitar, *Phys. Status Solidi C* 8, 2031 (2011).

- [37] K. A. Jones, T. P. Chow, M. Wraback, M. Shatalov, Z. Sitar, F. Shahedipour, K. Uduary, and G. S. Tompa, *J Mater Sci.* 50, 3267–3307 (2015).
- [38] K. B. Nam, M. L. Nakarmi, J. Y. Lin, and H. X. Jiang, *Appl. Phys. Lett.* 86, 222108 (2005).
- [39] S. F. Chichibu, H. Miyake, Y. Ishikawa, M. Tashiro, T. Ohtomo, K. Furusawa, K. Hazu, K. Hiramatsu, and A. Uedono, *J. Appl. Phys.* 113, 213506 (2013).
- [40] B. E. Gaddy, Z. Bryan, I. Bryan, R. Kirste, J. Xie, R. Dalmau, B. Moody, Y. Kumagai, T. Nagashima, Y. Kubota, T. Kinoshita, A. Koukitu, Z. Sitar, R. Collazo, and D. L. Irving, *Appl. Phys. Lett.* 103, 161901 (2013).
- [41] I. Bryan, Z. Bryan, B. Gaddy, L. Hussey, M. Bobea, R. Kirste, D. Irving, R. Collazo, and Z. Sitar, “Compensation in Si-doped  $\text{Al}_x\text{Ga}_{1-x}\text{N}$  thin films deposited by MOCVD on AlN single crystalline substrates”, ISGN-5, May 2014.
- [42] C. Stampfl, and C. G. Van de Walle, *Appl. Phys. Lett.* 72, 459 (1998).
- [43] Chris G. Van de Walle, and Jörg Neugebauer, *J. Appl. Phys.* 95, 3851 (2004).
- [44] M. C. Wagener, G. R. Jame, and F. Omnés, *Appl. Phys. Lett.* 83, 4193 (2003).
- [45] R. Collazo and N. Dietz, “The Group III-Nitride Material Class: from Preparation to Perspectives in Photoelectrocatalysis”, H-J. Lewerenz and L. M. Peter, RSC Publishing, pp 193–222 (2013).

## InAlN/AlGaN structures

---

### 7.1 Introduction

Indium aluminium nitride (InAlN) semiconductor alloys have attracted attention, because they can be in-plane lattice matched to gallium nitride (GaN) with an indium (In) composition of approximately 17-18%, which makes them promising candidates for use in distributed Bragg reflectors (DBRs) and high electron mobility transistors (HEMTs) [1, 2, 3]. However, there has been no report of InAlN as an active region material for an ultra-violet (UV) emitter. Currently, AlGaN-based UV LED devices are most widely employed, and AlGaN is a relatively well-understood alloy as an active region material, both in terms of the physics and growth conditions used [4, 5, 6, 7].

Wurtzite InAlN alloys are a possible alternative candidate for use in optoelectronic devices operating in wide spectral ranges covering from deep UV to infrared. The consideration of InAlN used as an active region material is inspired by the unique material properties of InGaN. For InGaN alloy materials, the “S” shaped temperature-dependence (TD) of photoluminescence (PL) peak energy is commonly observed and is a well-known manifestation of a strong carrier localization effect occurring in dot-like In-rich InGaN formed in the InGaN layer [8, 9, 10, 11], which can partially prevent carriers from reaching defects leading to a reduction of non-radiative recombination rate. This dot-like In-rich InGaN cluster is formed by In aggregation and phase separation of the InGaN layer because of the immiscibility of GaN and InN [9, 10, 11, 12, 13]. Meanwhile, a similar “S” shaped on the TDPL near band-edge (NBE) emission of InAlN have been reported by others [14, 15, 16, 17, 18, 19], which shows a potential strong carrier localization effect in InAlN alloy. Therefore, the interest of such an approach is to take advantage of such localisation by using InAlN as the quantum-well (QW) material as a replacement for GaN or AlGaN in the UV region.

InAlN growth is very challenging in obtaining high crystal quality epilayers compared with InGaN and AlGaN due to the significant difference in thermal stability and atom size mismatches between binaries InN and AlN [20]. Moreover, unintentional incorporation of Ga during epitaxial growth of InAlN thin films has been observed [21, 22, 23, 24]. Suk and Jeomoh et al. [21, 22] found that Ga-containing deposition on a wafer susceptor and on surrounding surfaces of uncooled parts in a growth chamber can be responsible for Ga in the InAl(Ga)N epilayer, while a GaN underlying layer or template below an InAl(Ga)N epilayer does not contribute to the Ga auto-incorporation effect.

The purpose of Section 7.2 is to study the structural and morphological properties of InAlN thin films grown on GaN, AlGaN and AlN buffer layers. Section 7.3 will concentrate on investigating the possibility of shallow UV (300 to 350 nm) InAlN multiple quantum-well (MQW) structures.

## **7.2 Growth of InAlN layers**

The growth window of good quality InAlN alloy is rather sharp and needs to be carefully optimized. The growth temperature needs to be reduced to limit the indium desorption, and  $H_2$  must be avoided due to reduction of indium incorporation [25]. In order to suppress Ga auto-incorporation [21, 22], the proper cleaning for reactor chamber and wafer susceptor should be performed before InAlN growth. The structural, morphological and optical properties of  $In_xAl_{1-x}N$  thin films grown on  $Al_yGa_{1-y}N$  buffer layers (i.e, GaN, AlN and AlGaN) with different growth temperature will be shown in this Section, which are important constituents of the active layers for Section 7.3 study.

### **7.2.1 Experimental details**

In order to minimize Ga incorporation issue, a clean susceptor was used with several AlN growth runs (3-step AlN growth) undertaken before  $In_xAl_{1-x}N$  growth run to “condition” the reactor chamber. The undoped GaN, AlN ( $\alpha$  and  $\beta$  as described in Section 4.5.3) and  $Al_{0.6}Ga_{0.4}N$  (grown on  $\alpha$ - and  $\beta$ -AlN as described in Section 5.2, growth series IV) templates were prepared by MOVPE growth. Prior to the growth of  $In_xAl_{1-x}N$  thin films on the templates, a 3-minute thermal anneal at 1060°C was carried out in order to clean the surface and remove any oxide layer. Then, the  $In_xAl_{1-x}N$  films were performed directly on these templates without any intentional intermediate layers. The growth temperature ( $T_g$ ) of the  $In_xAl_{1-x}N$  thin films was varied from 730 to 790 °C (A-730°C, B-755°C, C-780°C and D-

790°C). The V/III and TMIn/TMAI were kept constant for all  $\text{In}_x\text{Al}_{1-x}\text{N}$  epitaxial layers at 10,400 and 1, respectively. Typical structure and growth sequence of the  $\text{In}_x\text{Al}_{1-x}\text{N}$  growth are illustrated in Figures 7.1(a) and (b), respectively. Four growth runs were made as described with growth temperatures and templates and are shown in Table 7.1.

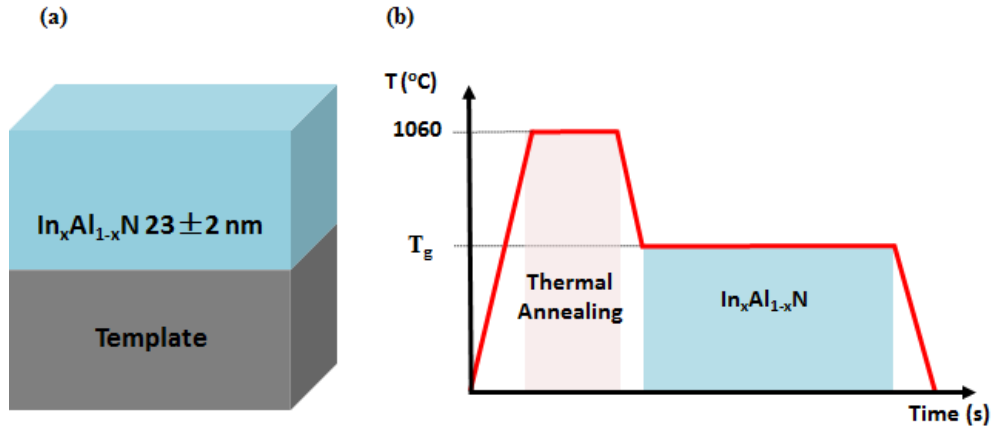


**Figure 7.1:** (a) Schematic of the  $\text{In}_x\text{Al}_{1-x}\text{N}$  structure and (b) growth sequence.

$T_g$ (°C)	1 $\alpha$ -AlN	2 $\beta$ -AlN	3 AlGaIn on $\alpha$	4 AlGaIn on $\beta$	5 GaN
730	Sample 1A	Sample 2A	Sample 3A	Sample 4A	Sample 5A
755	Sample 1B	Sample 2B	Sample 3B	Sample 4B	Sample 5B
780	Sample 1C	Sample 2C	Sample 3C	Sample 4C	Sample 5C
790	Sample 1D	Sample 2D	Sample 3D	Sample 4D	Sample 5D

**Table 7.1:** Sample name of 23 nm thick  $\text{In}_x\text{Al}_{1-x}\text{N}$  thin films grown on various templates at different growth temperatures.

In order to calibrate the compositions and growth rates of  $\text{In}_x\text{Al}_{1-x}\text{N}$  thin films, approximately 23 nm films were grown. X-ray diffraction (XRD) was used to measure the average lattice parameter using the peak positions of both the symmetric (0002) and asymmetric (10 $\bar{1}$ 5) reflections, found using the  $\omega$ -2 $\theta$  scan and  $\omega/\omega$ -2 $\theta$  reciprocal space maps (RSMs), respectively. These reflections were then used to calculate the  $\text{In}_x\text{Al}_{1-x}\text{N}$  compositions and strain states assuming Vegard's law to hold for these materials with isotropic strain in the c-plane and no Ga auto-incorporation into the epilayers. Literature values of the lattice parameters and Poisson ratio of AlN and InN were used as described in section 3.4.3. Growth rates were estimated from the thickness fringes observed in XRD (0002)  $\omega$ -2 $\theta$  scans (Figure.7.3). Surface morphology was assessed by atomic force microscopy (AFM) using tapping mode (Veeco Multimode<sup>TM</sup>). The AFM images were processed using WSxM free

software [26]. Room temperature photoluminescence (RT-PL) measurements were performed to investigate the optical properties of the samples using a 244 nm laser and detected using iHR320 Horiba imaging spectrometer equipped with a CCD camera and a photomultiplier.

## 7.2.2 Results and discussion

### Composition and strain of $\text{In}_x\text{Al}_{1-x}\text{N}$

The XRD full-width-half maximum (FWHM) values, lattice parameters and in-plane strain state ( $R_a$ ) of templates were summarized in Table 7.2. These templates are named as 1 ( $\alpha$ -AlN template), 2 ( $\beta$ -AlN template), 3 ( $\text{Al}_{0.6}\text{Ga}_{0.4}\text{N}$  grown on  $\alpha$  template), 4 ( $\text{Al}_{0.6}\text{Ga}_{0.4}\text{N}$  grown on  $\beta$  template) and 5 (GaN), respectively. The fully relaxed in-plane ( $a$ ) and out-of-plane ( $c$ ) lattice parameter were calculated using Equations 3.15 and 3.16 for the ternary alloys with variable Al composition ( $\text{Al}_x\text{Ga}_{1-x}\text{N}$  and  $\text{Al}_y\text{In}_{1-y}\text{N}$ ), as shown in Figure 7.2. The experimental results from GaN templates and  $\text{Al}_{0.6}\text{Ga}_{0.4}\text{N}$  templates grown on  $\alpha$ -AlN and  $\beta$ -AlN templates with different relaxation value ( $R_a$ ) are also shown in Figure 7.2, where the composition of  $\text{Al}_y\text{In}_{1-y}\text{N}$  for lattice matched growth on a particular template is given. If the in-plane lattice parameter of the growing  $\text{Al}_y\text{In}_{1-y}\text{N}$  thin film is larger than the in-plane lattice parameter of the underlying template,  $\text{Al}_y\text{In}_{1-y}\text{N}$  will be under in-plane compressive strain and out-of-plane tensile strain. These two plots give a good indication of expecting strain condition for a particular indium composition of  $\text{Al}_y\text{In}_{1-y}\text{N}$ , for example, the InAlN thin film with above 4% indium grown on  $\text{Al}_{0.6}\text{Ga}_{0.4}\text{N}/\beta$ -AlN will be under in-plane compressive strain.

	(1) $\alpha$ -AlN	(2) $\beta$ -AlN	(3) AlGaN on $\alpha$ -AlN	(4) AlGaN on $\beta$ -AlN	(5) GaN
$\text{FWHM}_{0002}$ (arcsec)	286	52	318	130	169
$\text{FWHM}_{10\bar{1}1}$ (arcsec)	600	1100	584	1074	334
( $\text{\AA}$ )	3.112	3.118	3.114	3.129	3.183
$c$ ( $\text{\AA}$ )	4.982	4.977	5.081	5.073	5.192
$R_a$ (%)	-	-	15 $\pm$ 5	45 $\pm$ 5	-

Table 7.2: Measured XRD FWHM values around the (0002) and (10 $\bar{1}1$ ) reflections, in-plane ( $a$ ), out-of-plane ( $c$ ) lattice parameters and in-plane relaxation ( $R_a$ ) of AlGaN on AlN templates. GaN and AlN templates are assumed that fully relaxed grown on c-sapphire.

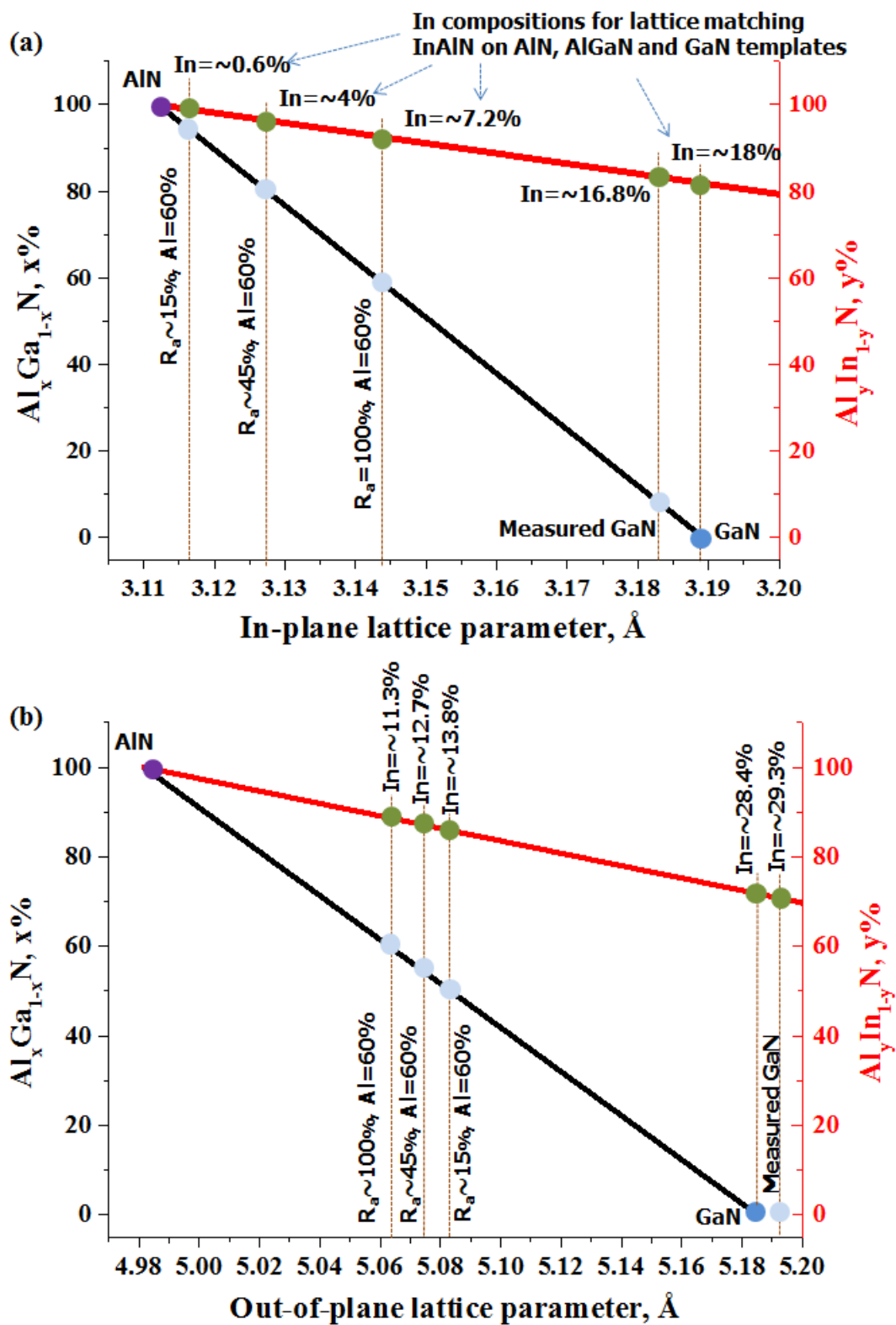


Figure 7.2: (a) in-plane and (b) out-of-plane lattice parameter of varied composition ternary alloys ( $\text{Al}_x\text{Ga}_{1-x}\text{N}$  and  $\text{Al}_y\text{In}_{1-y}\text{N}$ ) as calculated using linear Vegard's law and our templates as measured by XRD.

Figure 7.3 shows XRD symmetric (0002)  $\omega$ -2 $\theta$  scans of the  $\text{In}_x\text{Al}_{1-x}\text{N}$  thin films grown on the templates at different growth temperatures. Arrows indicate the weak and broad peaks of the (0002) zeroth-order Bragg diffraction corresponding to the  $\text{In}_x\text{Al}_{1-x}\text{N}$  thin films. The presence of clear diffraction fringes can be seen in these scans, which suggest that the epilayer thicknesses can be measured accurately by the fringe peak spacing, thus, the growth rates can be estimated. The thickness of  $\text{In}_x\text{Al}_{1-x}\text{N}$  thin films is  $23 \pm 1$  nm for all samples. It has been shown that there is no noticeable effect of template on the growth rate. Moreover, for the samples grown on the GaN and AlN templates, the thickness fringes are less visible at the lowest growth temperature as shown in Figures 7.3 (a) and (b), which indicates surface roughening and/or degradation of crystal quality for the  $\text{In}_x\text{Al}_{1-x}\text{N}$  layers as expected due to short surface migration of adatoms and the increased lattice mismatch to the underlying templates. Meanwhile, for the samples grown on the AlGaN/AlN templates, the diffraction thickness fringes are much clearer for sample grown on  $\text{Al}_{0.6}\text{Ga}_{0.4}\text{N}/\beta\text{-AlN}$  than grown on  $\text{Al}_{0.6}\text{Ga}_{0.4}\text{N}/\alpha\text{-AlN}$  at the lowest temperature indicating a relative uniform thickness and a smooth surface, as shown in Figures 7.3 (c) and (d).

In order to figure out the indium composition of  $\text{In}_x\text{Al}_{1-x}\text{N}$  thin films, the strain state must be estimated. Therefore, RSMs around the asymmetric  $(10\bar{1}5)$  reflection were carried out as shown in Figures 7.4 and 7.5. The  $(10\bar{1}5)$  RSMs reveal that the reciprocal lattice points of  $\text{In}_x\text{Al}_{1-x}\text{N}$  and underlying GaN templates are well-aligned in the  $Q_x$  direction as shown in Figures 7.4 (a-c), i.e., in-plane lattice match, indicating pseudomorphic growth of  $\text{In}_x\text{Al}_{1-x}\text{N}$  on GaN template, even with high indium content. These results are in overall agreement with the results obtained for similar MOVPE-grown InAlN layers [1, 27, 28, 29]. The RSMs reveal that the  $\text{In}_x\text{Al}_{1-x}\text{N}$  films grown on the  $\alpha\text{-AlN}$  and  $\beta\text{-AlN}$  templates are completely strained as shown in Figures 7.4 (d-i), apart from the samples 1A and 2A grown on the  $\alpha\text{-AlN}$  and  $\beta\text{-AlN}$  templates at  $730^\circ\text{C}$  [Figures 7.4 (d) and (g)]. As can be seen from the  $(10\bar{1}5)$  reflections, no clear InAlN peak has been observed for the sample 1A [Figure 7.4 (d)], and blurred and broad InAlN peak has been observed for the sample 2A [Figure 7.4 (g)], suggesting a relaxation of the InAlN epilayers and very poor crystal quality.

For the  $\text{In}_x\text{Al}_{1-x}\text{N}$  thin films grown on the  $\text{Al}_{0.6}\text{Ga}_{0.4}\text{N}/\text{AlN}$  templates, the  $(10\bar{1}5)$  RSMs reveal that none of them are fully coherent to templates as shown in Figure 7.5. The  $\text{In}_x\text{Al}_{1-x}\text{N}$  layers with indium contents between  $\sim 0.11$  and  $\sim 0.19$  show deviation from the coherent growth towards larger in-plane lattice parameters, indicating some relief of compressive strain in in-



plane direction. Furthermore, all samples around both the (0002) and the (10 $\bar{1}5$ ) reflections only showed one epilayer peak, so there was no evidence of phase separation or separation of strain, although it was broad and had a low intensity.

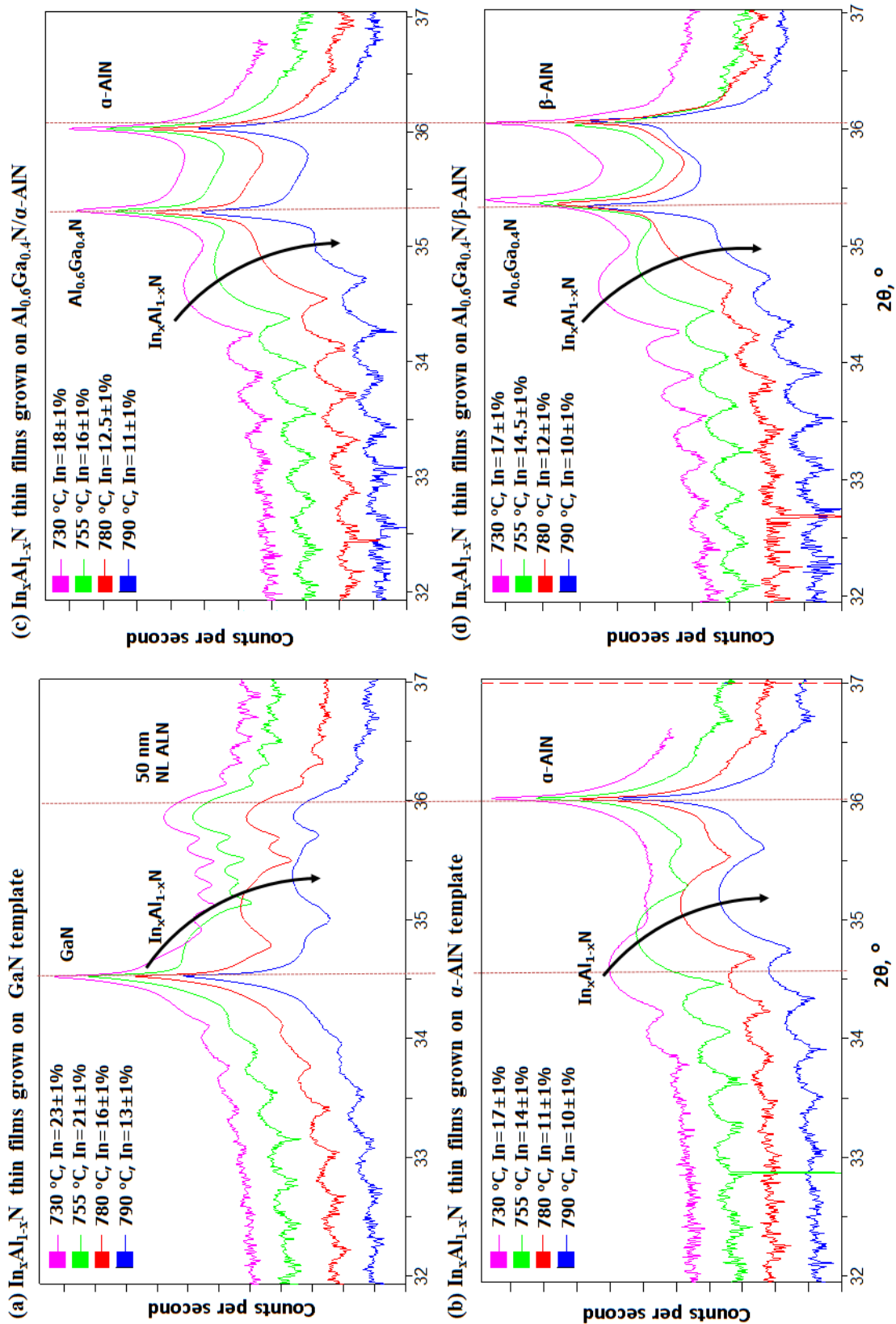


Figure 7.3: XRD (0002)  $\omega$ -2 $\theta$  scans of the  $\text{In}_x\text{Al}_{1-x}\text{N}$  thin films grown on the (a) GaN, (b)  $\alpha$ -AlN, (c)  $\text{Al}_{0.6}\text{Ga}_{0.4}\text{N}/\alpha$ -AlN and (d)  $\text{Al}_{0.6}\text{Ga}_{0.4}\text{N}/\beta$ -AlN templates at different growth temperature.

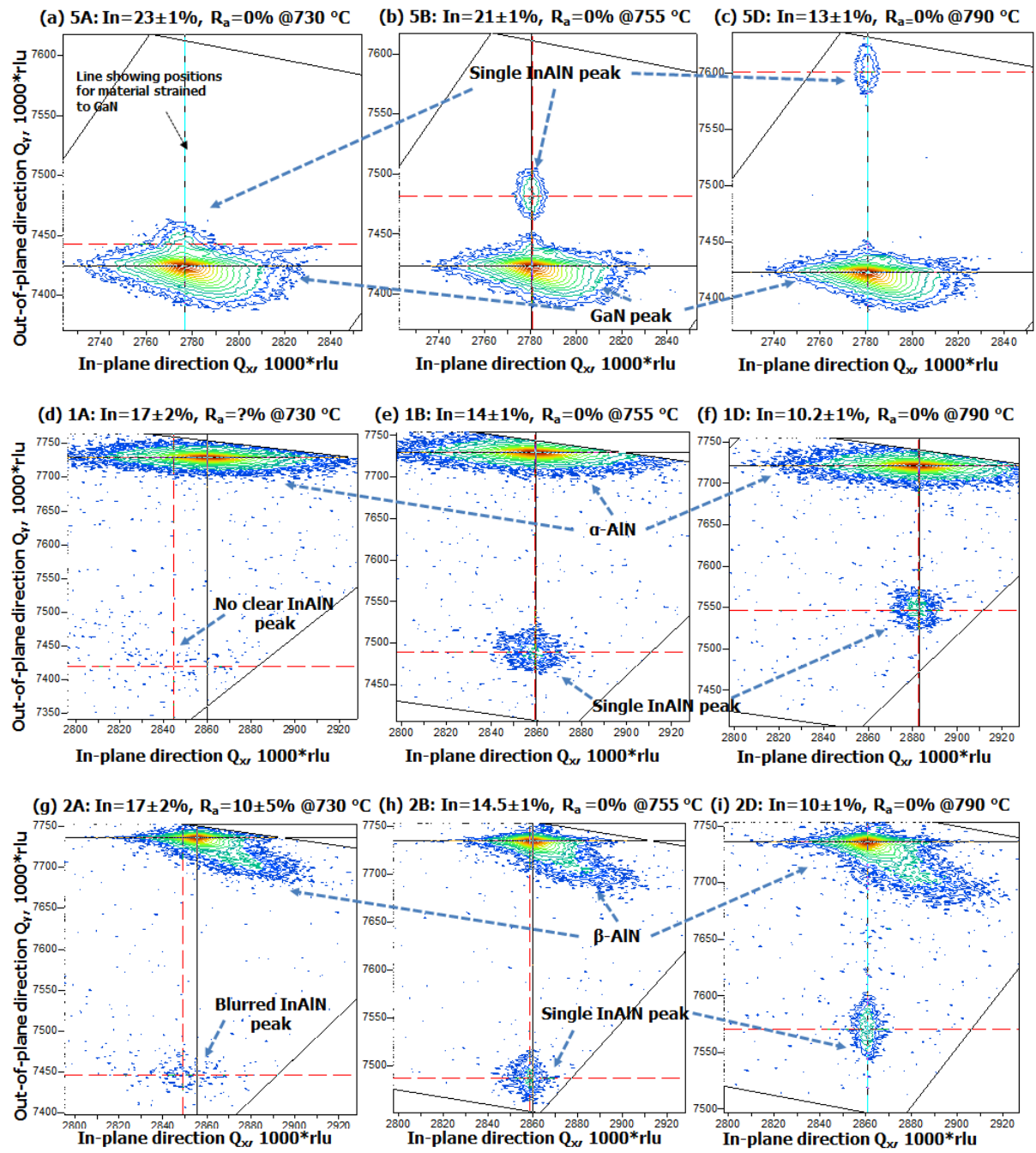
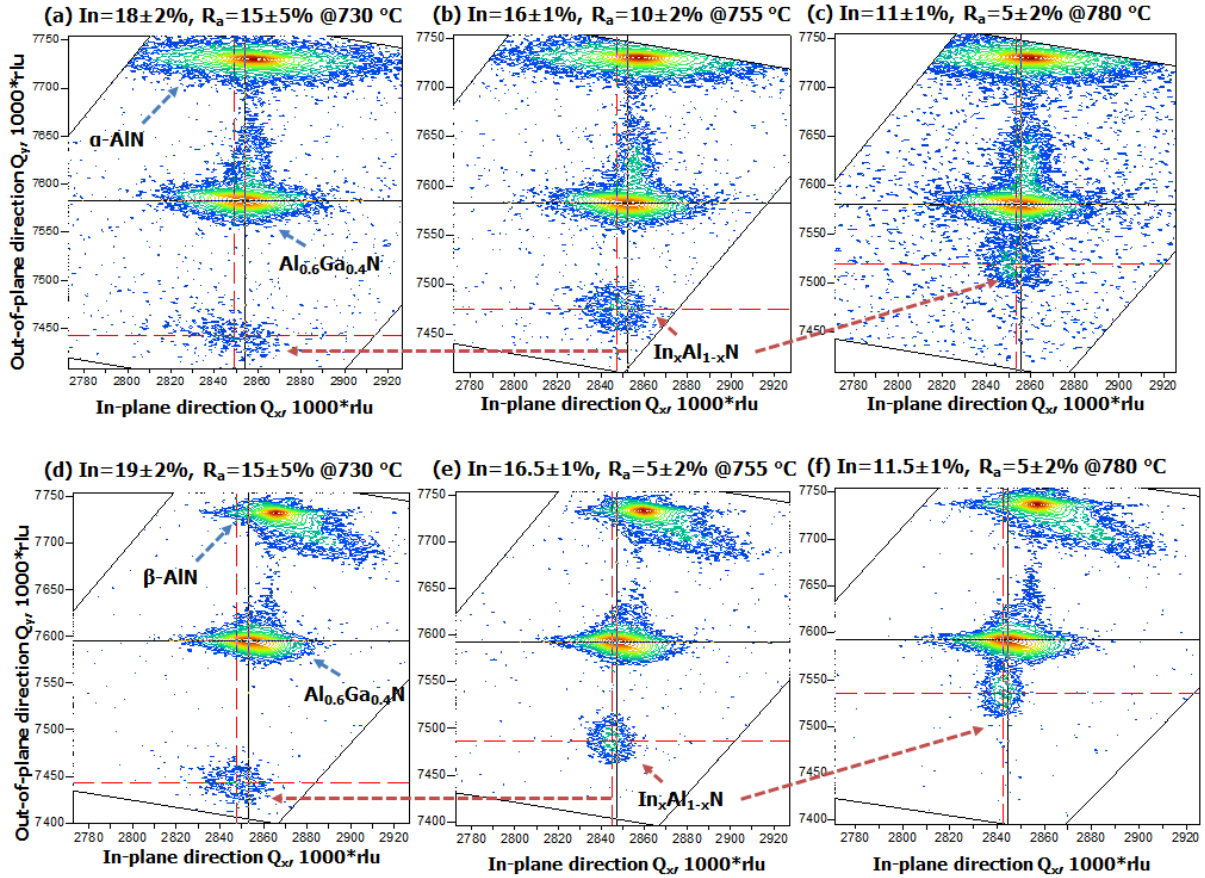


Figure 7.4:  $(10\bar{1}5)$   $\omega/2\theta$ - $\omega$  RSMs of  $\text{In}_x\text{Al}_{1-x}\text{N}$  thin films grown on the (a-c) GaN, (d-f)  $\alpha$ -AlN and (g-i)  $\beta$ -AlN templates with different growth temperature, respectively.



**Figure 7.5: (1015)  $\omega/2\theta$ - $\omega$  RSMs of  $\text{In}_x\text{Al}_{1-x}\text{N}$  thin films grown on the (a-c)  $\text{Al}_{0.6}\text{Ga}_{0.4}\text{N}/\alpha\text{-AlN}$  and (d-f)  $\text{Al}_{0.6}\text{Ga}_{0.4}\text{N}/\beta\text{-AlN}$  templates with different growth temperature, respectively.**

The composition of the  $\text{In}_x\text{Al}_{1-x}\text{N}$  epilayers was calculated from the average lattice parameters measured in XRD. Variation of InN molar fraction in  $\text{In}_x\text{Al}_{1-x}\text{N}$  with growth temperature grown on different templates is shown in Figure 7.6. Firstly, it has been observed that the higher temperature growths result in lower indium compositions because of a higher indium desorption rate. Secondly, the deviations of indium composition have been found showing that the indium incorporated into the epilayer is higher grown on larger in-plane lattice parameter templates than that grown on smaller in-plane lattice parameter templates. For example, an  $\text{In}_x\text{Al}_{1-x}\text{N}$  thin film grown at 730 °C, the indium composition of the sample 1A ( $\alpha\text{-AlN}$ ) is determined to be about 17%, a slightly lower In content as compared to sample 3A ( $\text{AlGa}\text{N}$  on  $\alpha\text{-AlN}$ ) with about 18% indium content. As for sample 5A ( $\text{Ga}\text{N}$ ), the In content was measured to be approximately 23%, indicating a significant increase in comparison to samples 1A and 3A.

The pronounced variation in the indium content may be caused by two effects. One phenomenon could be explained by the modification of the hydrostatic strain component [30, 31]. Hence, the bond length of the  $\text{In}_x\text{Al}_{1-x}\text{N}$  is affected, ultimately enabling more indium to

be incorporated under less compressive strain, while this “strain pulling effect” (“composition pulling effect”) is the more likely an alternative possibility. Another effect might be an influence of V-pits on the composition profile of  $\text{In}_x\text{Al}_{1-x}\text{N}$  samples. It has been proposed that the coalescence of V-pits in thick  $\text{In}_x\text{Al}_{1-x}\text{N}$  layers can lead to a higher or lower In content in the surface layers due to differential incorporation of In occurring on the concave or convex shaped surfaces of the V-pits [20, 32, 33]. V-pit features are observed in Figures 7.7 and 7.8 and will be discussed in the next section.

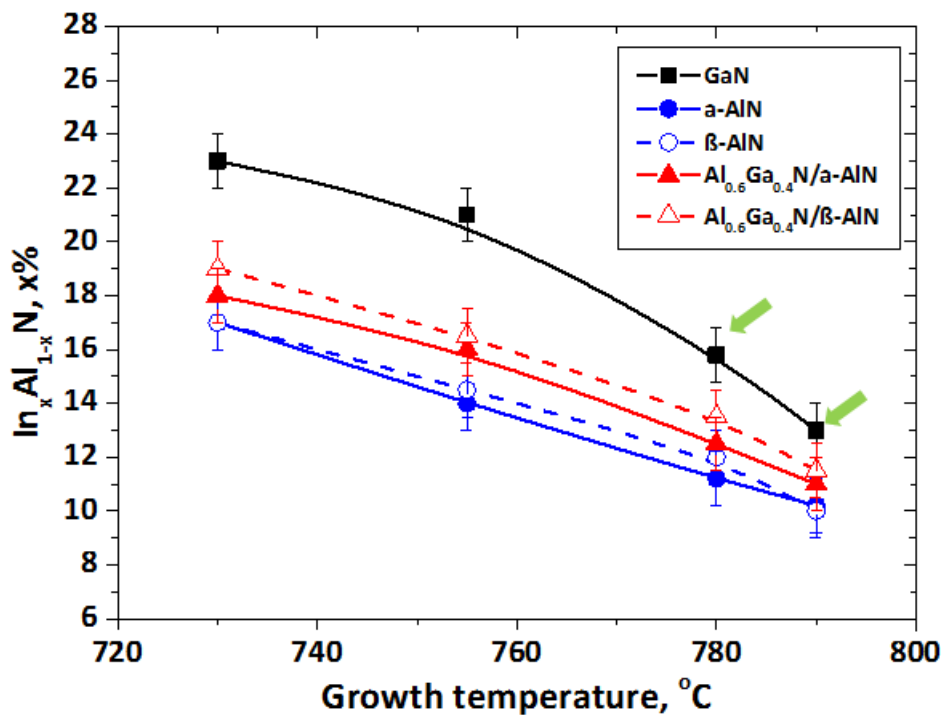


Figure 7.6: Variation of InN molar fraction in  $\text{In}_x\text{Al}_{1-x}\text{N}$  with growth temperature grown on different templates. Only two samples were grown under tensile strain (indicated with green arrows), rest of them were grown under compressive strain.

## AFM measurements

$1 \times 1 \mu\text{m}^2$  AFM images of the  $\text{In}_x\text{Al}_{1-x}\text{N}$  thin films grown on the GaN,  $\alpha\text{-AlN}$  and  $\beta\text{-AlN}$  templates are showed in Figure 7.7.

Figures 7.7 (a)-(d) display the evolution of the surface morphology of  $\text{In}_x\text{Al}_{1-x}\text{N}$  thin films grown on GaN templates at different growth temperatures. A high density of white dots has been observed for samples from 5A to 5D of approximately 5 nm in height and 20 nm in diameter for each dot. It is difficult to identify their origin. As measured by XRD (0002)  $\omega/2\theta$  scan, there was no peak at around  $16.5^\circ$ , suggesting they were not from metallic indium

droplets. The regular round surface hillocks of the order 100 nm in diameter become clearer with increasing growth temperature, which have been previously observed on InAlN by other research groups [1, 25, 34].

The similar trends of surface morphology evolution with respect to growth temperature have been also observed grown on  $\alpha$ - and  $\beta$ -AlN templates. At 730°C the surface consists of nanoscale three-dimensional (3D) islands  $40\pm 10$  nm in diameter for Sample 1A and 2A [Figures 7.7 (e) and (i)]. As the growth temperature increases to 755°C [Figures 7.7 (f) and (j)], the regular round hillocks are observed, with pits (or voids) some of which are linked to threading dislocations [35]. Further increase of growth temperature to 790°C [Figure 7.7 (g), (k), (h) and (l)], used to the hillocks stop having rounded sides and becoming instead more terraced, with each hillock having one or two concentric steps.

$1\times 1\ \mu\text{m}^2$  AFM images of the  $\text{In}_x\text{Al}_{1-x}\text{N}$  thin films grown on the  $\text{Al}_{0.6}\text{Ga}_{0.4}\text{N}/\alpha\text{-AlN}$  and  $\text{Al}_{0.6}\text{Ga}_{0.4}\text{N}/\beta\text{-AlN}$  templates are shown in Figure 7.8. At 730 °C [Figure 7.8 (a)] nanoscale 3D islands similar to those observed on AlN can again be seen in Sample 3A and these are slightly larger at 40 nm in diameter. On the other hand, a high density of pits appears in Sample 4A. The size of pit is around 20 nm in diameter, which should be a V-shaped void (V-defect). They are formed when a threading dislocation, usually generated at the InAlN/AlGaN, AlGaN/AlN and/or AlN/sapphire interface propagates up into the  $\text{In}_x\text{Al}_{1-x}\text{N}$  epilayer and ultimately opens up as an inverted hexagonal pyramidal pit on the film surface [36]. With further increasing growth temperature, the surface morphology evolution of the  $\text{In}_x\text{Al}_{1-x}\text{N}$  films on the  $\text{Al}_{0.6}\text{Ga}_{0.4}\text{N}/\text{AlN}$  templates exhibits a similar trend as the samples grown on AlN templates [Figures 7.8 (b-d) and (f-h)].

RMS roughness has been calculated for four  $1\times 1\ \mu\text{m}^2$  AFM images of each sample. The average results are plotted in Figure 7.9. The small scale roughness over a  $1\ \mu\text{m}^2$  field decreased as the epilayer temperature increased, perhaps because of increased surface diffusion at the higher temperatures promoting diffusion length of Al adatoms. Magalhães et al [20] suggested that high surface roughness promotes the formation of V-pits due to the preferential growth on inclined facets of the 3D surface structures and subsequent coalescence of these growth fronts. Therefore, the high density of V-pits which provide a local increase in the film surface area, should relieve some amount of strain and promote strain relaxation as seen in Sample 1A to 4A.



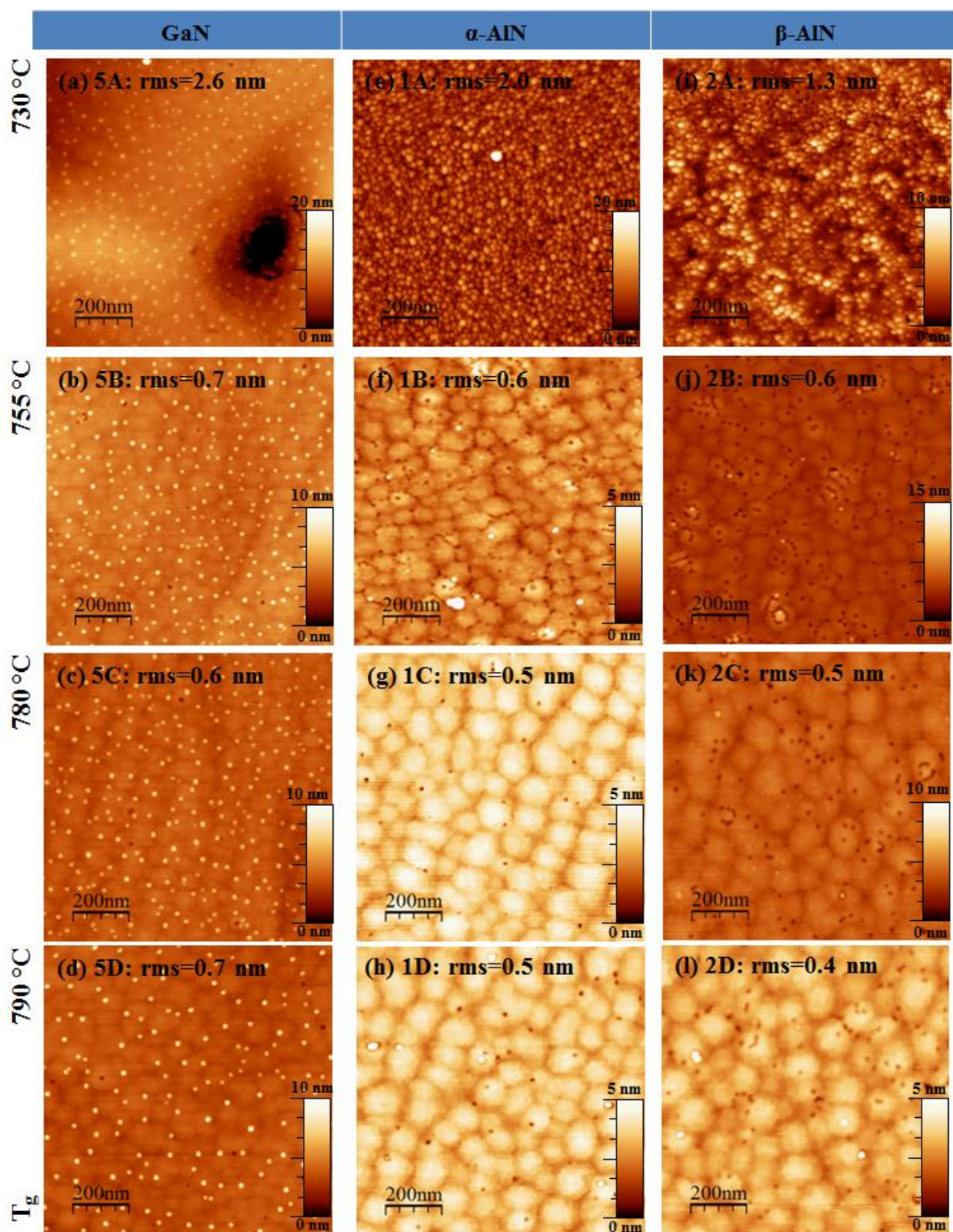


Figure 7.7:  $1 \times 1 \mu\text{m}^2$  AFM images of InAlN grown on GaN (a-d),  $\alpha$ -AlN (e-h) and  $\beta$ -AlN (i-l) templates with different growth temperature ( $T_g$ ).

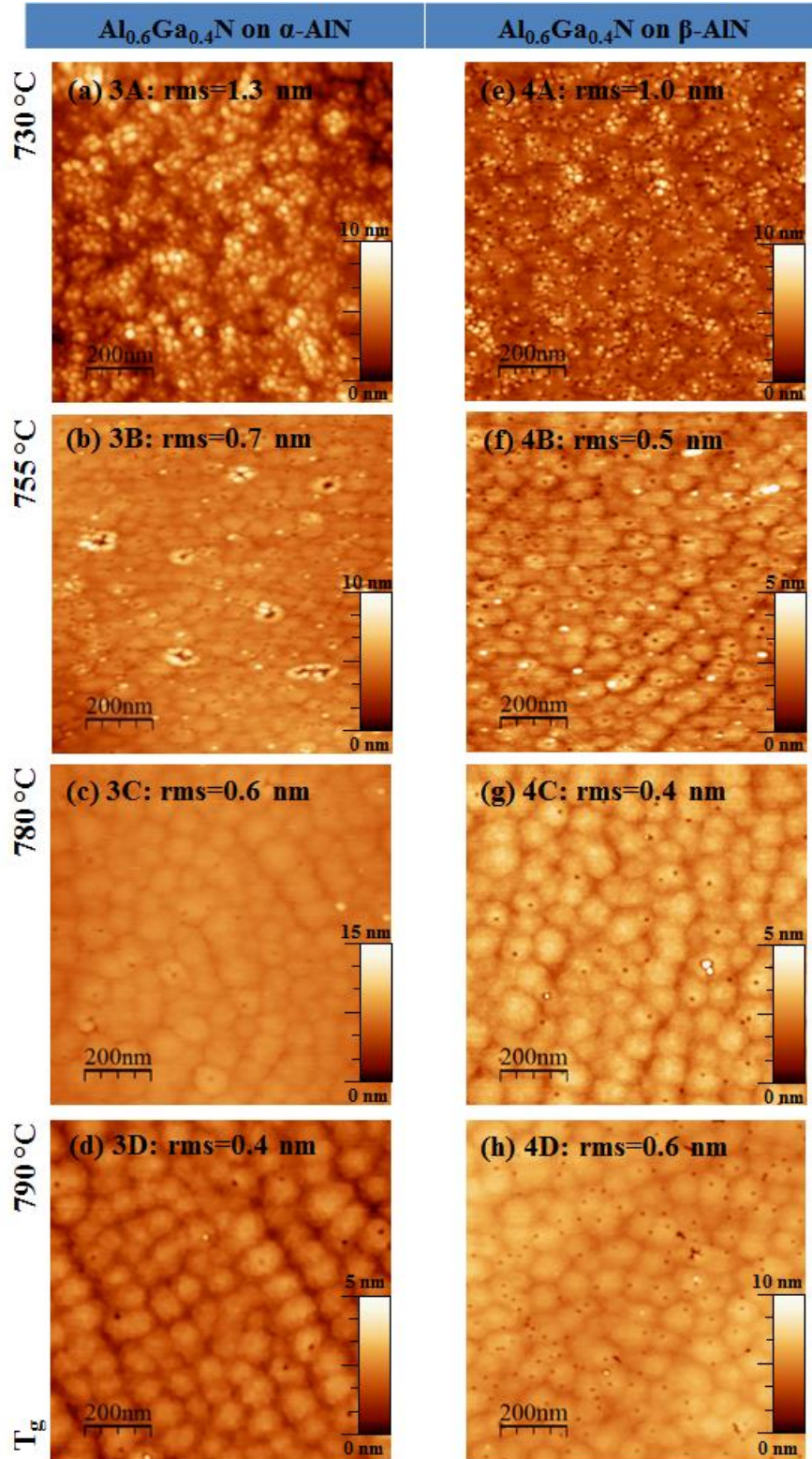


Figure 7.8:  $1 \times 1 \mu\text{m}^2$  AFM images of InAlN grown on  $\text{Al}_{0.6}\text{Ga}_{0.4}\text{N}/\alpha\text{-AlN}$  (a-d) and  $\text{Al}_{0.6}\text{Ga}_{0.4}\text{N}/\beta\text{-AlN}$  (e-h) templates with different growth temperature ( $T_g$ ).



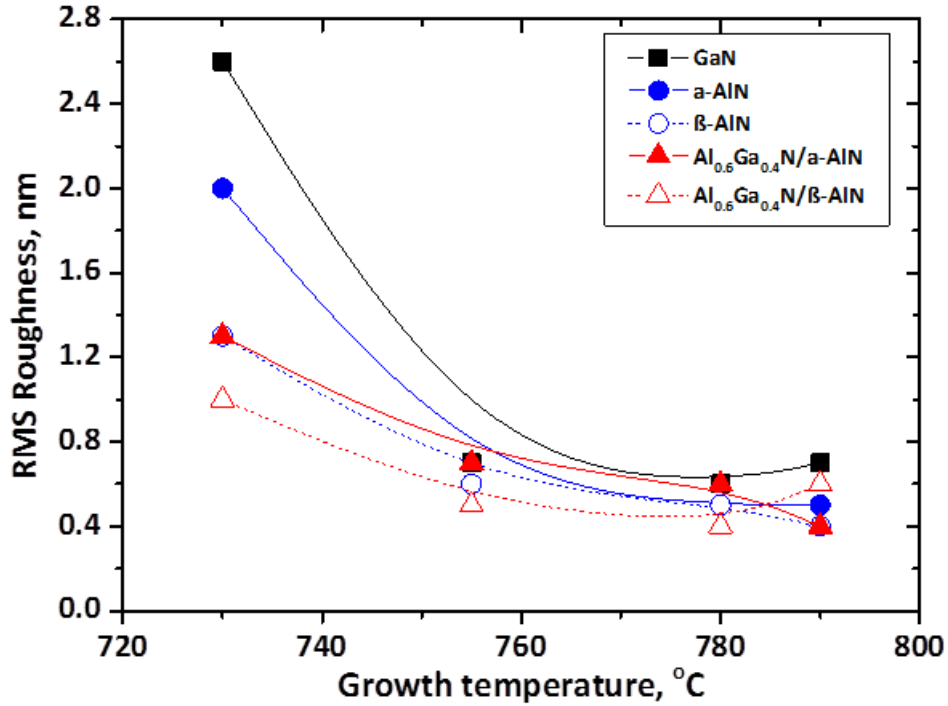


Figure 7.9: variation of surface roughness with growth temperature over a  $1 \times 1 \mu\text{m}^2$  AFM images grown on different templates.

## PL measurements

The 244 nm laser-excited RT-PL spectra of the  $\text{In}_x\text{Al}_{1-x}\text{N}$  thin films are shown in Figure 7.10. For the  $\text{In}_x\text{Al}_{1-x}\text{N}$  layers grown on GaN templates (Figure 7.10), they have a very sharp NBE emission peak at  $\sim 360$  nm with a FWHM of around 4 nm from the underlying GaN template, and a relatively broad emission band around GaN band-edge emission attributed to a band-to-band emission from the  $\text{In}_x\text{Al}_{1-x}\text{N}$  epilayer. It is consistent with the band-to-band luminescence we expected from the  $\text{In}_x\text{Al}_{1-x}\text{N}$  epilayer with the estimated In content. This  $\text{In}_x\text{Al}_{1-x}\text{N}$  band-to-band emission exhibits a clear blueshift with decreasing InN fraction. A similar behaviour has been observed in K. Wang et al [16]. Meanwhile, a yellow band luminescence centred at 2.25 eV (peak position is around 550 nm) is observed for all samples may due to the deep donor complex  $(\text{C}_\text{N}-\text{O}_\text{N})^0$  [37, 38]. The intensity of this defect-related emission around 550 nm increases as indium composition increases (reducing growth temperature) in the  $\text{In}_x\text{Al}_{1-x}\text{N}$  thin films, indicating that point defects maybe easier to generate at high InN molar fraction during InAlN growth.

For the  $\text{In}_x\text{Al}_{1-x}\text{N}$  layers grown on  $\text{Al}_{0.6}\text{Ga}_{0.4}\text{N}/\beta\text{-AlN}$  template [Figure 7.10 (b)], there are four main RT PL emission peaks in this spectrum: (1) a sharp peak at 260 nm, which is



attributed to the NBE emission from the AlGa<sub>x</sub>N buffer layer; (2) a relative broad emission band on the lower energy side, which is attributed to band-to-band emission from the In<sub>x</sub>Al<sub>1-x</sub>N epilayers (4A and 4B), apart from samples 4C and 4D; (3) defect-related indigo luminescence peak at around 410 nm, and (4) defect-related green and yellow band luminescence peak at around 540 nm. These defect-related luminescences could be principally from In<sub>x</sub>Al<sub>1-x</sub>N epilayers, as we do not observe such luminescence from undoped AlGa<sub>x</sub>N template. A general rise in defect-related indigo luminescence intensity and reduction in defect-related green and yellow band luminescence intensity with decreasing In content in the RT-PL spectra was found in both Figures [Figure 7.11 (a) and (b)]. Such a large peak position and intensity difference could be possibly ascribed to In composition fluctuations or to the presence of deep defects or impurities acting as preferential recombination centres.

Both figures [Figure 7.10 and Figure 7.11 (b)] show a stronger and clearer InAlN band-to-band emission with higher In content, which could be attributed to a stronger carrier localization effect. However, for In<sub>x</sub>Al<sub>1-x</sub>N thin films grown on Al<sub>0.6</sub>Ga<sub>0.4</sub>N/ $\alpha$ -AlN [Figure 7.11 (a)] and AlN templates, it is very difficult to distinguish the InAlN band-to-band emission, because other defect-related emissions are dominant, especially with lower In content. These results may indicate several possible effects: (1) the increase of compressive strain may improve the uniform distribution of In in In-rich InAlN epilayer, thus, less In cluster and phase segregation leading to a lower carrier localization effect for InAlN epilayers, (2) compressive strain in InAlN affects the defect formation energy in such thin films, and (3) the screw type dislocations may introduce more non-radiative recombination centres and enhance defect-related luminescence than edge type dislocations in InAlN thin films.

### 7.2.3 Conclusion

This work explores the possibility of the growth of In<sub>x</sub>Al<sub>1-x</sub>N on Al<sub>y</sub>Ga<sub>1-y</sub>N templates by MOVPE, which is important in facilitating the production of InAlN/AlGa<sub>x</sub>N UV LEDs.

XRD results indicate that the crystal quality of In<sub>x</sub>Al<sub>1-x</sub>N degrades as the indium composition increases. It also has shown that the indium incorporation increases as the growth temperature is decreased. Meanwhile, our observations demonstrate that the indium incorporation efficiency in *c*-oriented is governed by the underlying film strain state and/or possibly the inclined facets of V-pits. This will become a limitation towards growth of high indium

containing  $\text{In}_x\text{Al}_{1-x}\text{N}$  QW structures for long wavelength light emitting structures using  $\text{Al}(\text{Ga})\text{N}$  template.

A similar surface evolution has been found for the  $\text{In}_x\text{Al}_{1-x}\text{N}$  layers grown on  $\text{AlGaIn}$  templates as well as  $\text{AlN}$  templates. The growth temperature window is strongly limited due to  $\text{In}$  desorption, which in turn hinders the surface diffusion length of  $\text{Al}$  adatoms. As a consequence, it will be seen that surface kinetics plays a major role and have detrimental effects on the surface roughening.

Finally, RT luminescence from  $\text{In}_x\text{Al}_{1-x}\text{N}$  band-to-band emission is found to decay significantly with decreasing  $\text{In}$  content has been observed, it could be due to a decrease in the carrier localization effect or due to changes in the formation energy of non-radiative effect centres. Based on these results we think that  $\text{InAlN}$  can provide an alternative QW material for shallow UV light emitters with limited wavelength range at around 320 to 360 nm. In all case, a broad PL peak at lower energy side (2.0 to 3.3 eV) is attributed by a defect-band that develops with increasing  $\text{In}$  content.

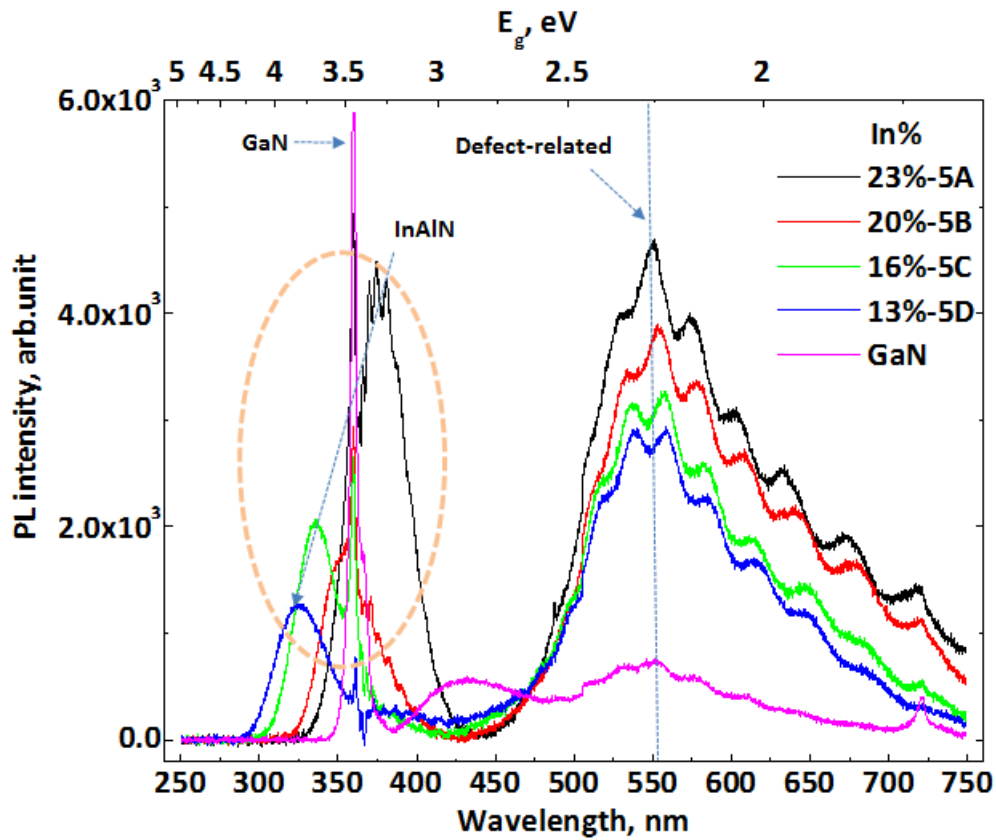


Figure 7.10: RT-PL excited by the laser at RT for  $\text{In}_x\text{Al}_{1-x}\text{N}$  thin films grown on GaN.

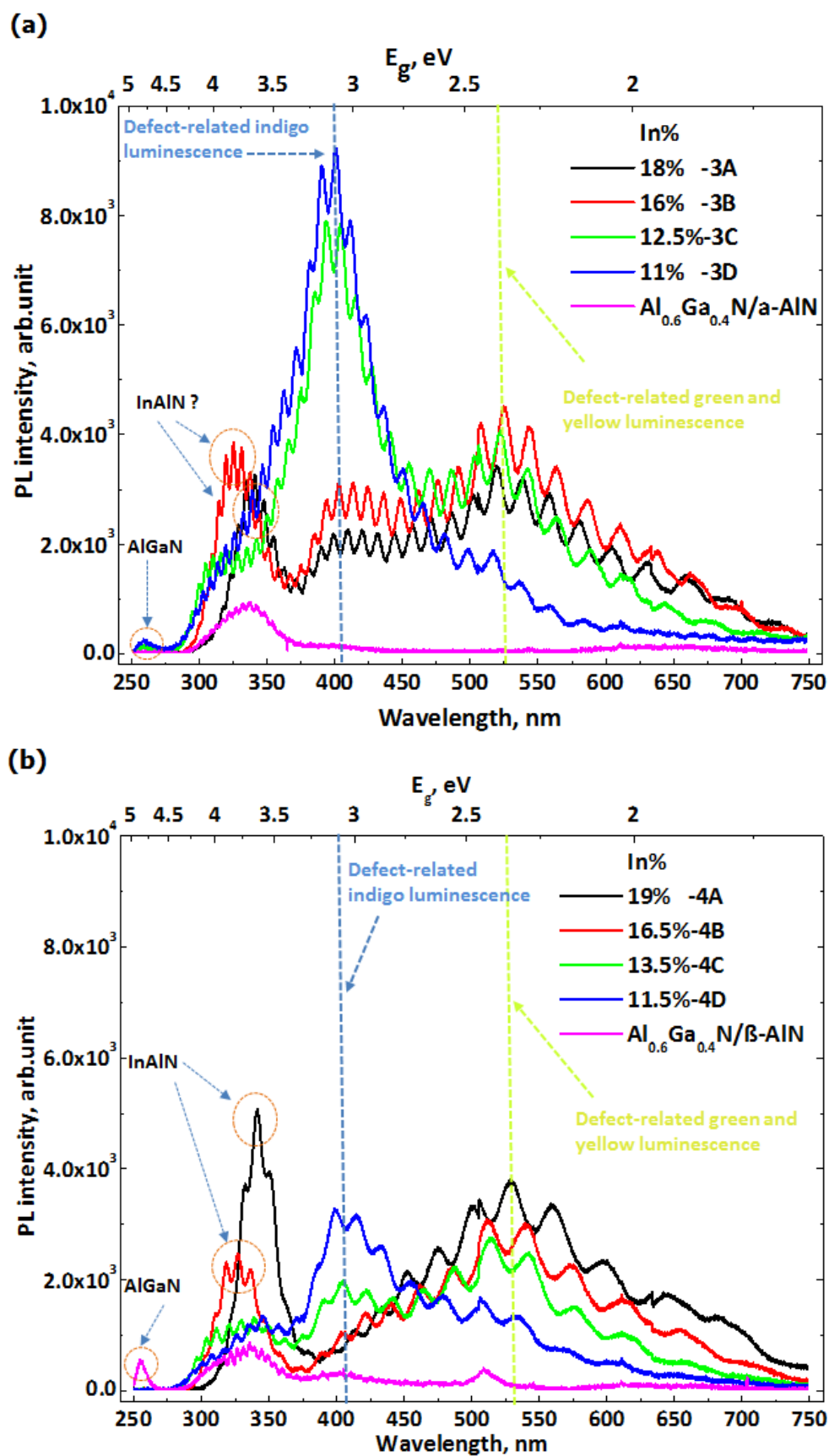


Figure 7.11: PL excited by the laser at RT for  $\text{In}_x\text{Al}_{1-x}\text{N}$  thin films grown on (a)  $\text{Al}_{0.6}\text{Ga}_{0.4}\text{N/a-AlN}$  templates and (b)  $\text{Al}_{0.6}\text{Ga}_{0.4}\text{N/}\beta\text{-AlN}$  templates.

### 7.3 InAlN/AlGaN multiple quantum wells (MQWs)

Generally, the light emission efficiency from a device active region depends on many factors, such as quantum well and barrier material quality, well width, barrier width, and band-offset ( $\Delta E_C$  and  $\Delta E_V$ ). After obtaining InAlN thin films in the last section, the target of this section is obtaining emission wavelength between 300 and 350 nm using InAlN as QW material. The microstructural and optical differences between samples with varying growth temperature of the QW structures will be studied.

#### 7.3.1 Experimental details

All samples were grown by metalorganic vapour phase epitaxy (MOVPE) on  $\alpha$ -AlN templates (as described in Section 4.5.3) in an Aixtron close coupled showerhead 3×2” MOVPE reactor using trimethylaluminium (TMAI), trimethylgallium (TMGa), trimethylindium (TMIn) and ammonia (NH<sub>3</sub>) as precursors.  $\alpha$ -AlN templates were loaded into the reactor and then heated in an ammonia–hydrogen ambient to a set point of 1110 °C with a holding time of 10 mins in order to clean the surface and remove any oxide layer.

The growth of the 5×InAlN/AlGaN MQWs was started with an AlN connecting layer of 100 nm thick to bury the regrowth interface, and followed by a 1  $\mu$ m-thick undoped Al<sub>0.6</sub>Ga<sub>0.4</sub>N buffer layer. In order to get the emission wavelength between 300 and 350 nm, the indium composition ( $y_{QW}$ ) of QWs were adjusted depending on growth temperature of quantum well ( $T_{QW}$ ) from 710 to 790°C with a constant QW width ( $d_{QW}$ ) of 2 nm. Due to only very minor changes in the growth rate of InAlN as shown in Section 7.2, the QW growth time was maintained constant at 18 seconds. In order to balance In desorption and barrier crystal quality, a quasi-two-temperature (Q2T) approach was employed, and about a 2 nm Al<sub>0.85</sub>Ga<sub>0.15</sub>N protective cap was grown at the QW growth temperature on each QW. After that, reactor temperature was ramped up to 1110 °C to grow about an 8 nm thick Al<sub>0.6</sub>Ga<sub>0.4</sub>N barrier. After the last barrier, the sample was cooled to room-temperature in NH<sub>3</sub> atmosphere to freeze the surface morphology. A schematic of the sample structure and Q2T approach are shown in Figure 7.12. Growth conditions are noted in Table 7. 3.

To analyse these samples, XRD was applied to probe the layer composition, thickness and strain state by using commercial software (X’pert Epitaxy, Philips). These can be easily measured for our samples as the epilayers are under symmetric biaxial stress and a reliable set of calculated elastic constants are available. The optical properties of the quantum well

will be probed by room-temperature (RT) photoluminescence (PL) spectroscopy. PL was excited using a 244 nm laser and detected using iHR320 Horiba imaging spectrometer equipped with a CCD camera and photomultiplier.

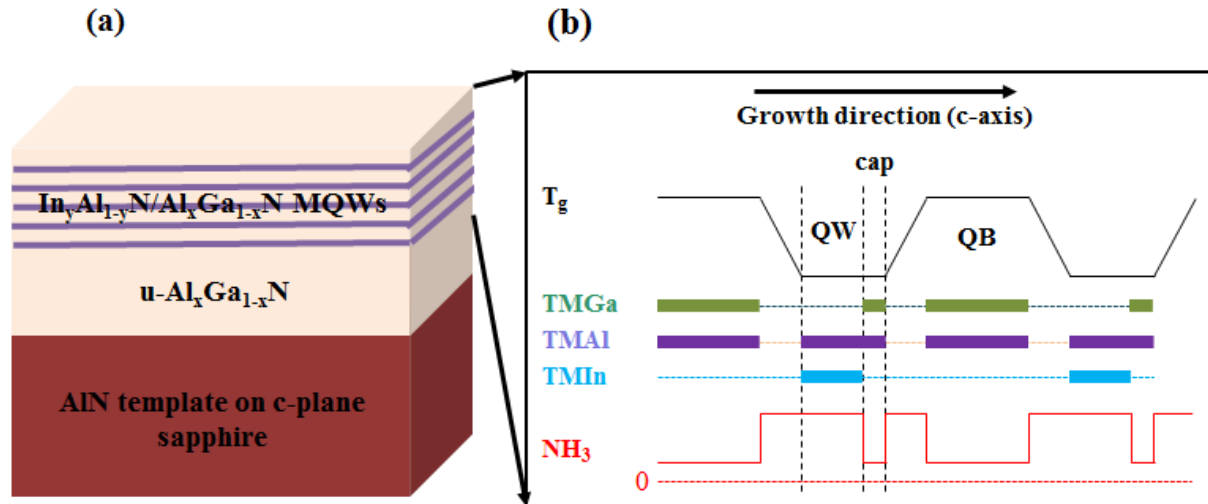


Figure 7.12: (a) A schematic of the MQWs sample structure and (b) Q2T approach for MQWs growth.

	T <sub>g</sub> (°C)	TMIn (μmol/min)	TMAI (μmol/min)	TMGa (μmol/min)	NH <sub>3</sub> (mmol/min)	Time (s)	Pressure (mbar)
QW	710-790	5	5.2	-	56	36	70
Cap	710-790	-	5.2	10.4	12.2	18	50
Barrier	1110	-	5.2	10.4	12.2	74	50

Table 7.3: Growth parameters for InAlN/AlGaN active region.

### 7.3.2 Results and discussion

In Figure 7.13, XRD (0002)  $\omega$ -2 $\theta$  scans show InAlN/AlGaN MQWs grown at 710, 730, 750 and 790 °C, respectively. Distinct interference fringes are observed indicating smooth surfaces and interfaces between each layer. The thickness of quantum well, barrier and cap layer as well as indium and aluminium composition of the samples were determined by simulations of (0002)  $\omega$ -2 $\theta$  scans with the use of XRD X'pert Epitaxy software. An exact model of sample structure QW grown at 710 °C was used as in Figure 7.12, fitting that obtained from XRD triple-axis measurement. It should be noted that some calibration runs were performed separately; for example, a thin AlGa<sub>0.3</sub>N cap layers grown at QW temperature

and ramped to AlGaIn temperature series, but their results are not shown in this thesis. As  $T_{QW}$  increases from 710 to 790 °C, the indium incorporation decreases substantially as shown in Figure 7.14, because of a large indium desorption rate. This is consistent with the results shown in Figure 7.6, Section 7.2.2.

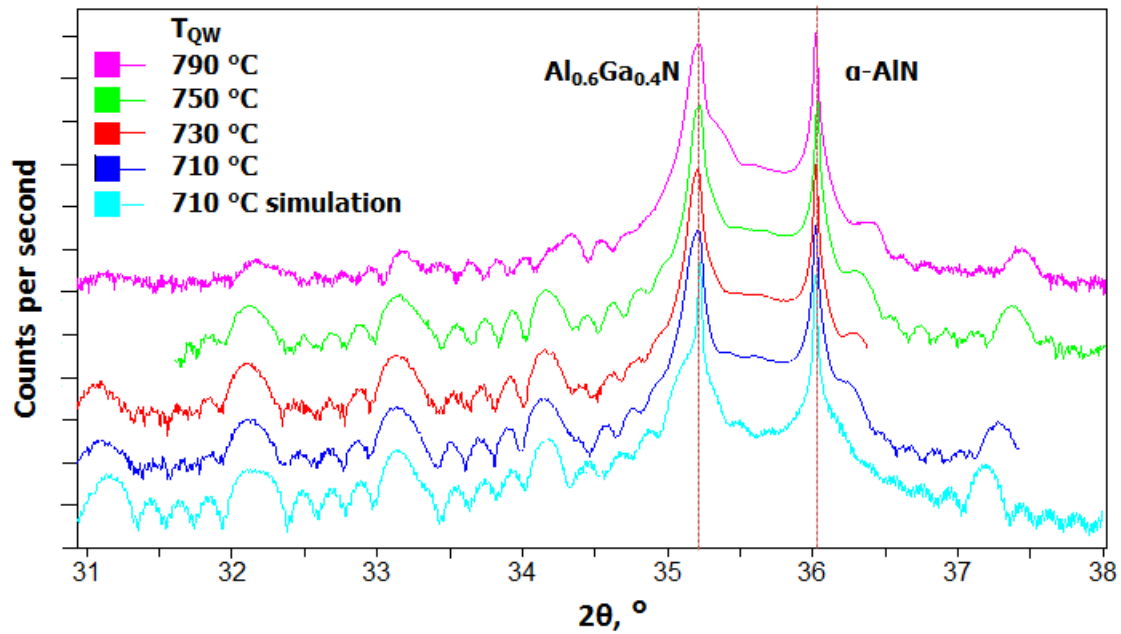


Figure 7.13: The growth of MQWs is confirmed by the satellite peaks of XRD (0002)  $\omega$ -2 $\theta$  scans. From those peaks, well barrier, well widths and In composition were estimated. The simulation of estimated values fit to that obtained for QW grown at 710 °C.

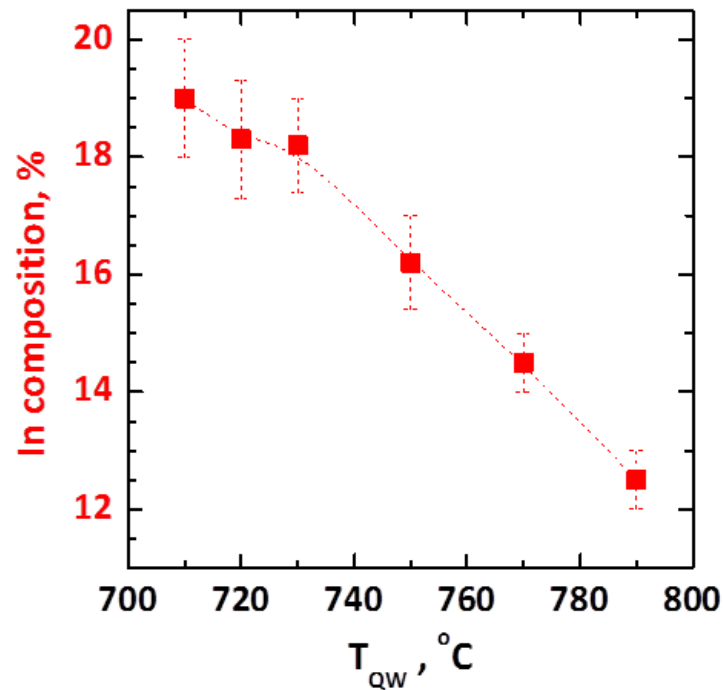
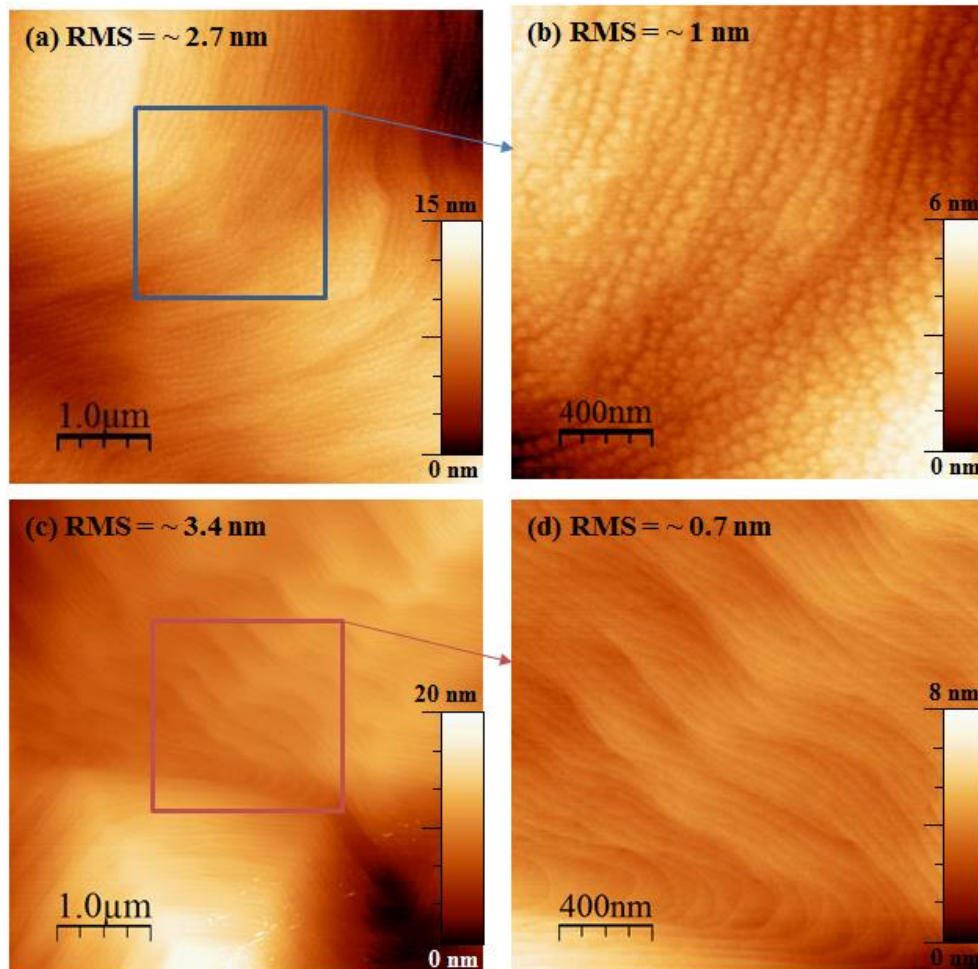


Figure 7.14: Indium content measured by XRD as a function of the InAlN quantum well growth temperature.

In order to investigate the surface morphology of the structures, AFM scans were performed. The surface morphology of MQW sample without last cap and barrier was studied and the representative AFM images are shown in Figures 7.15 (a) and (b). Granular surface structures exhibiting grain sizes between 30 and 60 nm become apparent for last 2 nm thick QW layer, and the RMS surface roughness is around 2.7 nm and 1.0 nm measured within  $5 \times 5 \mu\text{m}^2$  and  $2 \times 2 \mu\text{m}^2$  scans, respectively. On the other hand, the surface morphology of MQW sample with last cap and barrier are shown in Figures 7.15 (c) and (d). The clear atomic steps on the sides of the spiral hillocks were observed. The presence of large hexagonal hillock on the surface is associated with dislocations with a screw-component threading from the template, which is described in section 5.3.3. The RMS surface roughness is around 3.4 nm and 0.7 nm measured within  $5 \times 5 \mu\text{m}^2$  and  $2 \times 2 \mu\text{m}^2$  scans, respectively. These AFM scans suggest that sharp interfaces between QW, cap and barrier layers.



**Figure 7.15:** (a)  $5 \times 5 \mu\text{m}^2$  and (b)  $2 \times 2 \mu\text{m}^2$  surface morphology of MQWs without last cap and barrier layer; (c)  $5 \times 5 \mu\text{m}^2$  and (d)  $2 \times 2 \mu\text{m}^2$  surface morphology of MQWs with last cap and barrier layer by AFM measurements.

The RT PL spectra of InAlN/AlGaN MQWs samples are shown in Figure 7.16 (a). Four main PL features were in each spectrum: (1) a sharp peak at 260 nm, which is attributed to the near band-edge (NBE) emission from the AlGaN buffer layer; (2) a relatively broad emission band on the lower energy side, which is attributed to intrinsic emission from the  $\text{In}_x\text{Al}_{1-x}\text{N}$  QWs region (InAlN band to band emission); (3) defect-related indigo luminescence at 390-410 nm and (4) defect-related green and yellow band luminescence at 490-630 nm. Although high absorption of exciting light in MQWs region at high excitation energy is expected, the AlGaN buffer layers have also been excited either by the light penetrating the MQWs region or by the diffused excess carriers. In addition, a change in defect-related emission position and intensity are similar with our previous observation in Section 7.2. Comparison of InAlN/AlGaN MQWs PL spectra with that of AlGaN templates (as shown in Chapter 5) and 23 nm thick single InAlN epilayers series (as shown in previous Section 7.2) shows that these defect-related bands may attributed at least in point to the InAlN QW region. The trend suggests that the presence of deep defects or impurities act as preferential recombination centres with lower In content, lowering the near band edge intensity while increasing the indigo emission band.

The PL peak position ( $\lambda_{PL}$ ), integrated PL intensity ( $I_{PL}$ ) and full-width-half maximum of QW-related peak ( $FWHM_{PL}$ ) as function of indium composition are summarized in Figure 7.16 (b). The QW-related emissions are observed to shift from 308 nm (4.03 eV) to 358 nm (3.46 eV) as the InN molar fraction increases from 0.125 to 0.190 by changing QW growth temperature. The emission energy displays a linear dependence on the InN fraction in the studied composition range. Similar linear behaviours are also observed in literature data for InN molar fraction > 8% [39, 40, 41, 42, 43]. The PL peak intensities normalized to the brightest are plotted with solid square symbols. The highest PL intensity is obtained for QW grown at 730 °C. It is shown that the intensity significantly increases from the 790 °C sample to the 730 °C sample and then decreases. This drop could be explained by a high dislocation density that results from a large lattice mismatch between InAlN and AlGaN or that the lower growth temperature is leading to a higher degree of point defect incorporation within the InAlN QW. The FWHM of the QW-related emission peak for each sample was also calculated. The peak was found to sharper with increasing In content (lower QW growth temperature) with a linewidth of 28 nm at 710 °C indicating a good homogeneity of the indium distribution (taking into account the large bandgap different between AlN and InN).



### **7.3.3 Conclusion**

In this section, it was demonstrated that the RT optical properties of InAlN/AlGaIn MQWs were affected by In content (QW growth temperature). We found that the presence of deep defects or impurities acting as preferential recombination centres is dominant in RT-PL spectra with lower In content. As a result of optimisation, strong RT luminescence from InAlN/AlGaIn MQWs has been observed in the UV spectral range from 320 to 350 nm. This indicates that the InAlN alloys used as QW active region could be an alternative material for producing an intense emission in the shallow UV spectral range.

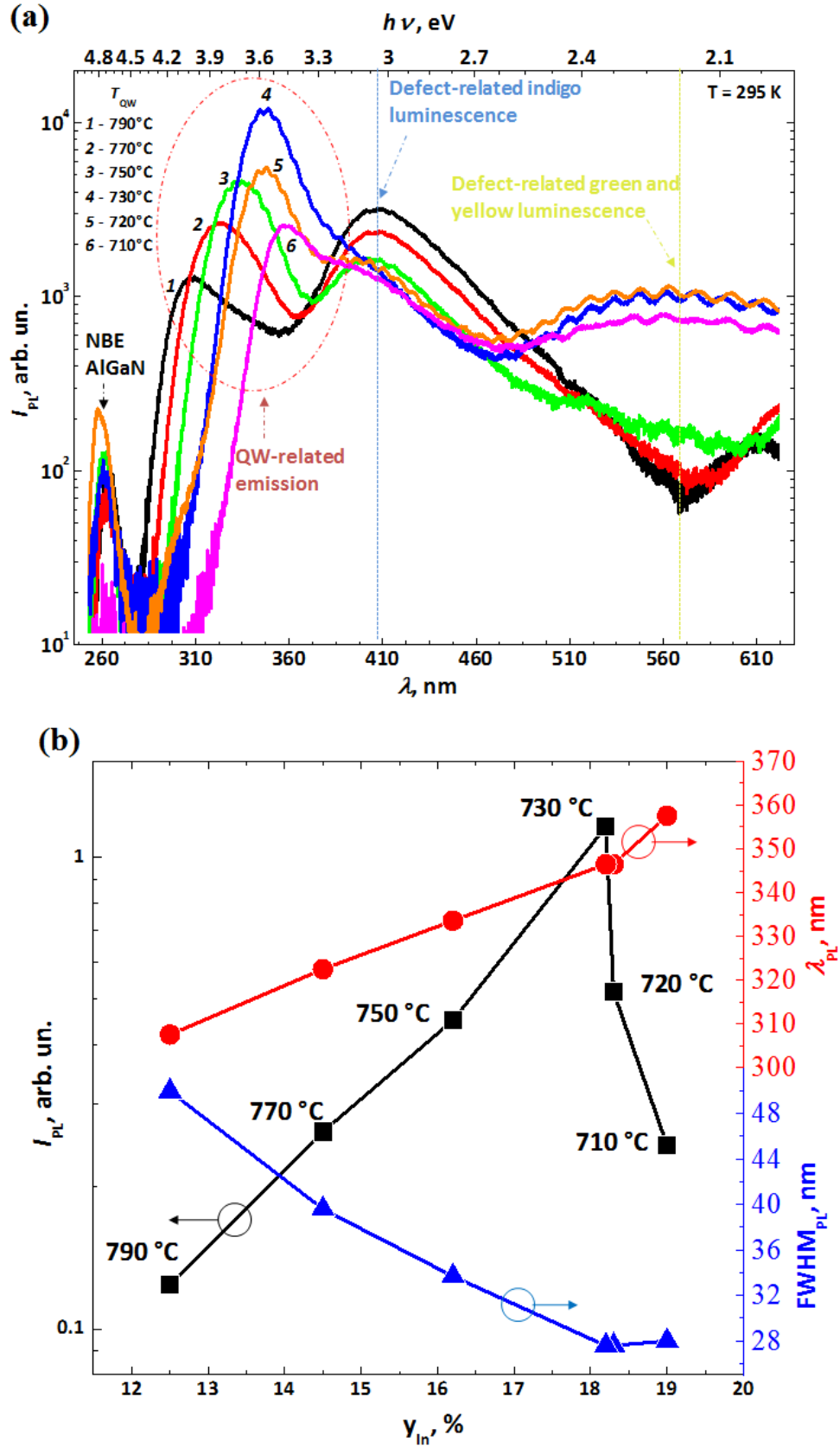


Figure 7.16: (a) RT PL spectra from InAlN/AlGaN MQWs region with different quantum well growth temperature ( $T_{QW}$ ). The dash circle indicates different emission. (b) Integrated PL intensity ( $I_{PL}$ ), PL peak position ( $\lambda_{PL}$ ) and  $FWHM_{PL}$  as functions of QW indium composition.

## 7.4 Reference:

- [1] R. Butte, J. F. Carlin, E. Feltin, M. Gonschorek, S. Nicolay, G. Christmann, D. Simeonov, A. Castiglia, J. Dorsaz, H. J. Buehlmann, S. Christopoulos, G. B. H. von Hogersthal, A. J. D. Grundy, M. Mosca, C. Pinquier, M. A. Py, F. Demangeot, J. Frandon, P.G. Lagoudakis, J. J. Baumberg, and N. Grandjean, *J. Phys. D.* 40, 6328 (2007).
- [2] D. Dadgar, F. Schulze, J. Bläsing, A. Diez, A. Krost, M. Neuburger, E. Kohn, I. Daumiller, and M. Kunze, *Appl. Phys. Lett.* 85, 5400 (2004).
- [3] M. Gonschorek, J. F. Carlin, E. Feltin, M. A. Py, and N. Grandjean, *Appl. Phys. Lett.* 89, 062106 (2006).
- [4] M. Matloubian, and M. Gershenson, *J. Electron. Mater.* 14, 633 (1985).
- [5] Y. Muramoto, M. Kimura, and S. Nouda, *Semicond. Sci. Technol.* 29, 084004 (2014).
- [6] H. Hirayama, N. Maeda, S. Fujikawa, S. Toyoda, and N. Kamata, *Jpn. J. Appl. Phys.* 53, 100209 (2014).
- [7] M. Shatalov, W. Sun, R. Jain, A. Lunev, X. Hu, A. Dobrinsky, Y. Bilenko, J. Yang, G. A. Garrett, L. E. Rodak, M. Wraback, M. Shur, and R. Gaska, *Semicond. Sci. Technol.* 29, 084007 (2014).
- [8] P. G. Eliseev, P. Perlin, J. Lee, and M. Osinski, *Appl. Phys. Lett.* 71, 569 (1997)
- [9] D. Watson-Parris, M. J. Godfrey, P. Dawson, R. A. Oliver, M. J. Galtrey, M. J. Kappers, and C. J. Humphreys, *Phys. Rev. B* 83, 115321 (2011).
- [10] H. Jeong, H. J. Jeong, H. M. Oh, C. H. Hong, E. K. Suh, G. Lerondel, and M. S. Jeong, *Sci. Rep.* 5, 9373 (2015).
- [11] Z. Li, J. Kang, B.W. Wang, H. Li, Y.H. Weng, Y. Lee, Z. Liu, X. Yi, Z.C. Feng, and G. Wang, *J. Appl. Phys.* 115, 083112 (2014).
- [12] S. Hammersley, D. Watson-Parris, P. Dawson, M. J. Godfrey, T. J. Badcock, M. J. Kappers, C. McAleese, R. A. Oliver, and C. J. Humphreys, *J. Appl. Phys.* 111, 083512 (2012).
- [13] Y. L. Lai, C. P. Liu, Y. H. Lin, T. H. Hsueh, R. M. Lin, D. Y. Lyu, Z. X. Peng, and T. Y. Lin, *Nanotech.* 17, 3734 (2006).
- [14] J. Kamimura, K. Kishino, and A. Kikuchi, *Phys Status Solidi RRL*. 6, 123 (2012).
- [15] S. Yamaguchi, M. Kariya, S. Nitta, T. Takeuchi, C. Wetzel, H. Amano, and I. Akasaki, *Appl. Phys. Lett.* 76, 876 (2000).
- [16] S. Chichibu, A. Uedono, T. Onuma, B. A. Haskell, A. Chakraborty, T. Koyama, P. T. Fini, S. Keller, S. P. DenBaars, J. S. Speck, U. K. Mishra, S. Nakamura, S. Yamaguchi, S. Kamiyama, H. Amano, I. Akasaki, J. Han, and T. Sota, *Nature Mater.* 5, 810 (2006).

- [17] K. Wang, R. W. Martin, D. Amabile, P. R. Edwards, S. Hernandez, E. Nogales, K. P. O'Donnell, K. Lorenz, E. Alves, V. Matias, A. Vantomme, D. Wolverson, and I. M. Watson, *J. Appl. Phys.* 103, 073510 (2008).
- [18] S. F. Chichibu, K. Hazu, K. Furusawa, Y. Ishikawa, T. Onuma, T. Ohtomo, H. Ikeda, and K. Fujito., *J. Appl. Phys.* 116, 213501 (2014).
- [19] V. Z. Zubialeovich, T. C. Sadler, D. V. Dinh, S. N. Alam, H. Li, P. Pampili, and P. J. Parbrook, *J. Lumin.* 155, 108 (2014).
- [20] S. Magalhães, I. M. Watson, S. Pereira, N. Franco, L. T. Tan, R. W. Martin, K. P. O'Donnell, E. Alves, J. P. Araújo, T. Monteiro, and K. Lorenz, *J. Phys. D: Appl. Phys.* 48, 015103 (2015).
- [21] S. Choi, H. J. Kim, Z. Lochner, J. Kim, R. D. Dupuis, A. M. Fischer, R. Juday, Y. Huang, T. Li, J. Y. Huang, F. A. Ponce, and J. H. Ryou, *J. Cryst. Growth.* 388, 137 (2014).
- [22] J. Kim, Z. Lochner, M. H. Ji, S. Choi, H. J. Kim, J. S. Kim, R. D. Dupuis, A. M. Fischer, R. Juday, Y. Huang, T. Li, J. Y. Huang, F. A. Ponce, and J. H. Ryou, *J. Cryst. Growth.* 388, 143 (2014).
- [23] E. Taylora, M. D. Smith, T. C. Sadler, K. Lorenz, H. N. Li, E. Alves, P. J. Parbrook, and R. W. Martin, *J. Cryst. Growth.* 408, 97 (2014).
- [24] M. D. Smith, E. Taylor, T. C. Sadler, V. Z. Zubialeovich, K. Lorenz, H. N. Li, J. O'Connell, E. Alves, J. D. Holmes, R. W. Martin, and P. J. Parbrook, *J. Mater. Chem. C.* 2, 5787 (2014).
- [25] T. C. Sadler, M. J. Kappers and R. A. Oliver, *J. Cryst. Growth.* 311, 3380 (2009).
- [26] I. Horcas, R. Fernandez, J. M. Gomez-Rodriguez, and J. Colchero, *Rev. Sci. Instrum.* 78, 013705 (2007).
- [27] K. Lorenz, N. Franco, E. Alves, I. M. Watson, R. W. Martin, and K. P. O'Donnell, *Phys. Rev. Lett.* 97, 085501 (2006).
- [28] O. Ambacher et al, *J. Phys.: Condens. Matter.* 14, 3399 (2002).
- [29] C. Hums, J. Blasing, A. Dadgar, A. Diez, T. Hempel, J. Christen, A. Krost, K. Lorenz, and E. Alves, *Appl. Phys. Lett.* 90, 022105 (2007).
- [30] B. Reuters, M. Finken, A. Wille, B. Holländer, M. Heuken, H. Kalisch, and A. Vescan, *J. Appl. Phys.* 112, 093524 (2012).
- [31] P. Horenburg, E. R. Bu, U. Rossow, H. Bremers, T. Langer, M. Klisch, and A. Hangleiter, "Strain dependence of In incorporation in m-plane GaInN/GaN multi quantum well structures", 11th International Conference on Nitride Semiconductors, Beijing (2015).
- [32] G. Perillat-Merceroz, G. Cosendey, J. F. Carlin, R. Butté, and N. Grandjean *J. Appl. Phys.* 113, 063506 (2013).

- [33] Q. Y. Wei, T. Li, Y. Huang, J. Y. Huang, Z. T. Chen, T. Egawa and F. A. Ponce, Appl. Phys. Lett. 100, 092101 (2012).
- [34] T. C. Sadler, M. J. Kappers, and R. A. Oliver, Phys. Status. Solidi. C. 6, S666 (2009).
- [35] T. C. Sadler, M. J. Kappers, and R. A. Oliver, J. Phys.: Conf. Ser. 209, 012015 (2010).
- [36] M. A. Moram, C. S. Ghedia, D. V. S. Rao, J. S. Barnard, Y. Zhang, M. J. Kappers, and C. J. Humphreys, J. Appl. Phys. 106, 073513 (2009).
- [37] M. A. Reshchikov, and H. Morkoç, J. Appl. Phys. 97, 061301 (2005).
- [38] D. O. Demchenko, I. C. Diallo, and M. A. Reshchikov, Phys. Rev. Lett. 110, 087404 (2013).
- [39] R. E. Jones, R. Broesler, K. M. Yu, J. W. Ager, E. E. Haller, W. Walukiewicz, X. Chen, and W. J. Schaff, J. Appl. Phys. 104, 123501 (2008).
- [40] E. Iliopoulos, A. Adikimenakis, C. Giesen, M. Heuken, and A. Georgakilas, Appl. Phys. Lett. 92, 191907 (2008).
- [41] E. Sakalauskas, H. Behmenburg, C. Hums, P. Schley, G. Rossbach, C. Giesen, M. Heuken, H. Kalisch, R. H. Jansen, J. Bläsing, A. Dadgar, A. Krost, and R. Goldhahn, J. Phys. D: Appl. Phys. 43, 365102 (2010).
- [42] T. Aschenbrenner, H. Dartsch, C. Kruse, M. Anastasescu, M. Stoica, M. Gartner, A. Pretorius, A. Rosenauer, T. Wagner, and D. Hommel, J. Appl. Phys. 108, 063533 (2010).
- [43] W. Kong, A. Mohanta, A. T. Roberts, W. Y. Jiao, J. Fournelle, T. H. Kim, M. Losurdo, H. O. Everitt, and A. S. Brown, Appl. Phys. Lett. 105, 132101 (2014).

## Conclusion and Future Work

---

### 8.1 Conclusions

The main aims of this thesis were to study and develop the growth of III-nitride materials, including AlN, u-Al<sub>x</sub>Ga<sub>1-x</sub>N, Si-doped Al<sub>x</sub>Ga<sub>1-x</sub>N, and In<sub>x</sub>Al<sub>1-x</sub>N using MOVPE technology in order to investigate their applicability for UV LEDs with emission wavelength between 300 and 350 nm. The study has both developed an understanding of these materials properties and also opened up more questions for analysis.

The growth of high quality AlN on sapphire is much more challenging compared to GaN because of the lower surface mobility of Al adatoms compared to Ga adatoms in addition to the stronger gas phase parasitic pre-reactions of precursors in the case of MOVPE growth of AlN. In Chapter 4, different growth methods of AlN have been described and discussed. The initial pre-treatment on c-plane sapphire were found to be critical for the final AlN epilayer surface morphology. Hence, a proper TMAI pre-treatment was necessary to enable a better Al coverage leading to a robust Al-polar AlN surface.

In addition, several types of surface feature were found in the AlN morphologies using two-step growth process. Among them, the step bunching feature occurred by using a high miscut angle c-sapphire in combination with a high growth temperature. The motion of the steps in a one dimension model has demonstrated that the step bunching feature can be explained by a long diffusion length of Al adatoms and downhill diffusion with the presence of negative SESB. This leads to the investigation of three-step growth, which was able to get rid of the step bunching and enhance the crystal quality of AlN. However, step bunching was found to reoccur on 0.36° miscut angle samples for AlGaN growth.

Finally, by carefully improving the respective growth conditions, we could decrease the dislocation density in AlN significantly by a three-step growth process as verified by reduced linewidths in X-ray diffraction and TEM studies. In an optimized three-step sample grown on

0.08°±0.02° miscut angle of c-sapphire, the (0002) and (10 $\bar{1}1$ ) XRD FWHM values of 2.5  $\mu\text{m}$  thick AlN template were 280 arcsec and 500 arcsec, respectively. The screw and edge type dislocation density in the AlN were reduced to around  $2.2\times 10^8\text{ cm}^{-2}$  and  $1.3\times 10^9\text{ cm}^{-2}$ , respectively, as estimated by TEM. An atomically smooth surface with an RMS roughness of around 0.3 nm achieved over ( $5\times 5\text{ }\mu\text{m}^2$  AFM scale).

In Chapter 5, control of alloy composition, the maintenance of compositional uniformity across a growing layer surface and reduction of dislocation density are essential requirements for the development of high quality Al-rich AlGa $\text{N}$  layers. Firstly, it has been shown that AlN epilayer surface morphology and crystal quality play a crucial role on these parameters for subsequently grown AlGa $\text{N}$  layers. Secondly, Ga desorption was found to be a critical issue leading to high Al content films, but it can be suppressed by increasing  $\text{NH}_3$  and the MO flow rate. Moreover, strain relaxation value in these films increased with increasing Ga content, and was consistently higher for epilayers grown on  $\beta$ -AlN template than on  $\alpha$ -AlN template, attributed to the high edge type dislocation density in  $\beta$ -AlN template. Therefore, Ga incorporation into AlGa $\text{N}$  was found to be less with the increase of the compressive strain due to “strain pulling effect” (compositional pulling effect). Finally, the surface morphology evolution can be summarized by considering the mean adatoms surface diffusion length to the original effective terrace width ratio ( $L_A/L$ ).

One important factor to develop UV LEDs is a high carrier concentration in Si-doped AlGa $\text{N}$  epilayer. In Chapter 6, we have demonstrated that the maximum electron concentration of  $1.3\times 10^{19}\text{ cm}^{-3}$  and  $6.4\times 10^{18}\text{ cm}^{-3}$  were achieved in n-type  $\text{Al}_{0.48}\text{Ga}_{0.52}\text{N}$  and  $\text{Al}_{0.6}\text{Ga}_{0.4}\text{N}$  epilayers grown on  $\alpha$ -AlN templates measured by Hall effect measurements. In this chapter, the impact of threading dislocation density in structural, electrical and optical properties were investigated and discussed. In our experiments, Si doping induced a reduction of compressive strain and an increasing undesired tensile strain in the AlGa $\text{N}$  epilayers and this change increased as the Si doping level increased. At high doping levels, Si-doped AlGa $\text{N}$  epilayers with lower edge type threading dislocation density (TDD) were less changed in their strain state, being crack free, contrary to epilayers with higher edge type TDD. In brief, the level of dopant related strain is strongly dependent on the edge-type and mixed type TDDs. Therefore, low TDD AlN templates can provide less strain relaxation, but more flexibility for any device growth process without crack formation. Meanwhile, we found that the higher rate of relaxation of compressive strain promoted flat surfaces, which could be explained by counterbalance between the surface free energy and the bulk strain energy near the surface.

Moreover, our experiments exhibit that the attempt to incorporate Si donors is accompanied by the spontaneous generation of large numbers of native defects coming from Al-vacancies with their corresponding complexes with oxygen, which show a parasitic cyan emission in lower energy band. The reduction of such defects will finally minimize the parasitic luminescence transitions and is the most indispensable condition for the improvement of the conductivity of Si-doped AlGa<sub>0.5</sub>N. A change in RT parasitic luminescence peak position was observed with variation of the Si/III ratio and Al content, which can be used as a preliminary method to judge the optimal Si doping concentration.

In Chapter 7, we investigated the In<sub>x</sub>Al<sub>1-x</sub>N thin epilayers grown on Al<sub>y</sub>Ga<sub>1-y</sub>N templates and have found that In incorporation efficient is affected by the underlying layer strain state and/or the appearance of V-defects. A smoother surface was observed as growth temperature increases due to promotion of surface diffusion for Al adatoms. In the RT PL measurements, a RT luminescence from In<sub>x</sub>Al<sub>1-x</sub>N band-to-band emission decays significantly with decreasing In content probably owing to carrier localization effect. Meanwhile, a broad peak has been observed at lower energy side (2.0 to 3.3 eV) due to defects, which develops with increasing In composition.

In the growth of InAlN/AlGa<sub>0.5</sub>N MQW structures, exposing InAlN to a higher temperature during the ramp to the AlGa<sub>0.5</sub>N barrier growth temperature (around 1100 °C) will suffer a significant In desorption. To overcome this issue, we have used Q2T technique to grow MQWs, about 2 nm of the AlGa<sub>0.5</sub>N cap grown at the same temperature as the InAlN well which protects the InAlN during the ramp to barrier temperature. As a result, strong RT luminescence from InAlN/AlGa<sub>0.5</sub>N MQWs has been observed in the UV spectral range from 320 to 350 nm, which indicates that the InAlN alloys used as QW active region could be an alternative material for producing an intense emission in the shallow UV spectral range.

## 8.2 Future work

Several issues in III-nitride materials growth beyond the present study are needed to be explored further. The recommended works are listed as below:

### 1) Further optimisation of AlN template growth

An initial improvement of crystalline quality of the AlN/c-sapphire template has been achieved in this thesis. However, there is still a room for further improvement in AlN, (1) improvement in reproducibility and (2) crystal dislocation density. Reproducibility has



always been a concern for AlN growth, mainly due to the reactor memory effects in Aixtron CCS reactor, where  $\text{NH}_3$  as a molecule can be trapped in the reactor including chamber surrounding surfaces and wafer susceptor, and only outgases when the susceptor is operating at high temperature.  $\text{H}_2$  baking about 30 mins before growth does not remove all the impurities in the reactor. Future work, including alternative baking recipes, further optimisation of growth parameters and use of epitaxial lateral overgrowth (ELOG) growth on nanoscale patterned AlN/sapphire template, is necessary to achieve high quality AlN/sapphire templates.

## **2) To enhance the electric properties of Si-doped AlGaN epilayers**

The high TDDs are currently the limiting factor in achieving high free carrier concentration and mobility in Si-doped AlGaN both in terms of the strain effects of silicon interacting with dislocations, and the possibility of preferential defect incorporation around dislocation cores. Regarding the Si-dislocation interaction, the models in the literature are still under debate. Our preliminary result showed that the edge type TDD played a significant effect on the strain relaxation process in Si-doped AlGaN. In  $\beta$  series experiments, our results revealed that the relaxation of compressive strain actually turned into tensile strain and eventually cracked the film. Therefore, in order to further understand how the dislocation interacts with point defects (vacancies), a systematic study of the effect of the crystal quality and Si-doping level in Si-doped AlGaN should be carried on by temperature-dependent PL, SEM-CL imaging and TEM characterization.

## **3) To enhance the PL intensity in InAlN/AlGaN MQWs**

The introduction of InAlN/AlGaN MQWs in the active region has been demonstrated. Meanwhile, in the InAlN thin films experimental series, the effect of strong compressive strain in the underlying template appears to give rise to deep level defects which acts as non-radiative recombination centres, which may suggest a change in defect formation energy with strain. It also might be possible that the formation of In clusters may be reduced under compressive strain, which might allow easier carrier diffusion to defects at room temperature and hence lower internal quantum efficiency (IQE). Variable temperature PL of these samples might allow further understanding here which should take into account the effect of polarization and strain relaxation of their optoelectronic properties.